INTERFERENCE EFFECTS ON THE DRAG OF BLUFF BODIES IN TANDEM

Thesis by
Keith Koenig

In Partial Fulfillment of the Requirements
for the Degree of
Doctor of Philosophy

California Institute of Technology
Pasadena, California

1978
(Submitted May 22, 1978)

ACKNOWLEDGEMENTS

This work has been supported by funds from the Ford-Exxon Energy Research Program of the California Institute of Technology and from National Science Foundation Grants ENG 75-03694 and ENG 77-23541.

I would like to express my gratitude to the many people to whom I am deeply indebted for their aid and service in making this effort possible.

To my advisor, Professor Anatol Roshko, whose foresight initiated this project and whose guidance carried it through.

To George Lundgren, Howard McDonald, Bob Seguine and George Willson for their workmanship and willing assistance in constructing the experimental apparatus.

To William Bettes and Dr. Paul Dimotakis for sharing their wisdom and experience during the experimentation.

To Jean Anderson for her advice and her obliging help in tracking down obscure references.

To Betty Wood for her patience and skills in doing the art work.

To Jackie Beard, Karen Cheetham, Marcia Clark, Susan Dycus and Kathy Franson for their kind, able and unselfish assistance in typing the manuscript.

To Till Liepmann whose talents and many hours of labor have enabled the success of this project.

To my family for their love and support.

And to my devoted wife Brenda, thank you is so inadequate.

ABSTRACT

The objective of this study is to obtain better understanding of the flow over two tandemly positioned bluff bodies in close enough proximity to strongly interact with each other. This interaction is often beneficial in that the drag of the overall system is reduced. Prototypes for this problem come from tractor-trailer and cab-van combinations and from various add-on devices designed to reduce their drag.

The object of the present investigation is an axisymmetric configuration which seems to have first been studied by Saunders (1966). A disc of diameter d_1 is coaxially placed in front of a flat faced cylinder of diameter d_2. For a given ratio d_1/d_2, there is a value of gap ratio, g^*/d_2 for which the drag of the system is a minimum. In the most optimum configuration, $d_1/d_2 = 0.75$, $g^*/d_2 = 0.375$, and the corresponding drag coefficient is 0.01, a remarkable reduction from the value of 0.72 for the cylinder alone. For each value of d_1/d_2, the minimum drag configuration g^*/d_2 appears to correspond to a condition in which the separation streamsurface just matches (joins tangentially onto) the rearbody. Support for this idea is furnished by comparison with results derived from free-streamline theory and from flow visualization experiments. However, when g^*/d_2 exceeds a critical value of about 0.5, the value of C_D, while still optimum, is almost an order of magnitude higher than for subcritical optimum gap ratios. The increase seems to be connected with the onset of cavity oscillations.

Measurements of the velocity field in the vicinity of the forebody have been made using a frequency-shifted laser-Doppler velocimeter. These measurements indicate an order of magnitude difference in the shear stress along the separation surface between optimum subcritical and supercritical geometries.

The drag characteristics of the axisymmetric forebody system are altered by modifying the shape of the component bodies. Modifications that change the conditions at separation from the frontbody, interfere with the cavity flow or effect the flow on the rearbody face can produce significant changes in the forebody drag.

For non-axisymmetric geometry (square cross-sections) the separation surface cannot exactly match the rear body and the subcritical minimum values of drag are higher than for circular cross-sections.

TABLE OF CONTENTS

LIST OF SYMBOLS

a - location of doublet in hodograph plane (Appendix B. 2)

a^2 - $\frac{h^2 + 1}{h^2}$ (Appendix B. 1)

A - point at infinity on free streamline (Appendix B. 2)

A - cross-sectional area

A_1 - frontbody frontal area

A_2 - rearbody frontal area

b - downstream distance to location where free streamlines become parallel

B - bias in measuring a particular particle velocity

B, B' - point on free streamline at which wake becomes parallel (Appendix B. 1)

B - center of plate (Appendix B. 2)

C - center of plate (Appendix B. 1)

C - edge of plate (Appendix B. 2)

C_D - drag coefficient

C_D - forebody-system drag coefficient based on A_2 and freestream dynamic pressure

$C_{D_{min}}$ - minimum forebody-system drag coefficient at optimum gap

$\tilde{C}_D$ - forebody drag coefficient referenced to base pressure (Section 7. 3)

C_{D_1} - frontbody drag coefficient based on A_1

C_{D_2} - rearbody drag coefficient based on A_2

$C_{D_{1f}}$ - front face drag coefficient of a semi-infinite half-body based on final half-body diameter

CD - forebody-system drag coefficient (C_D)

CDD1 - C_{D_1}

CDD2 - frontbody drag coefficient based on A_2

CDFACE - C_{D_2}

C_p - local surface pressure coefficient based on freestream dynamic pressure

C_{p_b}, $C_{p_{base}}$ - base pressure coefficient

C_{p_s} - constant pressure surface or free-streamline pressure coefficient

$C_{p_{slit}}$ - pressure coefficient at base of metric model

$C_p{}^*$ - cavity pressure coefficient at optimum gap

$\overline{C}_p$ - radius weighted average face pressure coefficient (Section 7.3)

d - particle diameter

d - flat plate width (Appendix B.1)

d' - final wake width (Appendix B.1)

d_1 - frontbody diameter

d_2 - rearbody diameter

$\underset{\sim}{ds}$ - vector element of length along free streamsurface

D - point on free streamline at which wake becomes parallel (Appendix B.2)

D - forebody-system drag force

D_1 - frontbody drag force

D_2 - rearbody drag force

D_{1f} - front face drag force of a semi-infinite half-body

D_s - constant pressure surface drag force

D_t - total drag force on metric model

E - point at infinity on free streamline (Appendix B.2)

EOx - offset voltage on MWT force balance processor (Appendix A)

EO_f - fine adjustment offset voltage

EO_c - coarse adjustment offset voltage

f_B - difference in Bragg cell frequencies (Appendix C)

f_{max} - maximum frequency response of a sphere in low Reynolds number flow

$F\text{-}Mx$ - output voltage of MWT force balance processor

g - frontbody to rearbody face gap

g^* - optimum gap for a given frontbody

h - parameter in Schwarz-Christoffel transformation (Appendix B.1)

$h(y)$ - focal volume spatial resolution envelope

I - point at infinity on free streamline (Appendix B.1)

k - U_s/U_∞ (Appendix B.1)

m - order of scattered beams from Bragg cell

m - doublet strength (Appendix B.2)

M - Mach number

M_f - number of fringe plane crossings required for valid measurement

n - index of refraction

n_i - number of fringe plane crossings for the $i^{\underline{th}}$ measurement

$\underset{\sim}{n}_x$ - direction cosine for free streamsurface

N - number of samples or measurements

N_f - maximum number of fringe planes in focal volume

p - local static pressure

p_s - pressure on free streamline

$p(u, y)$ - actual probability density of velocity

$\hat{p}(u, y_c)$ - probability density for measuring u at y_c

P - (% full rotation of potentiometer)/100 (Appendix A)

P - pitching moment (Appendix A)

q - dynamic pressure, $\frac{1}{2}\rho U^2$

q - magnitude of velocity vector (Appendix B.1)

q - complex velocity, u-iv (Appendix B.2)

Q - yawing moment (Appendix A)

r - variable of length in polar coordinates

r - radius from centerline of model

r_1, r_2 - frontbody and rearbody radius, respectively

r_c - corner radius on rearbody face

$r_s(x)$ - radial position of the separation surface

R - rolling moment (Appendix A)

Re - Reynolds number based on rearbody diameter and freestream velocity

RO - coarse offset resistor (Appendix A)

R_s - location of maximum positive C_p on rearbody face

s - fringe plane spacing

S, S' - edge of plate (Appendix B.1)

TF, TR - tabs forward and rearward modifications, respectively

u - streamwise velocity component

U - drag force (Appendix A)

U_1, U_2 - high and low speed shear layer velocities, respectively

U_s - maximum velocity on separation surface or free streamline

U_x - velocity of fringe plane crossings

U_y, U_z - velocities orthogonal to U_x and each other

v - radial velocity component

$u_{\pm}$ - velocity at $\pm 45^\circ$ to freestream direction

V - lift force (Appendix A)

V_L - voltage levels required for valid measurement

VS - vertical spoiler modification

w - complex potential

w - transverse velocity component

w_o - focal volume diameter

W - side force (Appendix A)

W - velocity parameter (Appendix D)

x - streamwise variable of position

y - vertical variable of position

y_c - location of focal volume center

z - complex variable of position

Zx - post-nulling voltage, MWT force balance processor

α - blockage ratio

α - angle of doublet with respect to x axis

δ - shear layer thickness based on maximum u component fluctuations

δ_ω - vorticity thickness

$\delta\nu$ - waveform generator noise

ΔC_D - error in drag coefficient

Δt_i - total time of flight to cross n_i fringe planes

ΔU - $U_1 - U_2$

$\Delta\nu_B$ - difference in Bragg cell frequencies

ϵ - M_f/N_f (Appendix D)

ζ - inverse complex velocity (Appendix B.1)

θ - angle between laser beams

θ - variable of angle in polar coordinates

λ_a - Bragg cell acoustic wavelength

λ_i - incident light wavelength

ν - kinematic viscosity

ν - complex velocity (Appendix B.1)

ν - Bragg cell acoustic frequency

ρ, ρ_f - fluid density

ρ_p - particle density

σ^2 - variance of local volume intensity distribution

τ - instantaneous Doppler signal period

τ - Reynolds shear stress

τ_p - particle response time constant

τ_m, τ_s - maximum shear stress on separation surface or free streamsurface

φ - velocity potential (Appendix B.1)

χ - Joukowski transformation variable (Appendix B.1)

ψ - velocity streamfunction

ω_a - Bragg cell acoustic frequency

ω_i - incident light frequency into Bragg cell

ω_s - Bragg scattered light frequency

subscripts and superscripts

$(\ )_b$ - base

$(\ )_{cr}$ - critical geometry

$(\ )_f$ - face

(x)d(y)g - $d_1/d_2 = x$, $g/d_2 = y$

$(\ )_i$ - i^{th} velocity measurement

$(\ )_{max}$ - maximum value

$(\ )_{min}$ - minimum value

$(\ )_s$ - free streamline or separation surface

$\overline{(\ )}$ - time average or mean value

$\widehat{(\ )}$ - estimated mean value

$(\ )'$ - fluctuation about the mean

$(\ )^*$ - optimum geometry

$(\ )_\infty$ - freestream conditions at infinity

$\langle\ \rangle$ - expected value

Figure

I. INTRODUCTION

1.1 Background

Flows about bluff bodies, that is bodies on which pressure forces dominate due to large regions of stagnating and separating flow, occur in many practical situations and have been the subject of numerous applied and fundamental studies through the years. One class of bluff body flows has received relatively little attention, however, until quite recently. Concern for the efficient use of energy has stimulated considerable interest in improving the fuel economy of ground vehicles by reduction of their aerodynamic drag. This has been shown to be particularly important for tractor-trailer trucks where aerodynamic drag accounts for one-half to two-thirds of the total power required at highway speeds (Hutton 1972, Servais and Bauer 1975). These vehicles are complex examples of a general class of flows in which one bluff body, in this case the trailer, lies in the wake of another, the tractor (or cab). There exists, however, only a very limited fundamental background on such bluff body configurations. Consequently, the understanding required to rationally approach the problem of reducing the drag of these bodies is lacking. With this situation as motivation, the present investigation has been undertaken with the aim of gaining a better understanding of the fluid mechanics associated with the drag characteristics of bluff bodies in tandem.

A substantial body of information now exists on the aerodynamic characteristics of tractor-trailers. Much of this information is reported or referenced in the proceedings of a number of conferences including Lissaman (1974), the SAE West Coast Meeting, August, 1975, and Sovran, et al (1978). One of the principal results from this work has been recognition of the importance of the flow over the vehicle's frontend; forebody drag (that is, the net downstream force exerted on the cab or tractor and face of the trailer) accounts for 60 to 80¢ (Mason and Beebe 1977, Buckley, Marks and Walston 1974) of the total aerodynamic resistance. Because of the relatively small contribution to drag arising from the underbody, skin friction and base drag and the difficulty which exists in reducing these losses (Mason and Beebe 1977, Marks, Buckley and Walston 1977) attention has primarily been focused on the combination of bluff bodies in tandem, the trailer face and the cab, which comprise the forebody.

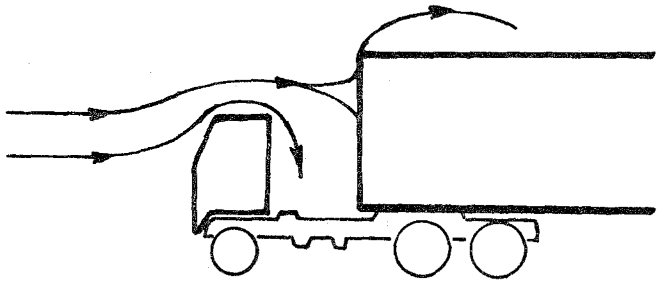

Figure from
Mason and
Beebe (1977)

The forebody is characterized by typical incompressible bluff body flow--large regions of stagnation on the cab and trailer faces and separation from their leading edges--and the drag is quite high. To reduce the drag, this stagnating and separating flow must be effectively eliminated. Streamlining the forebody by providing a bullet-shaped nose is a possible but impractical solution. A more feasible proposal is to effectively round the leading edges of the cab and trailer with fairings or vanes and thereby eliminate separation. This method has been applied (Lissaman 1975, Kirsch and Bettes 1974) with some success, drag reductions of 10 to 15% being reported. Another approach would be to size and position the existing frontbody, the cab, so that its wake interferes constructively or beneficially with the flow about the rearbody face thereby yielding a net decrease in the drag of the combination. This concept of beneficial interference has been used successfully in the past in rather different applications. It has been a common practice for many years in automobile racing to exploit the technique called drafting--that is two or more cars running nearly bumper-to-bumper (Romberg, Chianese and Lajoie 1971). The flow around the two is such that the drag on each is reduced and the group has a higher top speed than a car alone. Another application of beneficial interference has been the nose design of reentry vehicles. A sting or spike protruding from the blunt nose of a reentry vehicle causes a conical shaped separation region to form giving the forebody an effective conical shape and a much reduced drag (Beastall and Turner 1957, Guenther and Reding 1977).

With respect to trucks, a number of drag reduction devices based on this principle of beneficial interference have been developed and marketed recently. The majority of these devices mount to the roof of the cab and effectively change the location and nature of the flow separation on the cab. The intent is to guide the cab generated separation onto the trailer in such a way as to avoid stagnation of this flow on the trailer face and reseparation from the trailer edges. Reductions in total drag of 10-35% have been demonstrated by a number of investigators (Mason 1975, Cooper 1976, Buckley and Sekscienski 1975, Steers, Montoya and Saltzman 1975).

The work done concerning truck drag has been mainly oriented towards improving particular production vehicles. This is, in general, the situation that exists for the whole class of flows about groups of bluff bodies. In numerous instances the flow about groups of buildings, cables or structural members produces undesirable aerodynamic loads and a need exists for understanding how these forces are generated and how they may be reduced. Except for flows about two-dimensional cylinders, these problems have also generally been approached with improving only a particular situation in mind. The present experiment is intended to consider, on a more fundamental level, the fluid mechanics of flow past tandem bluff bodies in order to provide insight into the mechanisms of drag production and to examine the possibilities which may exist for beneficial interference. The results will hopefully be useful in a variety of situations where control of the aerodynamic loading on combinations of bluff bodies is desired.

1.2 Approach

In order to retain some features of practical three-dimensional flows, in particular those associated with tractor-trailers, and still have a geometry simple enough to illuminate fundamental flow phenomena, an axisymmetric configuration as shown in Figure 1 was selected for the initial studies. The object was to investigate the drag of a semi-infinite half-body, in this case a circular cylinder with a flat face. As shown by Prandtl and Tietjens (1934), in potential flow the integral of $(p-p_\infty)$ over the projected frontal area of any semi-infinite half-body in unbounded fluid is zero; suctions near the edges cancel the stagnation region near the center and the forebody is dragless.

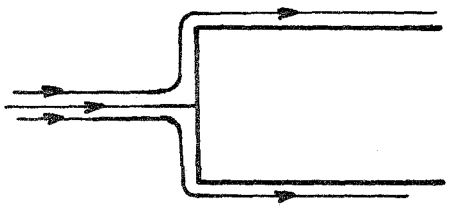

Potential $C_D = 0$

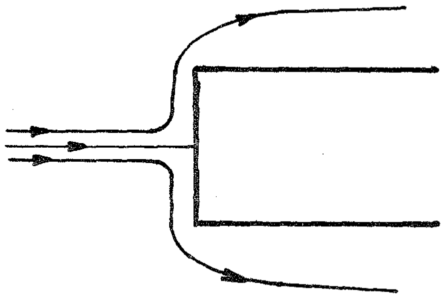

Real $C_D = 0.75$

In the real flow past a flat faced cylinder, however, the pressure gradients required to turn the flow around the corner of the face cannot be established. The flow then separates at the corner; the suction forces on the face are lost and a pressure drag results whose coefficient is nearly 0.75 (Hoerner 1965) based on the cylinder's cross-sectional area. This is quite close in magnitude to the drag coefficient of a trailer without a cab in front (Mason and Beebe 1977). If a disk is now placed coaxially in front of the cylinder the pressures on the cylinder face will be modified and consequently, its drag changed. In addition, the pressures and resulting force on the disk will be altered from the value in a free field, $C_D = 1.2$ (Hoerner 1965). Denoting the disk and the face of the cylinder by subscripts 1 and 2 respectively, the total drag on the forebody system (frontbody and face of the rearbody) will be

$$D = D_1 + D_2 = (C_{D_1}A_1 + C_{D_2}A_2)q_\infty \qquad 1.1$$

where A_1 and A_2 are respective cross sectional areas and q_∞ is the freestream dynamic pressure. The drag coefficient, C_D of the forebody system, based on the rearbody cross-section area is then defined as

$$C_D = \frac{D}{qA_2} \qquad 1.2$$

A configuration very similar to this was investigated by Saunders (1966). Having encountered some very early work done by Eiffel (1910) and described by von Mises (1945) which showed that the total drag of two equal diameter disks placed normal to the flow in tandem was less than that of a single disk alone, when properly spaced, he realized that such a concept might be applicable to tractor-trailer aerodynamics. His results, described briefly in his patent application for a truck drag reduction device, showed that the total drag of a disk-cylinder combination could be minimized for a suitable choice of diameter ratio d_1/d_2 and gap ratio g/d_2. In Saunder's experiments the total drag of the system, including skin friction on the sides and pressure drag on the base of the cylinder, was measured as a function of disk diameter and gap. The relative contributions of each of these components, the mechanisms by which the drag was reduced and the conditions for minimum drag were not, however, established in his studies.

It was the intent of the present work to consider in detail the nature of the flow about the forebody system. To do this the basic model studied was constructed so that the pressure forces acting on only the frontbody and a short forward section of the rearbody were measured. The purpose of the experiment was then to investigate how the drag of the forebody system depends on the various geometrical parameters involved--namely frontbody-diameter to rearbody-diameter ratio, d_1/d_2, frontbody-gap to rearbody-diameter ratio, g/d_2, frontbody shape, rearbody-face corner radius and rearbody cross-sectional shape and how it is distributed between the front and rear bodies. In addition, both qualitative and quantitative descriptions of the velocity and pressure fields about the forebody system were to be made. A description of the manner in which this investigation was carried out and presentation and discussion of the results follow.

II. EXPERIMENTAL DETAILS

2.1 Wind Tunnel

The bulk of experiments were carried out in the Merrill Wind Tunnel (MWT) located in the Graduate Aeronautical Laboratories, California Institute of Technology (GALCIT). This facility is a subsonic, closed circuit wind tunnel with a maximum dynamic pressure of 17 mm Hg corresponding to 60 m/sec at standard conditions. The test section, shown in Figure 2, is nominally 81 cm high by 117 cm wide and 264 cm in length, with a slight divergence in cross-sectional area to reduce the longitudinal pressure gradient caused by wall boundary layers. The test section is completely vented around its perimeter at the downstream end so that the static pressure inside is approximate atmospheric. Power is supplied via a 75 HP electric motor to a constant-speed, three-bladed propellor with continuously variable pitch. Tunnel velocity was monitored by measuring with a 0-100 mm Hg Barocel transducer the pressure difference between two sets of static pressure ports, one set at the exit of the settling chamber, the second at the inlet to the test section. This second set of ports also served as the reference for all other pressure measurements made during the experiments. A time constant on the order of 0.5 seconds was associated with the static pressure rings and tubing leading to the transducer. A pitot-static probe temporarily mounted on the tunnel centerline, halfway along the empty test section, was used to calibrate the tunnel pressure rings. This calibration showed that the difference between the two tunnel rings underestimated the dynamic pressure by 1% at q = 1 mm Hg, to 0.1% at 16 mm Hg. This error was considered acceptable and all the results were based on the uncorrected tunnel-ring measured dynamic pressure. The flow in the test section was also checked for freestream turbulence and flow angularity. These measurements were also made on the centerline, halfway along the test section. A constant temperature hot-wire anemometer with a maximum frequency response of about 500 Hz indicated rms fluctuations in the freestream velocity on the order of 0.4% at a tunnel velocity of 70 ft/sec (21.3 m/sec). It was not possible to make satisfactory measurements at higher velocities because the lifetimes of the wires were too short, apparently due to impacting particles in the flow breaking the wires. Flow angularity was determined by a five port spherical yaw head which indicated that the centerline velocity vector was within 0.3° of the axis of the tunnel. Based on these measurements the quality of the flow was considered satisfactory and no corrections of the indicated data were made.

2.2 Force Balance and Instrumentation

A six component force and moment balance was used to measure the aerodynamic loads acting on the test models. This unique force balance, which was designed and built by Professor Francis Clauser, is depicted in Figure 2 and described in detail in Appendix A. The model to be tested is supported by an aluminum framework which encircles the tunnel. This is, in turn, supported by six links, each of which connect through a flexure and tuning fork type spring to a Schaevitz linear variable differential transformer Model 050 DC-B that produces an electrical output proportional to the displacement of a separate movable core. Details are shown in Appendix A. Forces acting on the model displace the frame, springs and the cores of the Schaevitz coils. The resulting outputs, measured as voltages, are combined in an analog computer whose output is the desired force or moment in units of 1 volt = 1 kg of force or 1 kg-m moment. The schematic for the analog computer as it was used is also presented in Appendix A. The balance provides static load zeroing capability and had an RC time constant of 1 sec. A change in loading of 1 g is detectable. The output is linear and within 1% (on the lowside) of being 1 volt/kg over a load range from 10 g to 7 kg applied in the streamwise direction (pure drag). During testing the balance calibration was checked very frequently and no significant deviation was observed from the above characteristics; no corrections were required. Throughout the experiments the same electronics were used. Tunnel dynamic pressure was monitored with a Barocel Transducer 523-11 and Barocel Electronic Manometer 1083-54. Force and moment voltages were measured with a Keithley Digital Multimeter, Model 160. Model pressures were manifolded into 24 port Scanivalves and measured by a Barocel Transducer 511-11 feeding a Barocel Electronic Manometer 1014A and a Hewlett Packard Timer -Counter-DVM 5326B which provided variable integration times from 0.1 to 10 seconds. Instrument calibrations were periodically checked and all recommended maintenance and warm-up procedures followed.

2.3 Wind Tunnel Model

The basic model configuration with which most of this work was done is shown in Figure 1. The model was composed of a metric (i.e., connected to the balance) frontbody and a part metric, part non-metric rearbody. The metric portions of the model comprised the forebody system. The non-metric part of the rearbody was an axisymmetric, hollow cylinder 20.3 cm (8 in) in diameter, constructed from wood and plexiglass. Model blockage based on this diameter was 3.5% of the tunnel cross-sectional area. This dummy shell was rigidly connected to the tunnel walls by hollow streamlined struts but could be adjusted vertically and in yaw and pitch to provide alignment. The metric portion of the model, also axisymmetric, was connected to the balance by solid steel shafts running through the streamlined struts and a 1.25 in (0.49 cm) diameter aluminum tube of "sting" perpendicular to the shafts which could be moved longitudinally relative to the rearbody in order to change the frontobdy to rearbody gap. The sting was provided at each end with internal containers half-filled with lead shot to damp vibrations caused by unsteady aerodynamic loading. The metric part could also be adjusted vertically and in pitch and yaw. Care was taken to insure that no contact was made between the metric and non-metric components between which was a narrow, 0.16 cm (1/16 in) slot. The pressures in this slot were measured by eight static pressure orifices, 0.08 cm (1/32 in) in diameter, located on the dummy rearbody. The downstream end of the sting was also provided with a pressure port. Measurement of these pressures permitted the forebody system drag to be determined by subtracting from the total force acting on the forebody system the pressure forces on the metric model base. The face of the rearbody, which was flat with a sharp corner, had fourteen static ports staggered along two perpendicular radii to provide pressure distributions on the face and give some indication of asymmetries in the flow. Certain frontbodies, a special sting and the tunnel walls were also instrumented with pressure taps to yield more complete information on the cavity pressures and model blockage effects.

A variety of frontbodies could be mounted on the sting. However most of the measurements, unless otherwise noted, were made with machined, flat, circular disks 0.32 cm (1/8 in) thick with sharp, non-bevelled edges. The model was designed so that in addition to the force acting on the forebody system, the force acting on the frontbody alone could also be measured. This allowed the various contributions to the total drag to be determined.

2.4 Operational Procedures and Accuracies

The drag and pressure measurement procedure was as follows. With a given model configuration and the tunnel running at idle, the static loads indicated on the force balance were nulled. The tunnel was then brought up to the desired steady speed. The forces and moments were observed and hand recorded to four significant figures. The model pressures were time averaged and also hand recorded to four significant digits, the averaging time required depending on the degree of unsteadiness. The tunnel temperature was recorded. Observations on the nature of the flow, for example with the extensive use of tuft patterns, were made. If the given configuration was being run over a range of velocities, measurements were made with the speed both increasing and decreasing to check for hysteresis effects. At the end of a test run, with the tunnel again at idle, the forces were checked to insure that they had returned to zero, as a precaution against mechanical interference or electrical failure. Measurements were made at speeds from 25 to 190 ft/sec (7.6 to 59.7 m/sec); corresponding Reynolds numbers, Re, based on the rearbody diameter, d_2 = 8 in. (20.3 cm) and standard atmospheric conditions were 1×10^6. At higher velocities some model vibration existed but did not appear to seriously affect the results, as nothing unusual was observed. Most of the data points were measured at least twice, the more significant points up to twenty times. The average standard deviation in the calculated drag coefficients, for those cases with multiple measurements, was $\Delta C_D = \pm 0.004$ which corresponded to a measurement repeatability of ±12 g on the force balance or ± 0.031 mm Hg from the slot pressures at 8 mm Hg dynamic pressure. Model-induced flow unsteadiness, slight model asymmetries and misalignment with the mean flow vector were the probable sources of most of the measurement inaccuracies. The use of plexiglass and wood for much of the model introduced some asymmetries, while the different weights corresponding to the wide variety of gaps and frontbodies changed bending moments on the sting, and caused slight changes in pitch between configurations which were difficult to uniformly correct. However, due to the very large range of drag coefficients which were observed (over two orders of magnitude) and the emphasis in this study on relative C_D levels, the degree of repeatability in the measurements is satisfactory and does not represent any serious limitation on the results or conclusions which might be drawn from them.

2.5 Model Variations

Two other versions of the MWT model were also studied. On one of these the rearbody face of the axisymmetric model with a sharp corner was replaced by a face whose corner had a 1 in. radius. Pressure taps were included in the same locations as before and the same circular disks and frontbodies were used.

The third model was one of square cross-section, nominally 8 in. x 8 in., formed by sliding a square shell over the non-metric axisymmetric rearbody and replacing the circular cross-section metric parts with square components. The rearbody face had sharp edges and 25 pressure ports distributed over it. The frontbodies were square plates or a cab-like body designed to approximate a tractor-trailer. Each of these models was tested in a manner similar to that of the axisymmetric-sharp corner model, although not quite as extensively.

2.6 Flow Visualization

As a supplement to the wind tunnel work, flow visualization tests were conducted in the Free Surface Water Tunnel (FSWT)

(Ward 1976) also located in GALCIT. This facility has a 20 in. x 20 in. (7.87 cm x 7.87 cm) constant area test section 8 ft (2.44 m) in length. The upper surface is normally free although a cover plate may be used. Maximum speed is 25 ft/sec (7.62 m/sec); the Froude speed is 7.33 ft/sec (2.33 m/sec), at which a large standing wave appears. The flow visualizations were done at a speed much lower than this to prevent serious gravity wave effects. The models constructed for this facility were entirely non-metric and were essentially one piece except for the moveable frontbody. The frontbodies were provided with four dye injection tubes whose axes each made an angle of approximately 11° with the frontbody face. Diluted food coloring served as the dye and was gravity fed to any desired combination of the injection tubes. The 11° tube angle was a compromise between minimal disturbance of the flow field by the dye injection and physical constraints in model construction.

Each of the three basic rearbodies was studied with flow visualization for a variety of frontbodies. All observations were made at a flow speed of 3.3 ft/sec (1 m/sec) and a Reynolds Number of 1×10^5. This speed was high enough to allow comparison with the wind tunnel results and yet low enough to avoid serious surface effects and to minimize dispersion of the dye. Photographs of the resulting flow patterns were made using a 35 mm SLR camera with a 100 mm focal length F3.4 lens at shutter speeds from 1/15 to 1/1000 sec and either Tri-X black and white print film or high speed Ektachrome tungsten color slide film.

III. RESULTS FOR CIRCULAR CROSS-SECTION

3.1 Measurement of the Forebody-System Drag Coefficient

A prime objective of this study was to obtain as complete an understanding as possible of the incompressible aerodynamic behavior of a sharp-cornered axisymmetric rearbody with simple, flat-disk frontbodies situated coaxially in front. For this work, the most important characteristic is the forebody-system drag coefficient, C_D, which is presented in Figure 3, as a function of gap ratio, with disk-diameter ratio as the parameter. This coefficient is defined by

$$C_D = \frac{\text{Force from balance } - \int (p-p_\infty)dA \Big|_{\text{slit}}}{\frac{1}{2}\rho U_\infty^2 \, (\pi/4 d_2^2)} \qquad 3.1$$

The values presented are averages of several independent measurements (as many as 20), and the average standard deviation in the value of C_D is $\pm$ 0.004. No corrections for blockage, buoyancy (that is, the longitudinal tunnel pressure gradient), skin friction on the metric part of the rearbody and sting or error in transducer and force balance response have been applied. The quantitative values of these corrections are not clear although their qualitative effects can be assessed.

Blockage has the most significant effect on the measured drag, although, in this case the effect is rather surprising. For wind tunnel models on which the entire drag force is desired, blockage tends to cause the measured drag to be higher than the value in a free field. An example of the correction required is given in a method developed by Maskell (1965) and modified by

Cowdrey (1968). Here solid and wake blockage produce a change in drag of

$$\frac{\Delta C_D}{C_D} = \frac{\text{-Maximum Wake Cross Sectional Area}}{\text{Tunnel Cross Sectional Area}}$$

primarily due to increased suction on the downstream facing surfaces (i.e., the base). In the present case the base pressures on the metric portion of the model are subtracted out; only the forebody is of interest. The effect of blockage is to increase the local velocity past the model and lower the pressures acting on the surface. Consequently the base drag is increased, but the forebody drag is reduced. The magnitude of the effect can be seen by applying the result for potential flow (as shown by Morel 1978 and discussed in more detail in Section 7.3).

From Equation 3.1

$$C_D = \frac{D_{total} - \int (p-p_\infty) dA \Big|_{slit}}{q_\infty A}$$

Let $(\ )_b$ => slit and $(\ )_f$ => face.

Then

$$D_t = \int p dA_f - \int p dA_b = \text{total drag on body.}$$

Therefore

$$D_t = \int (p-p_\infty) dA_f - \int (p-p_\infty) dA_b + \overbrace{p_\infty \int dA_f - p_\infty \int dA_b}^{0}$$

or

$$D_{forebody} = D_t + \int (p-p_\infty) dA_b = \int (p-p_\infty) dA_f$$

or

$$C_D = \frac{\int (p-p_\infty) dA_f}{q_\infty A}$$

As shown by Morel (1978), for potential flow past a body in a tunnel,

$$C_D = \frac{\int (p-p_\infty) dA_f}{q_\infty A} = \frac{-\alpha}{1-\alpha}$$

where

$$\alpha = \frac{A_{\text{model}}}{A_{\text{tunnel}}}$$

is the blockage ratio. Consequently, for any finite blockage ratio the measured forebody drag is less than the free field value. For this experiment $\alpha = 0.03$ and the potential flow value of C_D is -0.03. The wake blockage will increase the effective α and cause further reduction in C_D from the free field value.

Correction for buoyancy is not applicable because the metric model base pressures are subtracted out. Skin friction can either contribute in a positive or negative manner to the total measured force depending on the extent of separation which in turn is a function of geometry. In any case its effect is at most $\Delta C_D = 0.01$, an estimate based on measurements of streamlined forebody drag for which there is no separation and essentially only skin friction (Norris and McGhee 1966). Calibrations of the instrumentation indicated that both dynamic pressure, q, and drag force were slightly underestimated on the average by 1% or less. These instrument errors are cancelling to first order and thus are quite negligible. The coefficients shown in Figure 3 are for Re $\doteq 5 \times 10^5$. As will be discussed later, this configuration displayed no significant dependence on Re above 10^5 save for one isolated geometry and thus the values at Re $\doteq 5 \times 10^5$ are considered representative of the behavior of this model at higher values of Re.

3.2 The Drag Coefficient of a Blunt Faced Cylinder

The value of C_D of the blunt faced cylinder with no front-body is determined in this experiment to be 0.722. Stanbrook (1964) has gathered measurements of the drag of blunt and hemispherical-faced circular cylinders over a large range of Mach numbers, M, from a variety of researchers. He has corrected these measurements when necessary to yield what he claims is the pressure drag coefficient acting on the cylinder face. To this blunt faced cylinder data he has fitted the curve $C_D = 0.758 + (0.296)M^2$, which agrees fairly well with the data Stanbrook has collected. The present experiments were run primarily at $M = 0.12$; applying Stanbrook's formula yields $C_D = 0.762$ and a discrepancy in the coefficient of 0.04 or 5%, which is considerably greater than the estimated error. Stanbrook had no data on blunt cylinders for $M < 0.3$; instead, he used $\int C_p dA$ over the face of a disk as reported in Fail, Lawford and Eyre (1959). In addition, the only values shown for $M < 0.4$ come from Polhamus (1957) who measured the entire force acting on a blunt cylinder of aspect ratio 10.94 (0.2% blockage, Re $= 7.3 \times 10^5$). Polhamus corrected only for base drag. Stanbrook applied the additional correction for skin friction including the effect of the face separation zone. Some scatter exists in Polhamus' data for $M < 0.5$ and an extrapolation of his results to the test Mach number of the present data is rather uncertain. Hoerner (1965) has estimated C_D of a blunt cylinder to be ~ 0.8 based on cavitation test pressure distributions from Rouse and McNown (1948). However, only 5 face taps were used in that series of tests and again the accuracy of the calculation is suspect. Figure 4 presents the distribution of pressure coefficient, C_p, along one radius of the blunt circular cylinder face (assuming symmetry) determined in the present study and compared with the results of Rouse and McNown. Although the shapes are similar, their results show larger values for C_p than the present data which would integrate to give a larger face drag coefficient, as Hoerner suggests. The tests of Rouse and McNown were conducted in an open throat water tunnel with solid blockage of 0.5% and $Re = 2.6 \times 10^5$. The water jet around a body in an open throat tends to expand into the surrounding air. If the jet overexpands, there will be a decrease in the jet freestream velocity causing a pressure rise in the mean flow past the body. This could account for the higher outboard pressures observed by Rouse and McNown. They reported, however, that there was no change in model surface pressures as blockage was increased, even to area ratios of 10%, suggesting that the jet expanded only enough to accommodate the blockage and the freestream velocity remained unperturbed. In contrast to these references, Norris and McGhee (1966) indicate that $C_D = 0.72$ for $M = 0.2$. They too measured the entire force acting on a 3.55 aspect ratio cylinder (0.8% blockage, $Re = 1.8 \times 10^6$) which they then corrected for base drag and skin friction but without including the effects of the face separation zone on the skin friction. The base C_p they observed was -0.04, a value somewhat less negative than values reported by other researchers. For example, Merz, Przirembel and Page (1977) collected a number of base pressures available in the literature and found $-0.1 \le C_p \le -0.2$. Norris and McGhee have speculated, based on their relatively high base pressure and on a result of Stanbrook (1966) showing that the separation bubble formed by a blunt cylinder reattached 3½ diameters downstream, that mean reattachment was occurring near the base and influencing its pressure. This in turn may have altered pressures in the recirculation region and at the face corner, thus influencing the drag. In the present experiment, tufts indicated that reattachment was well upstream of the base which had a mean $C_p \doteq -0.2$ and presumably there was no significant interaction between the model face and base. There are, apparently, very few other studies of blunt faced cylinders to which comparison can be made. Some results and references for cylinders of more rounded shape, intended for torpedo and submarine use, are available in the Hydroballistics Design Handbook (1955) although none of these are really applicable to the geometry in question. Effects of Re, freestream turbulence, M, corner radius, free surfaces, cavitation and measurement techniques may partially account for the discrepancies which have been observed, although incomplete information has been provided to do so. It is quite likely that blockage is largely responsible for the lower value of C_D found in this study compared to the values reported from other tests. The present blockage is 3% while the other studies discussed here have less than 1% solid area blockage. More importantly though, the lack of data and the disagreement in what does exist, even for such a basic body as this underline the need for more work in this area. Insomuch as there is disagreement and no generally accepted value for the incompressible drag coefficient of a blunt-faced cylinder exists, the value of 0.722 will be taken as the reference C_D for this work.

3.3 The Forebody-System Drag Coefficient

Figure 3 reveals three rather significant characteristics of the forebody behavior. First, nearly every combination of disk and gap used in front of the cylinder reduces the forebody drag; only with large disks at gap ratios greater than $1\frac{1}{2}$ does the drag exceed the free cylinder result of 0.722. The broad range of geometries for which drag is reduced would permit a great deal of flexibility in applying the shielding concept to practical situations. A second and rather remarkable feature is the existence for certain disk-gap combinations of extremely low net drag. In particular, for $d_1/d_2 = 0.75$, $g/d_2 = 0.375$ the measured value of C_D is only 0.010, a value hardly greater than that of a well shaped solid forebody system without separation, for which the drag is essentially skin friction. (Measurements presented later for such bodies give $C_D < 0.01$). Although only one configuration achieved $C_D = 0.010$, there exists a reasonably wide range of geometries whose $C_D < 0.05$, again making this concept quite attractive for design guidance, since it is possible to be "off design" in terms of geometry and still maintain a low drag configuration. The third feature to notice is the existence, for a given diameter ratio, of a gap ratio at which the drag is a minimum. It is important to observe that this optimum gap ratio, g^*/d_2, and the associated drag coefficient, $C_{D_{min}}$, are functions of the diameter ratio and, especially, that there is a substantial spread in the values of $C_{D_{min}}$ which are obtained.

Most of the curves presented in Figure 3 are reasonably smooth with only one extremum, a minimum, at g^*/d_2. There are several exceptions to this, however, notably the cases $d_1/d_2 =$ 0.531, 0.563 and 0.875. The first two of these show two closely spaced minima in C_D, the one at the larger g/d_2 being optimum. This behavior was repeatable and apparently does not represent experimental error. The flow for these configurations was fairly unsteady and this may account for the unusual shape of the curves. The curve for $d_1/d_2 = 0.875$ has a very sharp minimum at $g/d_2 =$ 0.094 and a much less pronounced minimum at $g/d_2 = 1.0$. Both of these were quite repeatable. The rather dramatic minimum at $g/d_2 = 0.094$ corresponded to a very steady and stable flow field, even when rather severe attempts were made to perturb it, as will be discussed later.

3.4 Asymptotic Limits

The asymptotic behavior for small and large gaps also deserves comment. For $g/d_2 \to 0$, C_D should approach the value of the blunt cylinder, 0.722. Because the disks used in this experiment were of finite thickness, there will be a small step on the cylinder face even at zero gap which could influence the flow and cause a departure from the simple blunt cylinder drag. In the limit of infinitely large separation, $g/d_2 \to \infty$, the drag should approach the sum of the free field values of each body separately, that is,

$$C_D \to C_{D_2} + C_{D_1} (d_1/d_2)^2 \doteq 0.722 + 1.15 (d_1/d_2)^2 \qquad 3.2$$

where 1.15 is nominally the value of C_D of a disk in a free field.

3.4a Flat Plate Drag

The drag of flat plates and disks normal to an unbounded uniform stream has been the subject of investigation for many years, Stanton (1903), Lanchester (1909), Eiffel (1910), Prandtl (1910), Weiselsberger (1915) and Prandtl (1923) being among the very early researchers interested in this type of flow. Other important studies include those by Shoemaker (1926), Knight (1926), Irminger and Nøkkentved (1930), Schubauer and Dryden (1935) and Fail, Lawford and Eyre (1959) who all considered disks or plates in air. Numerous cavitation tests, a number of which are collected or referenced in Eisenberg and Pond (1948), Plesset and Perry (1954) and Strück (1970) also exist. The principal message to be learned from this vast background of work is that the free field drag coefficient of a disk or plate has not been well established. It appears that in air, with free stream turbulence no greater than 3%, the value for C_D of a thin square plate or a circular disk lies between 1.1 and 1.2 with an average base pressure coefficient of ~ -0.4 for $10^4 < Re < 10^6$. The information available does not permit a more accurate statement of the drag. In water the drag coefficient depends approximately in a linear manner on the cavitation base pressure and ranges from 0.8 for $C_{p_{base}} = 0$ to 1.25 for $C_{p_{base}} = -0.56$ with 10% scatter throughout. As with the blunt faced cylinder, there are numerous effects which may be responsible for the variation in the measured values of the disk drag coefficient, e.g., freestream turbulence, blockage, model details, Re, M and cavitation effects and measurement technique peculiarities. Despite the disagreement about the exact value, two characteristics important to the present work are clear: the drag is large, $C_D \doteq 1.15$, and it is apparently the same for square plates and circular disks.

3.4b Influences of the Sting

For large gaps the forebody-system drag does exceed the blunt-faced cylinder C_D and appears to tend toward the asymptotic value given by Equation 3.2. The actual large gap behavior is slightly different than predicted by (3.2) however, and can be attributed to the influence of the finite diameter sting used to connect the frontbodies and rearbody face together. For large gaps and small d_1/d_2 in particular, the skin friction on the sting can become a sizeable percentage of the total frontbody drag. In addition, the presence of the sting reduces the areas on the frontbody and rearbody face which are exposed to pressure forces. The values of 0.722 for the cylinder face and 1.15 for the disk assume that the entire surfaces implied by d_2 and d_1, respectively, are subject to pressure forces; with the sting in place, the disk base area and rearbody face area are in fact reduced by $(\pi/4)\, d^2_{sting}$. A third contribution of the sting is its role in creating a rearward facing step on the disk and a forward facing step on the cylinder. In each case the flow field and pressure distribution will be modified from the free field behavior and will affect the drag. Although the sting alters the disk-cylinder behavior, its influence should only be important for very large gaps. For the configurations of greatest interest in this study the gaps are not large and corrections for sting interference, the exact nature of which are anyway unknown, have not been applied.

3.5 Results from Flow Visualization

3.5a The Blunt Faced Cylinder

The forebody-system drag coefficient (Figure 3) represents, in some way, the integrated effect of the flow field which surrounds a particular bluff body combination. Considerable insight into the nature and details of the flow itself can be obtained from simple flow visualization experiments. Figure 5 presents some results from visualization by dye injection in the water tunnel. For reference, Figure 5a shows the rearbody without the frontbody or sting support. As might be expected, there is a large region of separated flow which extends $1\frac{1}{2}$ to 2 diameters downstream of the face corners and accounts for the high value of $C_D = 0.722$. During the force measurements tufts located on the models were also carefully observed. For the rearbody-alone configuration, the tufts indicated reversed flow for a distance of a little more than $1\frac{1}{2}$ diameters downstream, as was also shown by total pressure boundary layer rakes mounted on the rearbody side. Pressure distributions given by Rouse and McNown (1948) show that C_p along the cylinder recovers to zero near 4 diameters. Stanbrook (1966) observed reattachment for $M = 0.70$ ($C_D \doteq 0.9$) to occur at $3\frac{1}{2}$ diameters. By $M = 0.7$ the flow near the face corners is transonic and it is not obvious that this result is applicable to the present case. As was noted earlier, Norris and McGhee (1966) inferred from their rather high base pressure that the flow over their model also reattached roughly $3\frac{1}{2}$ diameters downstream. Ota (1975), on the other hand, made detailed velocity and pressure measurements in the separated region formed by a blunt cylinder with 3.3% blockage, $Re \sim 5 \times 10^5$, aspect ratio 10 and 0.8% free-stream turbulence and found the flow to be fully reattached and C_p recovered by 1.6 diameters. The effects discussed earlier in reference to the drag coefficient of the blunt cylinder face may also explain this observed variation in reattachment length, although sufficient information for determining the exact causes as well as establishing any correlation between the drag coefficient and reattachment length is again lacking. In spite of these differences, it is clear that the blunt faced cylinder is characterized by a substantial region of separation downstream of the face and a correspondingly high drag coefficient.

3.5b Results for $d_1/d_2 = 0.75$

Figure 5c shows the flow for the disk $d_1/d_2 = 0.75$ at a gap slightly less than optimum, where $C_D = 0.021$. Figure 5d shows the flow for this disk at the optimum gap, $C_D = 0.010$. In both (5c) and (5d) the separation surface from the disk may be seen to join smoothly onto the edge of the rearbody, becoming a turbulent boundary layer on that body. The thinness of the separation surface and the small scale of the organized structures inherent in this shear layer are also quite apparent. Curiously, the reattachment at optimum (5d) does not appear to be quite as smooth as the flow in (5c); there is a small hump just upstream of the rearbody face. Nevertheless, in both cases the interference between the disk and rearbody flows is such as to eliminate the massive separation associated with the blunt faced cylinder (see Figure 5a) and the resulting drag is very low. In contrast, Figures 5e and 5f show the same disk at gaps much less and much greater than optimum, the values of C_D being 0.222 and 0.184 respectively. These values of C_D, an order of magnitude larger than optimum, are still only one-fourth to one-third the blunt cylinder result. The photographs show that the total separation is somewhat lessened, which accounts for the drag reduction. In (5e), however, there is stagnation on the rearbody face and reseparation, while in (5f) the thickness of the shear layer is increased and there are indications of large scale wake oscillations on the order of the rearbody diameter. In these cases, the failure of the separation surface to join smoothly onto the rearbody is manifested in an increase in forebody drag from the optimum case.

3.5c Unsteadiness

In general, the degree of unsteadiness in the flow about the forebody system as observed from dye, tufts and model virbrations increases with increasing C_D. Tufts on the rearbody sides were virtually motionless for the very low C_D configurations but exhibited extreme fluctuations and reversals at high C_D. Likewise the model itself vibrated considerably when the drag was high (although the dampers effectively kept the absolute amplitude low), sometimes with several distinct frequencies presumably due to higher frequency vortex shedding and lower frequency large scale wake oscillations.

3.6 Breakdown of the Forebody Drag

The contributions to the total drag from the disk and cylinder face are shown in Figures 6 and 7 respectively. The value of C_D in both cases is based on the rearbody diameter, d_2. Two independent methods were available to determine this drag breakdown--direct measurement of the disk force and integration of the rearbody face pressures. Agreement between the two methods varies from 0 to 30% of the disk drag, the larger discrepancies being for the smaller disks. For the blunt faced cylinder by itself, the face integral gives $C_D = 0.732$ as opposed to $C_D = 0.722$ from the force measurements, a disagreement of 1.3%. Presumably the errors are due to incomplete knowledge of the pressures near the face edge--the most critical region, since the pressures are weighted by their radii in determining C_D. The drag coefficients presented in Figures 6 and 7 are determined from direct force measurements for $d_1/d_2 \leq 0.375$ and from $\int C_p r dr$ for the remaining disks, since the disagreement for $d_1/d_2 > 0.375$ is less than 5% and more pressure distributions were available for presentation.

3.6a Disk Contributions

Figure 6 shows that the disk drag is always positive and reaches a maximum near the optimum gap, g^*/d_2. The curves level out for $g/d_2 > \frac{1}{2}$ which indicates a decreasing rearbody influence. The following table presents the values of C_D for several disks based on disk diameter at the maximum for each disk and up to the largest gap observed, $g/d_2 = 3$. The maximum values are much larger than the free field values due to increased base suction pressure, as will be discussed later. The large-gap drag coefficients are approaching the free field values but, as was discussed previously, are somewhat different.

Table 1 Drag coefficients of the frontbody based on d_1

d_1/d_2	$\frac{g}{d_2}@C_{D_{max}}$	$C_{D_{max}}$	$C_D@\frac{g}{d_2}=1.5$	$C_D@\frac{g}{d_2}=3.0$
0.25	1.5	1.384	1.384	
0.375	1.5	1.056	1.056	
0.5	3.0	1.131	0.995	1.131
0.625	0.75	1.247	1.088	
0.75	0.25	1.606	1.167	1.182
0.875	0.094	2.564	1.249	
1.0	0.75	1.410	1.324	1.265

3.6b Rearbody Face Contributions

The face drag, shown in Figure 7, displays trends similar to those of the forebody-system drag, that is a decrease from the simple blunt faced cylinder value, the possibility for very low drag and a minimum very near g^*/d_2 for a given disk. The drag also decreases as the disk diameter increases (up to a point) for a fixed gap. The drag reductions on the face in some cases are so great that C_D goes negative; the force on the face is actually a thrust.

3.6c Results for a Given Disk

The forebody-system drag and its breakdown for a given disk are presented in Figure 8 for selected geometries, each Figure referring to a particular d_1/d_2. The curve labelling is as follows: CD refers to the forebody-system drag coefficient, CDFACE to the rearbody face; CDD1 is the drag coefficient of the disk based on the disk diameter and CDD2 is the disk drag coefficient based on the rearbody diameter. An interesting characteristic displayed here is the flatness of the curves beyond the drag minimum for each disk. This is partly due to the scale of the Figures, but also indicates a slowly varying, long range interaction between the front and rear-bodies. The only curve that departs from this behavior is the one labelled CDD2 is Figure 8a. This particular case is not actually a disk but just the sting, protruding by itself. Inaccuracies in obtaining its drag coefficient are greatly amplified by the area ratio, $(d_1/d_2)^2 = 41$, which may partly account for the erratic behavior. Another factor may be variations of the reattachment and flow on the sting itself due to rearbody influences. Nevertheless, these

Figures are quite useful in identifying the source of the drag reduction. It is clear that the decrease in rearbody face drag greatly outweighs the drag increase of the disk and the net result can be a nearly dragless forebody.

3.7 Rearbody Face Pressure Distributions

Pressure distributions along the model surfaces which form the gap or cavity walls are especially helpful in understanding and explaining the drag behavior of the forebody. Figures 9 through 16 present the pressure coefficients, $C_p = \frac{p - p_\infty}{\frac{1}{2}\rho U_\infty^2}$, along a radius of the rearbody face for a number of disk-gap combinations. Accompanying each distribution is the drag coefficient at Re = 5×10^5 and, in many cases, a photograph of the flow at or near the gap in question. The measurements were actually made along two mutually perpendicular radii with the pressure taps staggered so that flow asymmetries or model misalignments could be detected. Deviations from pure axisymmetry were never totally eliminated however, and consequently some distributions display a zig-zagged or skewed nature. This slight skewness does not alter the basic results though, as will be shown, and can be disregarded.

3.7a $d_1/d_2 = 0.156$

Figure 9 gives the rearbody face pressure coefficients with the sting alone as a frontbody ($d_1/d_2 = 0.156$); gap (or sting length, in this particular case) increasing upward on the Figure. For all gaps, fairly large, positive pressures exist over the center three-fourths of the face, with the pressure decreasing but remaining positive near the edge. Thus, in all cases the separated flow from the sting stagnates inboard of the rearbody face edge. The flow then accelerates radially outward, reseparates at the edge and reattaches downstream. For this frontbody the rearbody drag is not very low, although comparison with the pressure distribution on the blunt faced cylinder with no frontbody (Figure 4) shows the face pressures even at the stagnation point are somewhat less and there is a net drag reduction. At intermediate gaps (c and d) the pressures inboard of $C_{p_{max}}$ decrease, then increase again near the center. This type of distribution is typical of pressures on the walls of an open cavity with flow over it, of which numerous examples abound (Johannesen 1955, Roshko 1955, McGregor & White 1970, Charwat et al 1961, Fox 1964, Rossiter 1964). It also suggests that recirculation exists within the cavity. The decreasing pressure corresponds to acceleration of the flow radially inward. Near the cavity bottom the flow must decelerate and turn again causing the inboard high pressure region to occur.

Study of the distributions in Figure 9 in sequence, starting with the smallest gap, reveals a migration of $C_{p_{max}}$ first radially outward then inward again. The location of the maximum positive pressure, $C_{p_{max}}$, is slightly outboard of the mean reattachment location of the frontbody separation streamsurface. Thus the radial motion of $C_{p_{max}}$ suggests the spreading and closing of the mean wake with downstream distance which would be observed were there no rearbody. This behavior may also be due to reattachment onto the sting itself and then reseparation at the forward facing step formed by the sting-rearbody face junction. Flow visualization indicates, however, that the separation does not reattach onto the sting for $g/d_2 < 0.75$; and, therefore, the stagnation point migration would appear, at least for $g/d_2 < 0.75$, to represent the downstream development of the mean sting wake.

As would be expected, for $d_1/d_2 = 0.156$ the changes in the average level of the face pressure and the shape of the distributions as the gap is increased closely agree with the behavior of the face drag coefficient in Figure 7. The gap for minimum face drag is $g/d_2 = 0.75$, which also is the gap for minimum forebody drag. Figure 9 shows that the face pressures at this gap are the least, thus demonstrating that this configuration should indeed give a minimum in face drag. The larger pressures at other gaps correspond with their non-optimum values of drag coefficient.

3.7b $d_1/d_2 = 0.25, 0.375$

Figures 10 and 11 present pressure distributions for diameter ratios of 0.25 and 0.375 respectively. There is little qualitative difference between the influence of these disks on the rearbody face and that of the sting. The pressures are all positive and drop off at the edge. A fairly broad stagnation region always occurs inboard. The decrease in both the face and forebody-system drag as the gap in increased up to g^*/d_2 and then the rise again in drag with further lengthening of the gap corresponds closely to changes in the pressures displayed by these profiles. Migration of the stagnation point with increasing gap is also observed for each of these frontbodies. There are, however, important systematic differences between the results for each diameter ratio as far as the pressure coefficient magnitude is concerned. For a given gap, the average pressure level on the face decreases with increasing d_1/d_2; the shielding effect of the frontbody is being enhanced as its relative size increases. In addition, the cavity-flow type distributions are becoming more pronounced indicating increased recirculation.

3.7c $d_1/d_2 = 0.5$

Distributions for $d_1/d_2 = 0.5$ are given in Figure 12. The trends noted for smaller disks are also evident here with one important difference -- for g/d_2 near and at optimum, the face pressures become negative. The pressures are such as to bring the average face C_p below zero, and the face drag is consequently also negative. It is, in effect, thrusting upstream. The concept that the frontbody simply shields the rearbody from stagnation of the freestream flow is not sufficient to explain the existence of negative rearbody face pressures. Instead, the development of a strong recirculating flow in the cavity along with the negative pressures associated with the base of the disk, which is now of sufficient relative size to act as more than just a shield or wind break, are responsible. The pressures do not become greatly negative however, because the flow associated with these geometries is rather unsteady. The separation streamline flaps considerably, occasionally bringing high velocity fluid from the external stream into the cavity; this flow then stagnates on the face and causes the instantaneous pressures within the cavity and the mean face pressure to be raised. Thus, although the rearbody face C_D is less than zero, it only slightly outweighs the increase in drag caused by the additional flat plate area of the frontbody, and the forebody-system drag is only moderately less than configurations with smaller disks.

One other feature of the distributions for this disk is worth mentioning. For the smaller gaps, $g/d_2 = 0.125$ and 0.25, the maximum in C_p is very peaked and the pressures inboard are nearly constant. This indicates a thin shear layer or separation streamline that does not entrain enough cavity fluid as it spans the gap nor inject enough fluid into the cavity at stagnation to induce an organized recirculation inside.

3.7d Reattachment on the Face

All configurations for which $d_1/d_2 < 0.625$ have rearbody face pressure distributions with a positive maximum C_p that exhibits a tendency to move radially as the gap is changed. If the location of $C_{p_{max}}$ corresponded to the edge of a disk wake with no rearbody, then plots of the radial location, R_s/r_1, of the stagnation point versus gap, g/r_1, for the various disks should collapse to the same curve. Such a plot is shown in Figure 17 along with an integrated mean streamline of a free disk wake from Strück (1970). Obviously, the normalized curves do not collapse; the rearbody does have a significant influence on the disk wake forcing the wake to be much thicker than normal. The effect decreases as the disk diameter increases, the maximum wake diameter for $d_1/d_2 \geq 0.5$ being about the same as a free disk wake. For gap ratios greater than 1.0, flow visualization indicates that the mean flow does reattach to the sting for the smaller disks. Consequently the interpretation of R_s becomes unclear, although it still corresponds to the original separation streamline from the frontbody. An additional feature to note is that for a given disk, the gap at which R_s/r_1 is the greatest also corresponds to the gap for minimum face drag and forebody-system drag. The shielding or interference effect of the frontbody is apparently optimized when the frontbody separation is pushed radially as far out as possible and the rearbody face area exposed to stagnation pressures is minimized.

Another interpretation of Figure 17 is also possible. The relative width of the mean disk wake apparently increases with decreasing diameter ratio. This behavior may reflect the influence of the rearbody corner as a desirable site for reattachment; the separation streamline is being driven towards the corner and the relative wake widths, therefore, are larger for smaller disks. Flow visualization generally showed that for all disks, except at small gap ratios, the separated flow tended to reattach quite near the corner. This indicates that the sharp downstream corner may, in fact, be a natural position for the reattachment of the shear layer to occur.

3.7e d_1/d_2 = 0.625, 0.75

The pressure distributions for diameter ratios 0.625 and 0.75 (Figures 13 and 14) exhibit some basic differences from the cases so far considered. These disks produce forebody-system drag coefficients an order of magnitude less than in the previous examples and the differences in distributions are consequently quite significant. It is observed that only for very short gaps are the pressure coefficients all positive. For small gaps the profiles are similar to those for $d_1/d_2 = 0.5$ at $g/d_2 \leq 0.25$ (Figures 12e and f), i.e., a peaked $C_{p_{max}}$ and constant inboard pressures. For larger gaps the face pressures, especially near optimum, are even more negative than the base pressures of a free disk. Two phenomena associated with the flow help explain this feature. First, it has already been noted that the separated flow from the smaller disks always stagnates inboard of the rearbody face edge with correspondingly higher cavity pressures. For the larger disks, the flow visualization and pressure profiles indicate that over a wide intermediate range of gaps, the separated flow from the disks reattaches very near the rearbody face corner and the cavity pressures are greatly reduced. The separation streamline in these cases more closely approximates a free streamline for which the pressure along the surface is constant and controlled by its initial curvature. Because the separation occurs normal to the freestream, the initial radius of curvature for these configurations is quite small and the corresponding pressure very low. It is this behavior of the separation as a highly curved, constant-pressure surface reattaching very near the rearbody corner that sets the large, negative level of the rearbody face pressure coefficients. The second factor contributing to the very negative minimum coefficients is the establishment of a strong recirculation within the cavity. This recirculation is maintained by a balance between entrainment of cavity fluid by the shear layer spanning the gap and injection of rotational or vortical fluid into the cavity when the separation surface reattaches. For some geometries the recirculation develops into a well-defined and stable vortex, clearly visible in the flow visualization and from the very low suction pressures in the face pressure distributions (Figure 14e).

One important difference exists however, between these two disks. For $d_1/d_2 = 0.625$, the pressure coefficients at the most outboard stations, even at optimum, are positive, indicating some stagnation just inboard of the corner. On the other hand, for $d_1/d_2 = 0.75$ the pressures are all negative, even at the edge. From the flow visualization it is apparent that only for rather large gaps, i.e., $g/d_2 > 1.5$, does the separation streamline from the disk $d_1/d_2 = 0.75$ stagnate on the rearbody face. For gaps at and near optimum, as has already been seen, the flow reattaches smoothly and tangentially onto the rearbody. But, even in off-optimum cases, the reattachment is on the corner or just downstream, not on the face. The consequences of this difference are significant. The pressures for the disk $d_1/d_2 = 0.625$ are quite low, the value of $C_{p_{min}}$ for gaps near optimum being around -0.5 to -0.6. However, by eliminating the small amount of stagnation which still remains, the face suction pressures can be doubled; $C_{p_{min}}$ near optimum for $d_1/d_2 = 0.75$ is less than -1.1 (Figure 14d). The rearbody face thrust is therefore also doubled and contributes to a substantial decrease in the total forebody-system drag. As is seen in Figure 14, eventually for $g/d_2 > 1.5$ the face pressures for both disks become positive. For these situations the disk is again simply shielding the rearbody from the full freestream dynamic pressure.

3.7f $d_1/d_2 = 0.875, 1.0$

Figures 15 and 16 present the distributions for two large disks, $d_1/d_2 = 0.875$ and 1.0. Except for $d_1/d_2 = 0.875$ at gaps less than g/d_2 = 0.125, these profiles are quite similar, being flat and negative. Flow visualization shows that the separation from the disk overshoots the rearbody face and corner and reattaches downstream. There is no indication of any organized motion in the cavity and the pressures are, consequently, uniform throughout.

The behavior of the disk, d_1/d_2 = 0.875, (Figure 15) for small gaps, at which the drag is very low, is more interesting. The distributions here are similar to the earlier examples of low drag geometries. The pressures are extremely low, reaching C_p = -2.2, and there is no face stagnation; flow visualization confirms that the separation rejoins at the rearbody corner. A sharp minimum in the pressure distribution again indicates that a strong cavity vortex exists and sits fairly far out radially.

3.8 Cavity Perimeter Pressure Distributions

With the aid of pressure distributions along the entire cavity perimeter, a complete decomposition of the forebody drag is available and a statement of the conditions at optimum and non-optimum geometries can be made. Figure 18 shows the cavity perimeter pressure distributions for three disks at their optimum gaps. These, and similar profiles, have been used to decompose the disk drag into its face and base components. This breakdown is presented in Figure 19 as the radius-weighted average face- or base-pressure coefficient versus gap ratio. (The only difference between these coefficients and the appropriate drag coefficient is the sign of the base pressure coefficient. A negative average base C_p contributes a positive drag coefficient.) The perimeter distributions

(Figure 18) show that for d_1/d_2 = 0.75 and 0.875 at their optimum configurations the disk base pressures are equal to the rearbody face pressures out to the disk radius. Thus the contributions to the total drag from these portions of the cavity walls are cancelling. This is not so for d_1/d_2 = 0.5 for which, even at optimum, the drag is substantial. Here there is only partial cancellation because the rearbody face coefficients are positive or only slightly negative while the disk base coefficients are all negative.

The primary result from the drag breakdown (Figure 19) is that over a very wide range of gaps, the disk face drag is essentially constant. Furthermore, when normalized by the disk diameter, the face drag becomes essentially constant, independent of both disk diameter and gap, with a value of $C_D \sim 0.75$. This behavior has two important consequences. First, the changes in disk drag are only the result of base pressure changes which, in turn, depend on the cavity flow. Second, the constancy of the disk face drag independent of configuration implies that the disk face pressure distributions are similar. Thus, the smallest disk that eliminates all stagnation from the rearbody face would be expected to give the lowest forebody-system drag, since the absolute extent of stagnation pressures, which now occur only on the disk face, will scale with the disk diameter.

3.9 The Conditions for Minimum Drag

The conditions for the most optimum (in terms of minimum forebody system drag) configurations can now be summarized. The most important feature is a steady separation surface which

(Figure 18) show that for d_1/d_2 = 0.75 and 0.875 at their optimum configurations the disk base pressures are equal to the rearbody face pressures out to the disk radius. Thus the contributions to the total drag from these portions of the cavity walls are cancelling. This is not so for d_1/d_2 = 0.5 for which, even at optimum, the drag is substantial. Here there is only partial cancellation because the rearbody face coefficients are positive or only slightly negative while the disk base coefficients are all negative.

The primary result from the drag breakdown (Figure 19) is that over a very wide range of gaps, the disk face drag is essentially constant. Furthermore, when normalized by the disk diameter, the face drag becomes essentially constant, independent of both disk diameter and gap, with a value of $C_D \sim 0.75$. This behavior has two important consequences. First, the changes in disk drag are only the result of base pressure changes which, in turn, depend on the cavity flow. Second, the constancy of the disk face drag independent of configuration implies that the disk face pressure distributions are similar. Thus, the smallest disk that eliminates all stagnation from the rearbody face would be expected to give the lowest forebody-system drag, since the absolute extent of stagnation pressures, which now occur only on the disk face, will scale with the disk diameter.

3.9 The Conditions for Minimum Drag

The conditions for the most optimum (in terms of minimum forebody system drag) configurations can now be summarized. The most important feature is a steady separation surface which smoothly and tangentially rejoins onto the rearbody sides. This reattachment occurs in such a way as to inject enough fluid into the cavity to maintain a strong recirculation and yet not cause stagnation on the face. Streamline curvature and recirculation in the cavity resulting from the tangential reattachment create very low cavity pressures and a strong suction peak located near the face edge. The cavity wall pressures on the disk, sting and inboard of the face suction peaks are fairly uniform and the pressures on the two opposing faces, the disk base and inner rearbody face, produce cancelling forces. Only the outer annulus of the rearbody face and the face of the disk remain to contribute to the forebody–system drag. The rearbody face thrusts upstream due to suction; the disk face experiences stagnation pressures and contributes positively to the drag. For $d_1/d_2 = 0.75$, $g/d_2 = 0.375$ these competing forces nearly cancel and the net drag coefficient is incredibly small, $C_D = 0.010$. Other configurations nearly attain this level but, either the disk is slightly too large, e.g., $d_1/d_2 = 0.813$ and 0.875, in which case the extremely large suction (as low as $C_p = -2.2$) acts on an insufficient area or it is too small and the suction forces are inadequate. Once smooth reattachment at the corner is lost, the balances which occur between the opposing cavity walls and between the exposed forward facing disk and cylinder faces no longer exist. The separation and shear layer are now more unsteady and the drag, although often less than that of the blunt faced cylinder, is much increased.

3.10 Other Studies of Tandem Bluff Bodies

As was noted in the Introduction to this work, only a handful of studies exists concerning the incompressible flow past simple bluff bodies in tandem. The earliest work seems to have been done by Eiffel (1910) in which the total force acting on two equal diameter, thin, circular disks normal to the flow and in tandem was measured. His results are shown in Figure 20 along with the forebody-system drag for $d_1/d_2 = 1.0$ and curves for prismatic bodies to be discussed shortly. For gaps on the order of one diameter or more the results of Eiffel and the present forebody drag measurements display identical trends and differ only by an additive constant. The difference, $\Delta C_D \sim 0.2$, can be attributed to the base pressure of the second disk although it is not quite negative enough (C_{p_b} normally ~ 0.4). The important point to note is that an optimum gap for minimum total drag exists and that it is the same for two rather different rearbodies.

The work of Saunders (1966) which was motivated by these results from Eiffel has been previously mentioned in the Introduction. His paper (actually a patent application) lacks sufficient information for many specific comparisons. He does, however, indicate that for a body composed of a disk coaxially mounted in front of a blunt faced cylinder the total drag is minimized when $d_1/d_2 = 0.7$, $g/d_2 = 0.35$, nearly the same as the most optimum geometry found here. Saunders indicates a 50% reduction in total drag which corresponds roughly to a 70% decrease in forebody-system drag, a substantial reduction but not as great as the 98.6% decrease observed in the present work.

Sawyer and Whitcomb (1971) investigated the drag characteristics of a bluff, axisymmetric rearbody in the wake of a cone as a proposed reentry vehicle. At $M = 0.2$ they observed the drag of the cone to have a maximum and the rearbody drag to have a minimum at some intermediate gap; the total drag monotonically increased. The peculiar shape of the bodies makes the applicability to this study quite limited, however.

Mair (1965) has considered the effects of placing disks behind a blunt based cylinder with the intent of reducing base drag of axisymmetric or three-dimensional bodies. He found that base drag could indeed be decreased by placing smaller disks behind, reductions up to 35% possible with one disk and 55% with two disks of decreasing diameter. The optimum geometry for one disk is $d_1/d_2 = 0.795$, $g/d_2 = 0.5$, a configuration very close to the most optimum case in the present work. Recirculation in the gap at optimum was also observed. Two important differences exist, however. The drag quickly rises with increasing gap and by one diameter all of the disks tested give a positive increment in drag. Secondly, the disk giving minimum drag also displays a very sharp maximum in C_D, an increment of 100% over that for the blunt base, at a gap less than optimum. This maximum is accompanied by large scale wake oscillations. Mair suggested that the pumping of high velocity freestream fluid into the cavity increases stagnation on the disk, raising the cavity pressure and increasing the drag. This is a mechanism similar to that proposed for the higher drag configurations in the current study although there is not such an increase in C_D as Mair observed.

Mair also filled the gap between the optimum disk and cylinder base with a streamlined fairing and found a 70% reduction in base drag with this boat-tailing treatment, twice the reduction due to the disk alone. He attributed the difference to overpressures on the edge of the upstream disk face due to stagnation which cannot exist with the fillin. He also suggested that the recirculation which exists in the gap with a disk alone is relatively unimportant since a similar external flow is generated by a solid afterbody. This is in contrast to the implications of earlier discussions in the current paper and will be considered later.

Bluff, building shaped bodies in tandem have been investigated by Kelnhofer (1973). In these experiments, two rectangular prisms of equal width and depth but different heights were mounted on the floor of a wind tunnel as shown in Figure 21. The drag force on one of the bodies was measured as their spacing, their relative heights and the freestream flow direction were varied. Due to the way in which the models were configured only some of Kelnhofer's results can be directly compared to the present work, however.

There is some question as to how Kelnhofer's results should be scaled so as to properly compare with the current data. Because his models were mounted on a ground plane it might be expected, from symmetry, that twice the rearbody height is the proper scaling quantity to agree with scaling by d_2, the rearbody diameter. However, the results indicate this may not be so, although this scaling has been used in the following figures.

Figure 21 presents the force on the frontbodies in Kelnhofer's and the present work for a height and diameter ratio of unity. Except for a slight difference in magnitude, the two curves are very similar. Figure 22 compares the force on the rearbodies for a variety of frontbody sizes. This figure shows that the decrease in rearbody drag with increasing frontbody size and the existence of optimum gaps for minimum rearbody drag are characteristics shared by both types of geometries. Kelnhofer refers to this effect as "sheltering". Regardless of the name, it appears that this interference effect occurs for a wide variety of body shapes. Figure 20 compares the total drag on both of Kelnhofer's bodies for a height ratio of unity with Eiffel's results and the forebody-system drag coefficient from the current work for $d_1/d_2 = 1$. This figure seems to imply that h_1 might be the more appropriate scale. In any case, the behavior of each geometry includes a significant reduction in drag and an optimum gap, indicating again the universality of the concept of beneficial interference between bluff bodies.

Flow past two-dimensional bodies in tandem has received considerably more attention since this type of flow often occurs whenever struts, cables, smoke stacks or structural components are near each other. Zdravkovich (1977) conducted experiments with two circular cylinders whose axes were normal to the flow in close proximity. He also made a critical survey of the literature on such flows. Two important characteristics of tandem cylinder flow relevant to the current work stand out in Zdravkovich's papers. First, the total drag of the two cylinders (Re greater than critical) is less than that of a single cylinder for all spacings up to, and probably greater than, 9 diameters, center-to-center. The minimum drag occurs when the cylinders touch, but the important feature is the beneficial interference between the two bodies, even for very large gaps. The other important characteristic is the existence of a critical gap, roughly 3½ diameters, at which there is a discontinuous change in the flow and the forces on the cylinders. For gaps less than this, the upstream cylinder does not experience vortex shedding. At 3½ diameters, shedding abruptly begins and the drag of both cylinders increases, although the total drag is still less than one cylinder by itself. This behavior may be similar to differences noted in the present study between disk-cylinder combinations that have smooth reattachment onto the rearbody and those that do not. The latter configurations exhibit much more unsteadiness and higher drag, even at their optimum gaps.

An interesting side note to the case of two-dimensional bodies in tandem is found in the work of Biermann and Herrnstein (1933) (who also conducted the large gap tests noted by Zdravkovich). They tested both bluff cylinders and streamlined struts in tandem. While the cylinders experienced a net drag decrease for all gaps, the struts showed a slight net increase over that of a single strut for all gaps, with a maximum at a spacing of 4 diameters. When large regions of separation on a single body are normally not present, it thus seems that interference between two is not always beneficial and care must be taken when such situations are encountered.

A vast literature exists on flows over a cutout, notch or cavity in a body or wall to which the two-body problem studied here belongs. See, for example, the references listed in Charwat et al (1961), Sarohia (1975) and Rockwell and Naudascher (1978). Except for the examples already discussed, these studies differ from the present one in several very important ways. First, they are primarily concerned with the acoustic and non-steady flow characteristics of the cavity; the drag is of only secondary interest (Roshko (1955) and McGregor and White (1970) being exceptions to this.) Second, and more important, they deal almost exclusively with cavities where the streamline at separation is essentially aligned with the freestream and the upstream and downstream wall heights are the same. This is in contrast to the present study where the separation is at right angles to the mean flow and there is a height difference between the walls. The effect of spoilers located upstream of cavities has received some attention but only with regard to minimizing oscillations. The extreme curvature of the streamline when it separates normal to the mean flow causes large negative pressures in portions of the cavity in some cases which, as has been seen, can have profound effects on the drag due to the cavity. For example, Roshko (1955) studied rectangular two-dimensional cutouts in a flat plate aligned with the free stream and found wall suctions no greater than $C_p = -0.06$. In comparison, this work has shown wall pressures as low as -2.2.

Some similarities do exist, though. The shape of the wall pressure distributions indicating recirculation in the cavities is much the same, although the magnitude of the pressures can be quite different. Also, the separation streamline reattaches at various places within the cavity depending on the gap. One result from Roshko (1955) is relevant to the current problem. He found that the skin friction coefficients along the walls were two orders of magnitude less than the pressure and pressure-drag coefficients in the cavity; skin friction in the cavity as a contribution to the drag is thus entirely negligible. Very little else of the remaining information on cavity flows is really applicable to the problem at hand and, for the most part, will not be discussed.

IV. SOME THEORETICAL CONSIDERATIONS

The situation for the very low drag cases is one of most favorable interference, in which the separation stream surface from the frontbody joins smoothly (in some sense) onto the rearbody, thereby minimizing the total extent of separation. As has been previously suggested, the separation surface in these cases might be assumed to be of constant pressure. If this assumption is made, a free-streamline analytical model can be used to calculate the gap corresponding to smooth flow onto the rearbody. In the case of free-streamline flow, this gap is simply the downstream distance at which the separated stream surface becomes parallel to the freestream, or tangent to the rearbody as shown in the inset sketch of Figure 23. In two dimensions, the potential flow free-streamline model can be analytically formulated using complex variables and conformal mapping techniques, such as given in Roshko (1954). For the axisymmetric case, the computations must be done numerically and are quite involved, as is evident from Strück (1970) or White and Kline (1975).

4.1 Concepts of Free-Streamline Flow

The calculations presented herein are two-dimensional and based on the notched hodograph free-streamline theory described in Roshko (1954). A different approach, but equivalent in concept, was suggested by Lissaman in a private communication. The details of these two analyses, which give the same results, are presented in Appendix B of this paper. Briefly, these methods are based on the assumption that a free streamline separates from the edges of a two-dimensional flat plate normal to the flow. On the plate base and in the wake downstream of the plate, the pressure is taken to be initially constant and less than or equal to freestream static pressure, an assumption consistent with experimental observations. Consequently, the pressure coefficient, C_{p_s}, on the streamline and the velocity, U_s, along the streamline will also be constant and given by $(U_s/U_\infty)^2 = 1 - C_{p_s}$. At some downstream location the flow will become parallel and eventually will return to uniform freestream conditions, p_∞ and U_∞. Specifying U_s or C_{p_s} then, will uniquely determine the wake width, d_2, and downstream distance, g, to that width relative to the plate width, d_1.

4.2 Wake Geometry

Shown in Figure 23 are the predicted wake geometries, g/d_2 and d_1/d_2, for a constant-pressure, two-dimensional streamline with C_{p_s} as the parameter. Computed axisymmetric geometries from Brennen (1969), who used a closed wake, Riabouchinsky model, and from Strück are shown for comparison. Also presented are the experimentally determined optimum geometries, g^*/d_2, for each value of d_1/d_2, from the current results. These have been taken from Figure 3, although there is some uncertainty in determining precisely the value of g/d_2 at which minimum C_D occurs. The favorable comparison between the measured and calculated gap ratios over the range $0.38 < d_1/d_2 < 0.88$ suggests that the separated flow pattern for minimum drag corresponds fairly well with a free-streamline model. For values of d_1/d_2 closer to unity, the good correspondence does not hold up, possibly because the pressure coefficient required to curve the separation streamline is tending to such large negative values that the pressure rise at reattachment is too great for the boundary layer to negotiate. For diameter ratios less than 0.38, the minimum values of C_D occur at values of gap width considerably smaller than for the free-streamline model. This is because for larger gaps, the separation surface begins to close itself ahead of the rearbody and becomes much more unsteady and the resulting flow field is quite different from that modeled by the free-streamline theory.

4.3 The Separation-Surface Pressure

Some other results from the free-streamline analytical model may also be used for comparison with the experimental results. In particular, the constant pressure associated with each diameter ratio can be compared to the measured pressure in the gap between the two bodies in the test configuration. To use the two-dimensional analytical result would be greatly in error -- compare the minimum pressure on a two-dimensional cylinder in potential flow, $C_{p_{min}} = -2$, to that on a sphere, $C_{p_{min}} = -1\frac{1}{4}$. An axisymmetric value is the appropriate one and can be estimated semiempirically without resorting to the complete numerical calculation.

If the free-streamline surface is temporarily regarded as solid (but remaining a constant pressure surface!), the semi-infinite half body so defined has zero drag in unbounded potential flow (Prandtl and Tietjens, 1934), i.e.,

$$D = \int (p - p_\infty)\, dA \Big|_{\text{projected frontal area}}$$

$$= D_{1f} + D_s = 0 \qquad (4.1)$$

where $D_{1f} = (p_{1f} - p_\infty) A_1 = C_{D_{1f}} \, q_\infty A_1$ is the contribution from the disk face and $D_s = (p_s - p_\infty)(A_2 - A_1) = C_{p_s} q_\infty (A_2 - A_1)$ is from the constant-pressure surface. Equation 4.1 can thus, equivalently be written as

$$C_{p_s} (A_2 - A_1) = - C_{D_{1_f}} A_1 \tag{4.2}$$

and if a second relation between $C_{D_{1_f}}$ and C_{p_s} can be established, then (4.2) will yield an expression for C_{p_s} in the model. A suitable relationship is available from experimental results as follows.

For an isolated disk, the total disk drag coefficient, C_{D_1}, is given by

$$C_{D_1} = C_{D_{1_f}} - C_{p_s} \tag{4.3}$$

where C_{p_s} is the wake and disk base pressure coefficient. An empirical expression for the dependence of C_{D_1} on C_{p_s} may be obtained from measurements of the drag of bodies with cavity wakes collected by Perry and Plesset (1953), for values of C_{p_s} down to -0.25 and from wind tunnel measurements collected by Strück (1970) for $-0.35 \leq C_{p_s} \leq -0.60$. These data for disks are well fitted by the expression

$$C_{D_1} = 0.80 (1 - C_{p_s}) \tag{4.4}$$

Thus from (4.3), $C_{D_{1_f}} = 0.80 + 0.20\, C_{p_s}$ which, when substituted into (4.2) along with the geometrical relation $A_1 / A_2 = (d_1 / d_2)^2$, gives for the base and separation streamsurface pressure coefficient the result

$$C_{p_s} = \frac{-0.80}{(d_2/d_1)^2 - 0.80} \qquad (4.5)$$

This semi-empirical result is shown in Figure 24 (down to values of C_{p_s} as low as - 3!) together with the single value determined by Strück from his numerical calculations and the two-dimensional, notched hodograph result.

In the present experiment, pressures were measured on the rearbody face for most geometries and on the entire internal cavity perimeter for selected configurations. The face pressure distributions for several discs at optimum conditions are collected in Figure 25. Significant differences between the various disks are readily apparent from this figure and indicate a wide range of flow fields, even for the optimum configurations. From these distributions, and the sting and disk base pressures when available, estimates of the effective pressure in the gap can be made. Average values of the gap pressure coefficient, $C_p{}^*$, based on the face distributions are plotted as circles in Figure 24; they are weighted toward values deeper in the cavity, the excursions near the top being attributed to dynamic effects associated with the reattachment region and the cavity vortex. The maximum excursions about the selected average values are indicated by bars. Also shown are the average disk base and sting pressures and pressures obtained on the very edge of the disk. Clearly some correspondence between the measurements and the free-streamline model exists. Similar to the case for the geometries at optimum, there is fair agreement between the semi-empirical axisymmetric value of C_{p_s} (Equation 4.5) and the measured average gap pressure for $0.5 < d_1/d_2 < 0.88$. The most important difference to note is that in the theoretical model C_{p_s} is always negative, but in the experiment $C_p{}^*$ becomes positive for $d_1/d_2 < 0.5$. The optimum configuration pressure distributions presented in Figure 25, as well as the flow visualization, clearly show that for $d_1/d_2 < 0.38$ the separation stagnates well inboard of the rearbody face corner and that the flow is quite unsteady. Consequently, the flow in these cases violates the theoretical assumptions and the observed disagreement results. For $d_1/d_2 > 0.88$ the theoretical requirement that $C_{p_s} \rightarrow -\infty$ accounts for the discrepancy when the frontbody diameter ratio approaches unity.

4.4 Estimating the Drag for Optimum Configurations

4.4a Momentum Balance

As a final comparison between theory and experiment, an attempt has been made to estimate the forebody system drag for the optimum geometries. Since the flow at optimum appears to be a more general example of uniform flow over a cutout in a flat surface, as was noted previously, it is constructive to compare the two cases as follows. For the cutout in uniform flow, the free-streamline solution is simply $p = p_\infty$ (or $C_{p_s} = 0$) on the streamline spanning the gap and in the gap itself, so that $C_D = 0$. In the real flow, viscosity and diffusion act on the free streamline, which is now the dividing streamline in the free shear layer, to produce a shear stress along it and a departure from $p = p_\infty$ on the cutout walls. The integral of the perturbed pressure over the walls plus a small negative contribution from the shear stress on the bottom (shown by Roshko (1955) to be negligibly small) gives the cavity drag. A momentum balance for the fluid enclosed by the cutout and the dividing streamline (realizing, by definition of the dividing streamline, that there is no net momentum flux into this control volume) gives

$$-\int pdA\Big|_{\text{walls}} + \cancelto{\sim 0}{\int \tau dA\Big|}_{\text{bottom}} + \int \tau dA\Big|_{\text{dividing streamline}} = 0$$

or

$$D = \int pdA\Big|_{\text{walls}} = \int_s \tau_s dA_s$$

where D is the cavity drag, τ_s is the shear stress on the dividing streamline and the last integral is taken over that surface. Extending this idea to the axisymmetric forebody system, the shear along the free surface is assumed to be similarly related to a pressure perturbation, $p - p_s$ on the cavity walls (i.e., the rearbody face and the frontbody or disk base) and any pressure perturbation on the free surface is neglected. Again, a momentum balance gives

$$D = 2\pi \int_s \tau_s r_s \underset{\sim}{n}_x \cdot \underset{\sim}{ds} = 2\pi \int_s \tau_s r_s dx \qquad (4.6)$$

where $\underset{\sim}{n}_x$ is the direction cosine for the free surface and $\underset{\sim}{ds}$ is a vector element of length along it. This momentum balance properly takes into account the fact that, in the inviscid, free-streamline, zero-drag case (i.e., potential flow with $C_p = C_{p_s}$ throughout the gap), the drag on the frontbody, including pressures on its front and back, is just balanced by the negative drag ($C_{p_s} < 0$) on the rearbody face. The extension to real flow assumes there is no net momentum flux through the cavity, and that the pressures on the frontbody face are unchanged from the potential flow solution. The pressure along the shear layer is also assumed constant. The assumption of unchanged disk face pressures seems reasonable in view of the results in Figure 19 which show the disk face drag to be essentially constant, independent of configuration and forebody system drag.

4.4b Evaluation of the Shear Stress and Drag

In order to evaluate the integral in (4.6), the value of the shear stress along the dividing streamline must be known. As a first approximation, the free shear layer across the gap might be taken as a completely developed (self-similar) turbulent flow at constant pressure. For such a flow, the value of τ_s is constant and a maximum along the dividing streamline, a result obtained from the application of similarity arguments and the boundary layer approximations to a two-dimensional turbulent mixing layer. The assumption that the path of integration, s, in (4.6) coincides with the dividing streamline introduces some approximation into the equation, as does the assumption that the value of τ_s is constant all the way to the reattachment point. With these assumptions and neglecting effects of curvature, the value of τ_s is taken from the measurements of Liepmann and Laufer (1947), namely $\tau_s = 0.0115\ \rho U_s^2$ where U_s corresponds to the flow velocity outside the free shear layer and hence is related to the corresponding pressure coefficient C_{p_s} (which is also $C_p{}^*$ for the gap) by $(U_s/U_\infty)^2 = 1 - C_{p_s}$. Making these substitutions, (4.6) becomes

$$D = 2\pi(0.0115)\rho U_\infty^2(1 - C_{p_s}) \int_{gap} r_s dx$$

The integral could be evaluated numerically if the shape of the free streamsurface, $r_s(x)$, were known. Instead, an average value $r_s = \frac{1}{2}(r_1 + r_2)$ is used, which is equivalent to assuming that the free streamsurface is a truncated cone. With this approximation the drag becomes

$$D = \tfrac{1}{2}\pi(0.0115)\rho U_\infty^2(1 - C_{p_s})(d_1 + d_2)\, g \tag{4.7a}$$

and the drag coefficient is

$$C_D = 0.046\left(1 + \frac{d_1}{d_2}\right)(1 - C_{p_s})\frac{g}{d_2} \tag{4.7b}$$

To obtain C_D as a function of d_1/d_2, Equation 4.5 is used for C_{p_s} and the two-dimensional free-streamline calculation for g^*/d_2, shown in Figure 23, since it appears to fit the measurements in the low drag range. The results are plotted in Figure 26 and compared with one value of C_D taken from Strück's single numerical, axisymmetric calculations and the experimentally observed minimum drag coefficients for each value of d_1/d_2 at the corresponding optimum gap, g^*/d_2.

Figure 26 suggests that the approximations made in obtaining Equation 4.7b are not unreasonable; good agreement is seen for intermediate values of d_1/d_2. For diameter ratios approaching zero, the drag coefficient determined by (4.7b) becomes unbounded. This is because C_{p_s} goes to zero and g/d_2 grows infinitely long since the radius of curvature (and hence g/d_2) of the separation streamsurface increases with increasing C_{p_s}. Integrating a finite shear stress over an infinite surface gives an infinite drag. For d_1/d_2 approaching unity, on the other hand, C_{p_s} becomes infinitely negative while g/d_2 goes to zero and it is not clear a priori what their product will be. For the two-dimensional case, where an exact theory is available, C_D becomes infinite, but for the present calculation the drag coefficient goes to zero.

Whatever the limiting behavior for the diameter ratio approaching one, the agreement between the theoretical and experimental values of C_D in the range $0.594 \leq d_1/d_2 \leq 0.875$ strongly suggests that in this range the flow over the gap is little different from simple cavity flow in which the shear layer is the classic turbulent mixing layer. The fact that the theory actually overpredicts the drag is a situation that deserves further investigation, however. On the other hand, for $d_1/d_2 \leqslant 0.6$, (i.e., $g^*/d_2 > 0.5$, from Figure 23) there is an abrupt departure of the experimental results for optimum drag from the theoretical ones. The measured drag is considerably greater than the theoretical result which suggests a radical departure from the flow conditions assumed in the model. These differences are the subjects of the following sections.

V. THE CRITICAL GAP RATIO

5.1 The Critical Geometry

For optimum gap ratios, g^*/d_2, less than about 0.5 ($d_1/d_2 > 0.6$) the flow, as experienced in the wind tunnel and as observed on the photographs of flow visualization in water, is well behaved. The separation surface is, of course, a turbulent free shear layer and it appears to develop normally. For larger gaps, however, it becomes unsteady on a much greater scale, comparable to the scale of the rearbody diameter, possibly suggesting some kind of gap-coupled oscillation or wake instability. Consequently, for optimum geometries having $g^*/d_2 > 0.5$, the conditions in the turbulent mixing layer are no longer those of a normal layer such as that studied in the Liepmann and Laufer experiment. Figure 27 presents the experimentally determined minimum drag coefficients, $C_{D_{min}}$, as a function of optimum gap, g^*/d_2. For $g^*/d_2 \leq 0.5$, the drag is very low, $C_{D_{min}} < 0.05$. For larger gaps there is a jump and then further increases in the experimental $C_{D_{min}}$ to values more than an order of magnitude higher as the gap is further increased. The message is clear: a critical gap length exists below which the flow is steady and the forebody drag extremely low; above the critical length large scale oscillations develop and the drag, although the configuration is still optimum in some sense, is high. From Figures 26 and 27 the critical gap and corresponding frontbody diameter can be defined as

$(g^*/d_2)_{cr} = 0.5$, $(d_1/d_2)_{cr} = 0.6$, the gap ratio being the more significant criterion if the flow is optimum. Smaller values of gap ratio will be defined as subcritical and larger ones supercritical. Figure 28 shows photographs of super- and subcritical optimum geometries. The conditions described above are clearly displayed.

5.2 Critical Gap Evidence

Evidence of a critical gap ratio can also be seen in some of the figures previously discussed. For example, it is possible that the critical condition is reached when the gap pressure coefficient passes through zero (Figure 24); this occurs at $d_1/d_2 = 0.5$ rather than 0.6, but as was noted, there is some uncertainty in the correct representative values for the gap pressures.

Also, the face pressure distributions for optimum gaps (Figure 25) show some interesting effects. In particular, the position of the minimum, which apparently corresponds to the position of a gap vortex, changes its radial location rather abruptly at the critical gap (and at $C_p = 0$), moving radially inward. The vortex, which for subcritical gaps appears well-defined and stable in the flow visualizations, also becomes less organized at the transition between flow regimes. The locus of the pressure maximum, which corresponds to the mean stagnation point of the separation streamline, also moves from its position at the face edge at subcritical gaps to an inboard location at supercritical geometries. The effect this has on increasing the drag has already been thoroughly discussed; the rearbody face stagnation essentially accounts for the increase in drag in going from sub- to supercritical configurations.

Figure 29 presents the data previously given in Figure 3 in terms of a contour plot. In this figure, contours of constant drag coefficient are plotted as a function of configuration, i.e., d_1/d_2 and g/d_2. Some error is present in the plot due to difficulty in fitting contours to steep gradients in the data. Superimposed on the figure are the experimental data for optimum geometries from Figure 26; the subcritical configurations are seen to form a well-defined depression in the figure. Other geometries that were not tested but that would also by subcritical are indicated. This suggests how this plot might serve as a useful engineering guide to predict sub- or supercritical flow geometries.

5.3 Critical Geometries in Other Flows

Several encounters with critical geometries by other researchers have previously been discussed. Mair (1965) observed a sudden change from steady low-drag flow to nonsteady high-drag flow near the base of a streamwise oriented cylinder as the gap between it and a downstream disk was varied. Zdravkovich (1977) documented an abrupt initiation of vortex shedding from an upstream two-dimensional cylinder and an increase in drag when the spacing between it and a similar downstream cylinder exceeded $3\frac{1}{2}$ diameters. Numerous other flows exhibit critical geometry behavior. Examples include the transition from open to closed cavities as discussed by Charwat, et al. (1961), the dependence of the existence of axisymmetric cavity oscillations on cavity dimensions observed by Sarohia (1975), and transition from attached to unattached flow on slanted bases found by Hucho and Janssen (1974) and Morel (1978). The common features of these critical geometries are the change from the steady, attached flow to an unsteady or oscillating, unattached flow, and a change from low drag to high drag (although these two changes do not necessarily accompany each other, as is the case for the slanted base flows). Knowledge of the existence of critical geometries, in the present case a gap below which very low forebody drag is possible, can be a very useful aid when designing for practical applications as well as providing deeper understanding into the behavior of flows about bodies.

VI. VELOCITY MEASUREMENTS

From the preceding discussions two important features of this tandem bluff body problem stand out. First, two distinct regimes of flow exist characterized by low drag and a steady, well organized shear layer, or high drag and large scale wake oscillations. Second, theoretical estimates of the drag for the low drag regime actually exceed the measured value of the coefficient. In order to examine the differences in the two regimes more carefully and to explain the theoretical overestimation of the drag it is quite clear that velocity measurements are required of the flow in the cavity and shear layer. There are some difficulties in making these measurements however; there are large oscillations in flow direction and magnitude, the mean flow direction is not known in general and the flow in portions of the cavity is reversed. The only instrument currently available to measure in such conditions is a frequency-shifted laser-Doppler velocimeter and is the instrument chosen in this experiment to provide detailed information on the velocity field in the vicinity of the forebody system.

6.1 Velocity Bias

The capability of the laser-Doppler to non-obtrusively measure the velocity is one of its most appealing features, especially in this experiment where objects in the flow can seriously disturb the flow state about the model. Other useful properties include the small sampling volume, high frequency response and linearity of the instrument. For this experiment, however, the most important feature is the ability of the laser-Doppler to unambiguously measure reversed flows when a frequency shift, or bias, is applied to the signal. When the fringes in the focal volume formed by two intersecting laser beams are stationary, a particle passing through it will produce the same Doppler shift as one moving at the same velocity in exactly the opposite direction. If the fringes are now set into motion, the number of fringe plane crossings, and hence the Doppler frequency, will be different for these two particles -- the particle moving with the fringes having fewer crossings, the opposing particle having more -- and the particle direction can be discerned. The fringes are made to move by shifting the frequency of one of the beams relative to the other, causing a moving interference pattern at their intersection and providing the necessary bias to determine the particle and thus fluid velocity.

6.2 Bragg Cells

In this experiment the frequency shifting was done by Intra-Action Corp. Model ADM-40 Acousto-Optic Deflector Modulators (referred to here as Bragg cells) which cause shifts in frequency of the light by the phenomenon of Bragg scattering. These cells consist of a rectangular prism of glass with a piezoelectric crystal at one end. The crystal is driven by a 30 - 50 MHz signal from a waveform generator driving a power amplifier at nominally 2 watts. Acoustic waves of the same frequency as the input then propagate through the glass, whose damping is such that there is minimal energy reflected from the end wall and the wave pattern in the cell is essentially one of simple propagation. Transfer of momentum and energy between the photons of the incident laser beam and the phonons of the acoustic waves causes a second light beam to be scattered for certain discrete angles of incidence (Gordon, 1966). The scattered light has a frequency, ω_s, given by the sum of the incident and acoustic frequencies,

$$\omega_s = \omega_i + \omega_a$$

and a direction relative to the incident beam of $2\sin(\theta/2) = \frac{\lambda_i/n}{\lambda_a}$ where θ is the angle between the incident and scattered light beams, λ_i/n is the optical wavelength in the Bragg cell medium and λ_a is the acoustic wavelength (Yariv, 1976). Because the Bragg cell is of finite span, the acoustic wavefronts are actually curved. Consequently, an infinite series of Bragg scatterings can occur and the output of the cell consists of a number of beams with frequencies $\omega_s = \omega_i \pm m\omega_a$, where m is the order of the scattering. The power in any given order can be controlled by varying the angle between the incident light and the Bragg cell aperture. As much as 85% of the incident power could be put into one of the first order scattered beams with the cells used in this experiment.

6.3 Optical Arrangement

The velocimeter used in this experiment was operated in the single-particle, dual-scatter and frequency-shifted mode. The optical schematic of the system is shown in Figure 30. The beam from a 5 mw helium-neon laser (Spectra-Physics, model 120), 6328 Å wavelength, is split by a 50-50 cube beam splitter to form two slightly diverging beams of roughly equal intensity. The beams are made to diverge so that their wavefronts appear to come from the same origin. For this experiment the divergence angle was set to 1 mrad when the actual angle should have been 20 mrad as was determined after the testing was finished. This error is reflected as an increase in the instrumental noise or bandwidth (Dimotakis, 1977). The instrumental width due to all the noise sources for this experiment was determined to be on the order of only 0.3% and consequently this divergence error requires no correction. Each beam next passes through a Bragg cell nominally driven at 40 MHz. For use in the laser-Doppler, the outputs of the Bragg cells fall onto a mask with a slit formed by two razor blades, shown in the inset to Figure 30, which allows only one beam of the desired frequency to pass through. The selection of ω_a and the order, m, will be discussed shortly.

Following the slit, as shown in Figure 30, is a dove prism which permits the plane of the input beams to be rotated about their optical axis, a rotation of θ in the dove prism producing a 2θ rotation of the beam plane. This rotation is necessary so that different velocity components in the flow can be measured. The beams are then focussed by a simple 50 cm focal length double-convex lens to a focal volume of roughly ellipsoidal shape. Due to small imperfections in the beam splitter and different scattering angles of the two Bragg cells, the two beams do not lie quite in the same plane and consequently do not completely overlap. The focal volume dimensions are approximately 0.3 mm in the direction of the normals to the fringes, 0.4 mm parallel to the fringe planes and 10 mm long. The fringe spacing, $(\lambda/2)\sin(\theta/2)$, is 7.77 μm which gives a conversion factor of 1.288 kHz/(cm/sec).

On the opposite side of the tunnel, as shown in Figure 30, a 20 cm focal length, 10.2 cm diameter, simple double-convex lens collects the scattered light, a thin strip of black tape masking off the two scattering beams. The lens focusses the scattered light onto a

0.5 mm diameter pinhole which is followed by an optical bandpass filter for the HeNe wavelength and a photomultiplier tube (RCA 8645). The transmitting and receiving optics are connected together by a superstructure and mounted on a digital 3-axis positioner capable of stepping 0.001 in. (0.0254 mm) in each direction so that the focal volume may be precisely located.

A second complete laser-Doppler velocimeter operating in the unshifted, multiple-particle, reference-scatter mode was used to monitor the freestream velocity near the entrance to the test section. Its output was simply the Doppler frequency averaged over 0.1 seconds.

6.4 Electronic Processing

The output of the photomultiplier passes through a current amplifier, then into a Hewlett-Packard Spectrum Analyzer 8552B/8553B for real time observation of the raw signal. The output also passes through a Krohn-Hite Band Pass Filter 3202R and into the processor designed and built by Prof. P. Dimotakis and D. Lang of C.I.T. The processor performs a series of tests designed to eliminate such things as higher harmonics from the current amplifier due to saturation caused by large amplitude bursts and the low frequency pedestal associated with the total time of flight of a particle through the focal volume.

For a particle burst to be considered valid, the filtered waveform into the processor must first exceed adjustable symmetric levels, $\pm V_L$, about zero as shown in Figure 31. After crossing both the positive and negative level settings, the next zero crossing from above by the input signal is taken as the beginning of a valid burst. Each succeeding zero crossing from above is counted and the total time elapsed from the beginning of the valid burst is recorded (in terms of clock pulses) provided several other conditions are satisfied. Each zero crossing must be preceded by a crossing of both the positive and negative level settings, V_L. In addition, the instantaneous period of the signal, τ, must be bounded by independently adjustable limits, τ_{min} and τ_{max}, i.e.,

$$\tau_{min} < \tau < \tau_{max}$$

Convenient settings for τ_{min} and τ_{max} are the inverses of the band-pass filter high and low frequency cutoff values, respectively. A third adjustable requirement is the number of fringes which must be crossed. This setting can be less than or equal to (LE), equal to (E), or greater than or equal to (GE) some value M_f. If at any time during the burst, the signal fails to meet the level and period criteria or if it satisfies the LE or E fringe requirements the processing of that burst is terminated. In Figure 31 the example input waveform fails to cross $-V_L$ and the processing ends. At this point the processor has stored the number of valid zero crossings, n_i, since the first and the total elapsed time, Δt_i. The time is determined in multiples of 10 nsec, 0.1 μsec or 1 μsec depending on the requirements of the flow. If the criterion on the number of fringes has been satisfied the measurement is considered valid; the information is transferred to the formatting electronics and the processor is ready for a new burst. The formatting electronics code n_i and Δt_i into a single 32 bit word and store it in a 2x (1024 x 32) high speed buffer memory. The memory then feeds a Kennedy 9100 digital tape recorder which accepts data at 120 kilobytes/sec where four bytes comprise one word. Consequently, the processing can handle sampling rates of 32,000 valid events/sec (or particles/sec in the focal volume). During this experiment sampling rates from 50 to 700 particles/sec were used; there was no limitation on frequency response due to signal processing. The period of the signal from the freestream monitoring LDV is also coded, along with an identification mark, by the processor and recorded at the beginning of selected records. In this manner drift in the tunnel velocity can easily and accurately be followed. The tape is processed by standard techniques on the IBM 370/158 operated by the Institute.

6.5 Bragg Frequency

The velocity measurements were made in the same facility and with the same model as the flow visualization experiments. All measurements were made at a nominal freestream velocity of 1m/sec corresponding to $Re = 1 \times 10^5$. The maximum Doppler shift to be expected from this flow is on the order of 200 kHz. The Bragg cells operate between 30 and 50 MHz. If only one cell is used the bias frequency is also 30 to 50 MHz. Thus, the desired signal is then only 0.5% of the total signal and can not be discerned from noise. The bias should be as small as possible and yet large enough to provide an unambiguous measurement. This is the reason two cells are used; one operates at 40 MHz, the other at 40 MHz + $\Delta\nu_B$ which can be set to as low a value as is required. A circuit designed and built by Dan Lang and discussed in Appendix C is used to add a 40 MHz crystal controlled signal with an adjustable $\Delta\nu_B$ from the Exact Electronics programmable waveform generator Model 605 to produce one of the Bragg cell inputs.

The other input is the original 40 MHz signal. Drift in $\Delta\nu_B$ was observed to be less than 0.1%. Bragg shifts of nominally 50, 100, 150 and 200 kHz were used during the testing, adjustment being made to insure that the measurement was always unambiguous in direction. The negative first order beams ($\omega_s = \omega_i - 2\pi$ 40 MHz and $\omega_i - 2\pi(40 \text{ MHz} - \Delta\nu_B)$) were the ones passed by the slit.

6.6 Operating Conditions

As was mentioned earlier, the total instrumental noise of the optics and processor was approximately 0.3% of $\Delta\nu_B$ as observed from high sampling rate measurements in a quiescent fluid. This corresponds to a rms velocity fluctuation in the worst case of 0.5% relative to the freestream velocity, for $\Delta\nu_B = 200$ kHz. The measurements were made almost exclusively with the number of fringes required for a valid burst set at greater than or equal to 20. The amplitude threshold requirement was adjusted to maintain the sampling rate around 200 samples/sec.

Particles in the water must be kept below some particular size in order that they follow the flow and also do not overlap fringes in the focal volume. Filtering of particles greater than 10 μm was done of the water. Low Reynolds number flow around a sphere is governed by a first order equation with a time constant $\tau_p = \frac{\rho_p d^2}{18\rho_f \nu}$ associated with it. Here ρ_f is the fluid density, ν is the kinematic viscosity, ρ_p the particle density and d the particle diameter. The frequency corresponding to a 1/e degradation in response is $f_{max} = \frac{1}{2\pi\tau_\rho}$.

For a 10 μm particle with a density three times that of water, $f_{max} =$

9000 Hz. Thus finer filtering is not required in order that the particles will follow the flow.

6.7 Positioning

Some difficulty existed in aligning the model precisely with the flow. This problem was mainly due to the existence of a free surface which deformed as a function of the model drag. The model was aligned by requiring as symmetric a velocity profile as possible, although the flow was never perfectly symmetric as will be seen in velocity profiles to be presented.

Another difficulty arose in connection with rotation of the beam plane which was required in order that different velocity components could be measured. In order for the focal volume and its image at the receiving pinhole to remain fixed in space during rotation, the optical axes of all components, transmitting and receiving, must fall on the same line and must be perpendicular to all walls of the water tunnel. This was a requirement that could not be met. Consequently, the focal volume and its image physically moved as the beam plane was rotated to measure different velocity components. This necessitated realigning the receiving optics after each rotation. More importantly, because the focal volume had moved an unknown amount, the zero location, defined as the upper corner of the rearbody face, also had to be reacquired after each rotation. This reacquisition of the zero could be done, on the average, to better than ± 0.003 in. or equivalently ± 0.25 focal volume diameters (0.3 mm) in both the radial and streamwise directions. There was negligible shift in the transverse (or azimuthal) location of the beams relative to the long dimension of the focal volume and the rotation angle could be set to within 5 seconds of arc, neither of these errors thus being of any consequence. The error in relocating zero is only of real importance in determining the Reynolds stress since this requires knowing the mean and rms values of velocity at a given point in two perpendicular directions, $\pm 45^{\circ}$ to the free-stream direction. However, the shear layers of interest are between 5 and 125 focal volume diameters thick (as determined from the flow visualization and later verified by the measurements) and an error of ± 0.25 diameters is consequently acceptable.

6.8 Data Processing

Data reduction with aid of the IBM computer is accomplished in two steps. The first step involves reading the tape, checking the raw data to insure that they satisfy the number of fringes and time of flight criteria previously set by the electronics, and constructing and pruning histograms of the instantaneous velocities. Finally the mean and rms velocities are computed for each run, making the proper corrections for the sampling bias towards higher velocity particles and the effect of velocity gradients. The histograms are formed by sorting the frequencies of the individual measurements into 100 bins spanning the range from $\frac{1}{\tau_{max}}$ to $\frac{1}{\tau_{min}}$. The histogram pruning removes measured velocities which are isolated from the main body of data and presumably represent anamolous particles or measurements.

The second step in the data reduction process involves combining the different velocity components to give the desired quantities: $\overline{u}, \overline{v}, (\overline{u}^2 + \overline{v}^2)^{\frac{1}{2}}, \sqrt{\overline{u'^2}}, \sqrt{\overline{v'^2}}$, $\overline{(u'^2 + v'^2)}$ and $\overline{-u'v'}$. In particular, given the components u_+, the velocity at $+45^\circ$ to the freestream and u_- at -45°, then

$$u_+ = \frac{1}{\sqrt{2}} \left(\bar{u} + u' - \bar{v} + v' \right) \qquad 6.1a$$

$$u_- = \frac{1}{\sqrt{2}} \left(\bar{u} + u' - \bar{v} - v' \right) \qquad 6.1b$$

These can be combined to give

$$\bar{u} = \frac{1}{\sqrt{2}} \left(\bar{u}_+ + \bar{u}_- \right) \qquad 6.2a$$

$$\bar{v} = \frac{1}{\sqrt{2}} \left(\bar{u}_+ - \bar{u}_- \right) \qquad 6.2b$$

$$\overline{(u'^2 + v'^2)} = \overline{u_+^2} - \bar{u}_+^2 + \overline{u_-^2} - \bar{u}_-^2 \qquad 6.2c$$

and

$$\overline{-u'v'} = -\tfrac{1}{2} \left(\overline{u_+^2} - \bar{u}_+^2 - \overline{u_-^2} + \bar{u}_-^2 \right) \qquad 6.2d$$

In addition $\bar{u}$, u', $\bar{v}$, and v' can be determined from direct measurements in their respective directions. However, all quantities can be determined from measurements in the freestream direction and at $\pm 45^\circ$, with a redundant determination of $\bar{u}$ possible. In this experiment some of the radial traverses included redundant measurements of $\bar{u}$ and also sometimes $\bar{v}$. Except in regions where the velocity magnitude is very small, estimates of $\bar{u}$ from direct measurement and as determined by Equation 6.2a are always within 10% of each other and usually within 5%. The differences can be mainly attributed to zero relocation errors and minor changes in the flow state about the model between the measurement runs. The flow changes occurred because the various components were measured at different times, often after the model configuration had been changed and then returned to the desired form.

6.9 Sampling Bias Correction

The sampling bias is corrected by a technique to be presented in the Third International Workshop on Laser Velocimetry, July, 1978, Purdue University by Dimotakis, Collins and Lang (1978). This technique is also developed in Appendix D of this work. Briefly, the probability of measuring a particular value of velocity is biased towards higher velocities when given a fixed focal volume and a uniform particle distribution that is independent of velocity. The expected value of velocity is, then, correctly given by an ensemble average of properly weighted instantaneous values as the number of samples becomes large, i.e.:

$$\frac{\displaystyle\sum_{i=1}^{N} \left(\frac{u_i}{B(u_i)}\right)}{\displaystyle\sum_{i=1}^{N} \left(\frac{1}{B(u_i)}\right)} \longrightarrow \langle u \rangle \text{ as } N \longrightarrow \infty$$

where N is the number of samples, u_i is the i^{th} instantaneous measurement, and $B(u_i)$ is the probability that u_i will be measured given that it exists. Hoesel and Rodi (1977) give a derivation which indicates that for a large number of samples and a uniformly seeded flow the bias is simply inversely proportional to the time of flight, Δt_i and the expected value is then

$$\langle u \rangle = \frac{\sum_{i=1}^{N} (u_i \Delta t_i)}{\sum_{i=1}^{N} \Delta t_i}$$

Dimotakis (1976) has developed an exact formulation of $B(u_i)$ which unfortunately requires knowledge of all three velocity components. However, as is shown in Appendix D, this formula can be simplified with the result that $B(u_i)$ is actually inversely proportional to the product $n_i \Delta t_i$ where n_i, the number of fringes encountered by a particle, is large. In this experiment $n_i \geq 20$ and the correction is considered valid. Consequently the mean (expected) value of any velocity component, $\overline{u}$, the mean square, $\overline{u^2}$, and rms, $\sqrt{\overline{u'^2}}$, are given by

$$\overline{u} \doteq \langle u \rangle = \frac{\sum_{i=1}^{N} (u_i n_i \Delta t_i)}{\sum_{i=1}^{N} (n_i \Delta t_i)} \qquad (6.3a)$$

$$\overline{u^2} \doteq \frac{\sum_{i=1}^{N} (u_i^2 n_i \Delta t_i)}{\sum_{i=1}^{N} (n_i \Delta t_i)} \qquad (6.3b)$$

$$\sqrt{\overline{u'^2}} \doteq (\overline{u^2} - \overline{u}^2)^{\frac{1}{2}} \qquad (6.3c)$$

6.10 Velocity Gradient Correction

Because the focal volume is of finite extent, in regions where the velocity gradients are large there can be a significant change in the mean velocity from one side of the focal volume to the other. In the worst case for this experiment, the mean velocity changed by 20% of U_∞ across the focal volume. This requires an additional correction of the mean and fluctuating values. As in described in Appendix E (from a private communication, Dimotakis (1978)), to second order

$$\hat{u}(y_c) = \overline{u}(y_c) + \frac{1}{2}\left(\frac{\partial^2 \overline{u}}{\partial y^2}\right)_{y=y_c} \sigma^2 \qquad (6.4a)$$

$$\hat{u}'^2(y_c) = \overline{u'^2}(y_c) + \left[\frac{1}{2}\frac{\partial^2}{\partial y^2}(\overline{u'^2}) + \left(\frac{\partial \overline{u}}{\partial y}\right)^2\right]_{y=c} \sigma^2 \qquad (6.4b)$$

where $(\hat{\ })$ indicates the estimated (or measured) value, $(\overline{\ })$ is the true value, y_c is the location of the center of the focal volume and σ^2 is the variance of the focal volume intensity distribution. The curvatures $(\partial^2/\partial y^2)$ of $\overline{u}$ and $\overline{u'^2}$ are small, giving a correction of 0.4% of the measured mean velocity in the worst case, and can be neglected. The square of the mean velocity gradient, $(\partial\overline{u}/\partial y^{2})^{2}$ is not small however, in portions of the shear layer, and this correction must be applied. Consequently the fluctuations reported here have been calculated by

$$\overline{u'^{2}}(y_c) = \hat{u}'^{2}(y_c) - \left(\frac{\partial\overline{u}}{\partial y}\right)^{2}_{y=y_c}\sigma^{2} \qquad (6.4c)$$

6.11 Measurement Program

Two frontbodies (both simple disks) were selected for study: $d_1/d_2 = 0.5$, which has a supercritical optimum, and $d_1/d_2 = 0.75$, having a subcritical drag minimum. The first disk was studied at two gaps, $g^*/d_2 = 0.75$ and $g/d_2 = 1.5$; the other disk at three gaps: $g^*/d_2 = 0.375$ and $g/d_2 = 0.125, 1.0$. Radial traverses through the model axis were made for at least one gap location and one rearbody boundary layer location for each configuration. Some gap traverses were actually made as many as four times in order that the components u, v, u + v and u - v could be measured, the latter two being required to compute the Reynolds stress, $\overline{-u'v'}$. Points on a given radial traverse were closely spaced on the upper half of the model but more widely spaced on the lower half and were only used as a check for symmetry. A particular model configuration, measurement point and beam plane angle (or velocity component) defined a run. Each run consisted of from 4 to 16 records of 1024 measurements each.

6.12 The Velocity Field

Samples of traverses through the cavity for two configurations are presented in Figures 32 through 39. The particular configurations selected are for the sub- and supercritical disks at their optimum gaps, g^*/d_2. For each geometry, four profiles are shown, presenting u, v, $\overline{(u'^2 + v'^2)}^{\frac{1}{2}}$ and $\overline{-u'v'}$ (all appropriately normalized by U_∞ or U_∞^2) at one axial gap location, $x/g = 0.67$ for the supercritical disk and $x/g = 0.5$ for the subcritical disk, x being measured in the streamwise direction from the disk base. These profiles characterize the mean behavior of the flow in and around the cavity and depict some of the fundamental differences between the two flow regimes.

The mean u component profiles are shown in Figures 32 and 33 for the supercritical and subcritical geometries, respectively. Similarly Figures 34 and 35 display the mean v profiles. Each of these figures has the same scale so comparisons are facilitated. The error bar type symbols actually represent $\pm\sqrt{\overline{u'^2}}$ and $\pm\sqrt{\overline{v'^2}}$ added to the means. No error bar indicates that the rms is less than the size of the mean velocity symbol; for these plots this is equivalent to $\pm 0.017\ U_\infty$. Some asymmetry in the flow between the top and bottom portions of each traverse is noticeable although it is most visible only near the center of the cavity. This lack of symmetry is a consequence of minor alignment problems discussed earlier and should not represent any serious limitation to the results. The Reynolds stress, $\frac{\overline{-u'v'}}{U_\infty^2}$, for the two cases and the turbulence intensity $\frac{\overline{(u'^2 + v'^2)}^{\frac{1}{2}}}{U_\infty}$, follow in Figures 36 through 39.

It is not at all surprising that there are distinct differences between the various profiles for the two regimes. The supercritical mean u profile (Figure 32) displays a thick shear layer with large velocity fluctuations in contrast to the thin, low fluctuation subcritical shear layer. From Figures 36 and 37 it is seen that the supercritical maximum velocity fluctuations are twice the subcritical values. A pronounced potential overshoot in velocity occurs just outside the subcritical shear layer with $(\overline{u^2 + v^2})^{\frac{1}{2}}$ having a maximum value, U_s, of 1.32 U_∞, while the corresponding supercritical overshoot, U_s, is 1.10 U_∞. Significant fluctuations in the subcritical flow occur only for radii less than that of the maximum potential overshoot, whereas the supercritical flow fluctuations persist well outside the location of maximum velocity. Interestingly, the mean velocities inside the cavity are not much different between the two regimes although there are considerably higher fluctuations for the supercritical flow. Both profiles show quite large reversed velocities deep in the cavity, $(\overline{u}/U_\infty)$ being around -0.5, verifying the recirculation inferred from the pressure distributions and flow visualization.

6.13 Shear Stress

Perhaps the most important difference between the two optimum regimes is shown in the streamwise Reynolds stress profiles, Figures 38 and 39. The shear in the subcritical flow is very small except for a narrow peak at the shear layer; the maximum stress is 0.0037 relative to ρU_∞^2. However, in the supercritical cavity large stresses exist throughout; the maximum stress normalized by ρU_∞^2 is 0.0232.

To properly compare these stresses with each other and with the value of the shear in a two-dimensional mixing layer, the stresses should be computed in the local coordinate system of the shear layer. The following equations transform the fluctuations and stress in the body (x, y) axis to coordinates normal and tangential to the shear layer which makes an angle of θ with the free-stream.

$$\overline{u'^2_s} = \overline{u'^2} \cos^2\theta + 2\overline{u'v'} \cos\theta \sin\theta + \overline{v'^2} \sin^2\theta \qquad 6.5a$$

$$\overline{v'^2_s} = \overline{u'^2} \sin^2\theta - 2\overline{u'v'} \cos\theta \sin\theta + \overline{v'^2} \cos^2\theta \qquad 6.5b$$

$$(-\overline{u'v'})_s = (\overline{u'^2}-\overline{v'^2}) \cos\theta \sin\theta + (-\overline{u'v'}) (\cos^2\theta - \sin^2\theta) \qquad 6.5c$$

The results of applying these transformations to the measurements at the location of the maximum shear stress are summarized in the following table. An asterisk denotes the optimum geometry.

Table 2. Shear layer characteristic in local coordinates at the location of maximum shear stress

Configuration		$\frac{x}{g}$	$\frac{U_s}{U_\infty}$	$\frac{\sqrt{\overline{u'^2_s}}}{U_s}$	$\frac{\sqrt{\overline{v'^2_s}}}{U_s}$	$\left.\frac{(-\overline{u'v'})_s}{U_s^2}\right\|_{max}$	$\frac{(-\overline{u'v'})_s\|_{max}}{\left.\sqrt{\overline{u'^2_s}}\sqrt{\overline{v'^2_s}}\right\|_{max}}$
*0.5d	0.75g	0.67	1.10	0.261	0.184	0.025	0.52
	1.5	0.75	1.08	0.225	0.159	0.013	0.35
*0.75d	0.375g	0.5	1.32	0.123	0.090	0.004	0.38
	1.0	0.625	1.24	0.160	0.122	0.009	0.44

The discrepancies between the semi-empirical calculation of the drag (Equation 4.7b, Figure 26) and the measured optima are now clear. The value chosen for the shear stress was $\tau_{max}/\rho U_s^2 =$ 0.0115, the value for a self-similar, two-dimensional, turbulent mixing layer as determined by integrating the velocity profiles presented in Liepmann and Laufer (1947). (It might be noted that integration of the velocity profiles in Wygnanski and Fiedler (1970) gives $(\tau_{max}/\rho U_s^2) = 0.015$.) In the present experiment the measured subcritical optimum shear stress is one-third the two-dimensional value while the supercritical flow has twice that stress. Thus, in terms of the magnitude of the Reynolds stress, $\frac{(-\overline{u'v'})_s}{U_s^2}$, these three flows--the subcritical and supercritical optimum geometries and the plane mixing layer--are quite different. The correlation coefficients, $\frac{(-\overline{u'v'})_s}{\sqrt{\overline{u'^2_s}}\sqrt{\overline{v'^2_s}}}$ do not vary nearly as much, however. Possible explanations for this behavior may involve the streamwise curvature of the shear layer and transverse stretching of the mixing layer vortices as they proceed downstream. Because of the axisymmetry of the flow a ring vortex shed from the disk must increase in circumference if it is to conform to the rearbody diameter.

For larger, non-optimum gaps Table 2 shows that both frontbodies produce stress closer to the two-dimensional results.

Measurements of stress profiles at other axial locations within the gap for the various configurations were not obtained. However, measurements of other characteristic quantities, to be discussed shortly, show little variation with downstream distance which suggests that the stress may be fairly constant also.

6.14 Improving the Estimate of the Optimum Drag Coefficient

If the measured stresses and shear layer velocities are used in Equation 4.7b, new estimates of the drag are obtained. For the supercritical optimum configuration the computed value of C_D as shown in Figure 26 is 0.059; the measured drag coefficient is 0.212 and using the measured values in Equation 4.7b gives 0.124. A second independent measurement of this configuration gave a shear stress of 0.030 based on $U_s = 1.09$ which yields a calculated drag coefficient of 0.149. The agreement is better using the experimentally determined values of the Reynolds stress but obviously some of the conditions assumed in arriving at Equation 4.7b are still violated in supercritical flow. On the other hand, for the subcritical optimum case Figure 26 shows $C_D = 0.031$, the measured drag coefficient is 0.010 and the measured values of stress, 0.004 and 0.005 (from a second independent measurement for which $U_s = 1.36$) yield $C_D = 0.012$. The agreement is very good, giving convincing proof that the subcritical flow is, in fact, a small perturbation to a potential free-streamline solution and that the drag is accounted for by the stress in the separation surface.

6.15 Maximum Fluctuations in the Shear Layer

Figure 40 presents the maximum u component rms fluctuations, $\frac{\overline{u'^2}}{\Delta U}$, for all the gap traverses made as a function of axial location along the gap. The velocity difference between the two streams, $\Delta U = U_1 - U_2$, is the proper normalizing quantity (Brown & Roshko 1974). In the cavity flows there is a non-zero velocity on the low-speed side of the shear layer and a potential overshoot of U_∞ on the high-speed side. The high-speed velocity can be estimated as the maximum overshoot velocity but it is very difficult to define the value of the velocity on the low-speed side of the shear layer, although it is probably rather small as can be seen from the profiles (Figures 32 and 33). For Figure 40 the change in velocity across the cavity shear layers has been taken as U_s which will give a lower bound on the fluctuations. On the ordinate axis are similar measurements made by other researchers of two-dimensional layers. The point from Spencer (1970) is for a mixing layer where the low speed stream velocity is 30% of the high speed velocity and the fluctuations are normalized by $U_1 - U_2$. The other two points involve mixing between a uniform stream, $U_1 = U_\infty$ and a quiescent fluid, $U_2 = 0$.

It is first noticed that there is little change with downstream distance of the maximum fluctuations, suggesting for this quantity, at least, that the shear flows are developing normally. There is considerable spread between the various cavity results about the two-dimensional values. Interestingly, the subcritical optimum case has the lowest fluctuations while the supercritical optimum has the highest even though other configurations shown here have greater drag.

6.15 Growth Rate of the Shear Layer

The growth rate for each traverse is depicted in Figure 41. The thickness, δ, of the shear layer as presented here is defined as the radial distance on a given traverse between the locations at which $\sqrt{\overline{u'^2}}/U_\infty$ is equal to one-half the maximum value of this quantity. Other definitions such as the velocity-profile maximum slope thickness (or vorticity thickness)

$$\delta_\omega = \frac{U_1 - U_2}{\left(\frac{\partial U}{\partial r}\right)_{\max}}$$

(Brown and Roshko 1974), or the thickness based on the locations of 95% U_1 and U_2, cannot be applied due to the ambiguity in determining U_1 and U_2. Even the definition based on $\frac{1}{2}\sqrt{\overline{u'^2}}_{max}$ is difficult to apply since in some instances, e.g., 0.5d 0.75g(this notation meaning $d_1/d_2 = 0.5$, $g/d_2 = 0.75$), the fluctuations on the cavity side never are as low as one-half the maximum. In these cases, twice the distance between the positions of $\sqrt{\overline{u'^2}}_{max}$ and one-half that value on the high speed side has been used. Points from two-dimensional layers are again included on the ordinate axis. When possible the $\frac{1}{2}\sqrt{\overline{u'^2}}_{max}$ definition has been used for these, although there is little difference between this definition and δ_ω. For example, the profile of Wygnanski and Fiedler (1970) yields $\delta/x = 0.217$ and $\delta_\omega/x = 0.215$.

Several interesting features are depicted in Figure 41. First, it appears that the growth rate is also fairly constant along the gap for a given configuration. In addition, there is good agreement between the growth rate magnitudes of several of the cavity layers and the two-dimensional layers. However, two cases, 0.75d 0.125g and 0.5d 0.5g display much faster growth. For these two configurations (the latter is a supercritical optimum geometry) the separation surfaces stagnate on the rearbody face, which apparently tends to thicken the shear layer. Of the other configurations, two are at large gaps and the third is the lowest drag subcritical geometry. The separation surface for these configurations are not subject to as severe a pressure rise, and the shear layer growth more closely resembles that of free mixing layers.

6.16 Velocity Vector Diagrams

The general nature of the mean cavity flow is best seen in the velocity vector plots depicted in Figures 42 through 46. These vectors are determined from the mean values of u and v of which Figures 32 and 34 are examples.

Except for the case shown in Figure 44, the lower half of each cavity is a region of nearly constant velocity reversed flow. This is a consequence of continuity and the axisymmetric geometry.

In Figure 45 the axisymmetric streamfunction, ψ, given by $u = \frac{1}{r}\frac{\partial\psi}{\partial r}$, $v = \frac{-1}{r}\frac{\partial\psi}{\partial x}$ has been calculated and some of the corresponding streamlines drawn. The streamline $\psi = -1$ represents the total amount of mass recirculating in the cavity while $\psi = 1$ indicates the corresponding mass flux in the outer flow. Along the separation surface, the radial location of the zero streamline in Figure 45 is less than 1% of the shear layer thickness away from the position of the maximum velocity fluctuations. This suggests that $\sqrt{\overline{u'^2}}_{max}$ is a reasonable criterion for locating $\psi = 0$ in this type of cavity flow.

The case shown in Figure 44 is a little different from the others. The inner two-thirds of the cavity shows nearly quiescent flow, which is consistent with the flat rearbody face pressure distribution (Figure 14f). Very little fluid is injected into the cavity at stagnation, and the cavity fluid is, for the most part, motionless.

6.17 Boundary Layer Profiles

The final results to be presented from the flow field measurements are boundary layer velocity profiles on the rearbody sides. These are shown in Figure 47. Here x now refers to the distance downstream from the rearbody face; y refers to the vertical distance from the surface. Not surprisingly, the boundary layer thickness increases with the forebody drag and with downstream distance. One interesting feature is the reversed flow shown for 0.75d 0.125g at $x/d_2 = 0.25$. From the flow visualization (Figure 5d) the separation off the rearbody face does not reattach until $x/d_2 = 1.0$, so the reversed flow shown in the velocity profile is expected. Profiles for the subcritical and supercritical optimum geometries are shown near reattachment, i.e., $x/d_2 = 0$. The potential overshoot is still significant for the subcritical case indicating that the flow is joining tangentially onto the rearbody side. No overshoot is apparent for the supercritical case which suggests its reattachment is not tangential.

6.18 Summary

In summary, several important features of the cavity flow and shear layer over the cavity have been revealed by the velocity measurements. The strong recirculation suggested by other measurements has been confirmed, with reversed velocities as high as 50% of freestream measured. Characteristic quantities of the shear layer, namely $\sqrt{\overline{u'^2}}_{max}/U_\infty$ and δ/x, have been seen to be essentially constant along the gap suggesting normal shear layer development. The magnitudes of these quantities differ in varying degrees from the values for two-dimensional free layers due to influences from the rearbody face and cavity recirculation. Most importantly is the recognition of significant differences in the values of maximum shear stress for the different regimes of subcritical, supercritical and free shear flow. These differences are also apparently consequences of the interaction of the shear layer with the rearbody and with the cavity recirculation and provide an explanation for the discrepancies between the experimental and computed determinations of the forebody drag.

VII. MODIFICATIONS TO THE AXISYMMETRIC MODEL

It is now of interest to inquire into the behavior of the forebody system drag if the flow around the axisymmetric body is perturb or if the model itself is modified in some way. For example, what happens if one interferes with the cavity flow by filling in the gap or if the flow separating off the frontbody is altered in initial inclination at separation or turbulence level by changing the frontbody shape or roughness? Also, what effects do Reynolds number and yaw have on the forebody system characteristics? To provide some insight into these questions a variety of tests were conducted in which these modifications and some associated phenomena were investigated, as will now be described.

7.1 Reynolds Number Effects

The question of Reynolds number (Re) effects is of major concern since this investigation is oriented towards large Re bluff body flows. For tractor-trailers, the prime motivation for this work, full-scale Re based on the square root of the frontal area is on the order of 5×10^6 at 55 mph (88 km/hr). The data presented in this study up to now have been from tests conducted at $Re = 5 \times 10^5$, a full order of magnitude below the prototype value. Although it was not possible to attain full-scale Re, 8×10^5 being the largest value possible in the Merrill Wind Tunnel with an 8 in (20.3 cm) diameter model, all configurations studied were run over a range of Re from 1×10^5 to 8×10^5. For this interval only one configuration of the nearly 220 studied displayed any significant response to changes in Re. There did seem to be a trend for the value of C_D to slightly decrease with increasing Re, although the change was never more than 5% over the range considered. In general, with sharp-cornered flat disk frontbodies and a sharp-cornered rearbody face no significant Re dependence of the models would be expected since the location of separation from each face is fixed. Because there was, in general, no effect of Reynolds number on the drag coefficient, the bulk of the detailed studies (pressure distributions, C_D repeatability, etc.) were conducted at Re = 5×10^5. At this tunnel speed the instrumentation was in its most accurate range, the model vibrations were negligible, the freestream velocity could be accurately maintained and the tunnel static temperature rise (due to drag losses) was not too great. In so far as the applicability of this work to higher Re flows is concerned, the lack of variation with Re and the fact that separation is fixed suggest that the results should be valid for much higher values of Re, even to those of, say, a full-scale tractor-trailer.

As was mentioned, one configuration, $d_1/d_2 = 0.875$, $g/d_2 = 0.125$, did exhibit a significant response to Re changes. Shown in Figure 48 is the drag coefficient of this disk as a function of Re with a polished disk face and a face on which roughness (an annulus of No. 120 sandpaper) was applied. The smooth-faced model shows a high drag level, $C_D = 0.38$, out to Re = 7×10^5 then a sudden transition to $C_D = 0.08$, nearly a factor of five decrease in drag. Upon decreasing Re, the low value of drag can be maintained down to about Re = 6.3×10^5 at which the drag suddenly jumps up again. Applying roughness to the disk face lowers both transition Reynolds numbers as well as apparently decreasing the minimum C_D obtainable to 0.045. With roughness the hysteresis region is longer and displays some unusual variations possibly representing an instability of the low drag flow field. No flow visualization photographs nor velocity measurements were made because it was not possible to reach the transition Re in the water tunnel. Tufts on the rearbody side did indicate separation extending roughly one diameter downstream of the rearbody in the high drag mode and fully attached flow at low drag. It is speculated that a transition in the separation stream surface occurs, possibly from laminar to turbulent flow, with the result that the increased entrainment of cavity fluid into the shear layer pulls the layer down onto the rearbody corner yielding a low drag, attached flow field. After this case of transition was found, careful observations were made of all configurations, especially of those with similar geometrical ratios but no other transitions were found. Even for the same disk at slightly smaller, $g/d_2 = 0.094$, and larger, $g/d_2 = 0.188$, gaps with roughness applied there was no tendency for any form of sudden change to occur.

The transition of this configuration from high to low drag is accompanied by the onset of an intense, audible whistling or cavity resonance. Resonance ceases when transition back to high drag occurs. Other geometries, all large disks at small gaps, also exhibit audible resonance, although for these other cases, this phenomenon does not necessarily imply low drag. For instance, $d_1/d_2 = 0.75$, $g/d_2 = 0.125$ for which $C_D = 0.222$ also whistles yet the drag is a factor of 20 greater than the minimum value for this disk which occurs for a geometry that does not resonate, at least audibly. Attempts to measure resonant frequencies were hampered by strong background noise due to the tunnel and no acceptable measurements were made. These resonances qualitatively display some of the features reported by Sarohia (1975). The frequency increases with freestream velocity and undergoes discrete jumps at certain velocities. At the transition velocities the frequency oscillates between the pre- and post-transition values. No discontinuities in drag occur at these transitions however, which suggests that the existence of resonance does not have a direct influence on the forebody system drag. Consequently, details of the resonance have not been further pursued.

7.2 Yaw

For ground vehicles, the influence of yaw angle is particularly important; the drag coefficient of a typical tractor trailer increases from 0.8 at 0° yaw (headwind) to 1.2 at 10° (Buckley & Sekscienski 1975). For an axisymmetric model out of ground effect on the other hand, the relevance of yaw, at least to ground vehicles, is really of academic interest only (although it does have applications, e.g., missiles in a cross-wind). For this reason detailed yaw studies were not done with the axisymmetric model, but were made instead with a square cross-section model to be discussed later. As was described in Experimental Details and also mentioned with regard to the rearbody face pressure distributions, there was some difficulty in accurately maintaining alignment of the axisymmetric model with the freestream however, and the small yaw angle introduced is consequently of concern.

During testing, model side and lift forces were monitored and these measurements, coupled with the rearbody face pressure distributions, gave a good indication whether the model was misaligned. It was sometimes not possible, though, to completely eliminate the asymmetries, a situation reflected in some of the face pressures, e.g., Figures 12d and 13d. For all the results reported herein the non-axial forces are ≤20% for $C_D < 0.2$ and ≤10% for $C_D > 0.2$. The influence of misalignment is indicated in Figure 49 where pressure distributions for different configurations, skewed and aligned, are plotted. Above each profile is the drag coefficient determined from that particular measurement run. In each case the misalignment is roughly 0.5° as was determined by the amount of adjustment required to give a smooth pressure profile. For Figure 49a, the percentage difference in drag, ΔC_D, is 4%; in 49b, $\Delta C_D = 3\%$, and the side forces for the skewed profile were 10% of the drag. For the case shown in Figure 49c, $\Delta C_D = 30\%$ and the side forces were also 30% but the absolute values are quite small and within the experimental repeatability since this is a very low drag configuration. The last comparison has no difference in drag and the side forces are 14% of the drag for both cases. It is clear from this that the face pressure distributions are considerably more sensitive to misalignments on the order of 0.5° than the drag coefficient and that it is possible to align the model to better than 0.5° by requiring a symmetric pressure profile and restricting the acceptable side forces, which has been done for all the results reported.

7.3 Hemispherical Frontbody

Just as adding a frontbody to the basic blunt cylinder modifies the pressure forces acting on both bodies, shaping the upstream face of the frontbody will also alter the flow and pressures of a given diameter and gap ratio configuration. An example of rather radical frontbody shaping is that of a hemispherical body with flat base and $d_1/d_2 = 1.0$. The results for such a body in front of the axisymmetric rearbody are shown in Figure 50. A surprising feature revealed by this figure is the apparently negative forebody system drag obtainable for $g/d_2 < 0.125$. This result seems disturbing at first and during the experimentation great care was taken to confirm that it was real. The balance and pressure measurement systems were repeatedly calibrated and found to be working properly. The model was disassembled, checked for interference, reassembled and tested again with the same results. In addition, the magnitude of C_D at $g/d_2 = 0$ is -0.016 which, from all indications, is outside the experimental noise. In view of these facts, it appears that the result is correct, and consistent with the other data taken in this experiment.

It must be remembered that the forebody system drag coefficient as presented here is, in reality, just the effective face pressure coefficient relative to freestream static pressure, p_∞, acting on the model forebody system, i.e.,

$$C_D = \frac{\int (p-p_\infty)\,dA}{qA}\Bigg|_{\text{forebody system}} = \frac{\bar{p}-p_\infty}{q} = \bar{C}_p \qquad 7.1$$

Obviously, if the effective face pressure, $\bar{p}$, is less than p_∞ then C_D can be negative. As shown by Morel (1978) for potential flow about a semi-infinite half body in a finite diameter wind tunnel this coefficient is always negative, in fact (see the Sketch below)

$$C_D = \frac{\bar{p}-p_\infty}{q} = \frac{-\alpha}{1-\alpha} \leq 0 \qquad 7.2$$

where

$$\alpha = \frac{A_{\text{model}}}{A_{\text{tunnel}}} = \text{Blockage Ratio}$$

In the present case, this potential flow value is $C_D = -0.032$ for $\alpha = 0.03$. This result is consistent with that of Prandtl and Tietjens (1934) who showed

$$\tilde{C}_D = \frac{\bar{p}-p_{\text{base}}}{q} = \frac{+\alpha}{(1-\alpha)^2} \geq 0 \qquad 7.3$$

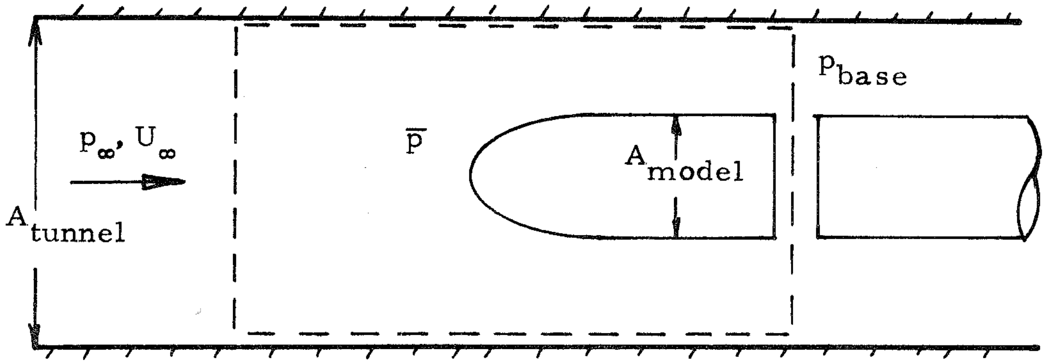

The drag coefficient as defined by Equation (7.1) or (7.2) becomes in terms of (7.3)

$$C_D = \tilde{C}_D + \frac{(p_{base} - p_\infty)}{q} = \tilde{C}_D + C_{p_{base}}$$

Even though $\tilde{C}_D$ is positive, $C_{p_{base}}$ is sufficiently negative to cause C_D to be less than zero, as a momentum balance in the control volume indicated in the Sketch shows. In the present experiments, $C_{p_{base}} = C_{p_{split}}$ is also always negative and apparently the flow for the hemispherical frontbody at zero and near-zero gaps is approaching the potential result.

A limited number of other investigations on hemispherical faced cylinders are available in the literature. Hoerner (1965) has integrated face pressure distributions given by Rouse and McNown (1948) and obtained the value 0.01 for the drag coefficient. As was the case for the blunt faced cylinder only 6 pressure taps were used and the calculation is suspect. Stanbrook (1964) corrects the data of Polhamus (1957) to yield $C_D = 0.02$ at $M = 0.3$. Compressibility may be becoming a factor at this value of M however, since the velocity overshoots to $M \sim 0.4$ on the shoulder of the face. The results of Norris and McGhee (1966) indicate $C_D = 0.009$ at $M = 0.2$. Again there is not enough information available to fully explain the differences between these various values of drag coefficient. Reynolds number and freestream turbulence are definitely important for flow around such a rounded body. For example, in the present test the drag coefficient steadily decreased with increasing Re until $Re = 3.5 \times 10^6$ after which it was constant. Blockage is the most likely reason for the different values of C_D, as was the case in Section 3.2 with the blunt faced cylinder. The present blockage is 3% while the other tests have less than 1% solid area blockage. The potential flow values are correspondingly $C_D = -0.03$ for this experiment and $-0.01 < C_D < 0.0$ for the other studies. It is worth noting that Hoerner has obtained $C_D < 0$ for slightly more streamlined shapes studied by Rouse and McNown; the possibility for negative forebody drag relative to freestream static pressure appears to be real.

In any case, the hemispherical frontbody at small gaps produces very low forebody-system drag. As the gap increases, the drag also steadily rises. Because the separation off the frontbody is tangent to the freestream flow, the separation surface can only turn into the cavity. Consequently stagnation occurs on the rearbody face and the system drag increases. Eventually the value of C_D exceeds the value for those disk configurations where $0.375 \leq d_1/d_2 \leq 0.75$ and $g/d_2 > 1.0$.

7.4 Minor Frontbody Shaping

The effects of shaping less radical than a full hemispherical head were also investigated. The results with plain disks indicate that, up to a point, increasing the drag of the frontbody, that is increasing its diameter, yields a net decrease in forebody drag. This is equivalent to decreasing the initial radius of curvature of the separation streamline. If the frontbody drag were changed by shaping, a similar result might be expected. To test this, two circular cross-section disks of different face form, as shown in the legend of Figure 51, were made. One body has a concave face where the tangent to the surface at the edge makes an angle of 45° upstream relative to vertical. The diameter of this body is $d_1/d_2 = 0.375$ and is referred to as the 'dish'. The other body, with $d_1/d_2 = 0.5$, is a section of a hemisphere where the tangent at the edge is 45° downstream relative to vertical. It will be referred to as the 'hemi'. C_D of the dish based on its own diameter is 1.072 at large gaps, while the value for hemi is 0.591. As would be expected, the dish shaped frontbody has higher drag than the more streamlined partial sphere. Forebody drag coefficients for these frontbodies are presented in Figure 51 along with the results for plain disks of the same diameters and some other modifications to be discussed shortly. At small values of gap the dish does, in fact, yield a lower net drag than the simple disks, which, in turn, are seen to be better than the hemi. As the gap increases, the other bodies become relatively more effective and eventually the dish gives the highest drag. Throughout the entire gap range the hemi behaves nearly identical to the smaller diameter flat disk. The larger disk provides the best reductions, although at larger gaps its own drag begins to degrade its performance. It is apparent from this, then, that changing the angle and radius of curvature of the separation streamline can significantly alter the drag behavior of a particular combination. This would be particularly useful if the diameter and gap ratios of a configuration are fixed. Then, minor shaping of the frontbody would effectively change the diameter ratio and could bring the configuration closer to optimum. It is of interest to note again that at small gaps the desired shaping increases the frontbody drag (e.g., the disk) while at large gaps streamlining the frontbody (the hemi for instance) is more productive.

7.5 Roughness

Effects of roughness on the frontbody face are indicated in Figure 51 for $d_1/d_2 = 0.5$ and in Figure 52 for $d_1/d_2 = 0.75$. Roughness on the face would essentially change the effective Re and the state of the boundary layer approaching the disk edge. As was mentioned earlier in connection with Re effects and is obvious from these figures, roughness has little if any influence on the forebody system drag of these disks. Other diameters were also tested with similar results. The only case of a flat disk frontbody where roughness has been observed to make a difference is that of $d_1/d_2 = 0.875$, $g/d_2 = 0.125$ for which a transition from high to low drag occurs with increasing Re. This behavior, shown in Figure 48, has been previously discussed. The lack of sensitivity to frontbody roughness may suggest a similar insensitivity of the forebody drag to small amounts of freestream turbulence, although this has not been studied in the present experiments.

7.6 Interfering with the Cavity Flow

The importance of the cavity flow in determining the forebody drag is another question of considerable interest. In subcritical geometries a vortex is present which appears to play a key role in maintaining the mass and momentum balances in the cavity and in lowering the outer rearbody face pressures to yield low drag. If this recirculation were interfered with, say, by filling in the cavity, the benefits of the gap vortex might be lost and the drag consequently increased. For supercritical flows, on the other hand, there are large scale oscillations of the shear layer and cavity flow and the drag is high. Filling in the gap for these cases may inhibit the large scale motions and reduce the drag.

To study the influences of interfering with the cavity flow, fillins were tested at gaps near optimum for three diameter ratios: $d_1/d_2 = 0.5$ which has a supercritical optimum gap and $d_1/d_2 = 0.75$ and 0.875, both of which have subcritical optima. The results of the first two disks are shown in Figures 51 and 52 with sketches indicating some of the physical geometries tested. For $d_1/d_2 = 0.5$, the fillin does give a decreased forebody drag; rearbody tufts also exhibit less fluctuation and reversal with the fillin. Interfering with the supercritical cavity flow apparently inhibits oscillations and may encourage a stable vortex to form in the corner of the forward facing step. This reduction in drag is similar to the effect of putting a splitter plate behind a bluff body, e.g., a circular cylinder as studied by Roshko (1954), where the splitter inhibits vortex shedding and decreases the drag. The larger disk, however, experiences an opposite reaction. Except at small gaps, the fillin increases the drag; near optimum gap the increase is a full order of magnitude. In this case the interference has destroyed some feature of the cavity flow, presumably the recirculation, which is necessary to the low level of fluctuations and the reattachment of the separation streamline at the corner. In both of these cases, interfering with the cavity flow has produced large drag changes and indicates the nature of this flow is quite important. This is in contrast to the suggestion by Mair (1965) that the vortex in his base cavities were of no fundamental importance since a fairing gave lower drag. It is possible in the present work that fairings might also give lower drag. The important thing is, however, that either a fairing or the vortex will be required. The absence of both, as shown in Figure 52, causes a drag increase.

For the largest disk, $d_1/d_2 = 0.875$, the fillin has no effect on the drag of optimum configuration. Apparently the low drag vortex is located far enough out radially so that the fillin interferes only slightly with its action. The transition which occurs at a slightly larger than optimum gap is prevented though, or else the transition Reynolds number is increased to a value greater than that which could be obtained in this experiment (i.e., $Re = 8 \times 10^6$). One other modification was made to this large disk ($d_1/d_2 = 0.875$). The optimum gap ($g^*/d_2 = 0.094$) was filled with an elliptical fairing that blended into the rearbody diameter. With a smooth face, the drag for this forebody is high, $C_D = 0.402$. The flow separates before the turning is completed. However with roughness, the flow around the elliptical corner is fully attached and the drag drops to $C_D = 0.020$, a value less than the simple disk value of 0.034. Other studies of rounding forebody corners, by Norris and McGhee (1966) and Rouse and McNown (1948), also indicate great reductions are possible. This will be further considered in the next section.

7.7 Summary

Several general conclusions are suggested by the various modifications to the axisymmetric sharp-cornered rearbody with flat disk frontbodies which have been discussed in this section. First, the basic character of the subcritical and supercritical flows is unaltered by the effects of Reynolds number over a range from 1×10^5 to 8×10^5, and the influences of small angles of yaw ($< 0.5°$). Second, both minor and radical shaping of the frontbody have a strong influence on the forebody drag by changing the frontbody drag itself and by modifying the separation streamline direction and pressure. Finally, the nature of the cavity flow does seem to be important; interference with it can be either beneficial or detrimental depending on the particular state of the undisturbed flow field.

VIII.ROUNDING THE REARBODY FACE

8.1 Corner Rounding

The high drag of the rearbody alone is a consequence of separation at the face edge. Eliminating this separation, as has been well demonstrated in the preceeding sections, can reduce the forebody drag, even to zero. Shielding and matching the separation to the rearbody is one approach. Another is to simply round the rearbody face edges thereby reducing the adverse pressure gradient and inhibiting separation. The hemisphere frontbody discussed earlier is an effective though extreme case of rounding. It has been well documented that this degree of rounding or shaping is more than necessary however. Norris and McGhee (1966) show that for elliptical forebody shapes as blunt as $a/b = 0.5$ (where the face is described by

$\frac{x^2}{a^2} + \frac{r^2}{b^2} = 1$) the drag is hardly any different from that of the hemisphere. The data of Rouse and McNown (1948) give pressure distributions for a flat faced body with a corner radius one-eighth the body diameter. Hoerner's integration of these gives $C_D = 0.2$, a factor-of-nearly-four decrease in the drag. Unpublished measurements of Breidenthal (1974), Figure 53, show how the drag of the blunt faced cylinder changes as the edge radius is progressively increased and as roughness is added. A radius of one-eighth the diameter with roughness is sufficient to produce an essentially dragless forebody. Numerous demonstrations of the effectiveness of rounding corners on box shaped vehicles now exist including those by Möller (1951), Carr (1968), and Saltzman, Meyer and Lux (1974). These studies also indicate that by $r_c/d_2 = 1/8$ most of the face separation has been eliminated and further rounding offers little improvement. The question then arises as to what effect a frontbody would now have on the forebody-system drag; rounding the face of a trailer may greatly decrease its drag, for instance, but what happens when the cab is added? To investigate this problem the rearbody of the present axisymmetric model was modified by the addition of a new rounded face. This face was machined aluminum, instrumented with pressure taps and had a corner radius of one-eighth the rearbody diameter. A series of measurements similar to, but less extensive than, those described for the sharp-cornered model were made. The results follow.

8.2 Forebody Drag

Figure 54 presents the forebody-system drag coefficient of the rounded rearbody with simple, flat disk frontbodies of varying diameters, d_1/d_2, and gaps, g/d_2. The Reynolds number for this figure is 5×10^5. At that value of Re, these measurements show the rearbody by itself to have $C_D = 0.222$, a level that is quite sensitive to Re and roughness however. Without roughness the value of C_D decreases from 0.240 at $Re = 1 \times 10^5$ to 0.129 at $Re = 8 \times 10^5$. Applying roughness (e.g. an annulus of sandpaper) drops the value to essentially zero by $Re = 5 \times 10^5$. This is readily explained by the pressure distributions shown in Figure 55 for the rearbody alone with and without roughness. Also shown is the distribution of a non-cavitating body from Rouse and McNown (1948). The abscissa in this figure is the distance along the face so that side pressures can also be seen. There are quite negative pressures on the rearbody corner (or shoulder), even without roughness, which cancel most of the inboard stagnation. Integrating this distribution gives $C_D = 0.189$ for the present data. The discrepancy between this and the measured value, 0.222, can be attributed to incomplete knowledge of the outboard pressures where the radius weighting is greatest. In any case, the drag is of a moderately low value. Tufts show that some separation back to one-half the rearbody diameter exists which indicates there is still room for improvement. Adding roughness, at a higher Re, provides the needed improvement. The tufts are now fully attached, the shoulder pressures become more negative and the drag goes to zero. Clearly, the smooth-faced, lower Re flow is accompanied by premature laminar separation on the shoulder. The addition of roughness (and the higher value of Re) creates sufficient turbulence to keep the flow fully attached and the drag is essentially eliminated.

The effects of roughness are duplicated at a lower value of Re, e. g., $Re = 5 \times 10^5$, when a thin disk of proper diameter ratio is added at zero gap as shown in Figure 54. For $0.156 < d_1/d_2 < 1.0$, the forebody drag drops near or to zero. In this case the small step caused by the disk is sufficient to trip the flow on the face and it remains attached around the shoulder. The sting alone ($d_1/d_2 = 0.156$) does not produce enough of a disturbance until

$g/d_2 = 0.125$. On the other hand the disk $d_1/d_2 = 0.875$ immediately loses its effectiveness for $g/d_2 > 0$. The separation from this disk reattaches too far downstream of the shoulder and the rounding benefits are lost. Eventually for each disk the drag begins to increase, the larger d_1/d_2, the greater the rise. Interestingly, the smaller disks show a decrease at large gaps, presumably a consequence of wake closure. The asymptotic value of C_D for large gaps with any disk would simply be the disk drag coefficient, as the rearbody face at high enough values of Re, would contribute nothing.

8.3 Drag Breakdown

Breakdown of the drag contributions from the rearbody face and disk are shown in Figure 56. The main feature to note concerning the rearbody face is that for $g/d_2 \leq 1.0$, the drag is always negative. Even with smaller disks for which stagnation occurs on the face, the suction on the shoulder is sufficient to make the value of C_D for the rearbody face less than zero. This is in contrast to the square-cornered model which has positive face drag for the smaller frontbodies. The disk drag curves are marked by their flatness indicating less upstream influence of the rounded rearbody than the sharp-cornered one.

8.4 Flow Field

Rearbody face pressure distributions (now plotted versus radius) and flow visualization (Figure 57 through 63) again provide details and explanations of the drag curve behavior. The same interpretations as discussed for Figure 9 through 16 are applicable here. For smaller disks the flow on the shoulder is mostly attached and the suction there clearly outweighs the face stagnation. Evidence for recirculation in the gap can be seen, e.g., 57b, 58c, and 60b. Larger disks, for which reattachment occurs fairly far outboard, do not exhibit the strong shoulder suction pressures. Instead, the general pressure level along the entire face is much decreased resulting in reduced drag. For $d_1/d_2 = 0.75$, the flow is still basically attached along the shoulder. Evidence of a gap ring vortex can also be seen in Figure 61c, for example, indicating the generality of this particular characteristic independent of the shape of the downstream cavity corner. The largest disk, $d_1/d_2 = 0.875$, produces separation that reattaches radially too far out to take advantage of the rounded shoulder and the total drag is fairly high. For this disk at small gaps the face pressures are uniform and moderately negative since the face is, in general, immersed in a constant pressure disk wake. It might be noted that although $Re = 1 \times 10^6$ for the flow in the photographs, a value below the critical Re of the rounded rearbody by itself, the flow is still attached on the shoulder for many of the configurations. The disks provide sufficient disturbance to energize the rearbody face boundary layer and keep it attached, even for Re as low as 1×10^5.

8.5 Comparison with Square-Cornered Results

To conclude this section it is useful to present a comparison of the square-cornered and rounded rearbody system drag. Shown in Figure 63 are the curves for two disks, $d_1/d_2 = 0.25$

and 0.75 (representing supercritical and subcritical geometries respectively) with the two different rearbodies. The benefits in rounding when a small diameter frontbody is used are obvious. Interestingly, the gap for minimum drag of the square-cornered configuration ($g/d_2 = 1.0$) is the same as the gap for maximum drag of the rounded body. As was noted in reference to Figure 17, the radial location of the rearbody face stagnation is also a maximum at this gap. For the square-cornered body the face separation and consequently the drag is minimized in this situation. But for the rounded model the thick, impinging shear layer does not have an opportunity to organize itself as a boundary layer before it reaches the shoulder and the possibility of large suctions are lost. However, even in this worst case (for the rounded rearbody) the square-edged model has more than twice the drag.

The situation is somewhat different for the larger disk. At small gaps, rounding definitely improves the flow. But when matching of the disk separation onto the rearbody becomes effective, rounding is no longer superior. In fact, at $g/d_2 = 0.5$, the square-corner drag is only one-third that of the rounded body. Throughout the range $0.375 \le g/d_2 \le 1.5$ the sharp-corner drag remains lower, a result supported by the face distributions, although the mechanism for this at large gaps is not completely clear. This behavior should be kept in mind in designing for practical situations requiring a frontbody. Rounding the rearbody is not always the most effective way to decrease drag. If matching of the separation surface to the rearbody is possible it may be exploited at times for greater gains.

IX. RESULTS FOR SQUARE CROSS-SECTION

At this point the flow about the forebody system of a semi-infinite axisymmetric cylinder has been considered for a wide variety of forebody configurations and modifications. It is now of interest to ask how the flow depends on the cross-sectional shape itself. In particular, for a square cross-section rearbody with smaller square plates in front, is it possible to realize the same large reductions in drag observed for the axisymmetric body? It might be expected that the situation is less favorable since the separation surface leaving the frontbody cannot remain square and so will not reattach smoothly everywhere onto the leading edges of the rearbody. A similar situation would exist in most practical applications and is reason to examine the effects of rearbody shape.

9.1 Forebody Drag

Limited tests of a square cross-section rearbody with symmetrically positioned, square, flat plate frontbodies were conducted, using procedures identical to those for the axisymmetric geometry. The basic results, that is the system forebody drag, are presented in Figure 64. This experiment determined the rearbody-alone drag coefficient to be 0.712, a value 1.3% below C_D of the axisymmetric rearbody. No other measurements of the face drag coefficient of a square cross-section cylinder apparently exist in the literature. Information on bodies such as this, for example Hoerner Chapter 3 and Nakaguchi (1978), include base and skin friction drag and are consequently of little use in establishing the face drag alone to any acceptable degree of accuracy. The nearly equivalent behavior of the axisymmetric and square rearbodies is to be expected, however. As was discussed in Section 3.4a, the considerable information available on thin plates normal to the flow shows that the values of the drag coefficients of both square and circular thin flat plates lie between 1.1 and 1.2. There seems to be no fundamental difference between the two. Thus it is not surprising that the two basic semi-infinite bodies discussed here also display no significant difference in their face drag coefficients. Nakaguchi shows that indeed there is little difference in the total drag as well for bodies whose length is greater than two diameters (or widths).

The face pressures on a centerline running perpendicular to the edge are shown in Figure 65 along with the axisymmetric distribution and the potential flow result for a two-dimensional step with a constant, $C_p = 0$ separation surface (which will have the most positive pressures of the family of constant pressure free-streamline results) for reference. Clearly there is very little difference between the experimental measurements, although it appears that the square model pressures are slightly lower near the edge, which may account for its lower drag. In any case, it is apparent that the two basic cross-sectional shapes behave essentially the same.

The results presented in Figure 64 show that, not only are the results for the basic bodies nearly identical, but the changes in forebody drag due to the addition of a frontbody are also very similar. Adding a frontbody, in general, reduces the drag. Also, a given frontbody has an optimum gap for minimum drag and very large reductions are possible. Resonance was also observed for some of these configurations. But, as with the axisymmetric geometry, the existence or absence of resonance appeared to be uncorrelated to the drag coefficient and was not studied in any detail. Also, these models demonstrate no variation of C_D with Re; the values shown in this figure are for Re = 5×10^5. There are two significant differences however, between the axisymmetric and square cross-sections. First, it is noticed that $d_1/d_2 = 0.875$ apparently does not give the sharp minimum in C_D at small gaps that its axisymmetric counterpart does. More importantly, although the minimum drag for the plate $d_1/d_2 = 0.75$, (i.e. $C_D = 0.065$ at $g/d_2 = 0.375$) is more than an order of magnitude less than the rearbody alone, it is still a factor of six greater than the value for the same configuration for the axisymmetric model. These two features are consequences of a fundamental difference between the two basic geometries and will shortly be discussed. Points denoted 'Cab' on the figure are also to be considered later. One other inference might be drawn from this figure. There again appears to be a distinction, though much less pronounced, between subcritical, e.g., $d_1/d_2 = 0.75$, and supercritical, e.g. $d_1/d_2 = 0.5$, geometries. The inability to clearly categorize the disks in this manner, however, is another consequence of the fundamental difference alluded to above.

9.2 Flow Field

Flow visualization, Figure 66, shows that, in the side view at least, the separation surface develops very much as in the axisymmetric case. At small gaps it stagnates on the face. Near optimum, the subcritical flow nicely matches the rearbody while the supercritical flow does not. For large gaps the shear layer develops large scale oscillations for both regimes just as before. In a like manner, the motion of tufts on the rearbody sides generally correlated well with the model drag, showing nearly fully attached flow at low drag and large regions of separation or intense fluctuations for the higher drag configurations. Some unusual tuft behavior occurred near the longitudinal (streamwise) edges, although attempts to locate a streamwise vortex along these edges or any other organized crossflow with a simple paddle wheel type vorticity meter were unsuccessful. Indications of the difference between the axisymmetric and square bodies are more evident in the face pressure distributions.

Contours of constant pressure over a quarter of the rearbody face for configurations representative of subcritical and supercritical geometries are shown in Figures 67 through 70 (the notation 0.75d 0.125g means $d_1/d_2 = 0.75$, $g/d_2 = 0.125$). In Figure 67, the gap is less than optimum. The subcritical plate has stagnation only near the diagonal corners. Inboard, the distribution is typical of recirculating cavity flow, with predominately negative coefficients. The supercritical distribution also indicates recirculation but here the pressures are all positive, consistent with the higher system drag of this configuration. Results for the optimum gaps are shown in Figure 68. Here, as was anticipated, the basic difference between the square and axisymmetric cross-sections becomes clear.

The subcritical plate has quite negative coefficients over much of the face and also suggests a well-defined ring vortex in the gap. But, at the diagonal corners the separation surface stagnates and the pressures are positive. This stagnation also raises the pressure level inboard a little above the axisymmetric values. Thus, the net effect is a considerable percentage increase in drag over what can be obtained if there is perfect matching everywhere. Further evidence for this source of drag has been obtained by introducing air into the cavity of the model used in the water tunnel. The bubble that forms gives a good impression of the shape of the free surface. This flow, as viewed from head on, is sketched in Figure 71. Indeed, there is good matching along most of the rearbody edges. But near the corner the separation surface forms a wedge shaped surface, stagnates on the rearbody face and turns inward; positive diagonal corner pressures and a rise in the general level are a natural consequence. It is this inability to match the separation surface to the diagonal corners of the rearbody that differentiates the axisymmetric and square cross-sections and accounts for the differences noted earlier. The supercritical plate at optimum still has positive face pressures, as in the axisymmetric case, which suggests that it does truly behave in a supercritical manner with large scale shear layer oscillations and incomplete matching everywhere. At a larger gap (Figure 69) the subcritical plate retains both the low drag features of a ring vortex and the high drag corner stagnation. The supercritical plate shows large variations around $C_p = 0$. In Figure 70 the subcritical plate at a gap much greater than optimum is compared with the rearbody alone. The plate still has a strong influence on the rearbody, with a large region of negative pressure evident. The general pressure level is higher now though, and the drag has correspondingly increased.

9.3 Comparison With Axisymmetric Model

A summarizing comparison of the effects of rearbody cross-sectional shape is shown in Figure 72. Again, a subcritical and supercritical frontbody have been chosen. The shape of the curves, as has been pointed out, is much the same for the two different rearbodies. The axisymmetric configurations show lower drag for both frontbodies with the decrease in absolute value about the same. But the percentage difference at optimum gap is 13% for the supercritical case and 650% for the subcritical. Obviously then, a geometry which can have perfect matching of the separation surface onto the rearbody is quite adversely effected by the inability to conform at the diagonal corners. On the other hand, the supercritical flow, which even at the axisymmetric optimum does not match well, experiences only a minor perturbation due to these same corners and is much less seriously influenced.

X. MODIFICATIONS TO THE SQUARE CROSS-SECTION MODEL

To conclude this investigation a brief study of the influences of various modifications to the square cross-section model have been made. The intent of this study is to bring the model closer to practical situations, specifically tractor-trailers, and to try to obtain some indication of the effectiveness of the concepts developed up to now when the geometry or flow is not so simple and symmetric. The choice of the square model for this study is dictated by the desire to make the results relevant in some sense to ground vehicles, bodies whose cross-sections are normally rectangular rather than round. No attempt has been made to model any particular vehicle or even to model general vehicle details (such as wheels). Only the most obvious physical parameters have been altered. Furthermore, it is not the purpose of this work to optimize any configuration or present formal design guidelines or criteria. Finally, due to the vast number of geometrical and flow combinations that are possible, only a sampling of configurations has been studied, their selection representing some of the more salient features of real flow situations.

10.1 Effects of Yaw

The influence of yaw angle on vehicles is extremely important. For example, Buckley and Sekscienski (1975) show that a typical tractor-trailer, which has a drag coefficient of 0.71 with no wind, will actually experience an average effective value of $C_D = 0.93$, a 31% increase, during the course of, say, a year of service due to natural winds and the effect of the resulting yaw.

Consequently, it is of interest to first know something about the yaw behavior of the simpler configurations which have been studied so far. Figures 73 through 75 show several examples of flow visualization and face pressure distributions for the square cross-section model at yaw with and without simple flat plate frontbodies. Contours of constant pressure coefficient are shown for the upper half of the rearbody alone at 10° yaw in Figure 73; above the plot the value of the forebody-system drag coefficient for this flow situation is noted in the body-axis coordinate frame which is the relevant frame for ground vehicle aerodynamics. Interestingly, the face of the rearbody alone experiences no increase in drag at 10° yaw. The windward side of the face shows a buildup of pressure relative to the unyawed flow due to stagnation; but this is balanced by lower than normal pressures on the leeward portion of the face as the flow accelerates in that direction, and the net change in drag is essentially zero.

Figure 74 shows the face pressures for a subcritical plate and a supercritical plate at their respective optimum gaps but at 10° yaw; flow visualization for these are shown in Figures 75a and b. The distributions are rather irregular, though less so on the windward side. The sting itself locally perturbs the flow, but not seriously, as was indicated by tufts on the rearbody face. Unfortunately, a reliable measurement of the drag for the subcritical configuration was not made, but the value is estimated to be $C_D \sim 0.3$, four times the unyawed coefficient. The supercritical geometry has $C_D = 0.580$, a factor of 2.6 over the 0° yaw case. Just as the diagonal corners of the square rearbody affect the subcritical geometry more than the supercritical, so does yaw produce a greater percentage increase in the drag of the well-matched square model. However, the subcritical plate at its optimum gap still has less drag when it is yawed. Although the separation surface now stagnates on the rearbody face for both cases, the extent of positive pressure coefficients is much greater for the supercritical model. The flow visualization (Figure 75) shows the larger stagnation region on the supercritical rearbody face.

A considerable amount of crossflow in the gap for both configurations can also be seen in Figure 75. This crossflow separates from the leeward edge of the rearbody face, and the pressures near this edge are not as low as they might be if the flow were matched. Although the drag substantially increases when the plate-rearbody configurations are yawed, it has not yet reached the level of the rearbody alone. The plates still retain some effectiveness in reducing the drag even at 10° yaw.

10.2 Side Force at Yaw

During the yaw experiments the side forces acting on the metric portion of the model were also monitored and a rather unexpected phenomenon was encountered. Rather than the side force being in the same direction as the transverse component of the velocity vector, for some cases it was actually into the wind. This behavior is shown for two configurations in Figure 76 where the sign convention is given in the inset sketch. The coefficient presented is the measured side force normalized by the freestream dynamic pressure and the side area of the metric portion of the model. Figure 76 shows that for negative yaw the side force is positive and vice versa; the model is trying to restore itself to symmetric flow. The effect is greater for the rearbody alone and quite linear for that model up to ±2° of yaw. Unfortunately, the side-force-component Schaevitz coil began to fail soon after these particular measurements were made and reliable results for other geometries and yaw angles were not obtained.

An explanation for this behavior of the side force is found in pressure measurements made at two locations on the centerline of the rearbody side. These side pressure coefficients are presented in Figure 77. Pressures were measured on only one side; but, by yawing the model equal positive and negative amounts, the pressures acting on both sides at once can be inferred. It is first noticed that for both configurations at zero yaw, the downstream pressure coefficient (tap no. 15) is more negative than the upstream value. Similar results are given for blunt face axisymmetric cylinder side pressures by Ota (1976) and Rouse and McNown (1948). Their measurements indicate the minimum pressure on the side is inside the separation bubble and located at $x/d_2 = 0.67$ and 0.63 respectively. In the present work pressure tap no. 14 is at $x/d_2 = 0.13$, no. 15 is at $x/d_2 = 0.5$ and the lower pressure at location 15 is to be expected. The pressures for the rearbody alone (denoted as No Frontbody on Figure 77) are consistent with the measured side force. The leeward pressures become more positive and the windward more negative as the model is yawed. Apparently, even up to 6° of yaw the flow stagnates on the rearbody face and separates at the edges with different length separation bubbles on either side of the model. The shorter bubble, with correspondingly more negative pressures, occurs on the windward side. Although the situation with a frontbody is more complicated, the net effect of the side pressures is to cause a side force which is also into the wind.

10.3 Flat Plate Frontbody Modifications

The results discussed so far in this chapter are summarized in Figure 78 along with a variety of other measurements.

Several modifications to the configuration $d_1/d_2 = 0.75$, $g/d_2 = 0.5$ (i.e., .75d .5g on the Figure) have been tried since this configuration is close to the geometrical height and gap ratios of tractor-trailers. At 10° yaw there is an increase in drag from $C_D = 0.082$ to 0.52; the matching which exists at 0° for this model is nearly eliminated at large angles of yaw. In an attempt to improve this situation, a vertical spoiler of height d_2 was mounted on the centerline of the rearbody face and protruded halfway into the gap. The results are quite dramatic (the points labelled .75d.5gVS in Figure 78). At 0° yaw the drag is slightly increased from 0.082 to 0.100, possibly because of interference with the reattaching flow near the spoiler. But at 10° the drag coefficient increases only to 0.288, a 56% decrease in the unmodified value. The spoiler prevents crossflow and separation off the leeward rearbody face and pushes the windward stagnation further outboard. The net result is a large reduction in the drag at yaw.

Two other quick alterations to this configuration have also been made. The plate has been mounted off-center with a plate edge and a rearbody side on the same plane. The solid plate has also been replaced by a centered, perforated plate of about 40% porosity. The latter plate by itself has C_D=0.98 as compared to 1.13 for a solid plate (de Bray (1956)). Increasing the porosity to 65%, however, cuts the drag down in half to $C_D = 0.55$. In the present work, both the off-center plate and the porous plate yield configurations whose drag coefficients are 0.437. The porous plate, although it has less drag by itself and reduces the general level of rearbody face pressures, cannot generate the large negative cavity pressures created when the plate separation joins smoothly onto the rearbody. The force is consequently higher. With the plate off-center, conditions no longer exist for proper matching and the drag here is also increased. However, near a ground plane an off-center plate may be required to insure matching, although the relative dimensions for optimum flow will be different. This can be seen in the second pair of photographs (c & d) in Figure 75. Here the same plate ($d_1/d_2 = 0.75$) mounted off-center is shown sitting on a ground plane. The optimum gap for this plate, when it is centered, is $g/d_2 = 0.375$. Due to symmetry about the ground plane it might be expected that the effective heights of the two bodies are now doubled and that the corresponding optimum gap should also be doubled. From the photos it is clear that this is indeed the case. At $g/d_2 = 0.375$ the plate separation overshoots the rearbody leading edge; the situation is far from optimum. However, at $g/d_2 = 0.75$ the separation now matches fairly well to the rearbody and the configuration approximates the optimum flow of a centered frontbody.

With the axisymmetric model, minor shaping of the frontbody can alter the effective frontbody size and bring it closer to optimum for a fixed gap. To see if this carries over to a square cross-section and, also, to see if the yaw performance can be improved, two simple modifications to a centered supercritical plate at its optimum gap (i.e., $d_1/d_2 = 0.5$, $g/d_2 = 0.5$) have been tried. Four tabs were mounted to the plate edges as shown in the Sketch below. The tabs forward (TF in Figure 78) form a concave surface facing the incoming flow while the tabs rearward (TR) give the plate a convex shape. The tab surfaces make an angle of ±45° (depending on their orientation) with the plate face and increase the characteristic dimension of the frontbody from $d_1/d_2 = 0.5$ to 0.588. The results obtained with

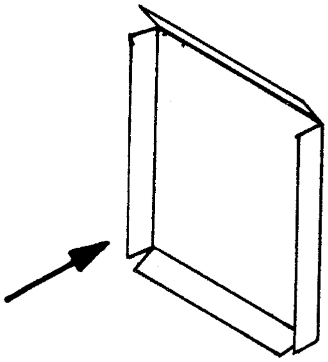

Tabs forward

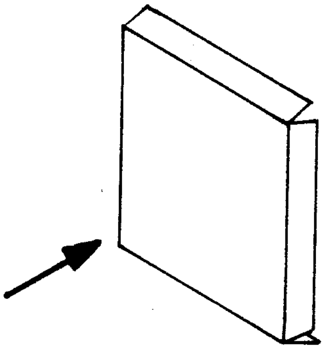

Tabs rearward

this shaping are shown in Figure 78. At 0° yaw, the tab forward (concave) frontbody yields the lowest drag followed by the TR model and finally the unmodified frontbody. This result is similar to the behavior of the circular shaped frontbodies shown in Figure 51. The concave face forces the separation surface radially outward as well as requiring it to turn more before it becomes aligned with the freestream. Consequently, the separation surface more nearly joins tangentially onto the rearbody than with the unmodified plate, and the cavity pressure is lowered. With the tabs rearward the separation is also brought closer to reattaching on the rearbody edge by virtue of the increase in frontbody size. The tab forward configuration is not as effective in lowering the face pressures as the concave form however, and the value of C_D for the convex frontbody is higher. At 5° yaw, the order of the three models is unchanged with respect to their value of C_D, although there is now little difference between the tabs forward and tabs rearward configuration. Finally at 10°, the convex frontbody configuration has the least axial resistance followed by the unmodified and tab forward models. Most of the tab rearward improvement comes from the windward surface which reduces crossflow through the gap and brings the windward separation surface closer to reattaching onto the rearbody edge.

10.4 Tractor-Trailer Simulation

The preceding modifications have concerned configurations with diameter and gap ratios which are typical of tractor-trailers. There is another important geometrical parameter still to be considered, however. The frontbody of a real vehicle configuration is not a thin plate but has considerable depth, up to six-tenths the rearbody diameter. In order to gain some feeling for the significance of this parameter and to look in general at a very simplified vehicle geometry, a cab shaped frontbody has been tested, again with the square cross-section rearbody. This body has a width equal to the rearbody width d_2, has $d_1/d_2 = 0.625$, is $d_2/2$ deep in the axial direction and mounts off-center so that the cab and rearbody bottom surfaces are flush; all edges are sharp. The proportions of this body relative to the rearbody are close to those of a typical cab-over-engine sleeper truck. No other details such as wheels and undercarriage, cooling flow or cab shaping have been reproduced. In addition the tests have been done away from a ground plane, a feature that must be kept in mind if the results are extrapolated to real configurations.

Shown in Figure 64 and also in Figure 79 is the variation in forebody drag of this cab-trailer model as a function of gap at 0° yaw. Figure 64 compares these results with the simple flat plate frontbodies previously discussed, while in Figure 79, results from two other investigations are presented. Several features stand out: the drag is always fairly large, has its lowest value at zero gap and has a very weak local minimum near $g/d_2 = 0.625$. It might be noted that the typical operating gap of a tractor-trailer is between $g/d_2 = 0.3$ and 0.5 (where d_2 for a truck is usually defined as the square root of the total frontal area).

The work of Mason and Beebe (1977) (shown in Figure 79) has been done with a fairly detailed model of a production vehicle on a ground plane at Re = 2×10^6. Their intent, however, has been to gain an understanding of the flow field of these vehicles rather than optimizing a particular vehicle. The results of Mason and Beebe display very similar trends to those of the current work. This suggests that the configurations studied in the present experiments do reproduce the more important geometrical properties of tractor-trailers. The measurements of Mason and Beebe actually include all contributions to drag, i.e., forebody drag plus skin friction, undercarriage and base drag. When corrections are made for these (reducing C_D by about 0.25), their results are not only qualitatively similar but are also very close in absolute value. This may be simply fortuitous, but it lends confidence to the usefulness of the current studies even though a ground plane is absent.

As is apparent from Figure 79, the influence of an off-center, thick frontbody on the forebody drag is considerably different from the influence of a centered, thin plate. At zero gap, the cab acts as a step and its separation can be generally guided onto the rearbody. Once a gap is created, the asymmetry causes a downflow through the gap and alters the flow. The separation streamwise moves downward, stagnates on the trailer face and the drag is increased. If the downflow is prevented by blocking the gap with a horizontal plate, as Mason and Beebe have also done, the drag only very slightly increases with gap, confirming the importance of the downflow for this type of configuration. Although it has not been tried, presumably if the cab is centered with respect to the rearbody, requirements of symmetry will prevent any downflow at 0° yaw. The drag, similar to the case for centered thin plates, should then be reduced.

Nakaguchi (1978) has treated simplified truck-like models, but also near a ground plane. His models, which are square in cross-section, lack any detail and the frontbody has the same cross-sectional dimensions as the rearbody (i.e., $d_1 = d_2$). The behavior of this model (Figure 79) is quite unlike that of the smaller height, off-center cabs. Nakaguchi's results show that the total drag (including skin friction and base drag) actually decreases as the gap is increased. This is a trend very similar to the behavior of the centered disk, $d_1/d_2 = 1.0$, with the axisymmetric rearbody which is also shown in Figure 79. In addition, if the forebody drag is extracted from Nakaguchi's data, the behavior is both quantitatively and qualitatively similar to the disk $d_1/d_2 = 1.0$. Apparently, despite the presence of a ground plane, enough symmetry remains in the flow about his model to prevent any significant gap crossflow and the net result is not much different from two equal diameter bodies in a free field. Nakaguchi also has measured the force acting on just his rearbody (or trailer). This is shown in Figure 80. Figure 80 also compares the axisymmetric rearbody and the disk $d_1/d_2 = 1.0$ with the force measured by Flynn and Kyropoulus (1952) on the trailer of a detailed wind tunnel model. The measurements of Flynn and Kyropoulus and of Nakaguchi include skin friction and base drag and consequently give a more positive value for the rearbody drag. Nevertheless, in all cases, even for a close simulation of a real vehicle, the rearbody has a net thrust on it due to negative pressure coefficients developed on its face. The decreasing thrust as the gap is enlarged for Nakaguchi's model does not occur for the axisymmetric geometry and is presumably a consequence of the ground plane proximity.

10.5 Decreasing Tractor-Trailer Drag

To conclude this portion of the experimental work, a series of modifications have been made to the square cross-section rearbody and cab-shaped frontbody as an exercise in applying the lessons learned from the preceeding studies. The intent is to see what improvements can be made to the basic truck-like geometry both in symmetric and yawed flow with the restrictions that the changes must be simple and practical. A practical change is one that cannot increase the total frontal height or width nor interfere with the vehicle's ability to pivot (or jack-knife) at the joint between the two bodies. (Figure 82 shows an example of such modifications.) One gap ratio, $g/d_2 = 0.5$, has been selected for this test series since it represents a common operating configuration. Many of the modifications to be discussed are used on production vehicles and do not necessarily represent any new method for reducing tractor-trailer drag. The purpose of this study is simply to document the possibilities for reducing drag.

With no modifications the cab-rearbody combination at $g/d_2 = 0.5$ has a drag coefficient of $C_D = 0.690$. The first change was to add a rounded lip or fairing to the four edges of the cab face. In principle, addition of a lip should be as aerodynamically effective as rounding the corners (Lissaman 1975) and in addition does not reduce a vehicle's volumetric efficiency. Only one set of fairings was tried, a semicircular section with $r_c/d_1 = 0.08$. With these in place the drag changes to 0.685, less than a 1% decrease. As has already been shown (for example Figure 53) rounding should continue to have benefits up to $r_c/d_1 = 0.125$; obviously the lip has insufficient radius. This lip was left on, however, for the remainder of the tests. Next, a series of cab mounted, flat plate deflectors, intended to provide the proper matching of the upper frontbody separation surface to the rearbody, were studied. Various heights, widths and axial locations of the deflector on the cab were tried; the best performance being obtained with a full width deflector at a gap, $g/d_2 = 0.75$ and a total frontbody height seven-eights the rearbody height. With the deflector and lip in place the drag coefficient is now 0.413. The last sequence of modifications consisted of vertical spoilers located on the rearbody face and the base of the cab and deflector whose purposes were to prevent gap crossflow and guide the separation from the cab sides onto the rearbody. The results of all these modifications are summarized in Figure 81. The sketch to the left of each measurement is the top view of the forebody system with the appropriate devices shown. The cab mounted horizontal deflector is the one previously noted as having the best performance. With only the lip in place the drag coefficient is 0.685 at 0° yaw and 0.957 at 10°. Successively adding the various spoilers continues to decrease the drag at both yaw angles until the last configuration shown is reached. This model, presented in a perspective view in Figure 82, has the best performance in both axial and yawed flow of any configuration tested. The values of C_D here are 0.363 and 0.495 at 0° and 10° respectively and represent 47% reductions from the drag coefficient of the unmodified model.

Once more, it should be emphasized that this was not an exercise in optimization, but rather a demonstration of possibilities and that other factors, most notably the ground plane and body details, must be considered in any practical applications. Nevertheless, from these results it is clear that even a complicated, high drag body such as a cab and trailer can exploit the concept of beneficially interfering with the flow to yield geometries with a much reduced drag force on the forebody, without resort to radical shaping or fairings.

XI. CONCLUSIONS

11.1 Summary of Results

a. The most important result is presented in Figure 3. The forebody drag of a blunt square-cornered cylinder of diameter d_2 is high, $C_D = 0.722$. Positioning a disk of diameter d_1 coaxially in front can decrease the extent of separation through beneficial interference between the front and rearbody flow fields and yield a net reduction in drag. In some cases, the reduction is nearly two orders of magnitude; the lowest value of C_D observed is 0.010 for $d_1/d_2 = 0.75$, $g/d_2 = 0.375$. It is also found that for each diameter ratio, d_1/d_2, there is an optimum gap ratio, g/d_2, for which the drag is a minimum.

b. In the cases of very low drag the separated flow from the frontbody forms a thin, turbulent shear layer which joins tangentially onto the rearbody. Well organized recirculation then exists within the cavity. A consequence of this flow field is that the rearbody face is exposed to pressures considerably below free-stream static pressure. These low pressures, acting on the outer radial portions of the rearbody face, balance the stagnation pressures on the frontbody face, and the axial force on the forebody system is very small.

c. The thin, smoothly reattaching frontbody separation streamsurface suggests a free-streamline model of the flow. A two-dimensional, free-streamline theory prediction of the wake geometry behind a flat plate agrees quite well with the experimentally determined, axisymmetric, optimum geometries over the range of diameter ratios $0.38 \leq d_1/d_2 \leq 0.88$ (Figure 23). Empirically correcting the two-dimensional results for the axisymmetry of the present configurations gives satisfactory agreement between predicted and measured wake pressures for $0.5 \leq d_1/d_2 \leq 0.88$ (Figure 24).

The optimum forebody drag can also be estimated by making a cavity momentum balance and using the semi-empirical results for the wake geometry and pressure and an assumed value of the shear stress, τ_s, along the free streamline. Reasonable agreement is found between the estimated and experimental minimum values of C_D for $0.6 \leq d_1/d_2 \leq 0.88$. Two important features of this comparison (Figure 26) are observed. There is an abrupt jump of the experimental optimum values of C_D away from the estimated values at $d_1/d_2 \sim 0.5$. In addition, for $0.6 \leq d_1/d_2 \leq 0.8$ the experimental optimum values of C_D are actually less than the estimated values.

d. Flow visualization shows that for diameter ratios between 0.6 and 0.88 at the optimum gap, there is nearly smooth reattachment of the flow onto the rearbody and the separation surface itself is simply a thin, turbulent shear layer. On the other hand, for diameter ratios outside this range the shear layer undergoes large scale oscillations and is much thicker. This change in the shear layer behavior and the sudden departure of the experimental drag minima from the free-streamline results suggest the existence of a critical geometry. This critical geometry is more properly defined in terms of the gap ratio $(g^*/d_2)_{cr} = 0.5$

for which the corresponding diameter ratio of $(d_1/d_2)_{cr} = 0.6$. For optimum geometries whose gaps are less than critical (subcritical geometries), a thin shear layer spans the gap between the front and rearbodies, and the drag is very low. For larger-than-critical, optimum gaps (supercritical), the frontbody separation surface becomes unstable on a larger scale. The resulting drag, though still less than that of the rearbody-alone, is much higher than in the subcritical case.

e. Investigation of the flow field with a frequency-shifted laser-Doppler velocimeter reveals several important features of the sub- and supercritical flow regimes. The supercritical regime is characterized by large fluctuating velocities and a maximum shear stress, $\tau_s = -\overline{u'v'}/U_s = 0.019$, almost twice the value, 0.0115, found for a two-dimensional, self-similar mixing layer. For the subcritical regime, on the other hand, the magnitude of the velocity is one-half the supercritical values and the maximum shear stress, $\tau_s = 0.0021$, nearly an order of magnitude less than the supercritical stress. Using these measured stresses in the semi-empirical estimation brings the calculated values of C_D into much closer agreement, especially for the subcritical geometries, with the experimental results.

The velocity measurements also verify that cavity recirculation, which is suggested by pressure distributions and flow visualization, actually exists. Reversed velocities greater than $0.5\ U_\infty$ are observed near the bottom of the cavity. The streamwise development of the separation-surface shear layer is generally similar to that in two-dimensional mixing layers, the growth rate and magnitudes of the maximum streamwise fluctuations being fairly constant along the surface. The magnitudes of the growth rate and fluctuations vary, however, from the values for the subcritical optimum which are comparable to the two-dimensional free shear layer values to more than twice those values for the supercritical optimum. The Reynolds stresses, however, in the subcritical case are not only much smaller than in the supercritical case but are even much smaller than in a normal plane mixing layer.

f. The drag of axisymmetric configurations where the frontbodies are thin, flat disks is essentially independent of small angles of yaw ($< 0.5^\circ$) and of Reynolds number (Re) effects for $10^5 < Re < 8 \times 10^5$. Shaping the frontbody or interfering with the cavity flow can significantly alter the forebody-system drag, although the nature of the change in drag depends strongly on the particular configuration being modified (Figures 51 and 52).

The possibility for negative forebody drag has been demonstrated by the results for a hemispherical frontbody at zero and small gaps (Figure 50). This is a consequence of blockage which causes increases in local velocities past the model and corresponding decreases in the local surface pressures.

g. Rounding the corners of a blunt faced cylinder to a radius of one-eighth the cylinder diameter is sufficient to yield a very low drag forebody at sufficiently high values of Re. Thin disk frontbodies at very small gaps decrease the Reynolds number required for low drag, fully attached flow to occur. The drag eventually increases, however, as the gap increases (Figure 54), and in some cases exceeds the value for the corresponding square cornered configuration.

h. The behavior of a square cross-section model (Figure 65) is similar in many respects to the axisymmetric cross-section behavior. With no frontbody, the drag is high, $C_D = 0.712$. Addition of flat plate frontbodies produces forebody systems with reduced drag and with optimum gaps at which the drag is a minimum. Large reductions in drag are possible, $C_D = 0.065$ being the lowest value observed. The very low drag coefficients observed for the axisymmetric subcritical model ($C_D = 0.010$) are not possible for the square cross-section, however. This is a consequence of the inability of the frontbody separation surface to match the rearbody at its diagonal corners. For supercritical geometries the influence of the rearbody corners is diminished because the shear layer has become quite thick.

i. The drag of the square cross-section forebody increases as the flow becomes asymmetric due to yaw or off-center frontbodies. These situations can be improved, however, by adding additional surfaces to the forebody to guide the separated flow onto the rearbody. Applying this principle to a simulation of a tractor-trailer truck has demonstrated reductions in forebody drag of nearly 50% for both unyawed and yawed (10°) flows (Figure 82).

11.2 Concluding Remarks

The possibilities for large decreases in the drag of a wide variety of forebody systems have been clearly demonstrated. This study has also defined the nature of the flow about these bodies both qualitatively and quantitatively. There still exists a virtually endless list of physical and geometrical parameters which may be examined, however. The influences of shaping and yaw have been only superficially considered, and the effect of a ground plane, which is a major parameter in possible applications of this study, has been completely set aside. More detailed flow measurements, especially with respect to the reattachment zone and the scale of the shear layer fluctuations are also desirable. Studies of any of these topics would provide valuable information that is necessary for a complete understanding of interference effects of tandem bluff bodies.

In closing, two particular ideas for reducing forebody-system drag might be suggested. The existence of the cavity vortex has been indicated as an essential feature of the low drag flow fields. It might be possible to enhance this vortex by filling and shaping the cavity interior and thereby produce a further decrease in drag. With respect to the square cross-section rearbody, if the diagonal corners are removed or if the rearbody is slightly reshaped, the frontbody separation surface may then be able to better match the rearbody, and the drag will be lower. These suggestions are two of, most certainly, many possibilities for further reducing the drag of configurations composed of bluff bodies in tandem.

APPENDIX A

MWT Balance and Processor Details

A ring made of box beams encircles the tunnel test section but floats free of the tunnel (Figure A1). The model on which forces are to be measured is suspended from this ring. The ring is held in place by six bars or links that terminate on the room ceiling and wall and the tunnel reservoir section wall. At each termination point (Figure A2) is a flexure which transmits only axial loads, a tuning fork style spring that converts force into a displacement and a Schaevitz linear variable differential transformer Model 050 DC-B (Schaevitz coil) that transforms displacement of an iron slug centered in the surrounding coil into a voltage. Three links run in the streamwise direction and contribute to the drag, roll and pitch measurements; two are vertical and contribute to lift and roll and the third is orthogonal to the other two and contributes to the side force and roll as is sketched below along with the sign convention.

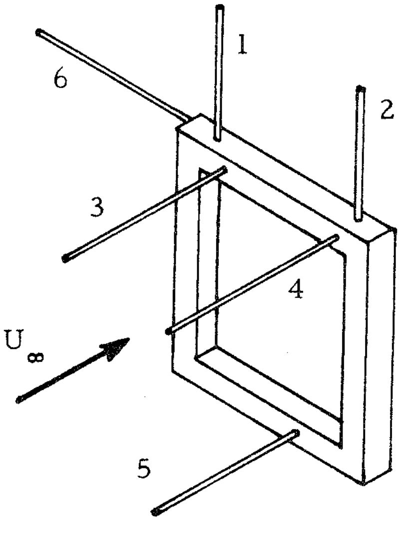

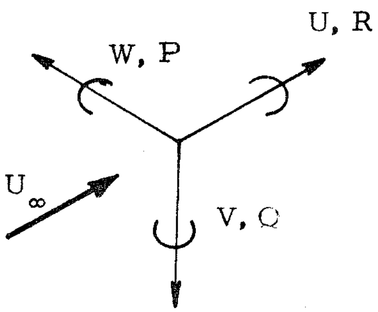

The output of each Schaevitz coil is an input into the MWT Force Balance Processor shown in Figure A3 which combines the voltages of each coil in the proper manner to yield the three forces and moments acting on the model in units of 1 volt = 1 kg force of 1 kg-m moment. The Processor also provides the capability of zeroing out or nulling static loads. This is accomplished by a summing amplifier whose inputs are the Schaevitz coil output, a voltage, EO_f, from a potentiometer for fine zeroing and a fixed resistor, EO_c, for coarse adjustment. This is diagrammed below.

Let P = (% full rotation of potentiometer)/100.

Then,

$$EO_f = \frac{(30P-15)10K}{50K\ P(1-P) + 220K(\text{or } 220K \| 300K)}$$

$$EO_c = \pm 15 \frac{10K}{RO}$$

$$EO = EO_f + EO_c.$$

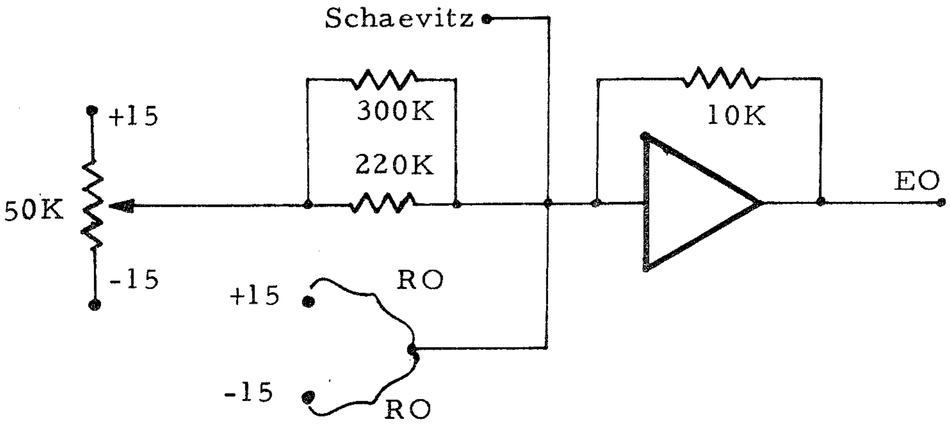

At the location noted ZERO 1 etc., in Figure A3 the voltage as the Processor was used in this experiment, is

$$Z1 = -IN1 \frac{10}{12.34} + EO1 \qquad Z4 = -IN4 \frac{10}{12.24} + EO4$$

$$Z2 = -IN2 \frac{10}{12.34} + EO2 \qquad Z5 = -IN5 \frac{10}{13.18} + EO5$$

$$Z3 = -IN3 \frac{10}{12.34} + EO3 \qquad Z6 = -IN6 \frac{10}{3.15} + EO6$$

where Z refers to ZERO and IN for the Schaevitz voltage. With no aerodynamic loads acting on the model, each potentiometer, P, and each coarse resister, RO, are set so that Z1, Z2, ... Z6 are all zero. Before this is done it is important to insure that the slug of each Schaevitz coil is nearly centered so that the maximum range of the Balance is available and that the Schaevitz coil is in its linear operating condition.

With the balance statically nulled, when the aerodynamic loading is applied, each Z will then correspond to the additional deflection of the Schaevitz coil slug due to aerodynamic forces and will thus represent these forces. The remainder of the Processor combines the Schaevitz outputs to yield the desired forces and moments in the units previously mentioned. Just before the final output (F-M) is a RC combination which provides an effective time constant of 1 second to damp oscillations arising from the flow. The Processor output, which is read by a digital voltmeter, is labelled F-M1, .., F-M6 on the right hand side of

Figure A3 and is

$$U = \text{Drag} = \text{F-M1} = -\left(Z3\ \frac{200}{200} + Z4\ \frac{200}{200} + Z5\ \frac{200}{200}\right)$$

$$V = \text{Lift} = \text{F-M2} = -\left(Z1\ \frac{200}{200} + Z2\ \frac{200}{200}\right)$$

$$W = \text{Side} = \text{F-M3} = -\left(Z6\ \frac{200}{773}\right)$$

$$R = \text{Roll} = \text{F-M4} = -\left(Z1\ \frac{200}{291} - Z2\ \frac{200}{291} + Z6\ \frac{200}{78.1} - Z6\ \frac{200}{773}\right)$$

$$Q = \text{Yaw} = \text{F-M5} = -\left(-Z3\frac{200}{309} + Z4\ \frac{200}{305} - Z5\ \frac{200}{1396}\right)$$

$$P = \text{Pitch} = \text{F-M6} = -\left(Z3\ \frac{200}{277} + Z4\ \frac{200}{280} - Z5\ \frac{200}{357} + U\ \frac{200}{771}\right)$$

as the computer was configured for this experiment.

Figure A4 shows Channels 7 and 8 which were not used but are available for other measurements such as angle of attack or tunnel velocity. Also shown is the switching diagram. Two switches enable access to various parts of the circuit so that the raw signal from the Schaevitz (IN), the nulled voltage (ZERO) or the final output (F-M) can be observed. An additional setting is available for such quantities as the force coefficient although this was also not used.

Figure A5 shows the wiring diagram of the Processor as viewed from the top. All resistors and capacitors in the unit are easily replaced if different scaling is desired or if the Schaevitz coil or springs are changed.

APPENDIX B

Free-Streamline Analysis

The problem is to determine the wake size and shape formed by free streamlines separating from the edges of a two-dimensional flat plate normal to a uniform, incompressible, potential flow. The essential assumption is that in the wake, on the back side of the plate and along the free streamline the pressure, represented by the coefficient $C_{p_s} = (p_s - p_\infty)/q_\infty$ is constant and less than or equal to zero. With this assumption the flow can then be treated by complex analysis with the aid of conformal mapping and the hodograph (or velocity) plane to yield solutions for the free-streamline shape as a function of the parameter C_{p_s}. This problem was first studied by Kirchhoff (1869) who assumed $C_{p_s} = 0$ which results in a wake that becomes unbounded in width far downstream. A closer approximation to the real flow is $C_{p_s} < 0$ which is actually observed (Fage and Johansen 1927). A free-streamline solution to this problem which included $C_{p_s} < 0$ was developed by Roshko in his paper on the notched hodograph technique (1954). (This paper also presents arguments justifying the use of free-streamline concepts with such separated flows.) This approach is seen to be a great improvement over the Kirchhoff solution although Roshko's paper does contain some minor errors. As discussed in Chapters 9 and 11 of Robertson's book on hydrodynamics (1965), a variety of techniques applying the hodograph plane to free-streamline problems are available. Lissaman (1975) suggested one alternative approach to the flat plate problem although he did not go through the calculational details. In order to justify the theoretical calculations presented herein and to correct the errors which are present in Roshko's paper, the details of both solutions to the wake shape of a flat plate will be now described.

Both solutions apply complex analysis where the following fundamental terminology is defined.

$z = x + iy$ is the complex variable of position

$w = \varphi + i\psi$ is the complex potential where φ is the potential and ψ is the stream function

$\nu = dw/dx = u - iv$ is the complex velocity where u is the streamwise (x) component and v is the transverse (y) component

$= qe^{-i\theta}$ where q is the velocity magnitude and θ the direction measured counterclockwise from the x axis

B.1 Notched Hodograph

Sketch 1 shows the flow in the z or physical plane

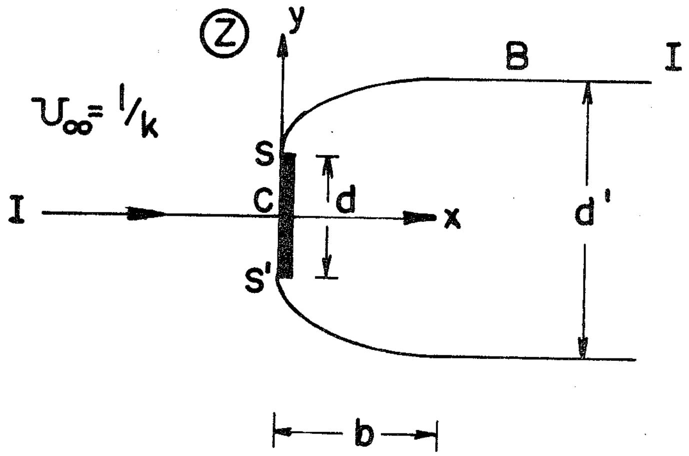

Sketch 1

Uniform flow at $U_\infty = 1/k$ approaches from the left. From symmetry, the $\psi = 0$ streamline stagnates at the plate center, C , where it splits, follows the plate surface, separates at the edges, S and S' and forms two separation streamlines. At separation and along the free streamline the velocity is constant and taken to be unity so that $C_{p_s} = 1 - (q_s/U_\infty)^2 = 1 - k^2$. Specifying k then defines the approach flow speed and the wake pressure. The solution consists of mapping z onto the plane of the complex potential w through the medium of the hodograph plane, ν . Once the mappings are known the solution is given completely by

$$\left.\begin{aligned} z &= \frac{dw}{\nu} = z(w) \\ q^2 &= |\nu|^2 = q(w) \end{aligned}\right\} \qquad B.1$$

The hodograph plane is shown in Sketch 2. Along the face

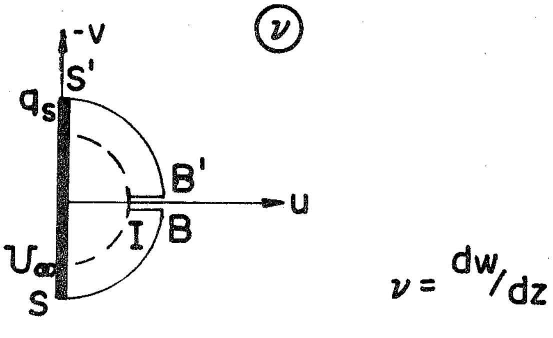

Sketch 2

of the plate the flow has only a v component. At the edges it separates with a velocity $q_s = kU_\infty$. Along the free streamline the velocity magnitude remains q_s while the direction changes until the flow becomes parallel, hence the semicircular arcs from

S' to B' and S to B. Infinitely far downstream the flow must return to freestream conditions, I , and the notch is thus formed connecting B and B' to I. The dashed arc represents the Kirchhoff hodograph for which $q_s = U_\infty$.

It is desired to map z into the complex potential plane w as shown in Sketch 3. Because the region of interest in z , that is the plate and free streamlines, forms the $\psi = 0$ streamline,

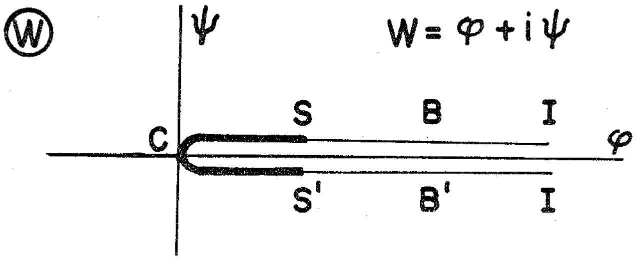

Sketch 3

the map in w is very simple -- the plate and streamlines are folded onto the φ axis and run in the positive φ direction because φ must continuously increase along this particular streamline. In order to accomplish this mapping several intermediate planes or mappings are needed. The entire sequence from the z to the w plane is shown in Sketch 4.

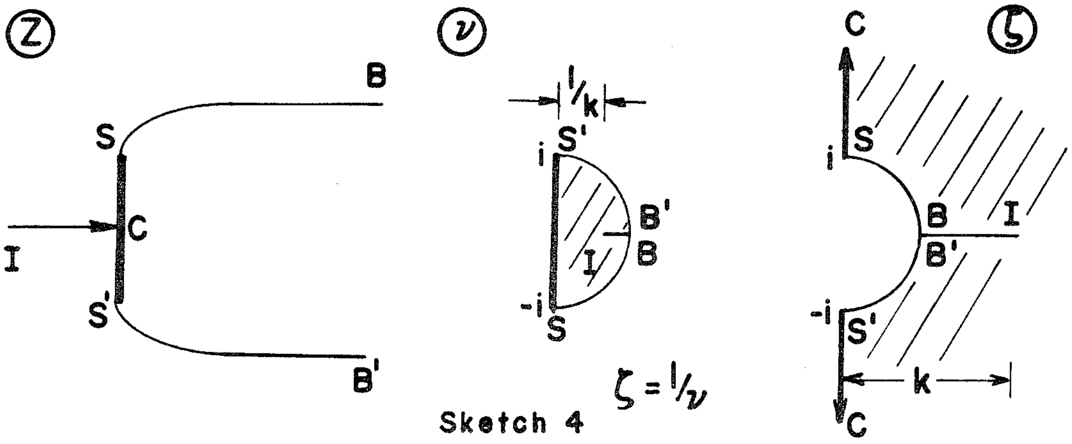

Sketch 4

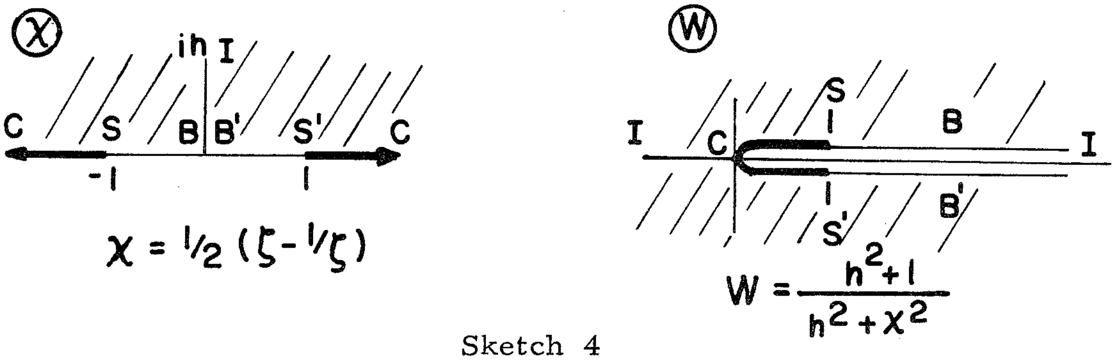

Sketch 4

The light shading indicates where a region in one plane maps in another. Multivalued functions (with branch points) arise when the inverse of these mappings are found to obtain $z(w)$ (the forward mapping gives $w(z)$). Choosing the proper branches requires insuring the forward and inverse mappings are consistent which requires knowledge of where the various regions map. With this criteria carefully observed, the forward and inverse mappings are given below.

Forward: Given $\nu = dw/dz$ then

$$\zeta = 1/\nu = dz/dw$$

$$\chi = i/2\ (\zeta - 1/\zeta) \ \ldots \text{ Joukowsky transformation}$$

and $$w = (h^2+1)/(h^2+\chi^2) \ldots \text{ Schwarz-Christoffel transformation}$$

where $U_\infty = 1/k$, $h = (k^2-1)/2k$ and $a = (k^2+1)/(k^2-1)$ (to be used shortly).

Inverse:

$$\chi = \left(\frac{h^2+1}{w} - h^2\right)^{\frac{1}{2}}$$

$$= ih\sqrt{\frac{r_1}{r_2}}\ e^{\frac{i}{2}(\theta_1 - \theta_2)}$$

where $0 < \theta_1, < 2\pi,\ 0 < \theta_2 < 2\pi$

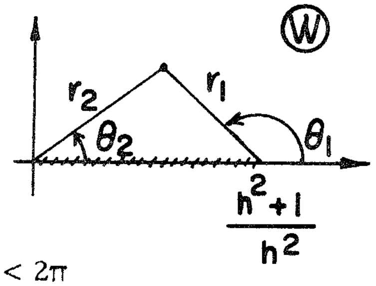

$$\zeta = -i(\chi + (\chi^2 - 1)^{\frac{1}{2}}) \qquad \text{B.2a}$$

$$= -i(\chi + \sqrt{r_1 r_2}\ e^{\frac{i}{2}(\theta_1 + \theta_2)}) \qquad \text{B.2b}$$

where $-\pi < \theta_1, < 2\pi, \ 0 < \theta_2 < 2\pi$

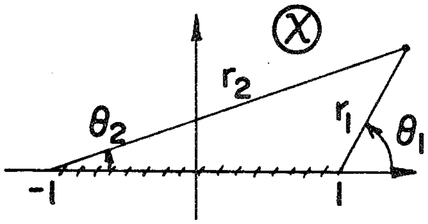

The expression for χ applied to the path C → S → B in the w plane (i.e., $0 < \varphi < \frac{h^2+1}{h^2} = a^2, \ \psi = 0^+$) gives

$$\chi = -(\frac{h^2+1}{\varphi} - h^2)^{\frac{1}{2}} \ldots \text{ ordinary square root}$$

For the path B → I (i.e., $a^2 < \varphi, \ \psi = 0^+$)

$$\chi = +(\frac{h^2+1}{\varphi} - h^2)^{\frac{1}{2}}$$

Substitution into (B.2b) yields the following

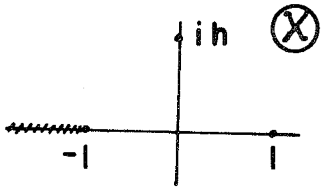

$\underline{0 < \varphi < 1}$ $\quad r_1 = 1 + |\chi|, \ \theta_1 = \pi$

$\quad r_2 = |\chi| - 1, \ \theta_2 = \pi$

$$\Longrightarrow \quad \zeta = i\{(\frac{h^2+1}{\varphi} - h^2)^{\frac{1}{2}} + [(h^2+1)(\frac{1}{\varphi} - 1)]^{\frac{1}{2}}\}$$

and using $h = \frac{k^2-1}{2k}, \ a^2 = \frac{h^2+1}{h^2}$

$$\Longrightarrow \quad \zeta = i(\frac{k^2+1}{2k})\left[\sqrt{\frac{1}{\varphi} - \frac{1}{a^2}} + \sqrt{\frac{1}{\varphi} - 1}\right] \qquad \text{B.3a}$$

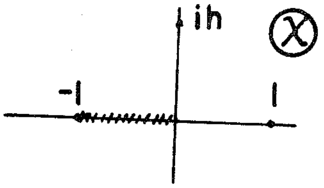

$\underline{1 < \varphi < a^2}$ $r_1 = 1 + |\chi|, \quad \theta_1 = \pi$

$r_2 = 1 - |\chi|, \quad \theta_2 = 0$

$$\Longrightarrow \quad \zeta = [(h^2+1)(1 - \frac{1}{\varphi})]^{\frac{1}{2}} + i(\frac{h^2+1}{\varphi} - h^2)^{\frac{1}{2}}$$

or

$$\zeta = (\frac{k^2+1}{2k})\,[\sqrt{1 - \frac{1}{\varphi}} + i\sqrt{\frac{1}{\varphi} - \frac{1}{a^2}}\,] \qquad \text{B.3b}$$

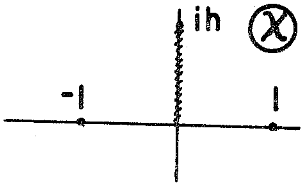

$\underline{a^2 < \varphi}$ $r_1 = \sqrt{1 + |\chi|^2}, \quad \theta_1 = \pi - \tan^{-1}(|\chi|)$

$r_2 = \sqrt{1 + |\chi|^2}, \quad \theta_2 = \tan^{-1}(|\chi|)$

$$\Longrightarrow \quad \zeta = (h^2 - \frac{h^2+1}{\varphi})^{\frac{1}{2}} + [(h^2+1)(1 - \frac{1}{\varphi})]^{\frac{1}{2}}$$

or

$$\zeta = (\frac{k^2+1}{2k})\left[\sqrt{\frac{1}{a^2} - \frac{1}{\varphi}} + \sqrt{1 - \frac{1}{\varphi}}\right] \qquad \text{B.3c}$$

Now $\zeta = dz/dw \Rightarrow z = \int \zeta dw = \int \zeta d\varphi$ is the solution along the upper branch of the streamline (i.e., $\psi = 0^+$). The variable φ in Equations B.3 is real and the integration to yield $z(w) = z(\varphi)$ can be done using ordinary (real) calculus and principal branches. Evaluating then $z = \int \zeta(\varphi)\, d\varphi$ over each of the regions in φ and requiring $z = 0$ at $\varphi = 0$ and continuity of φ at $\varphi = 1$ and a^2, gives:

$\underline{0 < \varphi < 1}$

$$z = i\,\frac{k^2+1}{2k}\left[\frac{1}{a}\sqrt{\varphi(a^2 - \varphi)} - a\tan^{-1}\sqrt{\frac{a^2}{\varphi} - 1} + \sqrt{\varphi(1 - \varphi)} - \tan^{-1}\sqrt{\frac{1}{\varphi} - 1} + \frac{2k^2}{k^2 - 1}\,\frac{\pi}{2}\right] \qquad \text{B.4a}$$

$\underline{1 < \varphi < a^2}$

$$z = \frac{k^2+1}{2k}\bigg[\sqrt{\varphi(\varphi - 1)} - \ln(\sqrt{\varphi} + \sqrt{\varphi - 1}) + i(\frac{1}{a}\sqrt{\varphi(a^2 - \varphi)} - a \tan^{-1}\sqrt{\frac{a^2}{\varphi} - 1}$$

$$+ \frac{2k^2}{k^2-1}\frac{\pi}{2}\bigg] \qquad \text{B.4b}$$

$\underline{a^2 < \varphi}$

$$z = \frac{k^2+1}{2k}\bigg[\frac{1}{a}\sqrt{\varphi(\varphi - a^2)} - a\ln(\sqrt{\varphi - a^2} + \sqrt{\varphi}) + \sqrt{\varphi(\varphi - 1)}$$

$$- \ln(\sqrt{\varphi} + \sqrt{\varphi - 1}) + a\ln a + i\frac{2k^2}{k^2-1}\frac{\pi}{2}\bigg] \qquad \text{B.4c}$$

The coordinates of points S and B are now desired as they represent the edge of the plate and the location at which the wake becomes parallel. They are found by substituting $\varphi = 1$ and a^2 respectively into Equation B.4b

$$S = z(1) = \frac{k^2+1}{2k}\bigg[0 + i(\frac{1}{a}\sqrt{a^2 - 1} - a\tan^{-1}\sqrt{a^2 - 1} + \frac{2k^2}{k^2-1}\frac{\pi}{2})\bigg]$$

$$= i(\frac{k^2+1}{2k})\bigg[\frac{\pi}{2} + \frac{2k}{k^2+1} + \frac{k^2+1}{k^2-1}\tan^{-1}(\frac{k^2-1}{2k})\bigg] \qquad \text{B.5a}$$

where use has been made of $\tan^{-1}\beta = \pi/2 - \tan^{-1}(1/\beta)$

$$B = z(a^2) = \frac{k^2+1}{2k}\bigg[a\sqrt{a^2-1} - \ln(a + \sqrt{a^2-1}) + i(0 + \frac{2k^2}{k^2-1}\frac{\pi}{2})\bigg]$$

$$= (\frac{k^2+1}{k^2-1})^2 + \frac{k^2-1}{2k}\ln(\frac{k-1}{k+1}) + i\frac{\pi}{2}k(\frac{k^2+1}{k^2-1}) \qquad \text{B.5b}$$

In Roshko's notation the plate width, d, (d_1 in the present paper), the wake width, d', (d_2) and the downstream distance to parallel flow, b, (g) are then given by

$$d = 2\mathrm{Im}(S)$$

$$d' = 2\mathrm{Im}(B)$$

$$b = \mathrm{Re}(B)$$

or the gap and diameter ratios are

$$\frac{b}{d'} = \frac{g}{d_2} = \frac{1}{\pi k}\left[\frac{k^2+1}{k^2-1} + \frac{k^2-1}{2k}\,\ln\left(\frac{k-1}{k+1}\right)\right] \qquad \text{B. 6a}$$

$$\frac{d}{d'} = \frac{d_1}{d_2} = \frac{k^2-1}{\pi k^2}\left[\frac{\pi}{2} + \frac{2k}{k^2+1} + \frac{k^2+1}{k^2-1}\tan^{-1}\left(\frac{k^2-1}{2k}\right)\right]$$

$$= \frac{1}{\pi k^2}\left[2k\,\frac{k^2-1}{k^2+1} - \pi + 2(k^2+1)\tan^{-1}k\right] \qquad \text{B. 6b}$$

the second form of d/d' being more convenient.

B. 2 Alternative Approach Suggested by Lissaman (1975)

Consider the flow and hodograph mapping as shown in Sketch 5.

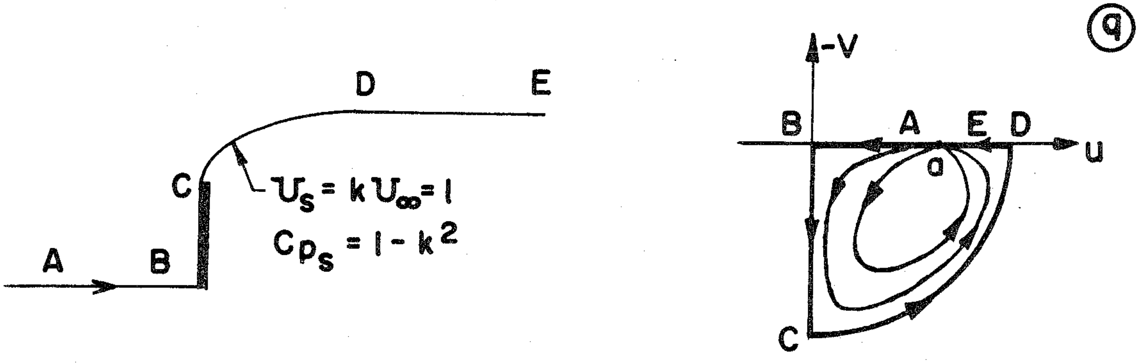

Sketch 5

(The notation has been slightly changed; q refers to the complex velocity and a to the point at infinity.)

This is simply one-half the flow described for the notched hodograph. The boundary, ABCDE, forms the $\psi = 0$ streamline. Other streamlines in the flow will trace out curves contained inside $\psi = 0$ and closed at point a as indicated in the Sketch. This flow pattern, although in the hodograph rather than physical plane, is just that of a doublet located at the point a and its appropriate images. Since analytic functions are invariant with transformation and the character of any singularities is basically unchanged (Robertson 1965, pg. 353) then a similar doublet will appear in the real flow. Consequently, the potential w can be written for the doublet in the q plane and then transformed to z by $q = dw/dz$ or $z = \int dw/q$. The problem is now simply to obtain an expression for $w(\nu)$ which then is integrated for $z(w)$.

The potential of a two-dimensional doublet located at $z = z_o$ of strength m whose axis (defined positive going from the sink to the source) makes an angle α with the positive x axis is given by

$$w = \frac{-me^{i\alpha}}{z - z_o}$$

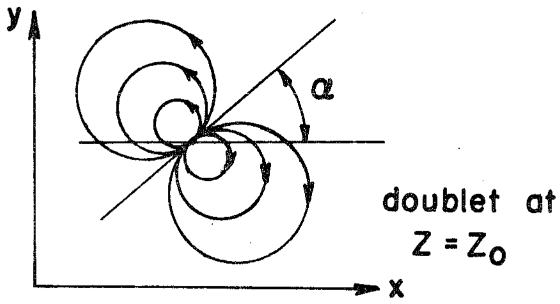

In the situation of Sketch 5, the doublet is located at $q = a$ and makes an angle π with the horizontal axis, and its potential is thus $w = -me^{i\pi}/(q-a) = m/(q-a)$. Now the $\psi = 0$ streamline imposes boundaries on the flow pattern which must be satisfied by appropriate images. Segment DEAB is a plane of symmetry which the doublet, with $\alpha = \pi$, automatically satisfies. Segment BC requires symmetry in the plane $x = 0$ and the boundary CD requires the image of a doublet "in a cylinder", to use the terminology of Milne-Thomson (1960). A method for obtaining the proper images in the plane $x = 0$ and in the cylinder, $r_o = 1$, is described in Milne-Thomson, sections 8.43 and 8.81. Applying it to the present case gives the following image system (Sketch 6) and the complex potential, where the doublet strength has been taken to be unity (since it will later be normalized out anyway).

$$w = -\left[-\frac{1}{q-a} + \frac{1}{q+a} + \frac{1}{a^2}\,\frac{1}{q-\frac{1}{a}} - \frac{1}{a^2}\,\frac{1}{q+\frac{1}{a}}\right] \qquad \text{B.7}$$

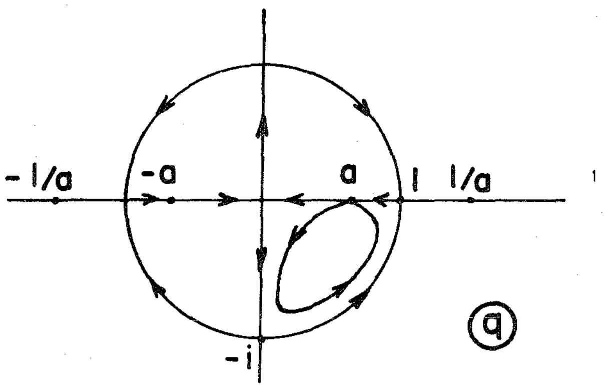

Sketch 6

The desired solution is $z = \int \frac{dw}{q} = \int \frac{dw}{dq}\,\frac{dq}{q}$. Taking the required derivative of (B.7) gives

$$\frac{dw}{dq} = -\left[\frac{1}{(q-a)^2} - \frac{1}{(q+a)^2} - \frac{1}{a^2}\,\frac{1}{(q-\frac{1}{a})^2} + \frac{1}{a^2}\,\frac{1}{(q+\frac{1}{a})}\right]$$

and the expression for $z(q)$ becomes

$$z(q) = -\int\left[\frac{1}{q(q-a)^2} - \frac{1}{q(q+a)^2} - \frac{1}{a^2}\,\frac{1}{q(q-\frac{1}{a})^2} + \frac{1}{a^2}\,\frac{1}{q(q+\frac{1}{a})^2}\right]dq \qquad \text{B.8}$$

The integrand, call it $f(q)$, has poles at $q = 0$, a, -a, 1/a and -1/a and has no branch points. The pole at $q = 0$ is removable since

$$\lim_{q\to 0} qf(q) = \lim_{q\to 0}\left[\frac{1}{(q-a)^2} - \frac{1}{(q+a)^2} - \frac{1}{a^2}\,\frac{1}{(q-\frac{1}{a})^2} + \frac{1}{a^2}\,\frac{1}{(q+\frac{1}{a})^2}\right]$$

$$= \frac{1}{a^2} - \frac{1}{a^2} - 1 + 1 = 0$$ (see, e.g., Churchill, 1960, p. 158)

and thus presents no difficulties. The only other singularity in the region of interest (i.e., the fourth counter-clockwise quadrant) is at $q = a$ and it can be avoided by deforming the path of integration suitably. The indefinite integral for z can therefore be obtained by real calculus although its evaluation at any point will require proper selection of branch cuts.

Each term in the integral has the form

$$\int \frac{du}{u(a+bu)^2} = \frac{1}{a(a+bu)} - \frac{1}{a^2}\ln(a+bu) + \frac{1}{a^2}\ln u + C_o \qquad \text{B.9}$$

where the $\ln$ terms will require suitable branch cuts and the constant C_o will be determined by requiring $z = 0$ at $q = 0$. Applying (3) to (2) gives

$$z(q) = -\frac{1}{a}\left[\frac{-1}{q-a} + \frac{-1}{q+a} + \frac{1}{q-\frac{1}{a}} + \frac{1}{q+\frac{1}{a}}\right] - \frac{1}{a^2}\left[-\ln(q-a) + \ln(q+a)\right]$$

$$- \left[\ln(q-\tfrac{1}{a}) - \ln(q+\tfrac{1}{a})\right] + C_o \qquad \text{B.10}$$

Branch points exist at $q = a, -a, 1/a$ and $-1/a$. To avoid cuts in the region of interest the branches are chosen vertically as shown in Sketch 7, with the range for the arguments of the $\ln$ terms also giving continuous solutions across the negative imaginary and positive real.

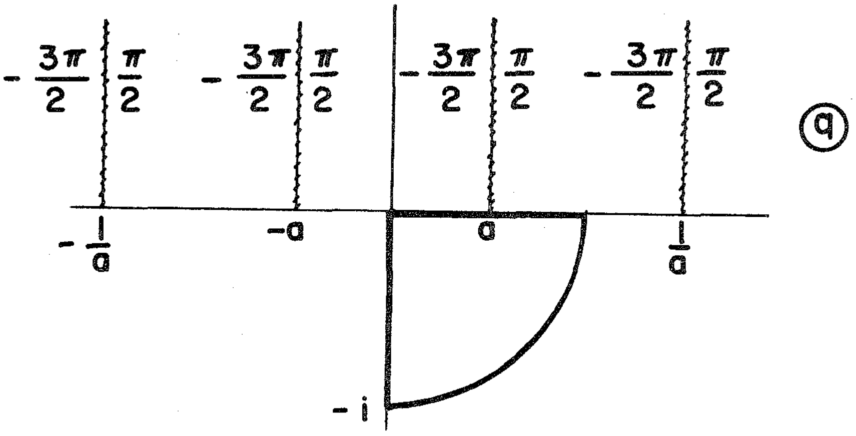

Sketch 7

With this selection of branches (B.10) can now be evaluated. The constant is first determined so that $z(0) = 0$, which gives

$$C_o = i\pi\left(1 - \frac{1}{a^2}\right)$$

The locations of points $C\ (q = -i)$ and $D(q = 1)$ are the values of interest since they again correspond to the edge of the plate and the location of parallel wake flow. Evaluating (B.10) with the branches and integration constant as determined above yields

$$z(-i) = -i\left[\frac{2}{a}\left(\frac{a^2 - 1}{a^2 + 1}\right) - \frac{\pi}{a^2} + 2\left(1 + \frac{1}{a^2}\right)\tan^{-1} a\right] \qquad \text{B.11a}$$

$$z(1) = \frac{-2}{a}\left(\frac{a^2 + 1}{a^2 - 1}\right) - \left(\frac{1}{a^2} - 1\right) \ln\left(\frac{1 + a}{1 - a}\right) + \frac{i\pi}{a^2} \qquad \text{B.11b}$$

The normalized wake width, d_1/d_2, and gap (downstream location of parallel flow), g/d_2, are then

$$\frac{d_1}{d_2} = \frac{\mathrm{Im}\,(z(-i))}{\mathrm{Im}\,(z(1))} \quad , \quad \frac{g}{d_2} = \frac{\mathrm{Re}\,(z(1))}{2\,\mathrm{Im}\,(z(1))}$$

Recognizing that $a = 1/k$, the value of the freestream velocity, gives the final wake geometry

$$\frac{g}{d_2} = \frac{1}{\pi k}\left[\frac{k^2 + 1}{k^2 - 1} + \frac{k^2 - 1}{2k} \ln\left(\frac{k - 1}{k + 1}\right)\right] \qquad \text{B.12a}$$

$$\frac{d_1}{d_2} = \frac{1}{\pi k^2}\left[2k\left(\frac{k^2 - 1}{k^2 + 1}\right) - \pi + 2(k^2 + 1)\tan^{-1} k\right] \qquad \text{B.12b}$$

which are identical to Equations B.6, the results of the notched hodograph.

As can be seen from these equations, the wake geometry is solely dependent upon the wake pressure, or equivalently, the overshoot in velocity at separation. Specifying the pressure or velocity fixes the parameter $k = U_s/U_\infty = (1 - C_{p_s})^{\frac{1}{2}}$ and determines the wake.

APPENDIX C

Bragg Cell Frequency Generation

It is desired to drive each Bragg cell so that their difference in frequency, f_B, is tunable, stable and on the order of 100 kHz. If two independent (and thus uncorrelated) sources are used, then their noise is given by

$$\delta\nu = \sqrt{\delta\nu_1^2 + \delta\nu_2^2}$$

$$\delta\nu/\nu = \sqrt{(\delta\nu_1/\nu)^2 + (\delta\nu_2/\nu)^2} \simeq \sqrt{2}(\nu_1/\nu)(\delta\nu_1/\nu_1) \qquad \text{C.1}$$

where $\nu_1 \doteq \nu_2$.

For a typical oscillator $\delta\nu_1/\nu_1 \sim 10^{-5}$, and the nominal Bragg cell frequency is $\nu_1 = 40$ MHz. Using these numbers in (C.1) gives $\delta\nu/\nu \sim 0.005$. If the oscillators are locked together, then ν_1 and ν_2 are no longer uncorrelated, and $\delta\nu/\nu \sim \delta\nu_1/\nu_1 = \delta\nu_2/\nu_2 \sim 10^{-5}$ and a considerably lower instrument noise results.

If a mixer is used to add 40 MHz and f_B, it will generate a spectrum as shown below.

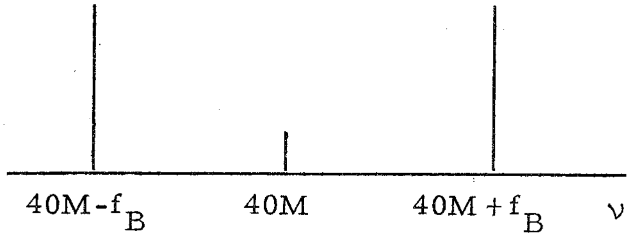

Crystal notch filters are required to isolate the desired side band, and the frequency of the generator will be fixed by the notch filter. To circumvent this problem, a nonlinear, digital phase-locked loop, upper side band generator has been designed and built by Prof. Paul Dimotakis and Dan Lang of Caltech to produce a pure upper side band as depicted in the sketch below.

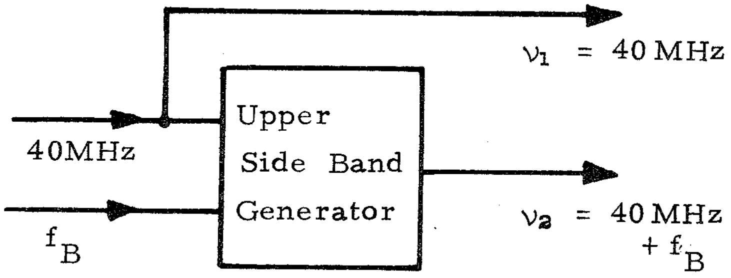

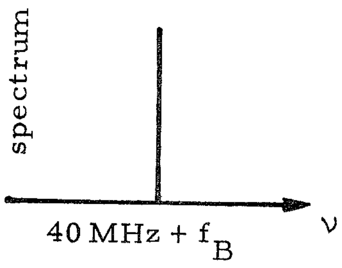

The difference frequency, f_B, accepted by the generator can range from 10kHz to 10 MHz and provides the flexibility needed to optimize measurements in a recirculating zone.

APPENDIX D

Laser-Doppler Sampling Bias Correction

From Equation 19b of Dimotakis (1976) for stationary fringes, the sampling bias of making a measurement of the magnitude of velocity normal to the fringe planes, $|U_x|$ is

$$B\ (|U_x|;\ \epsilon) \ = \ |U_x| W(1 - \epsilon^2 W^2) \text{ if } \epsilon^2 W^2 \ \leq \ 1 \qquad \text{D.1}$$

where ϵ is the ratio of the minimum acceptable number of fringe plane spacings that must be crossed to the total number in the overlap volume, $\epsilon = M_f/N_f$, and

$$W^2 \ = \ 1 + \frac{U_y^2 \ \sin^2 \ (\theta/2) + U_z^2}{U_x^2 \ \cos^2 \ (\theta/2)} \qquad \text{D.2}$$

The coordinate frame takes x perpendicular to the fringes, y and z the other orthogonal directions and θ is the angle between the beams.

A given i^{th} measurement actually consists of two independently determined quantities: Δt_i, the total time of flight across the focal volume, and n_i, the number of fringe plane spacing crossings, or equivalently, $|U_{x_i}|$, the magnitude of the fringe plane crossing velocity, and n_i. The bias in making this particular measurement is given by

$$B\ (|U_{x_i}|,\ n = n_i) \ = \ B(|U_{x_i}|, n \geq n_i) - B(|U_{x_i}|, n \geq n_i + 1) \qquad \text{D. 3}$$

Substituting (D.1) into this expression then yields

$$B\ (|U_{x_i}|,\ n_i) = |U_{x_i}|\, W_i^3\ \frac{(2n_i + 1)}{N_f^2} \propto |U_{x_i}| W_i^3 (2n_i + 1) \qquad \text{D. 4}$$

Equation D.4 is the sampling bias associated with the measurement of $|U_{x_i}|$ and n_i for the i^{th} valid particle crossing the focal volume when the fringes are stationary.

If the fringes are in motion then the fringe spacing requirement becomes

$$(\nu_B \pm \nu_D)\Delta t_i \geq M_f \qquad \text{D.5}$$

where ν_B is the Bragg shifted frequency and ν_D is the Doppler shift. Expression D.5 is equivalent to

$$U_T \Delta t_i \geq M_f s \qquad \text{D.6}$$

where $U_T = U_f \pm U_x = (\nu_B \pm \nu_D)s$, and s is the fringe plane spacing. It is now required to recompute the particle trajectory through the focal volume requiring that it now satisfies the inequality in (D.6). This is done beginning with equation 15 of Dimotakis (1976). When this is done it is found that the same solution for the trajectory, equation 16 of Dimotakis (1976), results only with a new fringe plane crossing parameter, $\epsilon_B = \epsilon/(U_T/U_x)$, replacing ϵ.

Now, from (D.1) and (D.3) it is easily shown that

$$B(|U_{x_i}|, n_i) = |U_{x_i}| W^3 (\epsilon_{n_i+1}{}^2 - \epsilon_{n_i}{}^2) \qquad \text{D.7}$$

If ϵ now goes to $\epsilon' = \epsilon/a$, then

$$B'(|U_{x_i}|, n_i) = B(|U_{x_i}|, n_i)/a^2$$

by (D.7) and, using (D.4), it is finally seen that for moving fringes,

$$B(|U_{x_i}|, n_i) = \frac{|U_{x_i}| W_i^3 (2n_i + 1)}{(U_{T_i}/U_{x_i})^2} = \frac{U_{x_i}{}^3 W_i^3 (2n_i + 1)}{U_{T_i}{}^2} \qquad \text{D.8}$$

Now $U_x{}^2 W^2 = \dfrac{U_x{}^2 \cos^2\theta/2 + U_y{}^2 \sin^2\theta/2 + U_z{}^2}{\cos^2\theta/2}$

Taking θ small and recognizing that $U_x = u$, $U_y = -w$, $U_z = v$ gives

$$U_x{}^2 W^2 \propto u^2 + v^2$$

or

$$U_x{}^3 W^3 \propto (u^2 + v^2)^{3/2}$$

But $(u^2 + v^2)^{1/2} \propto 1/\Delta t$, that is, the time of flight is inversely proportional to the magnitude of the total velocity vector through the focal volume. Also $U_T = ns/\Delta t \propto n/\Delta t$. Therefore Equation D. 8 for the bias becomes

$$B(|U_{x_i}|, n_i) \propto \frac{(1/\Delta t_i)^3 (2n_i+1)}{(n_i/\Delta t_i)^2} = \frac{(2n_i+1)}{n_i{}^2 \Delta t_i} = \frac{2+1/n_i}{n_i \Delta t_i} \propto \frac{1}{n_i \Delta t_i}$$

for large n_i, and the weighting for a given velocity measurement is then

$$B^{-1}(|U_{x_i}|, n_i) \propto n_i \Delta t_i \qquad \text{D. 9}$$

APPENDIX E

Bias Due to a Velocity Gradient

Consider a velocity gradient and a focal volume of finite extent as in Sketch 1. Then the probability density $\hat{p}(u, y_c)$ for measuring u at the center of the focal volume, $y = y_c$, is the convolution of the probability density of the actual velocity, p(u, y), with the spatial resolution envelope, $h(y-y_c)$, of the focal volume. This envelope is a function of the intensity distribution within the focal volume, i.e.,

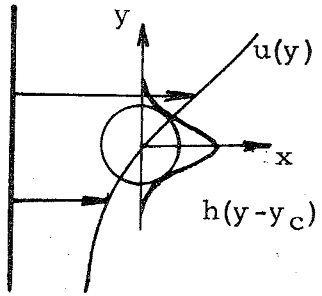

Sketch 1

$$\hat{p}(u, y_c) = \int_{-\infty}^{\infty} p(u, y)h(y-y_c)dy$$

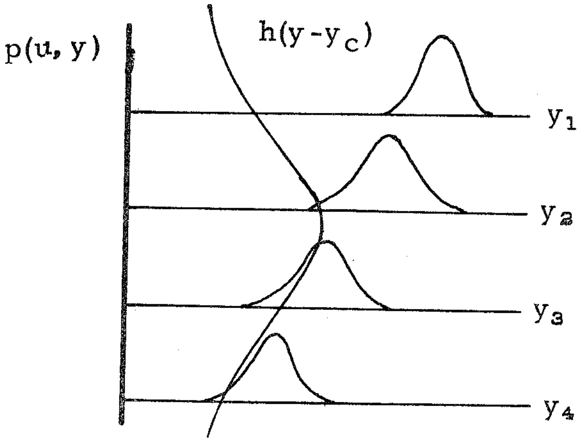

Sketch 2

$$h(y) = h_0 e^{-2(2y/w_0)^2} \qquad \text{E.1}$$

where w_0 is the focal volume diameter, and is normalized by

$$\int_{-\infty}^{\infty} h(y)dy = 1 \qquad \text{E. 2}$$

The estimated (or measured) mean velocity $\hat{u}(y_c)$ at $y = y_c$ is then

$$\hat{u}(y_c) = \int_{-\infty}^{\infty}\left\{\int_{-\infty}^{\infty} u\, p(u,y)du\right\} h(y-y_c)dy = \int_{-\infty}^{\infty} \overline{u}(y)h(y-y_c)dy \qquad \text{E. 3}$$

and the mean square fluctuation $\hat{u}'^2 = (y_c)$ is given by

$$\hat{u}'^2(y_c) = \int_{-\infty}^{\infty}\left\{\int_{-\infty}^{\infty} (u-\overline{u}(y_c))^2 p(u,y)du\right\} h(y-y_c)dy \qquad \text{E. 4}$$

where the second expression in (E. 3) follows from the definition of the mean, $\overline{u}(y)$.

Expanding $\overline{u}(y)$ in a Taylor series about $y = y_c$ and substituting into (E. 3) gives

$$\hat{u}(y_c) = \overline{u}(y_c) + (\partial\overline{u}/\partial y)_{y_c}\int_{-\infty}^{\infty}(y-y_c)h(y-y_c)dy$$

$$+ \tfrac{1}{2}(\partial^2\overline{u}/\partial y^2)_{y_c}\int_{-\infty}^{\infty}(y-y_c)^2 h(y-y_c)dy + \text{H. O. T.}$$

The second term is zero since h(y) is an even function. The integral in the third term is the definition of the variance of the focal volume intensity distribution, σ^2. Therefore $\hat{u}(y_c)$ becomes

$$\hat{u}(y_c) \doteq \overline{u}(y_c) + \tfrac{1}{2}(\partial^2\overline{u}/\partial y^2)_{y_c}\sigma^2 \qquad \text{E. 5}$$

and is seen to be independent of the velocity gradient.

Substituting $(u-\overline{u}(y_c))^2 = (u-\overline{u}(y))^2 + (\overline{u}(y) - \overline{u}(y_c))^2$

$$+ 2(u - \overline{u}(y))(\overline{u}(y) - \overline{u}(y_c))$$

into (E. 4), recognizing

$$\overline{u}^2(y) = \int_{-\infty}^{\infty} (u-\overline{u}(y))^2 p(u, y)du$$

and expanding $\overline{u}^2(y)$ in a Taylor series about $y = y_c$, gives for $\hat{u}^2(y_c)$

$$\hat{u}'^2(y_c) \doteq \overline{u'}^2(y_c) + \left[\frac{1}{2}\frac{\partial^2(\overline{u'}^2(y))}{\partial y^2} + (\partial\overline{u}/\partial y)^2\right]_{y=y_c} \sigma^2 \qquad \text{E. 6}$$

Thus, the measured fluctuations are strongly dependent on the velocity gradient and require a correction.

A Gaussian distribution is properly expressed by

$$h(y) = h_0 e^{-y^2/(2\sigma^2)}$$

where σ^2 is the variance. But from (E. 1) $-y^2/(2\sigma^2) = -2(2y/w_o)^2$ and therefore

$$\sigma = \frac{w_0}{4} \quad . \qquad \text{E. 7}$$

REFERENCES

Beastall, D. & Turner, J. 1957 "The effect of a spike protruding in front of a bluff body at supersonic speeds." ARC R. & M. no. 3007.

Biermann, D. & Herrnstein, W. H., Jr. 1933 "The interference between struts in various combinations." NACA Rep. no. 468.

Breidenthal, R. E. 1974 "Forebody drag of an axisymmetric bluff body." Ae 105 Project Report, California Institute of Technology.

Brown, G. L. & Roshko, A. 1974 "On density effects and large structure in turbulent mixing layers." J. Fluid Mech. 64, 775-816.

Buckley, F. T., Jr., Marks, C. H. & Walston, W. H., Jr. 1974 "An assessment of drag reduction techniques based on observations of flow past two-dimensional tractor-trailer models." In Conference/Workshop on Reduction of Aerodynamic Drag of Trucks. (ed. P. B. S. Lissaman), pp. 15-32. California Institute of Technology.

Buckley, F. T., Jr. & Sekscienski, W. S. 1975 "Comparisons of effectiveness of commercially available devices for the reduction of aerodynamic drag on tractor-trailers." SAE 750704.

Carr, G. W. 1968 "The aerodynamics of basic shapes for road vehicles. Part 1: Simple rectangular bodies." Motor Industry Research Assn. Rep. no. 1968/2.

Charwat, A. F., Dewey, C. F., Jr., Roos, J. N. & Hitz, J. A. 1961 "An investigation of separated flows--Part 2: Flow in the cavity and heat transfer." J. Aerosp. Sciences, 28, 513-527.

Cooper, K. R. 1976 "Wind tunnel investigations of eight commercially available devices for the reduction of aerodynamic drag on trucks." Roads and Transportation Assn. of Canada Natl. Conf. Proc. Quebec City.

Cowdrey, C. F. 1968 "Two topics of interest in experimental industrial aerodynamics: Part 1 Application of Maskell's theory of wind tunnel blockage to some large solid models." In Wind Effects on Buildings and Structures Symp. Loughborough Univ. of Tech. England, paper 29.

de Bray, B. G. 1957 "Low speed wind tunnel tests on perforated square flat plates normal to the airstream: Drag and velocity fluctuation measurements." ARC C. P. no. 323.

Dimotakis, P. E. 1976 "Single scattering particle laser-Doppler measurements of turbulence." AGARD Symp. Non-intrusive Instrumentation in Fluid Flow Res., Saint Louis, France, paper 10.

Dimotakis, P. E. 1977 "Laser-Doppler velocimetry momentum defect measurements of cable drag at low to moderate Reynolds numbers." Naval Construction Battalion Center Contract no. N62583/77-M-R541.

Dimotakis, P. E. 1978 "Correction of laser-Doppler velocimeter measurements for effects of velocity gradients." (private communication).

Dimotakis, P. E. & Lang, D. B. 1974 "Single scattering particle laser-Doppler velocimetry." Bull. Am. Phys. Soc. no. 1145.

Dimotakis, P. E., Lang, D. B. & Collins, D. J. 1978 "Laser-Doppler velocity measurements in subsonic, transonic, and supersonic boundary layers." Proc. Third Intl. Workshop on Laser Velocimetry, (to be held July, 1978) Purdue Univ.

Eiffel, G. 1910 Resistance De L'Air. Sect. 5. H Dunod et E. Pinat.

Eisenberg, P. & Pond, H. L. 1948 "Water tunnel investigations of steady state cavities." The David W. Taylor Model Basin Rep. no. 668.

Fage, A. & Johansen, F. C. 1927 "On the flow of air behind an inclined flat plate of infinite span." ARC R. & M. no. 1104.

Fail, R., Lawford, J. A. & Eyre, R. C. W. 1959 "Low speed experiments on the wake characteristics of flat plates normal to an air stream." ARC R. & M. no. 3120.

Flynn, H. & Kyropoulos, P. 1962 "Truck aerodynamics." Transactions of SAE, 70, 297-308.

Fox, J. 1964 "Surface pressure and turbulent airflow in traverse rectangular notches." NASA TN D-2501.

Gordon, E. I. 1966 "A review of acoustooptical deflection and modulation devices." Proc. IEEE, 54, 1391-1401.

Guenther, R. A. & Redding, J. P. 1977 "Fluctuating pressure environment of a drag reduction spike." AIAA Paper no. 77-90.

Hoerner, S. F. 1965 Fluid Dynamic Drag. Hoerner Fluid Dynamics.

Hoesel, W. & Rodi, W. 1977 "New biasing elimination method for laser-Doppler velocimeter counter processing. Rev. Sci. Instrum. 48, 910-919.

Hucho, W. H., Janssen, L. J. & Emmelmann, H. J. 1976 "The optimization of body details--a method for reducing the aerodynamic drag of road vehicles." SAE 760185.

Hutton, T. D. 1972 "An investigation of the feasibility of reducing fuel costs by reducing aerodynamic drag." Freightliner R & D Memo Rep. no. 72-02.

"Hydroballistics Design Handbook." 1955 NAVORD Rep. no. 3533.

Irminger, J. O. V. & Nøkkentved, C. 1930 Wind Pressure on Buildings. First Series, (translated by A. C. Jarvis & R. Halfdan-Nielsen), pp. 24-28.

Johannsen, N. H. 1955 "Experiments on supersonic flow past bodies of revolution with annular gaps of rectangular section." Phil. Mag. Ser. 7, 46, 31-39.

Kelnhoffer, W. J. 1973 "Neighboring body effects on bluff body form drag." Proc. Midwestern Mechanics Conf. 13th, pp. 111-124. Univ. of Pittsburgh.

Kirchhoff, G. 1869 F. Reine angew. Math. 70, 289.

Kirsch, J. W. & Bettes, W. H. 1974 "Feasibility study of the S^3 airvane and other truck drag reduction devices." Systems, Science and Software.

Knight, M. 1926 "Wind tunnel standardization disk drag." NACA Tech. Note no. 253.

Lanchester, F. W. 1909 "Notes on the resistance of planes in normal and tangential presentation and on the resistance of ichthyoid bodies." British Advisory Committee for Aeronautics R. & M. no. 15.

Liepmann, H. W. & Laufer, J. 1947 "Investigations of free turbulent mixing." NACA Tech. Note no. 1257.

Lissaman, P. B. S. (ed.) 1974 Conference/Workshop on Reduction of Aerodynamic Drag of Trucks. California Institute of Technology.

Lissaman, P. B. S. 1975 "Development of device to reduce the aerodynamic resistance of trucks." SAE 750702.

Lissaman, P. B. S. 1975 "Free streamline flow for a shielded body." (private communication).

Mair, W. A. 1965 "The effect of a rear-mounted disc on the drag of a blunt-based body of revolution." Aeronaut. Quart. Nov., 350-360.

Marks, C. H., Buckley, F. T., Jr. & Walston, W. H., Jr. 1977 "A study of the base drag of tractor-trailer trucks." ASME 77-WA/FE-18.

Maskell, E. C. 1965 "A theory of the blockage effects on bluff bodies and stalled wings in a closed wind tunnel." ARC R. & M. no. 3400.

Mason, W. T., Jr. 1975 "Wind tunnel development of the drag-foiler--a system for reducing tractor-trailer aerodynamic drag." SAE 750705.

Mason, W. T., Jr. & Beebe, P.S. 1977 "The drag related flow field characteristics of trucks and buses." General Motors Research Publ. no. 2257.

McGregor, O. W. & White, R. A. 1970 "Drag of rectangular cavities in supersonic and transonic flow including the effects of cavity resonance." AIAA J. 8, 1959-1964.

Merz, R. A., Przirembel, C. E. G. & Page, R. H. 1977 "Subsonic axisymmetric near-wake studies." AIAA Paper no. 77-135.

Milne-Thomson, L.M. 1960 Theoretical Hydrodynamics, 4th edn. MacMillian Co.

Moeller, E. 1951 "Luftwiderstandsmessungen am VW-Lieferwagen." Automobiltechnische Zeitschrift, 53, 153-156.

Morel, T. 1978 "Theoretical lower limits of forebody drag." General Motors Research Publ. no. 2655.

Morel, T. 1978 "The effect of base slant on the flow pattern and drag of three-dimensional bodies." In Aerodynamic Drag Mechanics of Bluff Bodies and Road Vehicles. (eds. G. Sovran, T. Morel & W. T. Mason, Jr.), pp. 191-226. Proc. of Symp. At General Motors Research Laboratories, Plenum.

Nakaguchi, H. 1978 "Recent Japanese research on three-dimensional bluff-body flows relevant to road-vehicle aerodynamics." In Aerodynamic Drag Mechanics of Bluff Bodies and Road Vehicles. (eds. G. Sovran, T. Morel & W. T. Mason, Jr.), pp. 227-286. Proc. of Symp. at General Motors Laboratories, Plenum.

Norris, J. D. & McGhee, R. J. 1966 "Effects of bluntness on the subsonic drag of an elliptical forebody." NASA TN D-3388.

Ota, T. 1975 "An axisymmetric separated and reattached flow on a longitudinal blunt circular cylinder." J. App. Mech. June, 311-315.

Plesset, M.S. & Perry, B. 1954 " On the application of free streamline theory to cavity flows." Extrait Des Mémories Sur La Mécanique Des Fluides offerts a M. D. Riabouchinsky à l'occasion de son Jubilé Scientifique Publications Scientifiques et Techniques Du Ministére De L Air«Hors Serie».

Polhamus, E. C. 1957 "Effect of nose shape on subsonic aerodymanic characteristics of a body of revolution having a fineness ratio of 10.94." NACA RM L57F25.

Prandtl, L. 1910 "Einige für die Flugtechnik wichtige Beziehungen aus der Mechanik»Etwas über den Luftwiderstand." ZFM. 1, Heft 1/2, 3/4, 6 und 7.

Prandtl, L. 1923 Ergebnisse der Aerodynamischen Versuchsanstalt zu Göttingen. II Lieferung.

Prandtl, L & Tietjens, O. G. 1934 Applied Hydro- and Aeromechanics. (translated by J. P. Hartog). Sect. 77-81. Dover Publications.

Romberg, G. F., Chianese, F., Jr. & Lajoie, R. G. 1971 "Aerodynamics of race cars in drafting and passing situations." SAE 710213.

Robertson, J. M. 1965 Hydrodynamics In Theory and Application. Prentice-Hall, Inc.

Rockwell, D. & Naudascher, E. 1978 "Review: Self-sustaining oscillations of flow past cavities." (To be published in Transactions of ASME, J. Fluids Engr. circa June, 1978).

Roshko, A. 1954 "A new hodograph for free streamline theory." NACA Tech. Note no. 3168.

Roshko, A. 1954 "On the drag and shedding frequency of two-dimensional bluff bodies." NACA Tech. Note no. 3169.

Roshko, A. 1955 "Some measurements of flow in a rectangular cutout." NACA Tech. Note no. 3488.

Rossiter, J. E. 1964 "Wind tunnel experiments on the flow over rectangular cavities at subsonic and transonic speeds." REA Tech. Rep. no. 64037.

Rouse, H. & McNown, J. S. 1948 "Cavitation and pressure distribution: Head forms at zero angle of yaw." State University of Iowa Studies in Engineering, Bulletin 32.

Saltzman, E. J., Meyer, R. R. , Jr. & Lux, D. P. 1974 "Drag reductions obtained by modifying a box-shaped ground vehicle." NASA TN X-56027.

Sarohia, V. 1975 "Experimental and analytical investigation of oscillations in flows over cavities." Ph.D. thesis, California Institute of Technology, Pasadena.

Saunders, W. S. 1966 "Apparatus for reducing linear and lateral wind resistance in a tractor-trailer combination vehicle." U.S. Patent no. 3,241,876.

Sawyer, J.W. & Whitcomb, C.F. 1971 "Subsonic and transonic pressure distributions around a bluff afterbody in the wake of a 120° cone for various separation distances." NASA TN D-6569.

Schubauer, G.B. & Dryden, H.L. 1935 "The effect of turbulence on the drag of flat plates." NACA Rep. no. 546.

Servais, R.A. & Bauer, P.T. 1975 "Aerodynamic devices can significantly reduce the fuel consumption of trucks: Experience with CECA Designs." SAE 750707.

Shoemaker, J.M. 1926 "Resistance of a fifteen-centimeter disk." NACA Tech. Note no. 252.

Sovran, G., Morel, T. & Mason, W.T., Jr. (eds.) 1978 Aerodynamic Drag Mechanics of Bluff Bodies and Road Vehicles. Proc. of Symp. at General Motors Research Laboratories, Plenum.

Spencer, B.W. 1970 "Statistical investigation of turbulent velocity and pressure fields in a two-stream mixing layer." Ph.D. thesis, Mechanical Engineering Dept., Univ. of Illinois, Urbana-Champaign.

Stanbrook, A. 1966 "Experimental pressure distributions on a plane-nosed cylinder at subsonic and transonic speeds." ARC R. & M. no. 3425.

Steers, L. L., Montoya, L. C. & Saltzman, E. J. 1975 "Aerodynamic drag reduction tests on a full-scale tractor-trailer combination and a representative box-shaped ground vehicle." SAE 750703.

Strŭck, H. G. 1970 "Discontinuous flows and free streamline solutions for axisymmetric bodies at zero and small angles of attack." NASA TN D-5634.

von Mises, R. 1945 Theory of Flight, Dover Publications.

Ward, T.M. 1976 The hydrodynamics laboratory at the California Institute of Technology. Graduate Aeronautical Laboratory, California Institute of Technology.

Weiselsberger, C. 1915 "Untersuchungen mit kreisrunden Platten und ebenen Trăgflachen." Zeitschrift fŭr Flugtechnik und Motorluftschiffahrt, Sept. 25.

White, J.W. & Kline, S.J. 1975 "A calculation method for incompressible axisymmetric flows, including unseparated, fully separated, and free surface flows." Stanford University Dept. of Mech. Engr. Rep. MD-35.

Wygnanski, I. & Fiedler, H.E. 1970 "The two-dimensional mixing region." J. Fluid Mech. 41, 327.

Yariv, A. 1976 Introduction to Optical Electronics, pp. 337-353. Holt, Rinehart & Winston.

Zdravkovich, M.M. 1977 "Review of flow interference between two circular cylinders in various arrangements." Transactions of ASME, J. Fluids Engr. December, 618-632.

Zdravkovich, M.M. & Pridden, D.L. 1977 "Interference between two circular cylinders; series of unexpected discontinuities." J. of Ind. Aerodynamics, 2, 255-270.

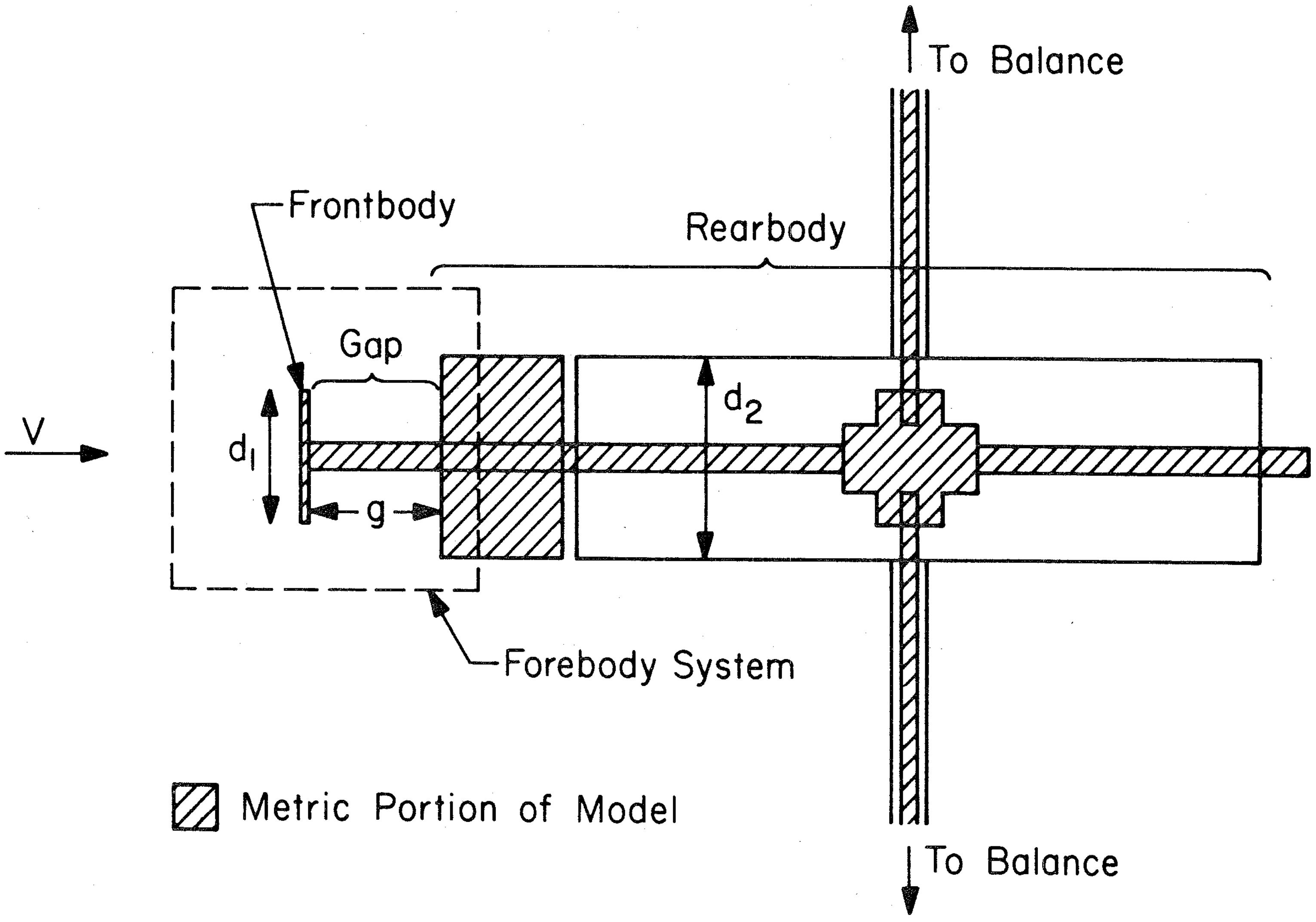

FIGURE 1 EXPERIMENTAL MODEL

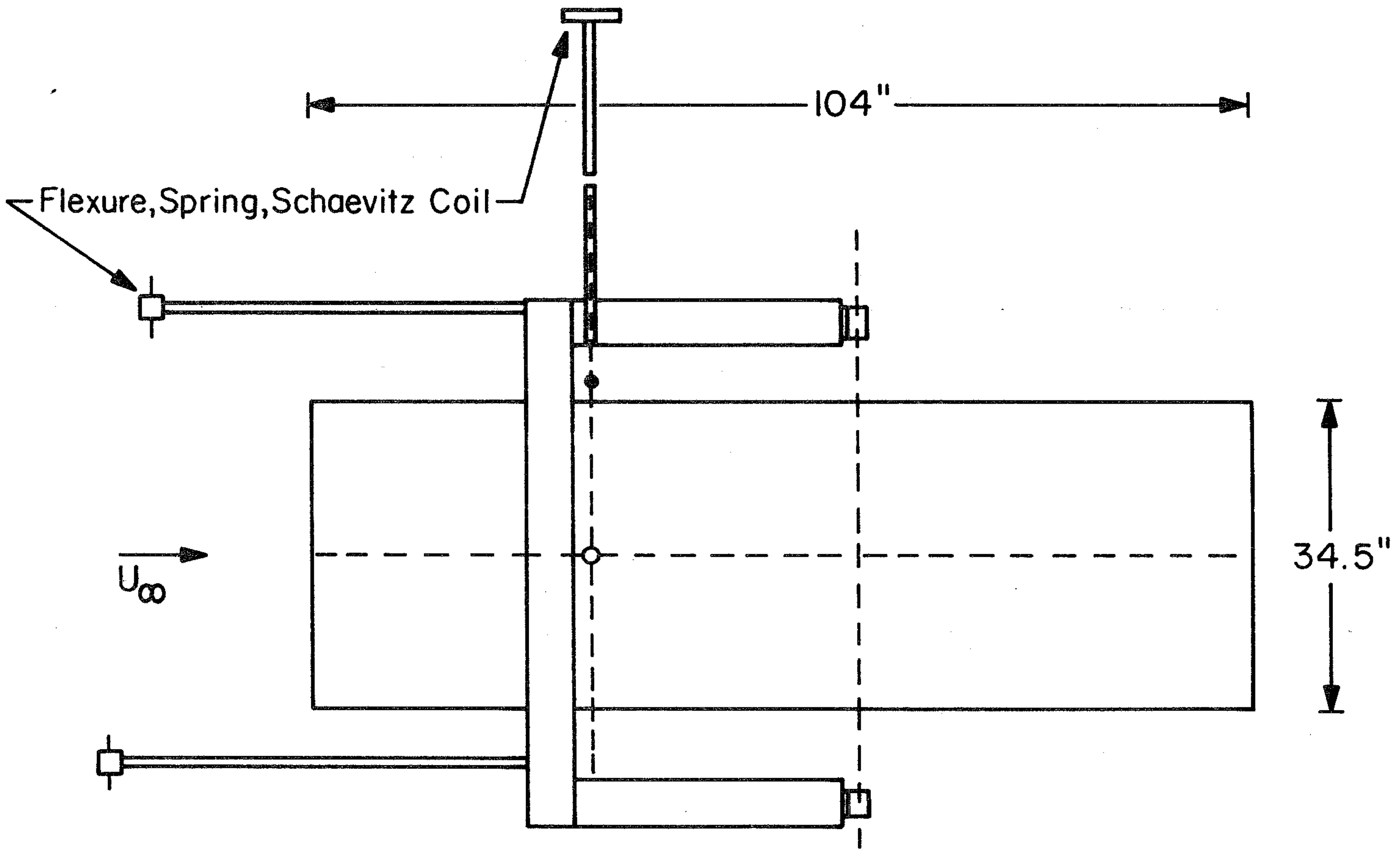

FIGURE 2 MERRILL WIND TUNNEL TEST SECTION AND FORCE BALANCE

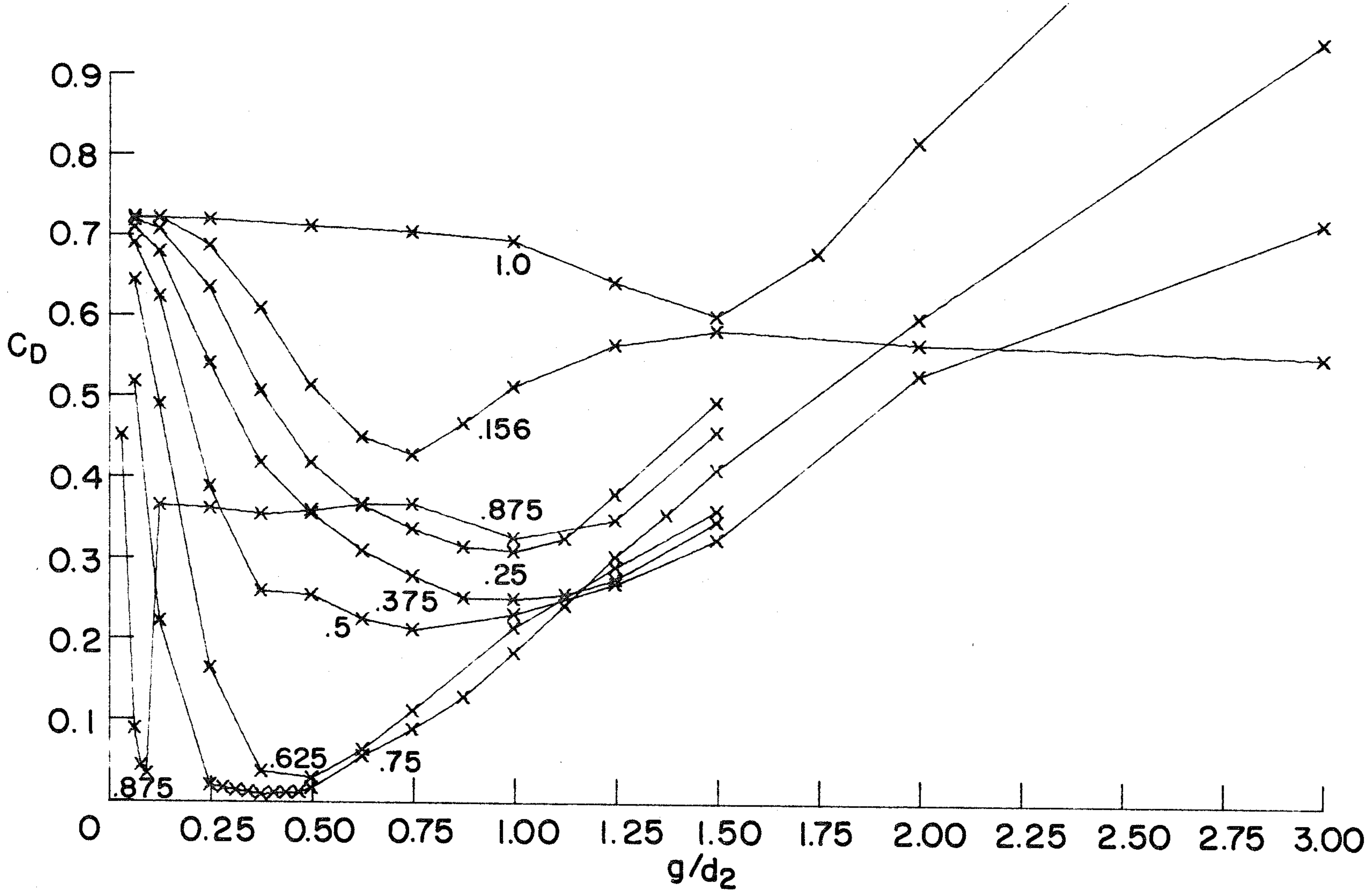

FIG. 3a AXISYMMETRIC FOREBODY SYSTEM DRAG

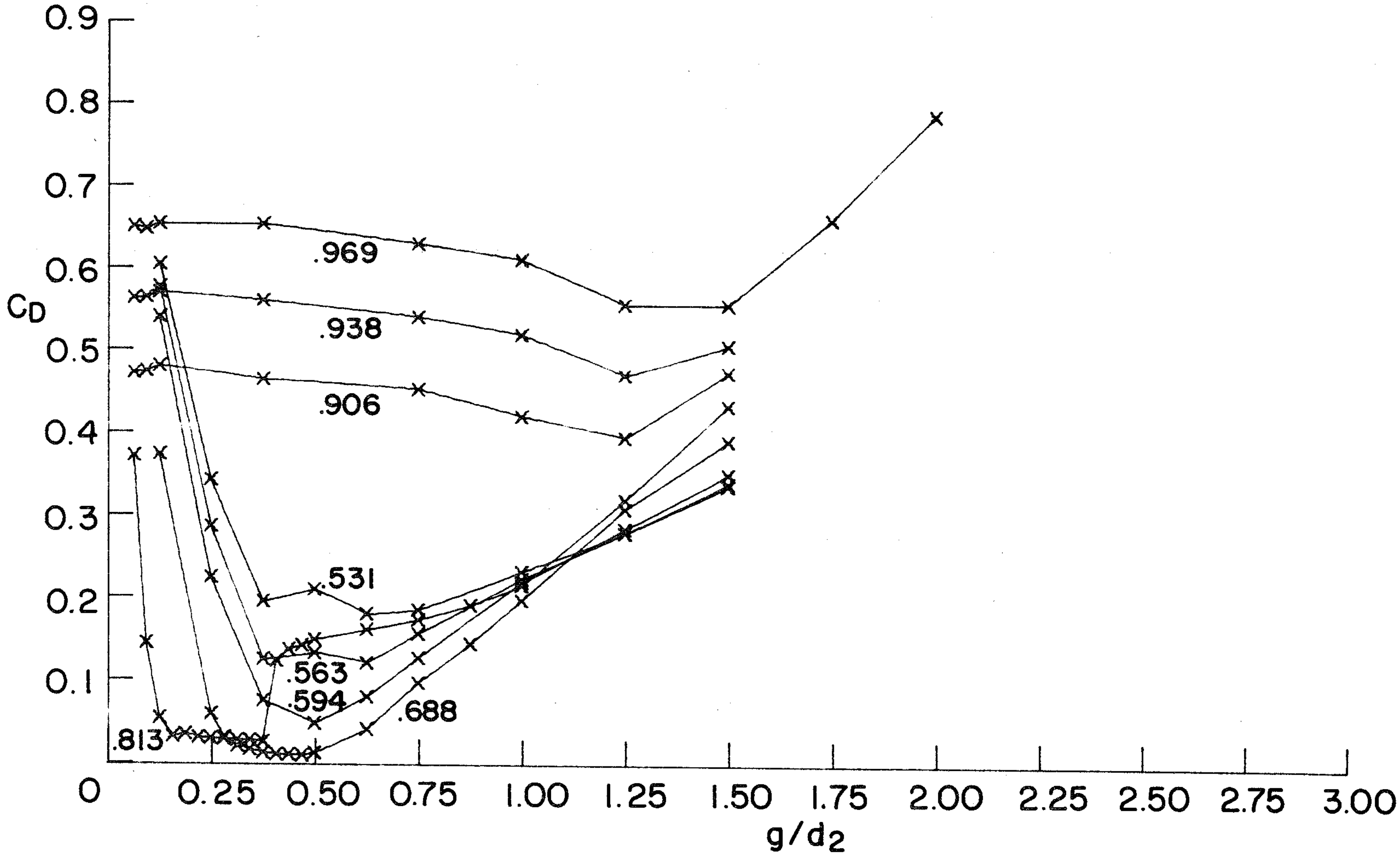

FIG. 3b AXISYMMETRIC FOREBODY SYSTEM DRAG

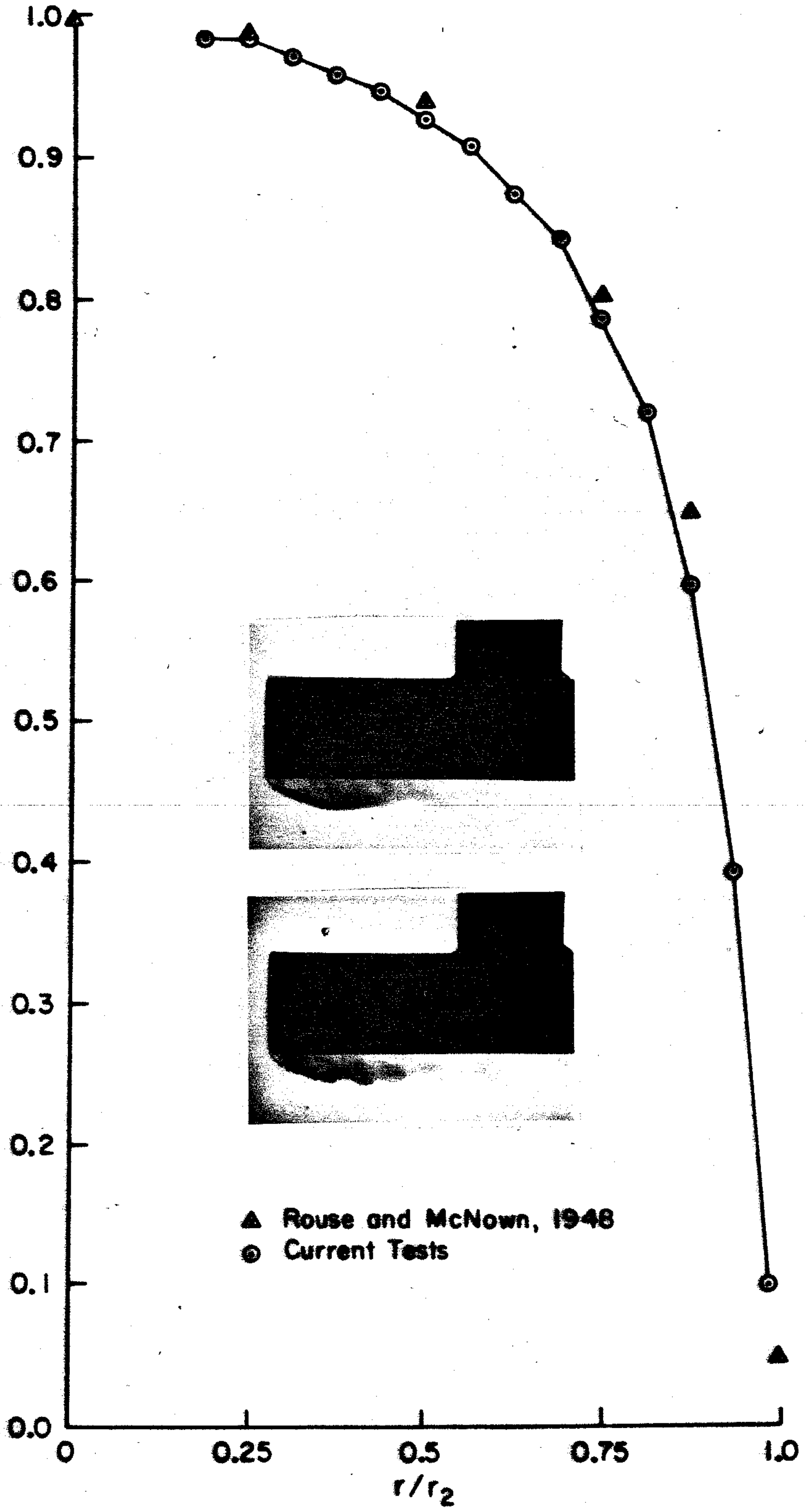

FIGURE 4 BLUNT CYLINDER FACE PRESSURE DISTRIBUTIONS

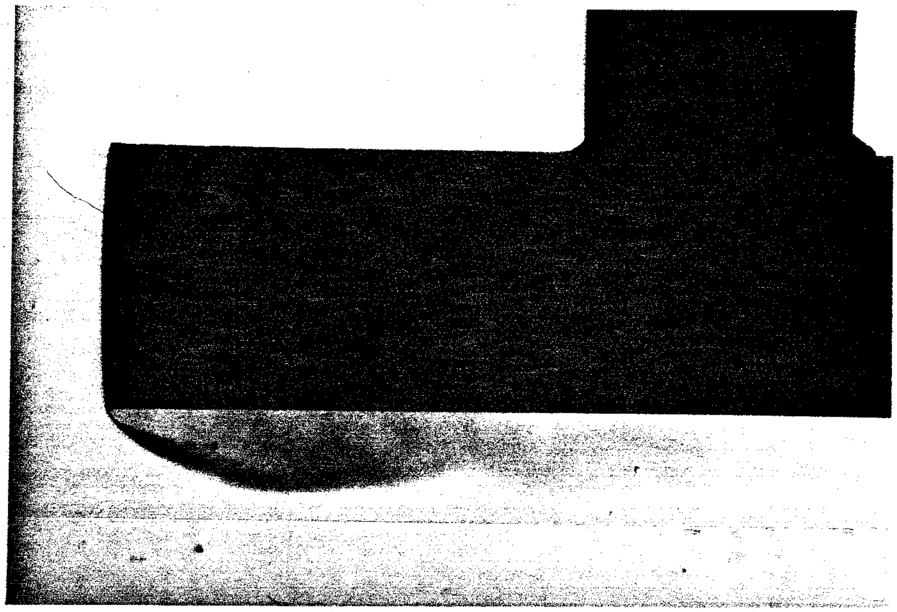

a) No Frontbody, C_D = 0.722, Shutter Speed = 1/15 second

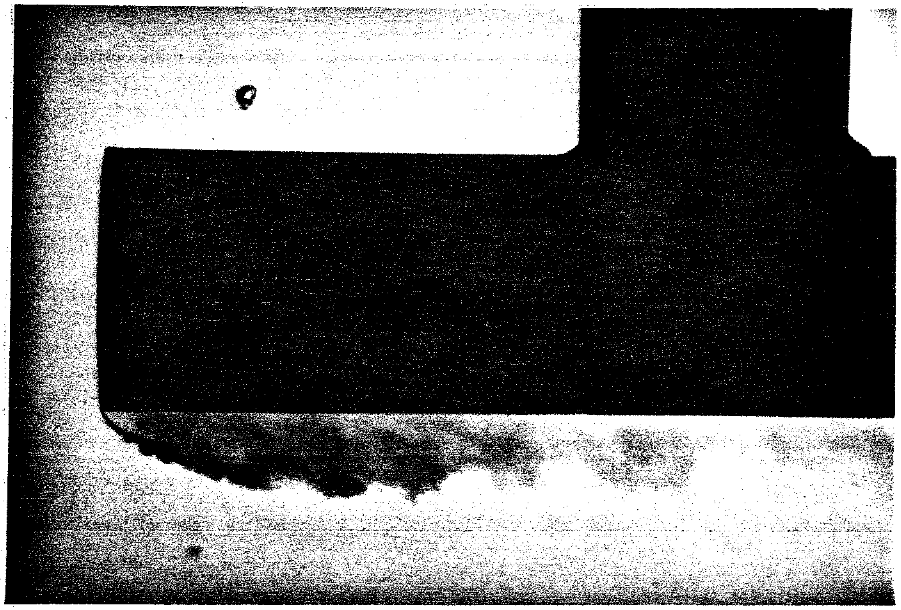

b) No Frontbody, C_D = 0.722, Shutter Speed = 1/1000 second

FIG. 5a & b AXISYMMETRIC FLOW VISUALIZATION

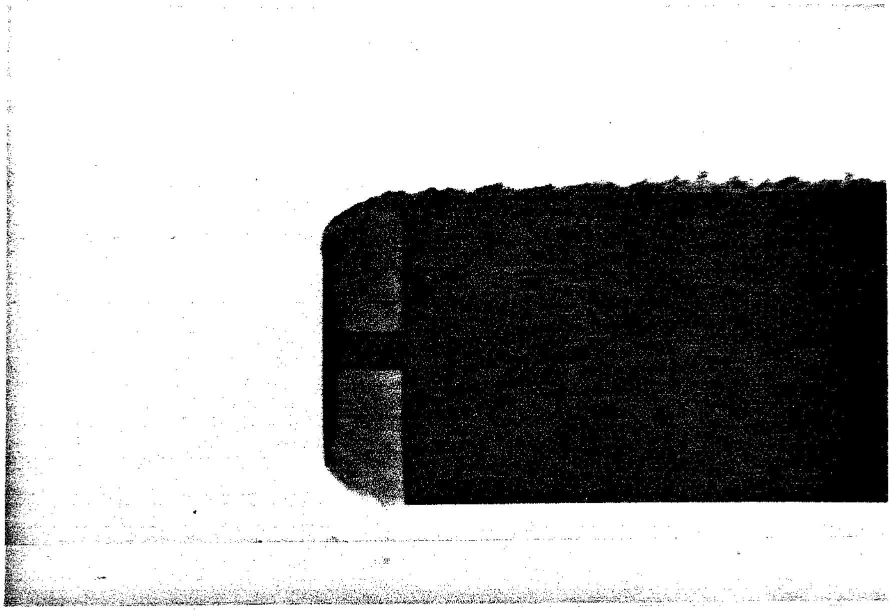

c) $d_1/d_2 = 0.75$, $g/d_2 = 0.25$, $C_D = 0.021$

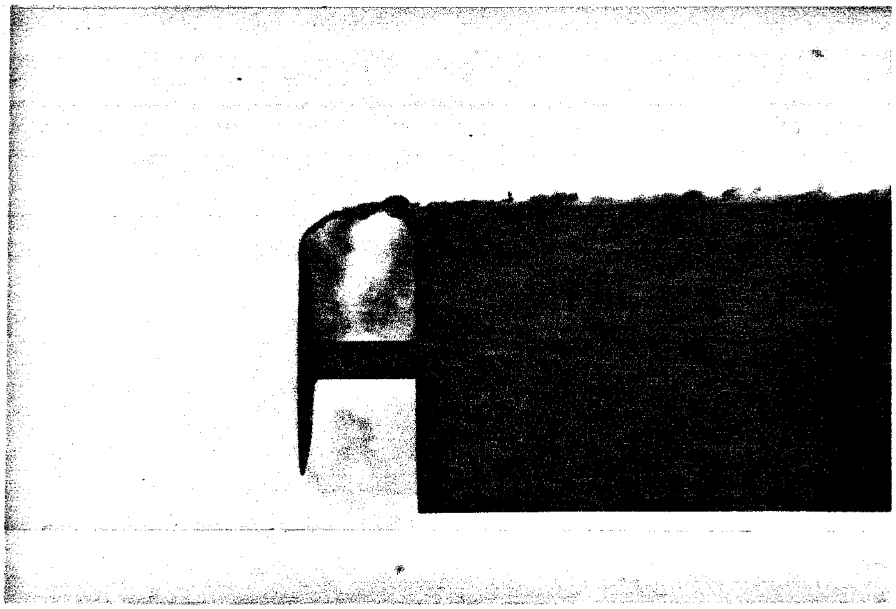

d) $d_1/d_2 = 0.75$, $g/d_2 = 0.375$, $C_D = 0.010$

FIG. 5c & d AXISYMMETRIC FLOW VISUALIZATION

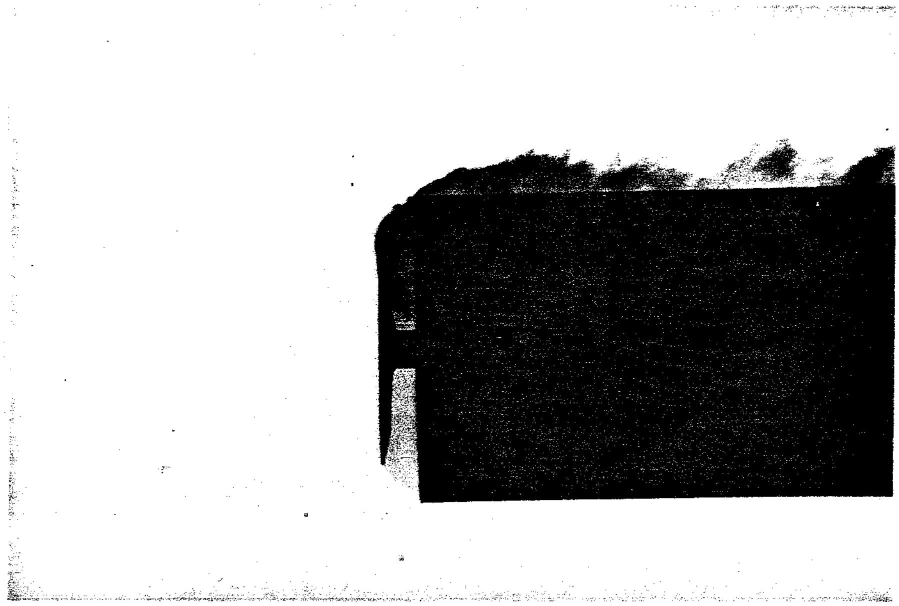

e) $d_1/d_2 = 0.75$, $g/d_2 = 0.125$, $C_D = 0.222$

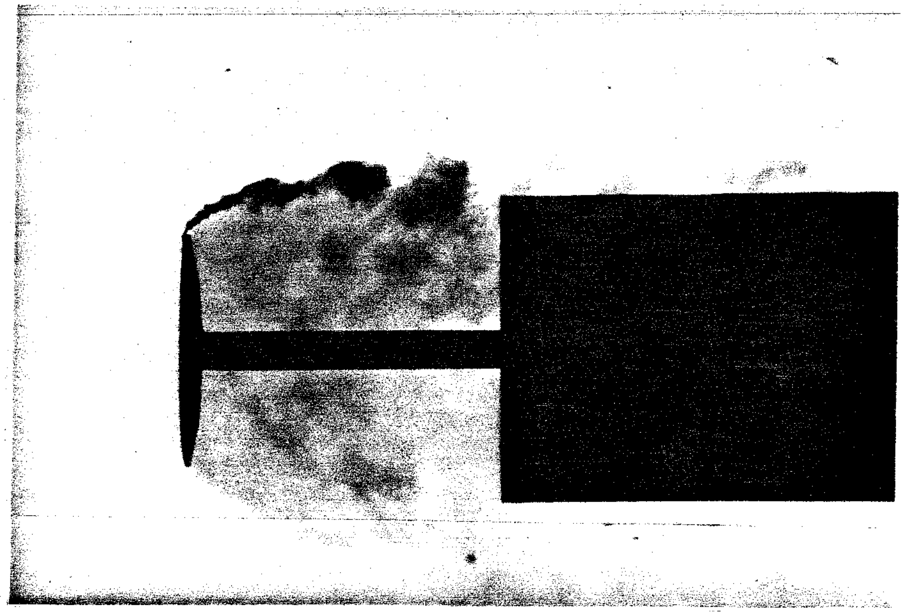

f) $d_1/d_2 = 0.75$, $g/d_2 = 1.0$, $C_D = 0.184$

FIG. 5e & f AXISYMMETRIC FLOW VISUALIZATION

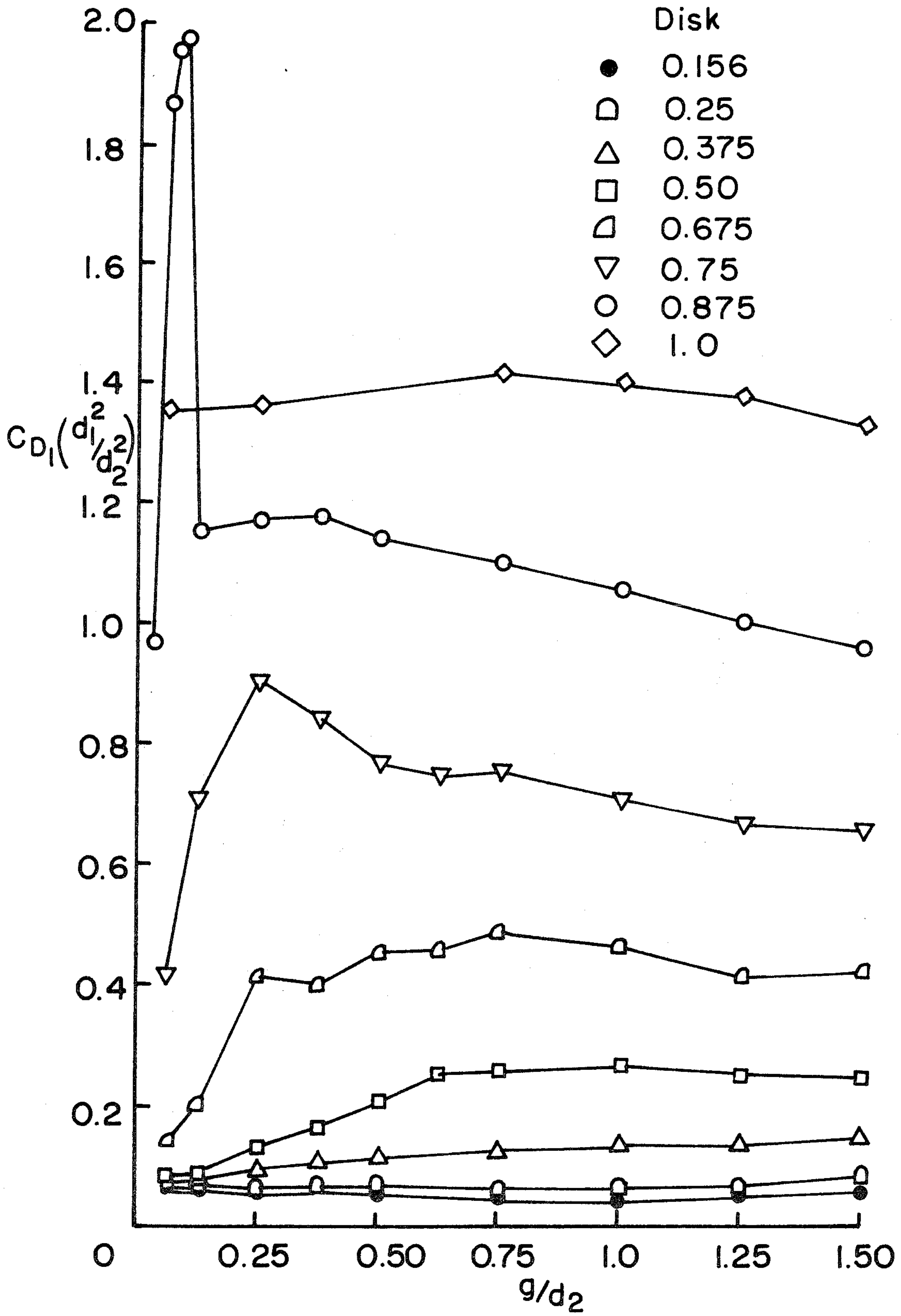

FIG. 6 DISK DRAG COEFFICIENT

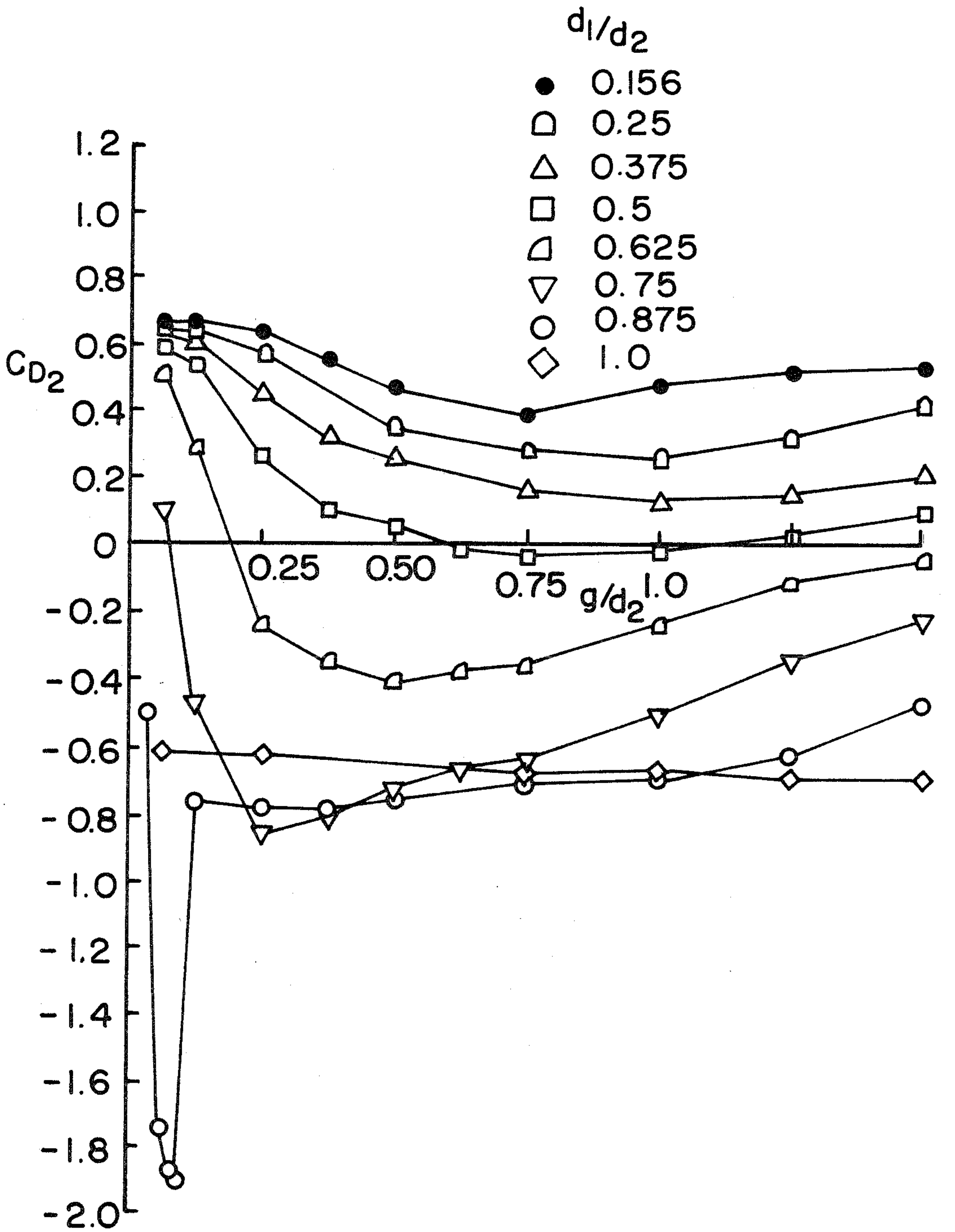

FIG. 7 REARBODY FACE DRAG COEFFICIENT

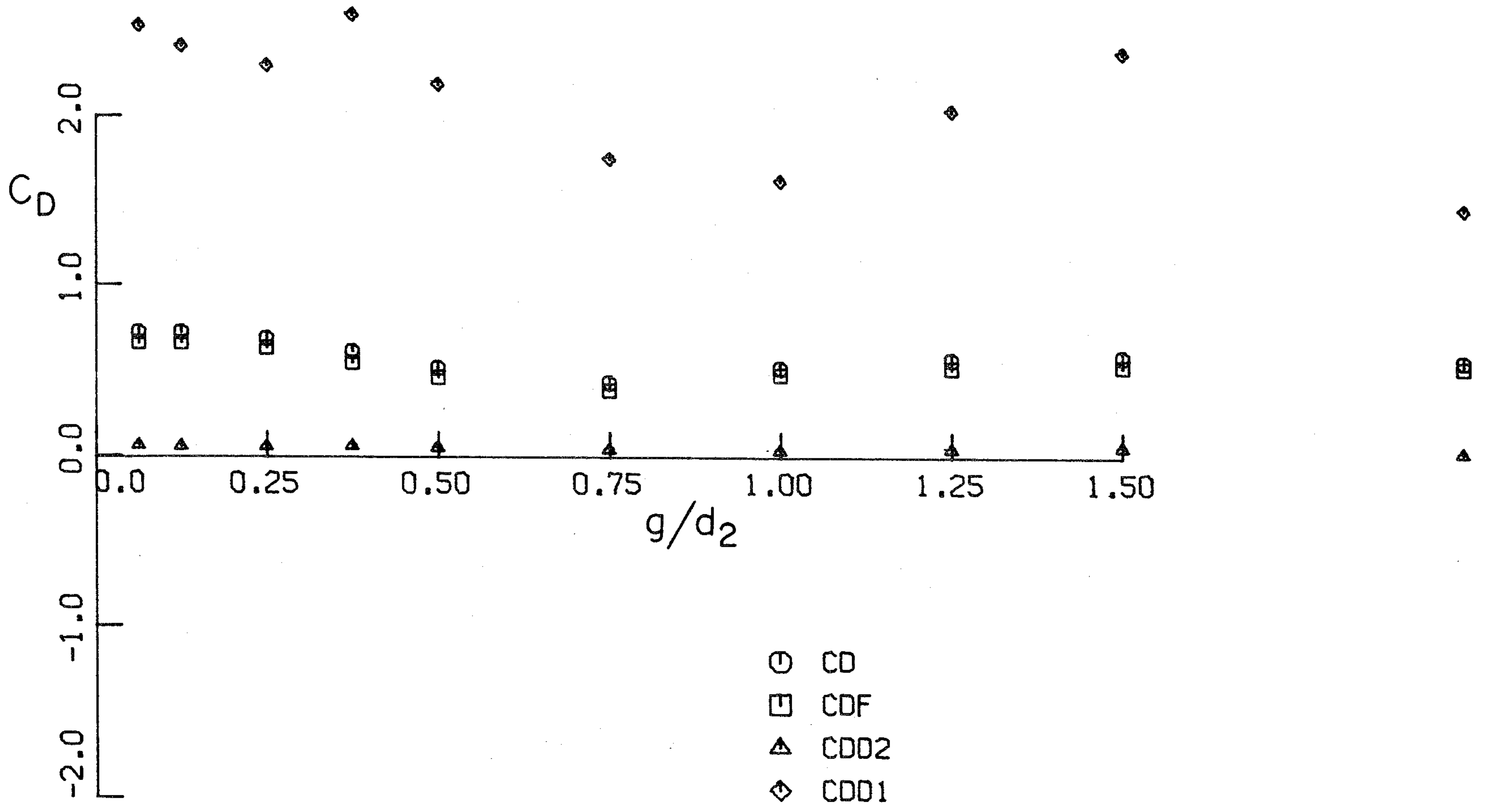

FIGURE 8a DRAG CHARACTERISTICS $d_1/d_2 = 0.156$

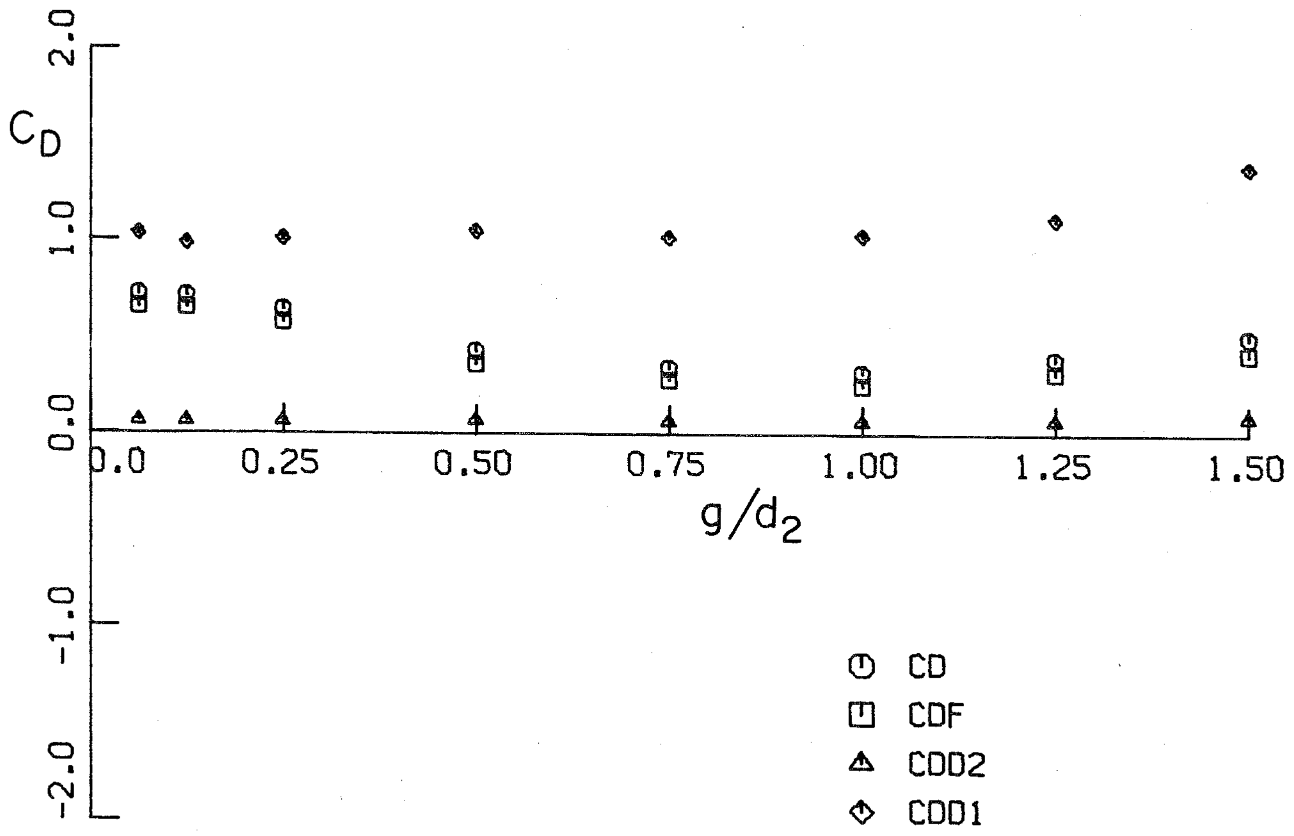

FIGURE 8b DRAG CHARACTERISTICS $d_1/d_2 = 0.25$

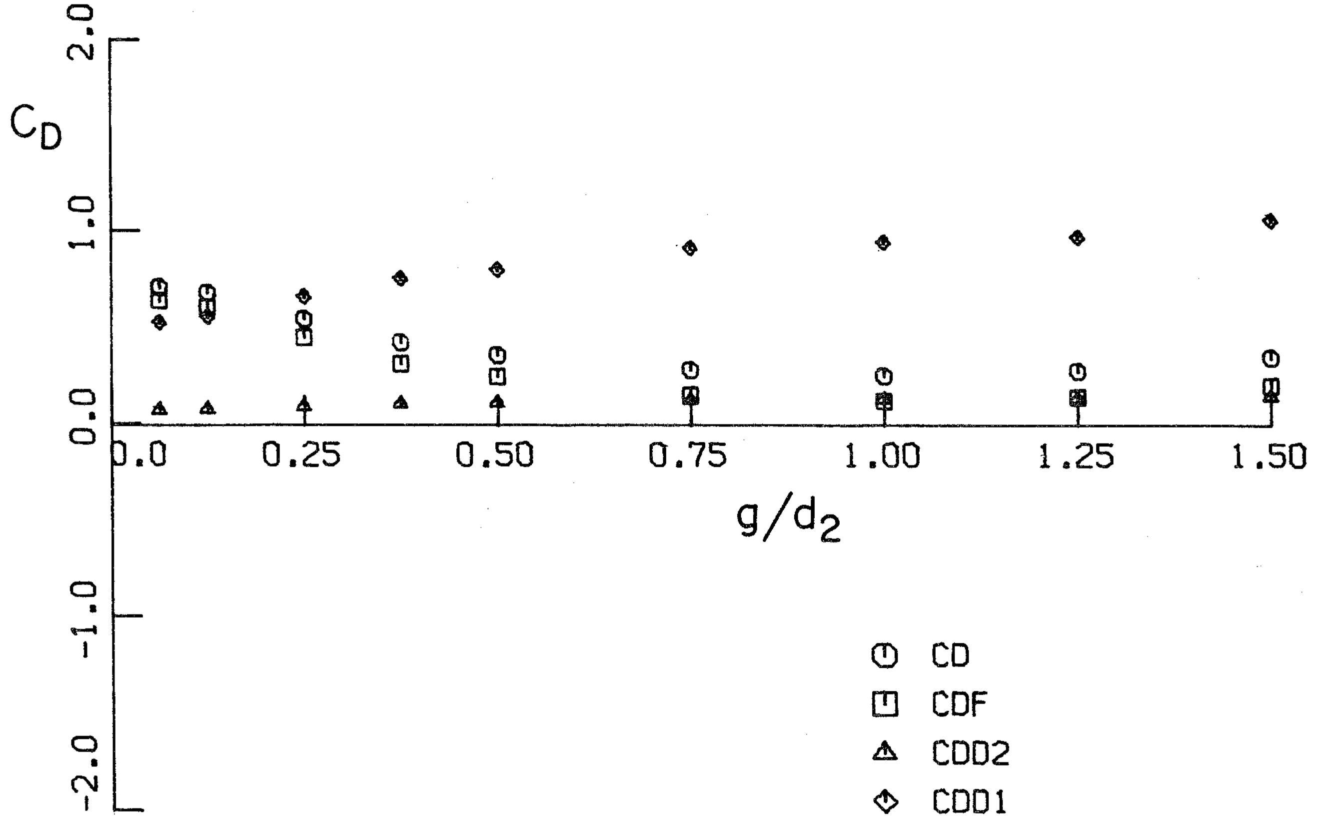

FIGURE 8c DRAG CHARACTERISTICS $d_1/d_2 = 0.375$

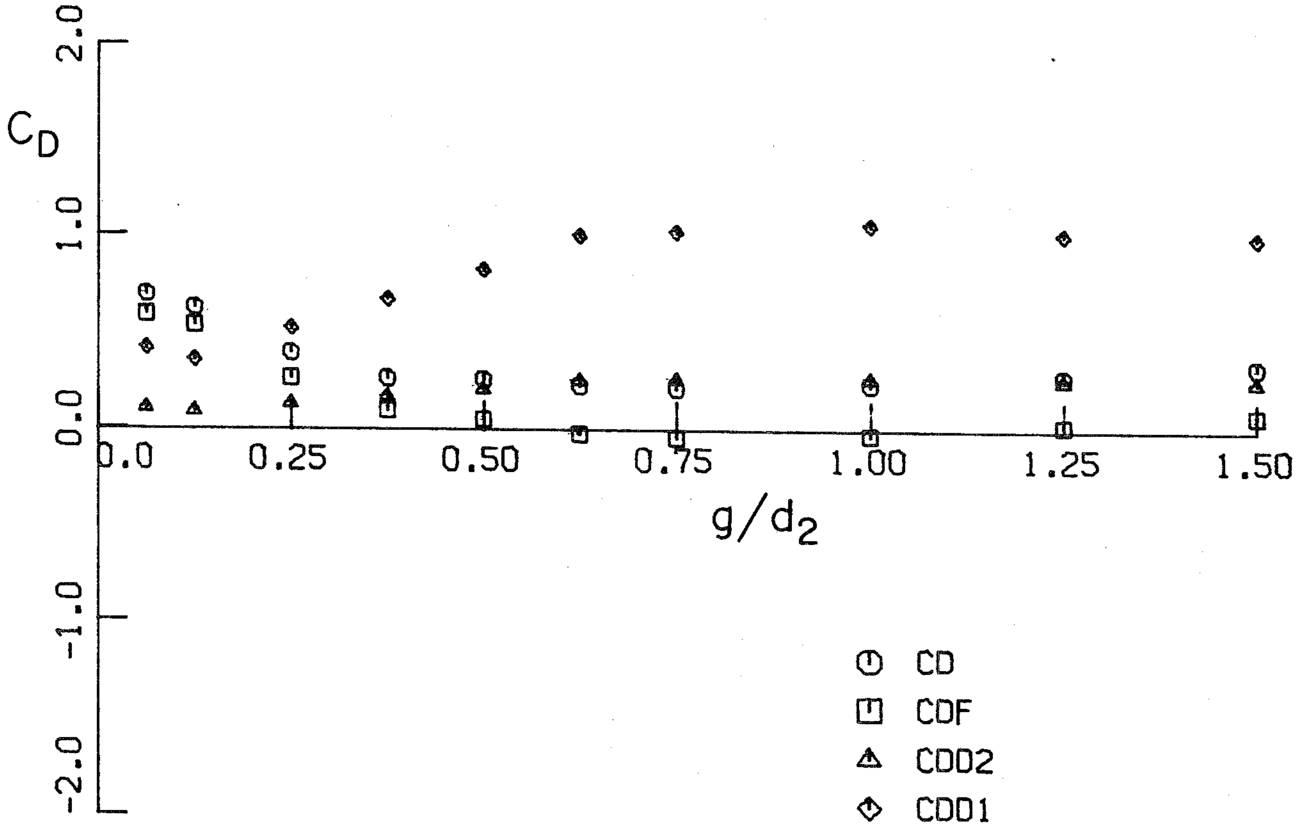

FIGURE 8d DRAG CHARACTERISTICS $d_1/d_2 = 0.5$

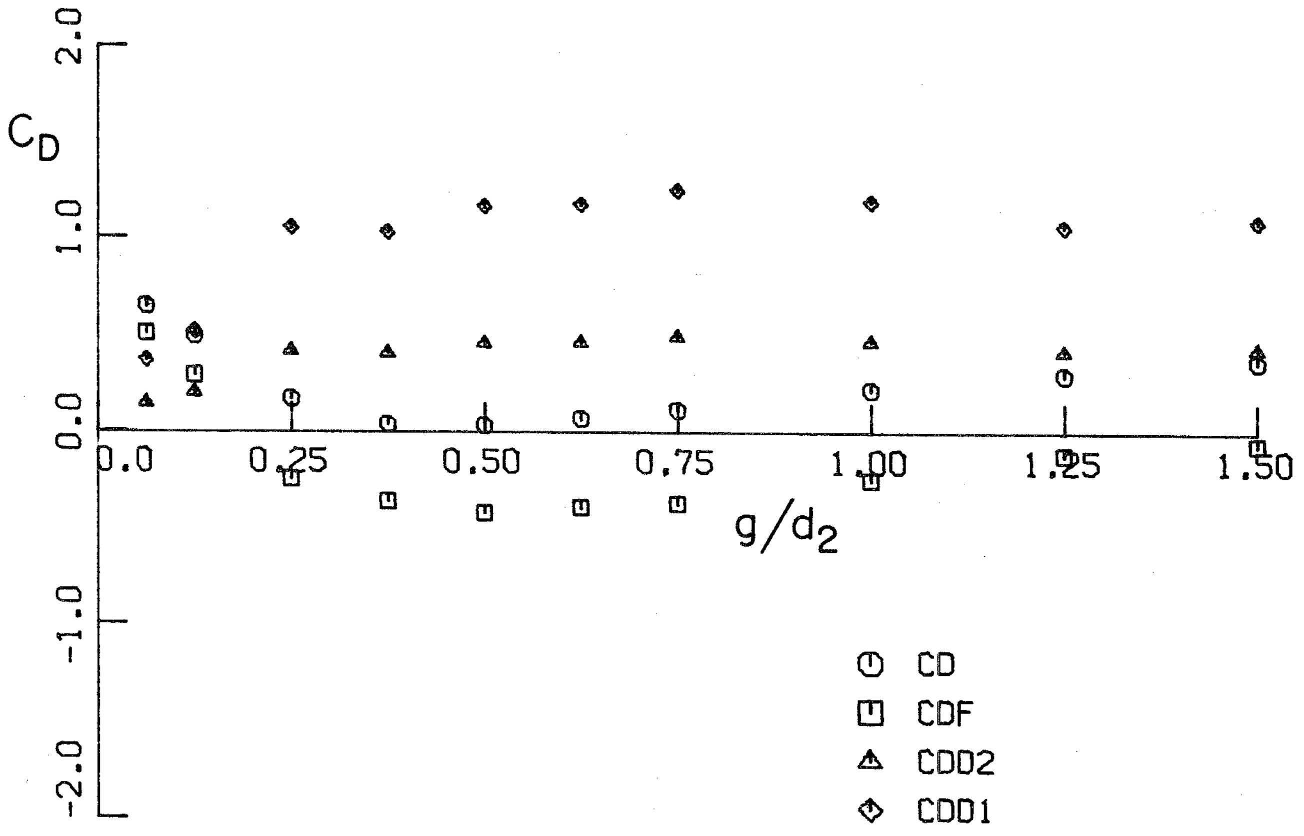

FIGURE 8e DRAG CHARACTERISTICS $d_1/d_2 = 0.625$

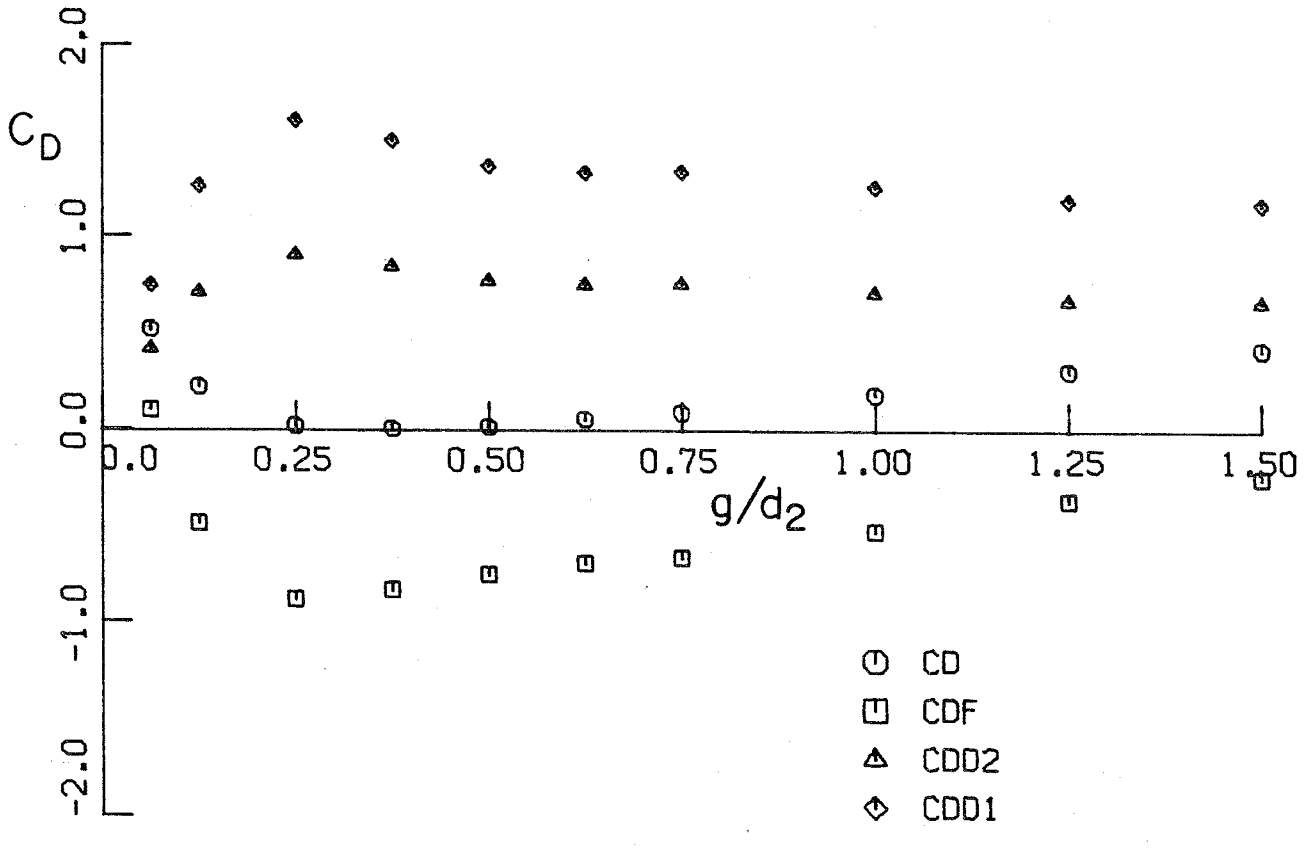

FIGURE 8f DRAG CHARACTERISTICS $d_1/d_2 = 0.75$

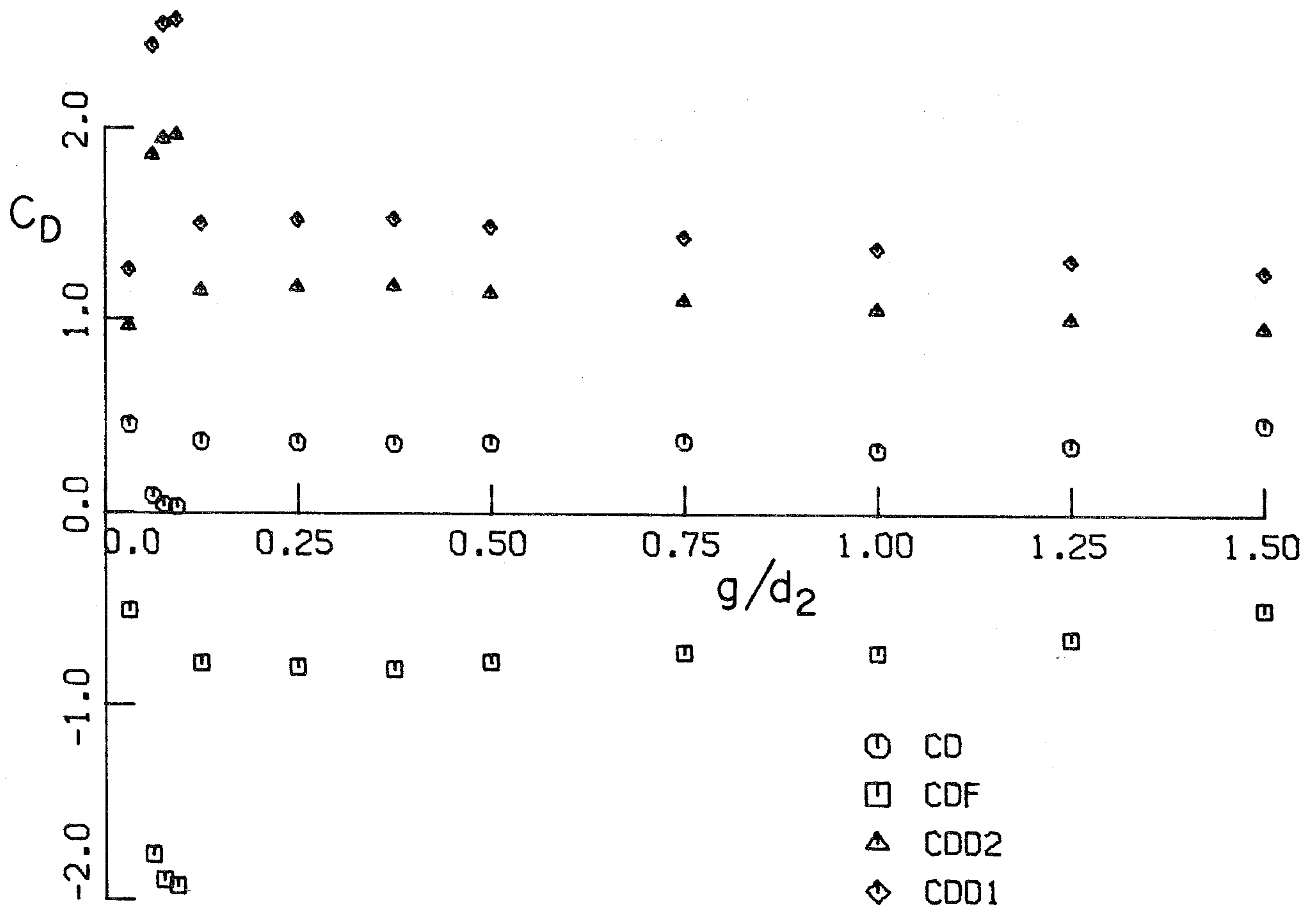

FIGURE 8g DRAG CHARACTERISTICS $d_1/d_2 = 0.875$

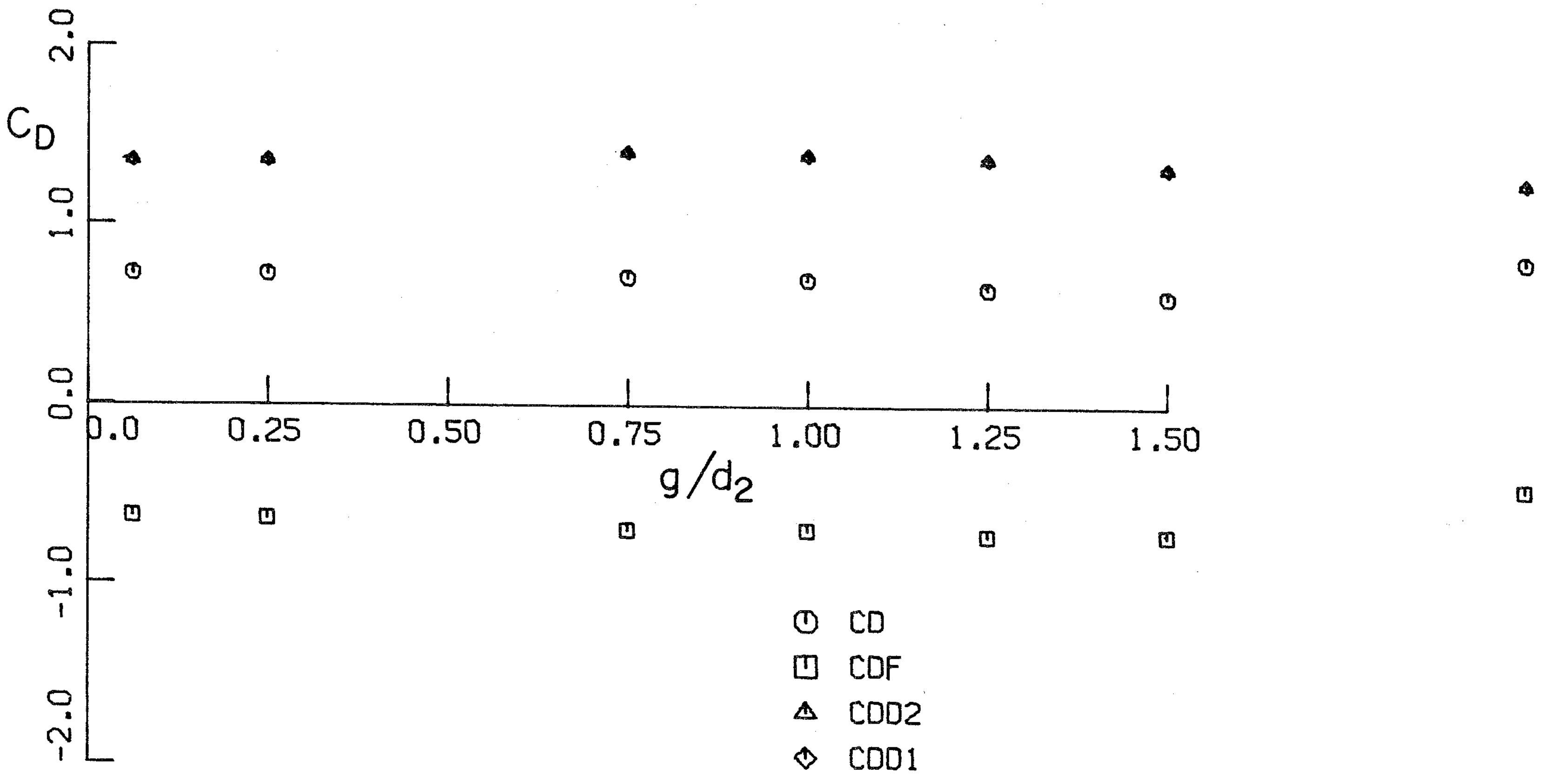

FIGURE 8h DRAG CHARACTERISTICS $d_1/d_2 = 1.0$

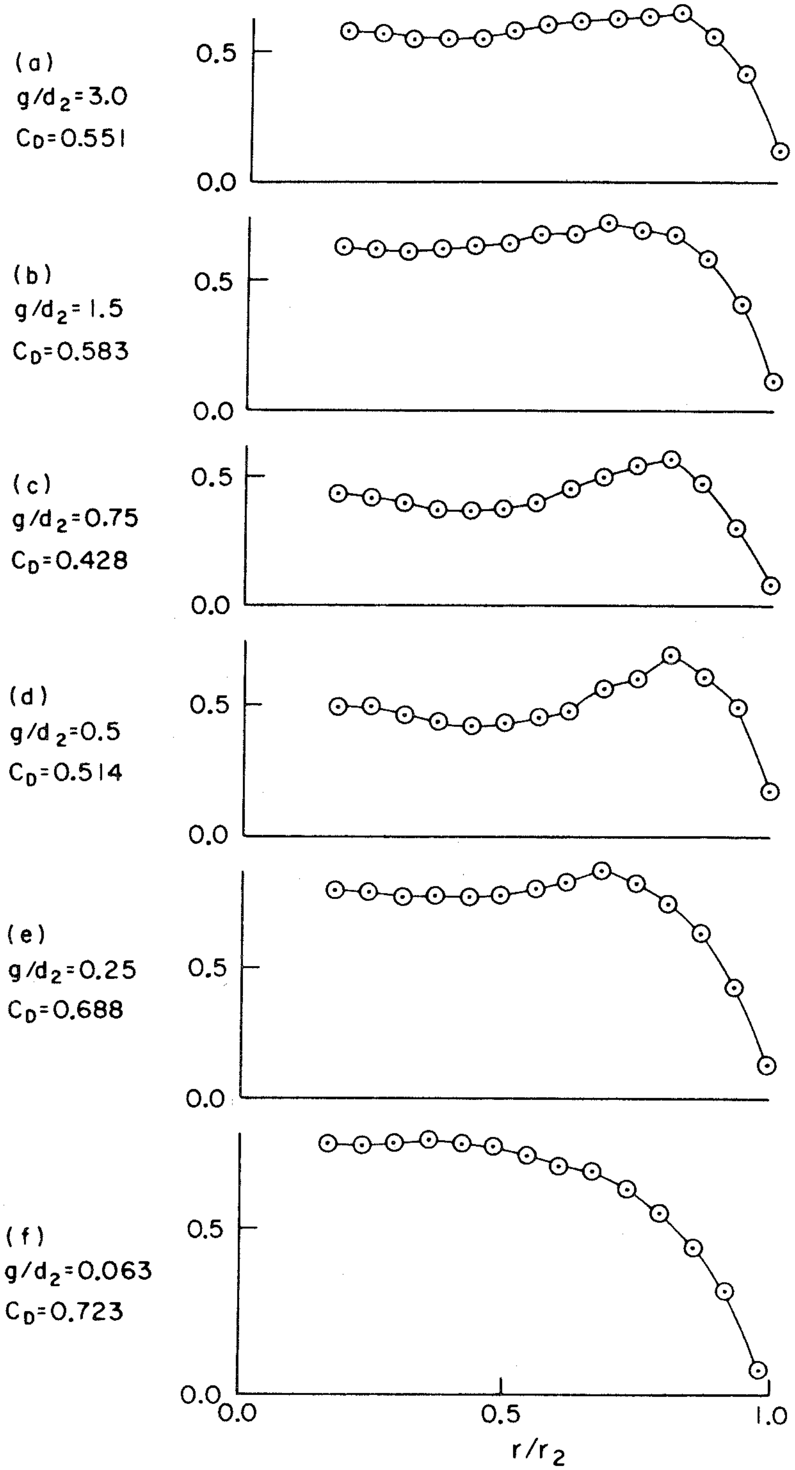

FIGURE 9 FACE PRESSURE DISTRIBUTION, $d_1/d_2=0.156$

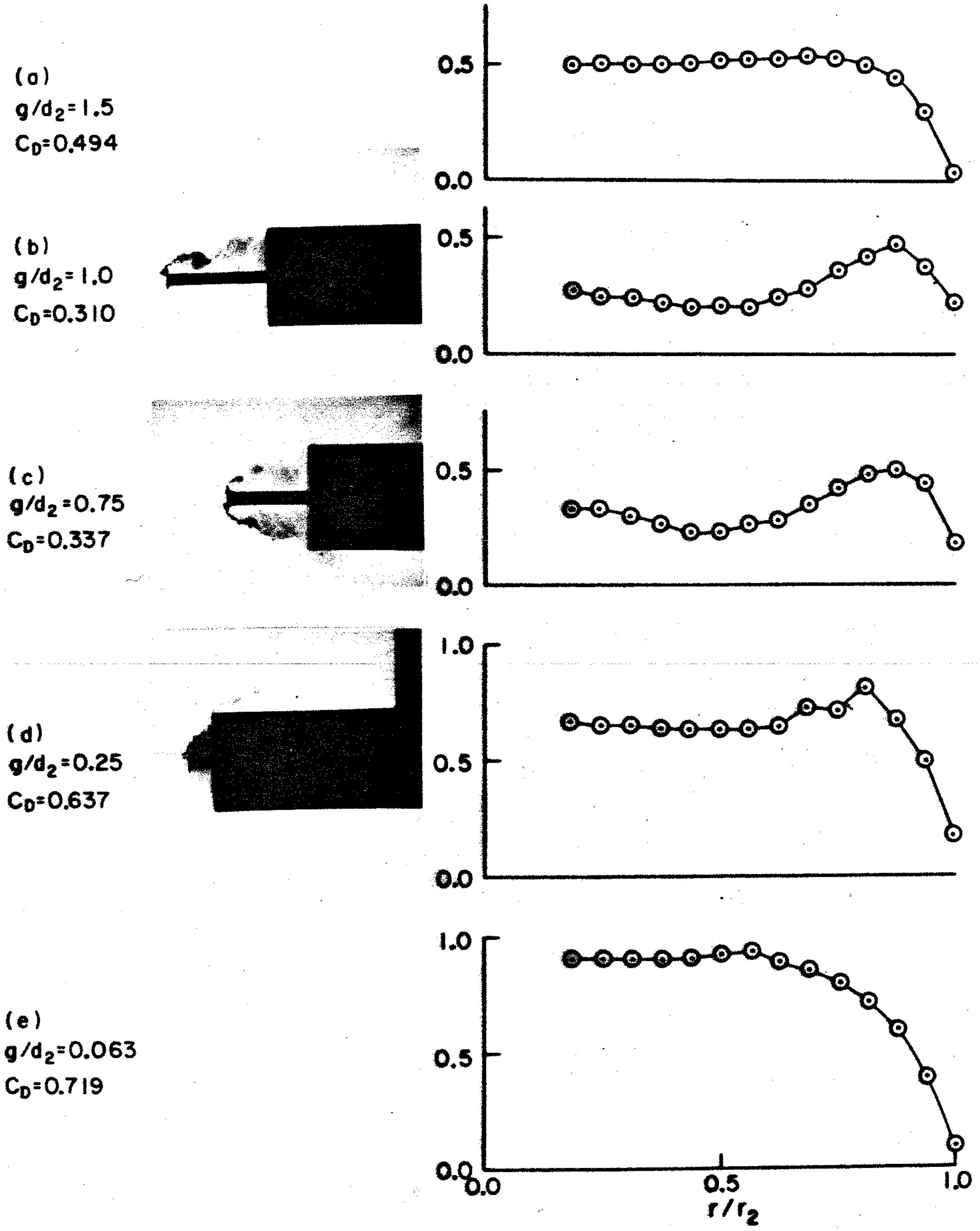

FIGURE 10 FACE PRESSURE DISTRIBUTION, d_1/d_2=0.25

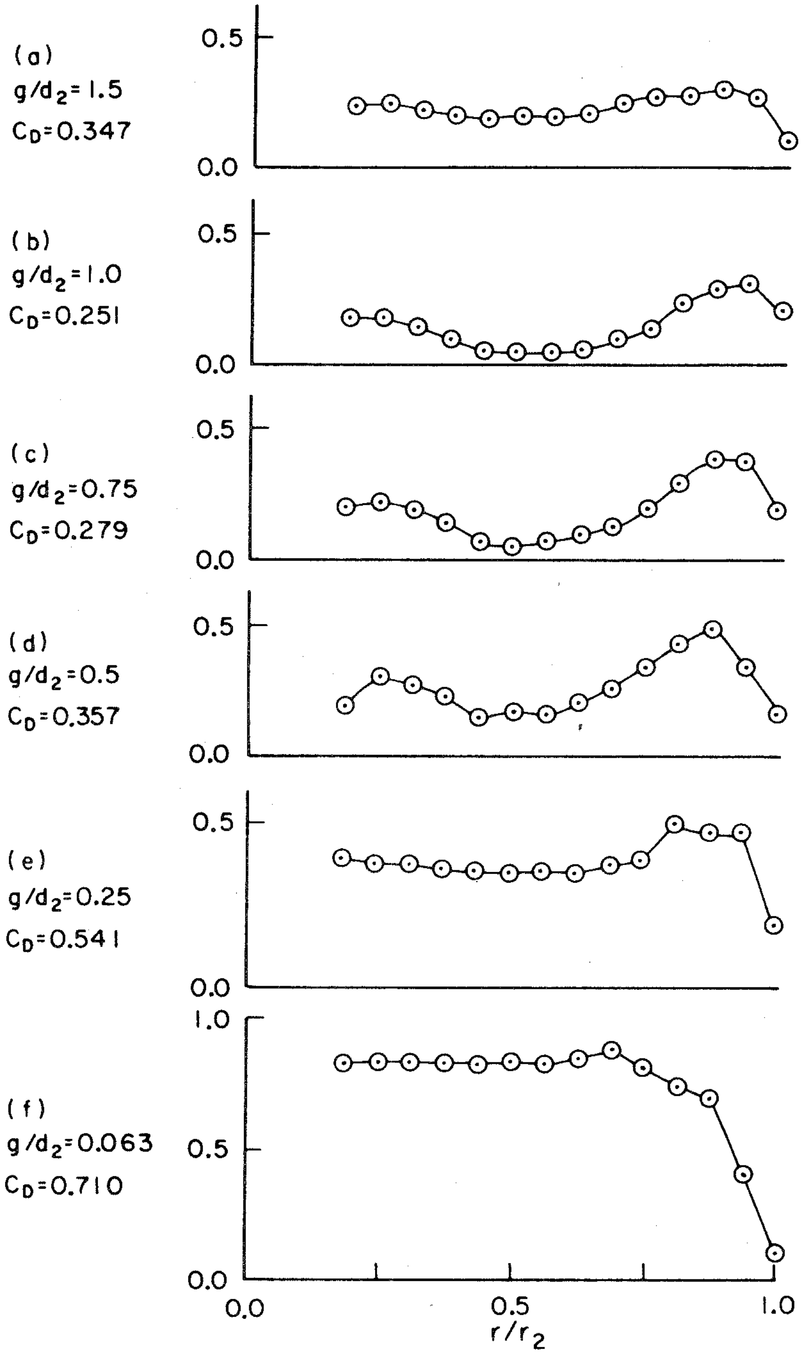

FIGURE 11 FACE PRESSURE DISTRIBUTION, $d_1/d_2=0.375$

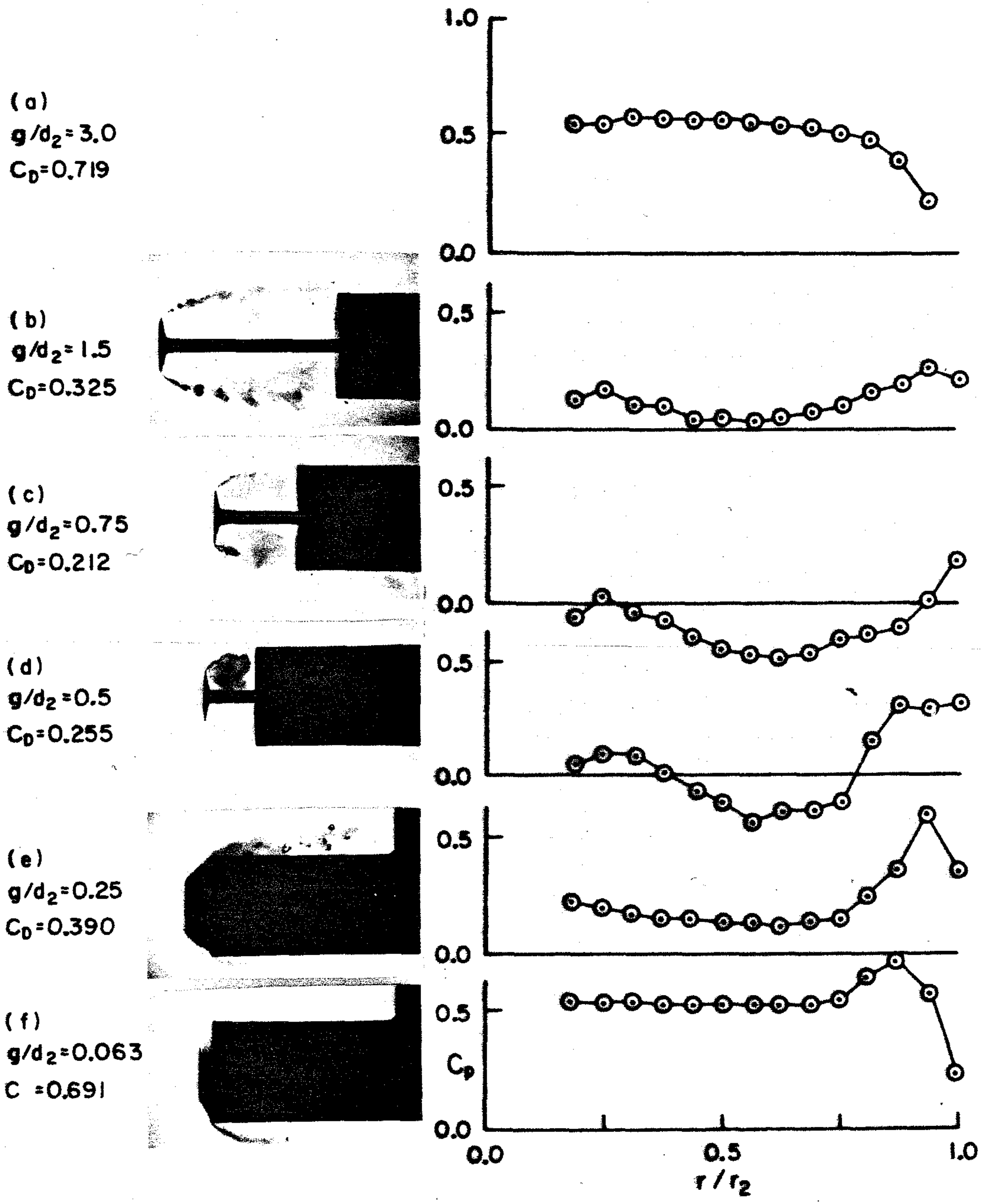

FIGURE 12 FACE PRESSURE DISTRIBUTION, $d_1/d_2=0.5$

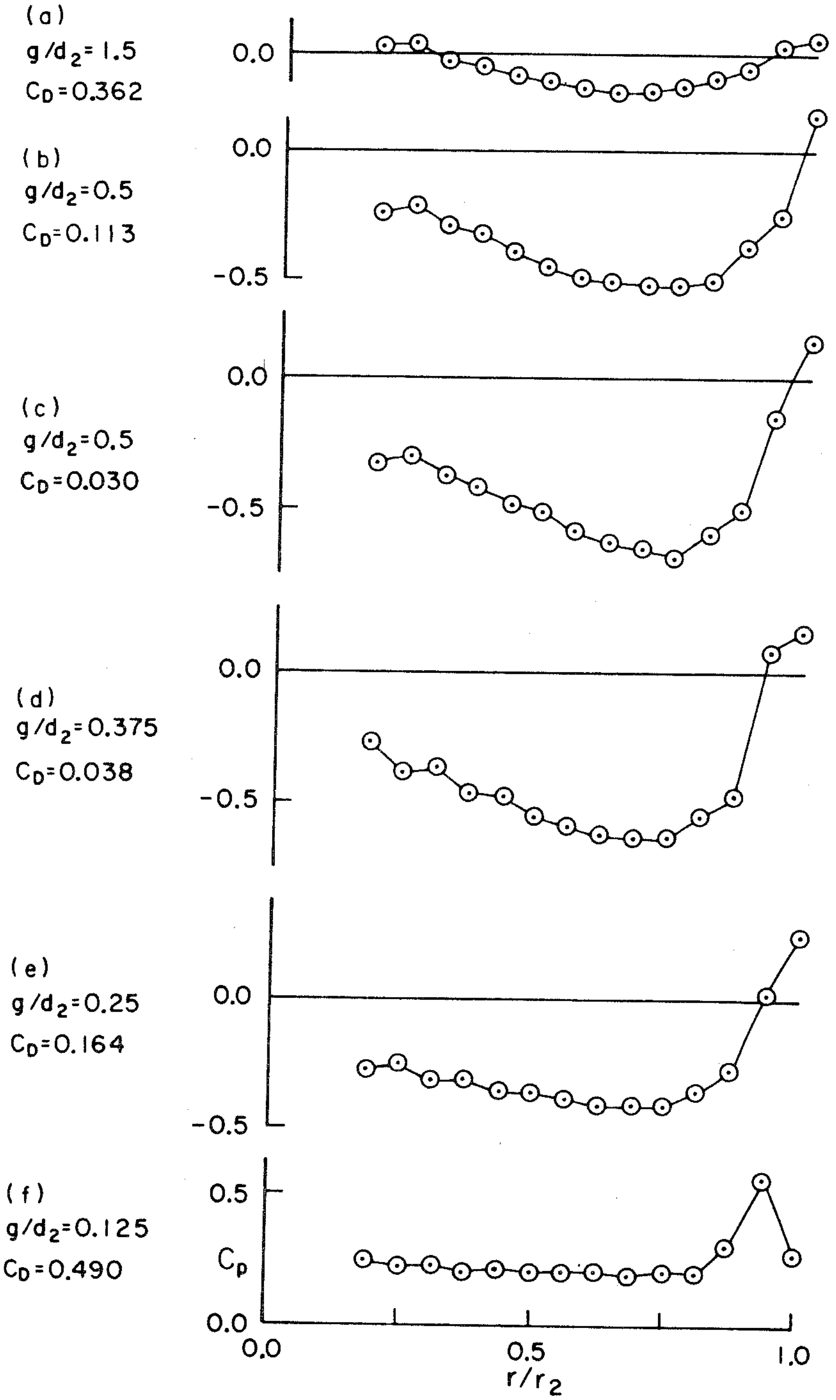

FIGURE 13 FACE PRESSURE DISTRIBUTION, $d_1/d_2=0.625$

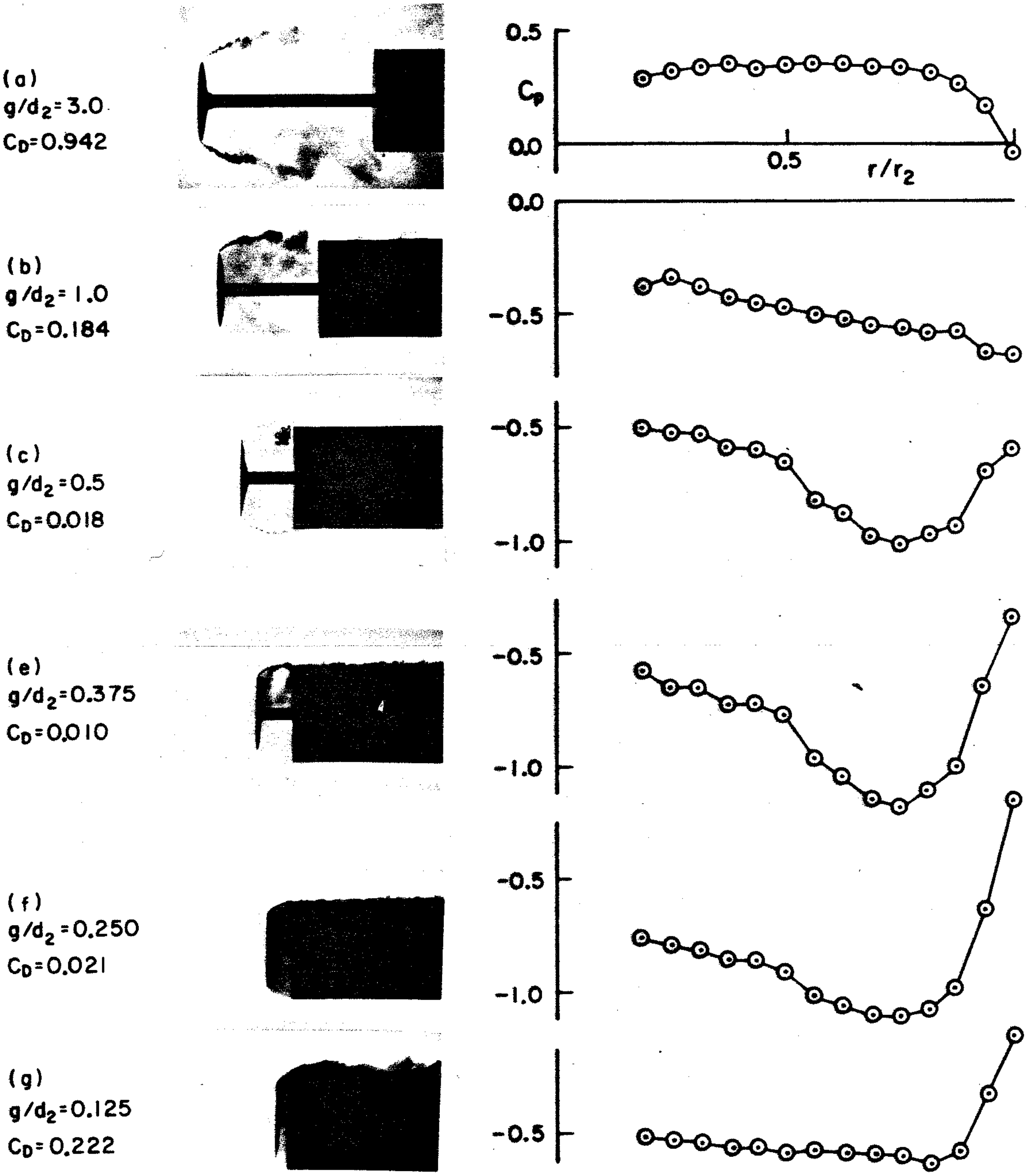

FIGURE 14 FACE PRESSURE DISTRIBUTION, $d_1/d_2=0.75$

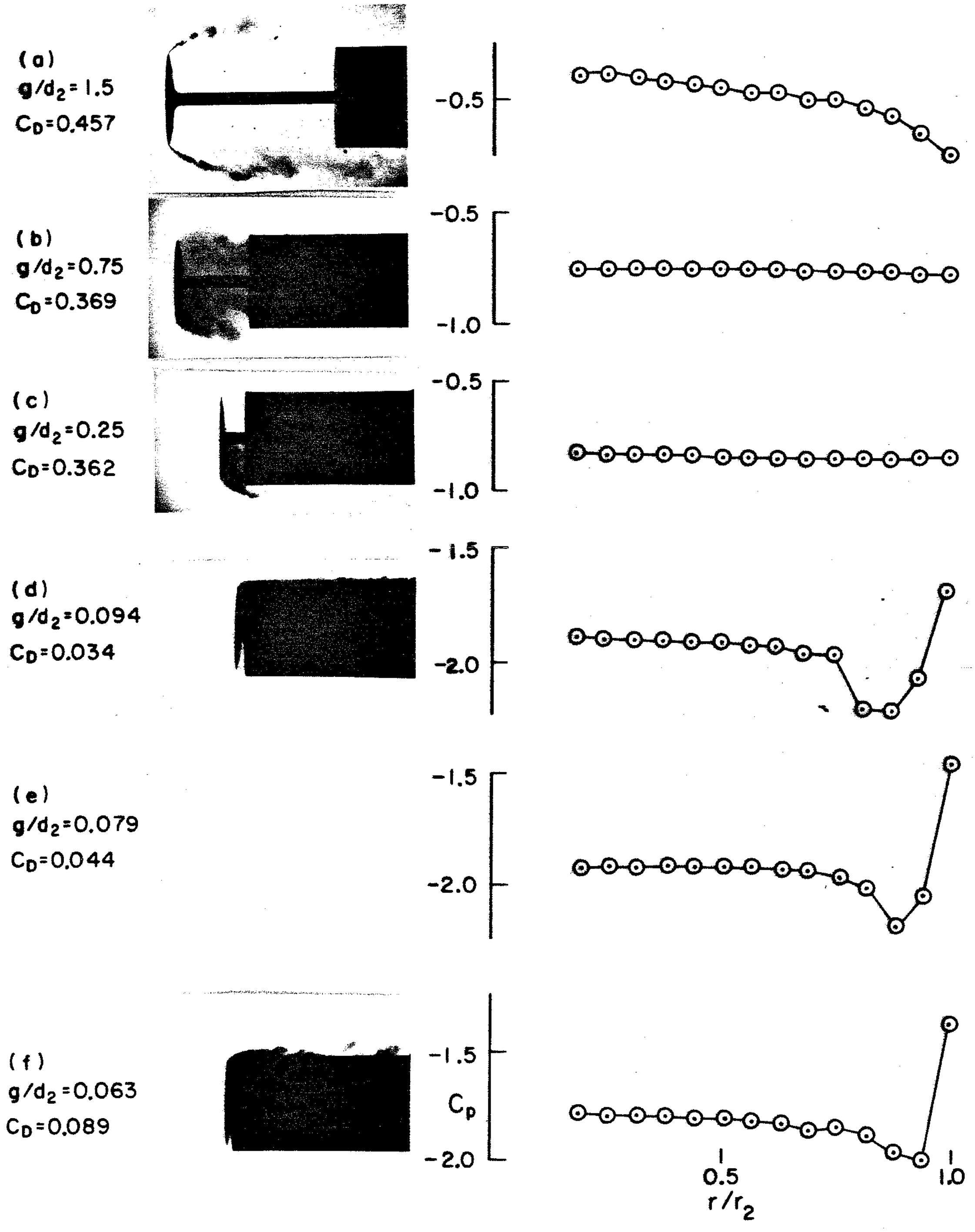

FIGURE 15 FACE PRESSURE DISTRIBUTION, $d_1/d_2=0.875$

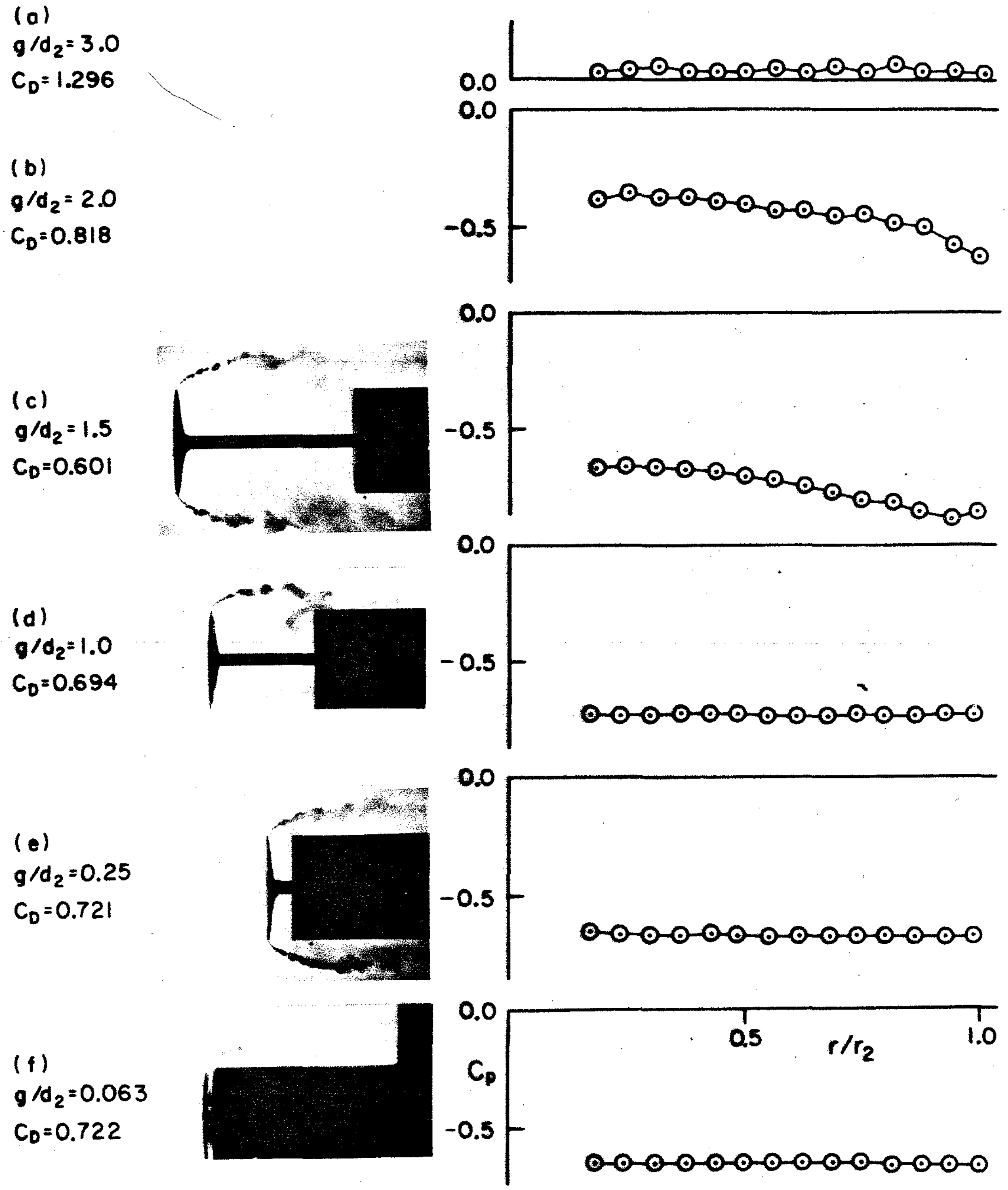

FIGURE 16 FACE PRESSURE DISTRIBUTION, d_1/d_2= 1.0

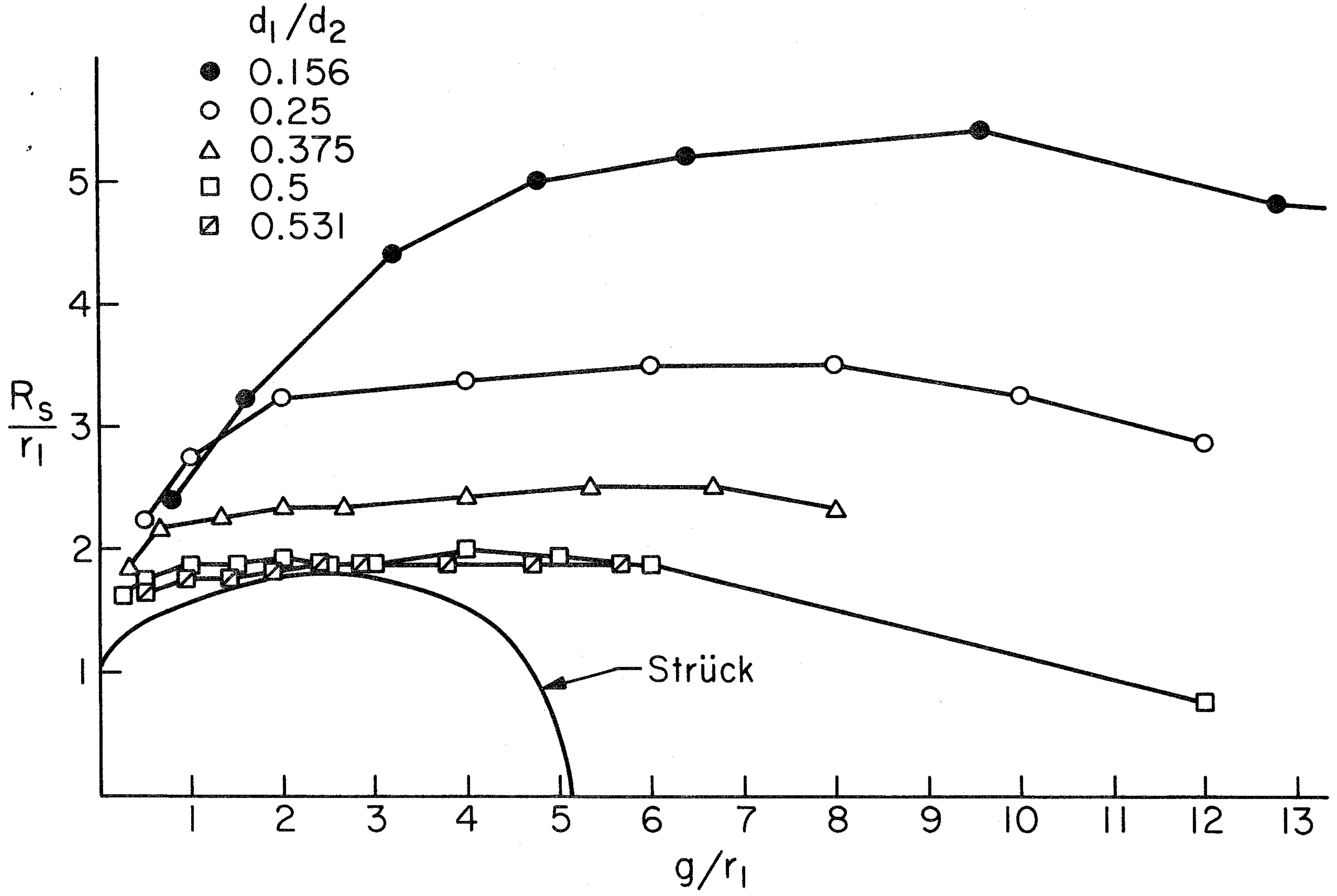

FIGURE 17 RADIAL LOCATION OF REARBODY FACE MAXIMUM PRESSURE

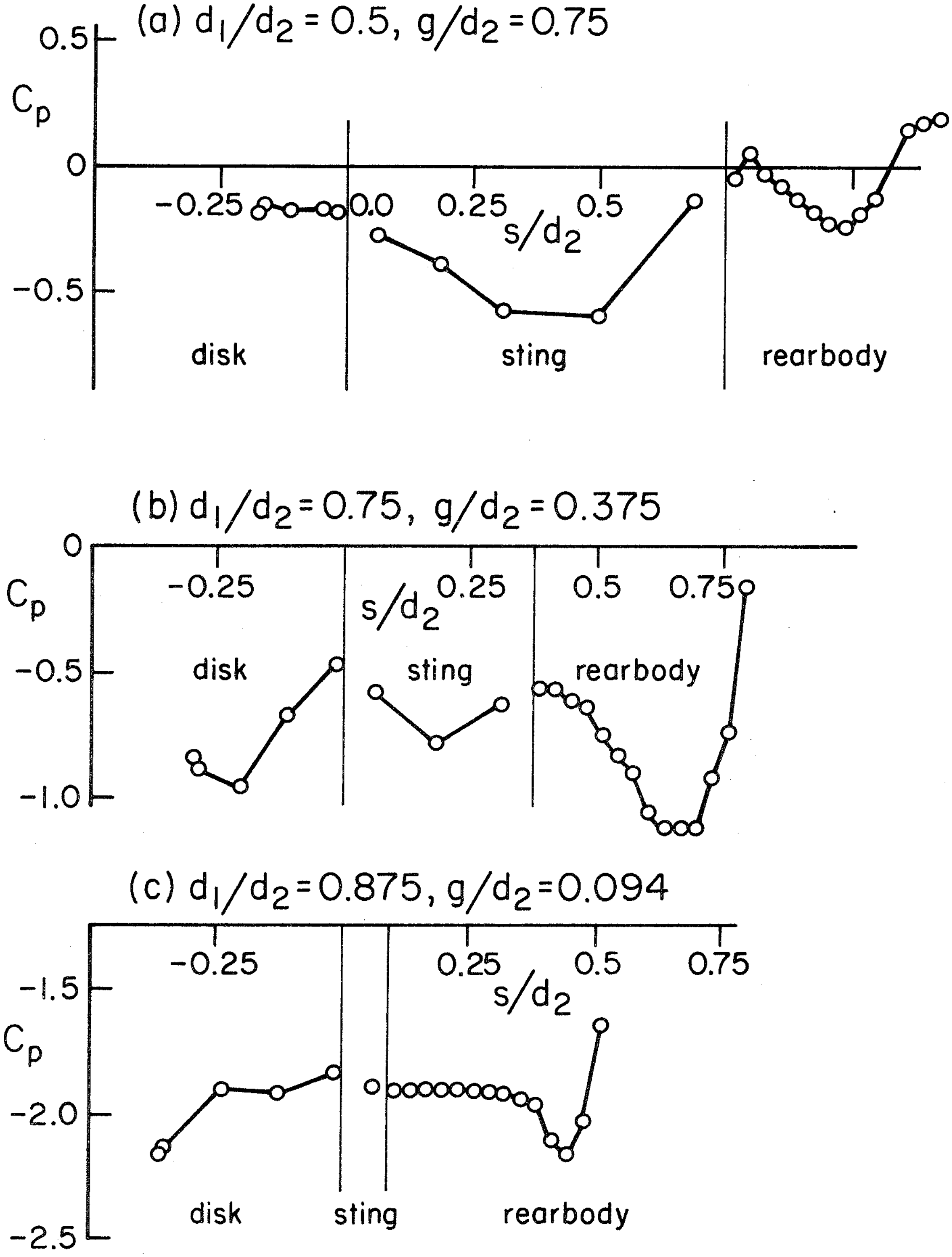

FIGURE 18 CAVITY WALL PRESSURE DISTRIBUTIONS

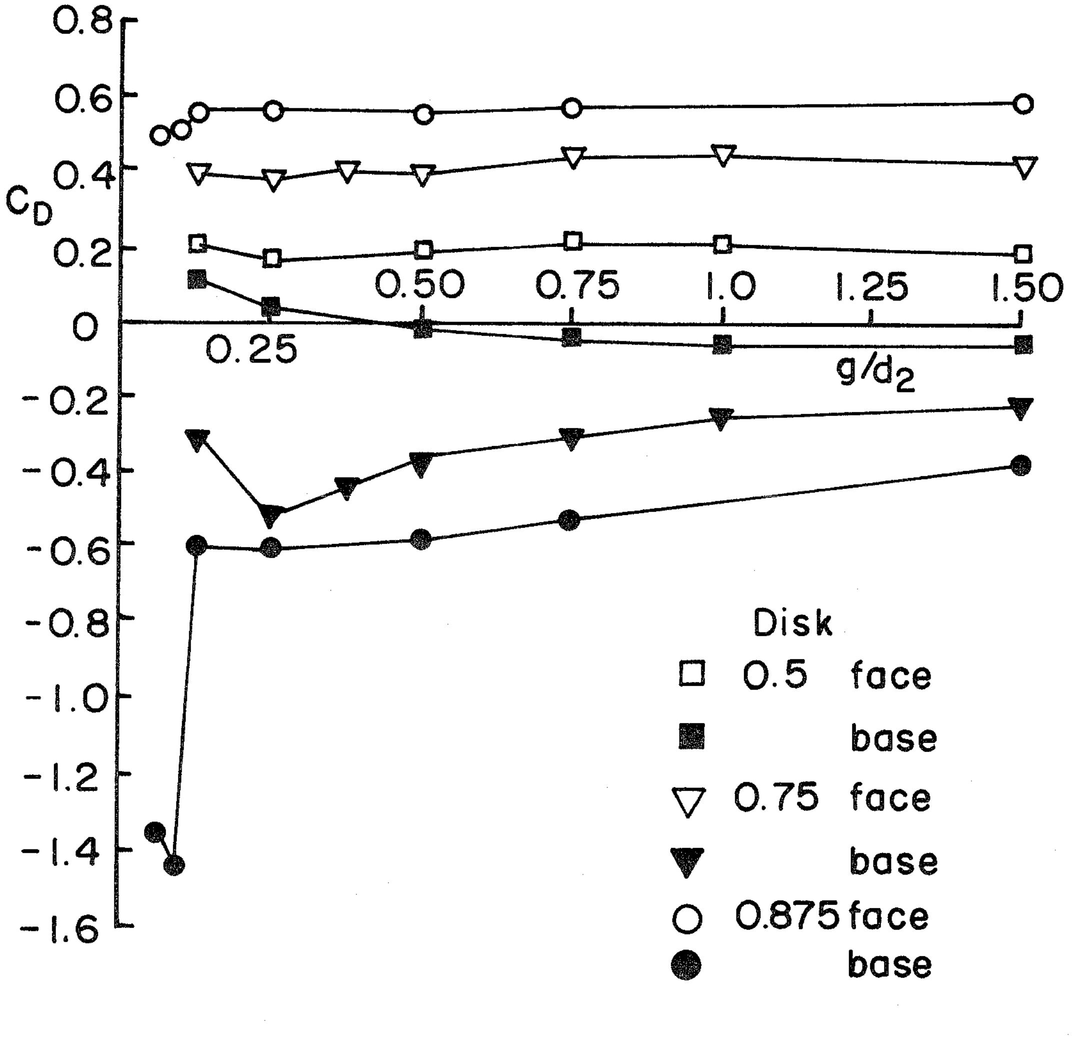

FIG. 19 DISK DRAG COEFFICIENT BREAKDOWN

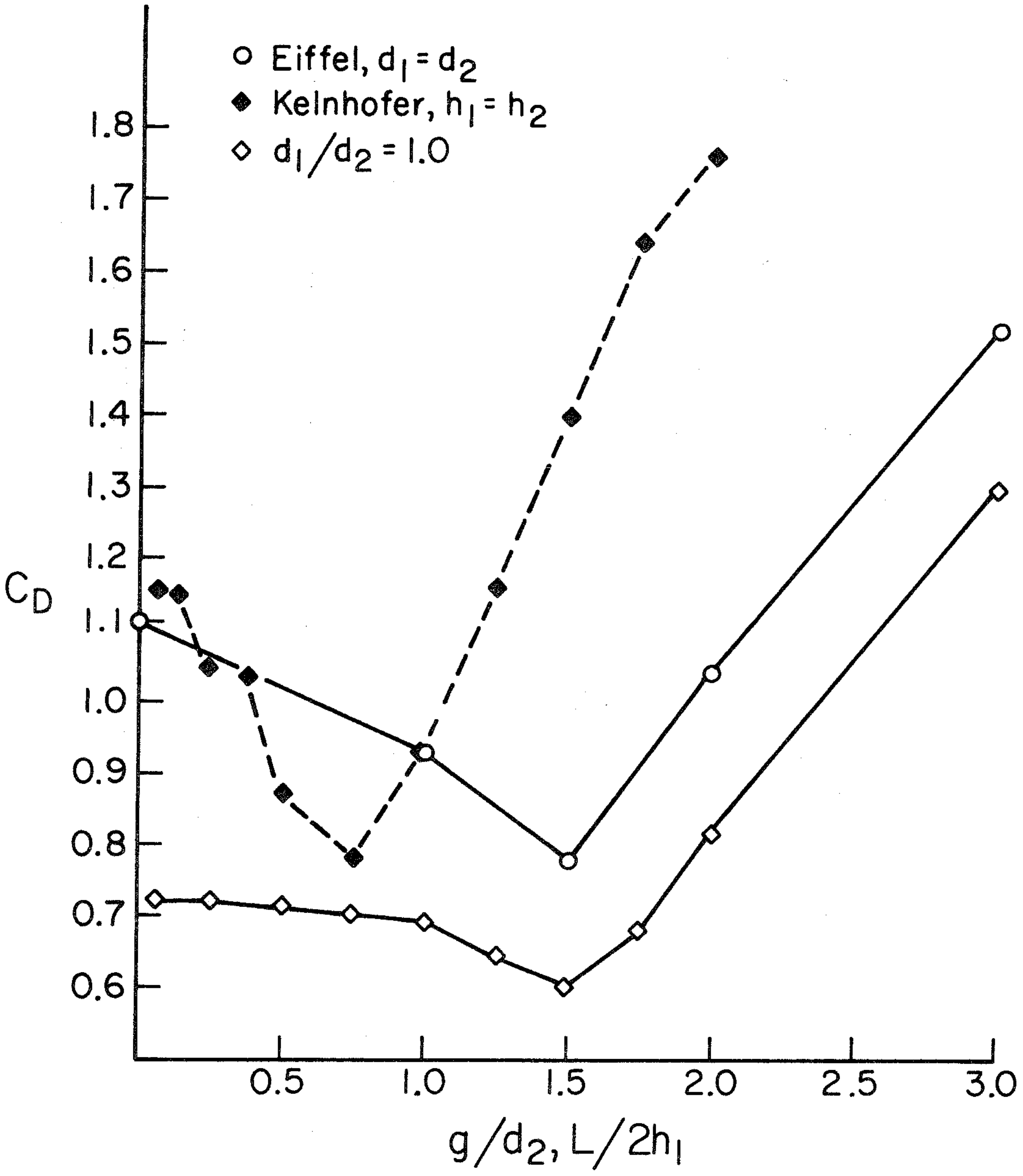

FIGURE 20 COMPARISON OF TANDEM BLUFF BODY DRAG FOR VARIOUS GEOMETRIES

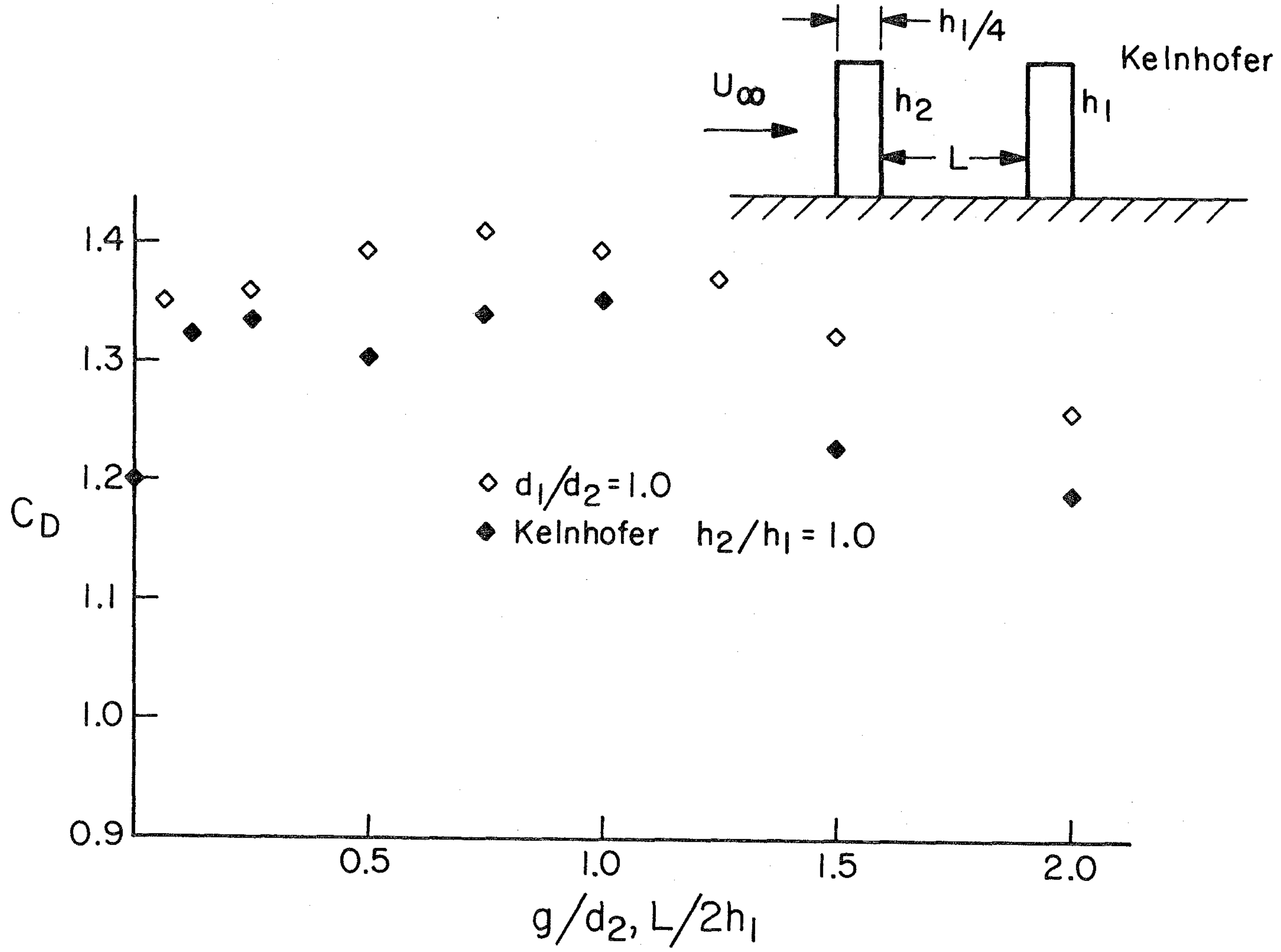

FIGURE 21 COMPARISON OF FRONTBODY DRAG, AXISYMMETRIC AND BUILDING SHAPED GEOMETRIES

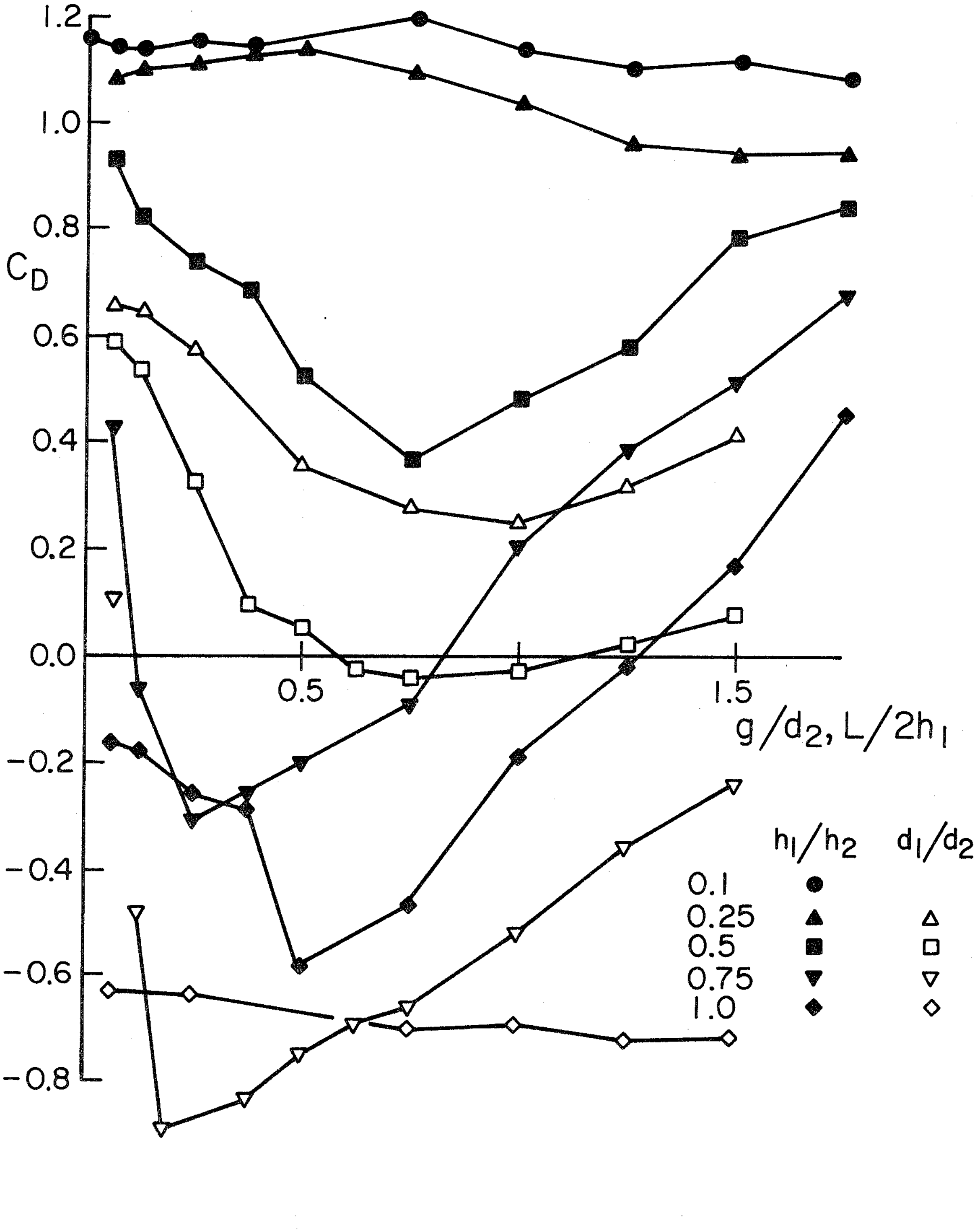

FIGURE 22 COMPARISON OF REARBODY DRAG, AXISYMMETRIC AND BUILDING SHAPED GEOMETRIES

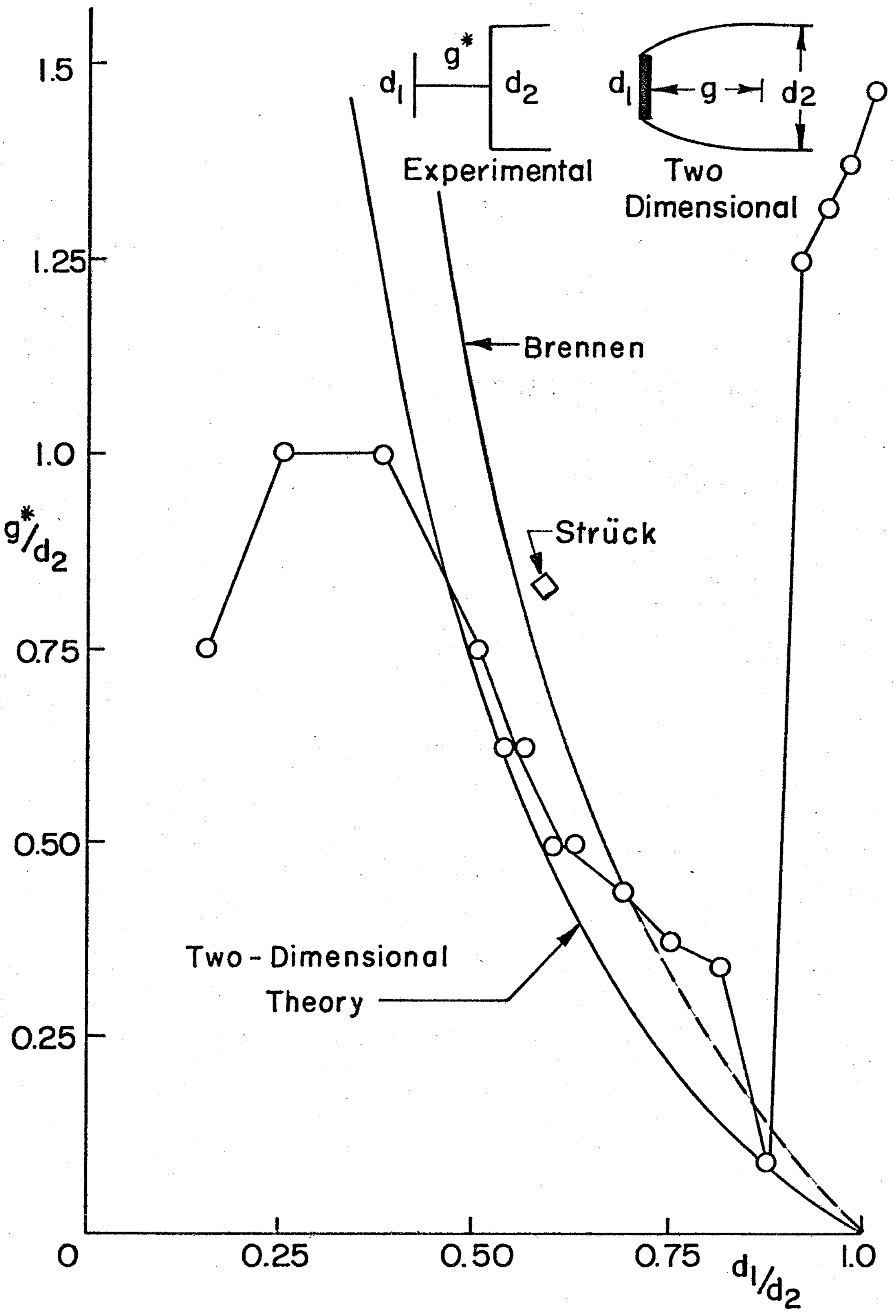

FIG. 23 OPTIMUM GAP

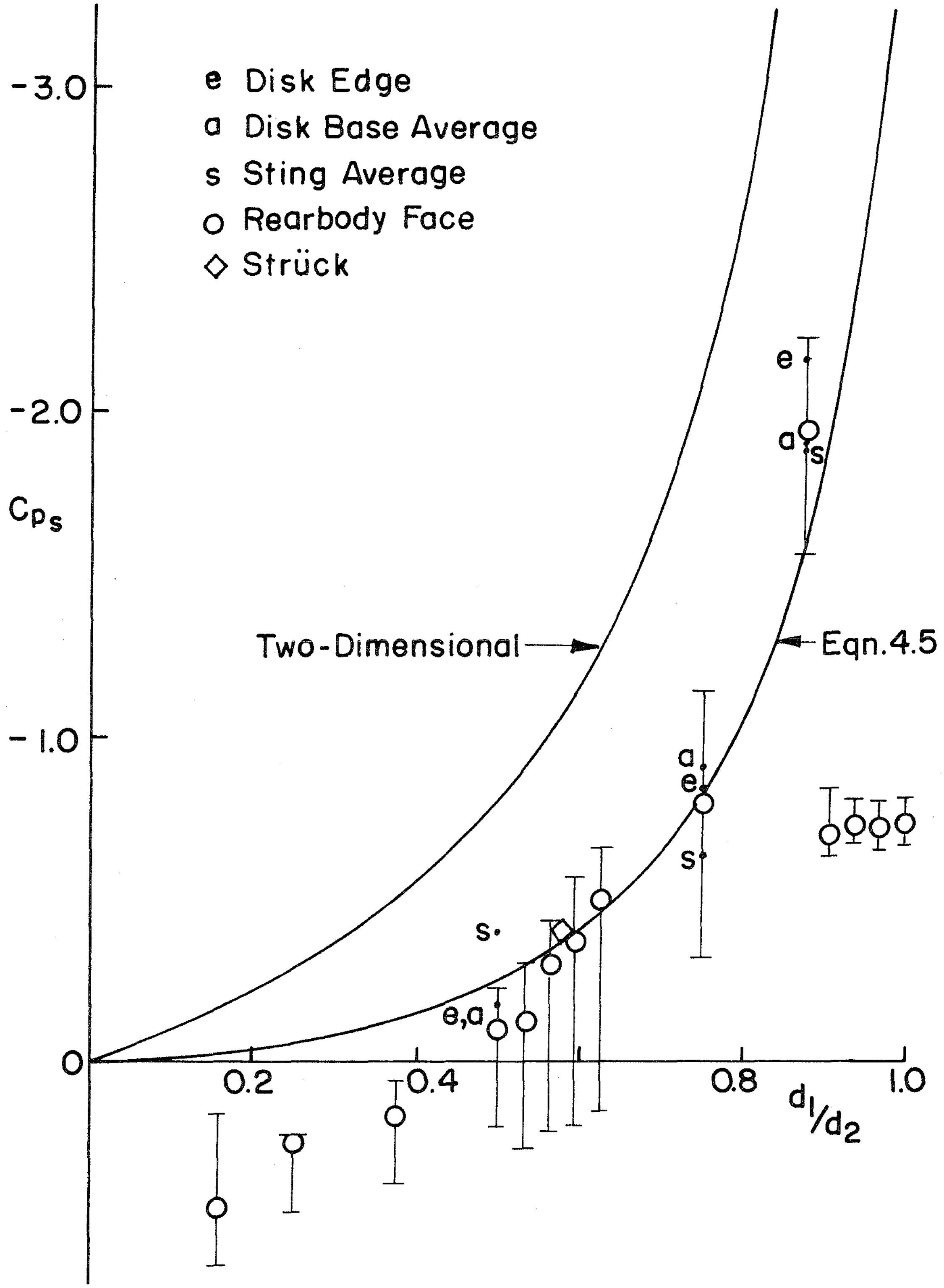

FIG. 24 OPTIMUM GAP PRESSURE

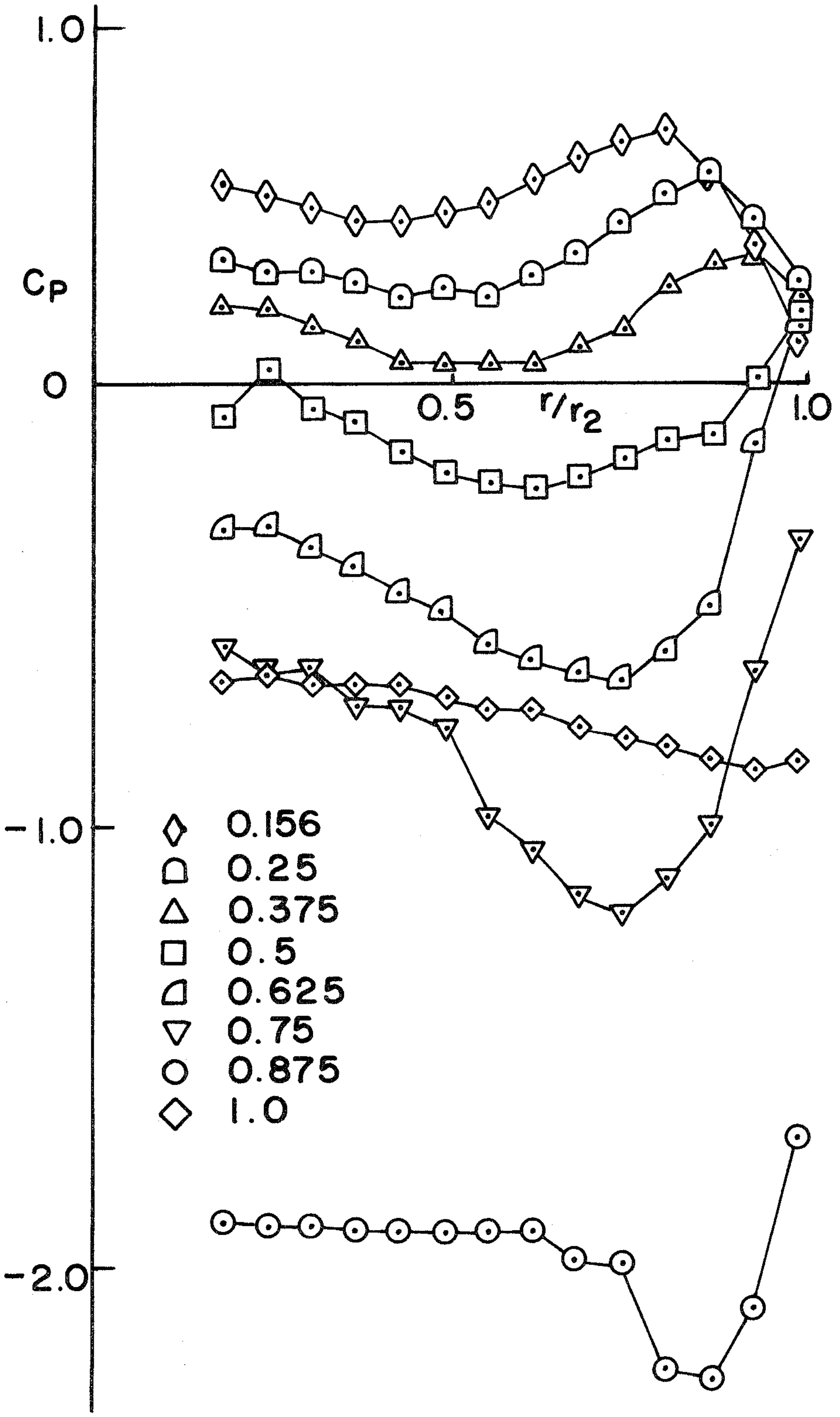

FIG. 25 FACE PRESSURE DISTRIBUTIONS AT OPTIMUM GAP

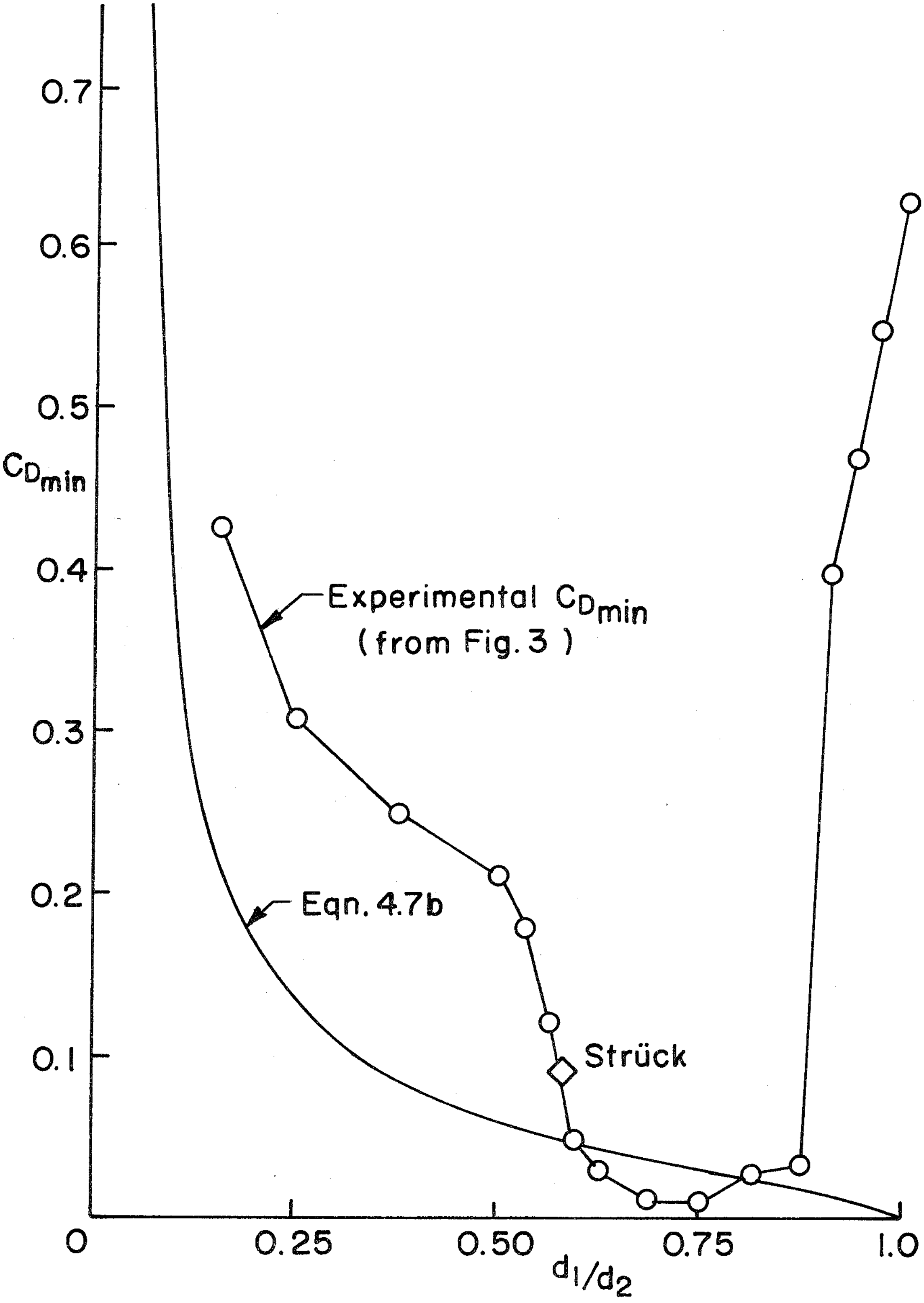

FIG. 26 COMPARISON OF $C_{D_{min}}$ AND AXISYMMETRIC CAVITY MOMENTUM BALANCE

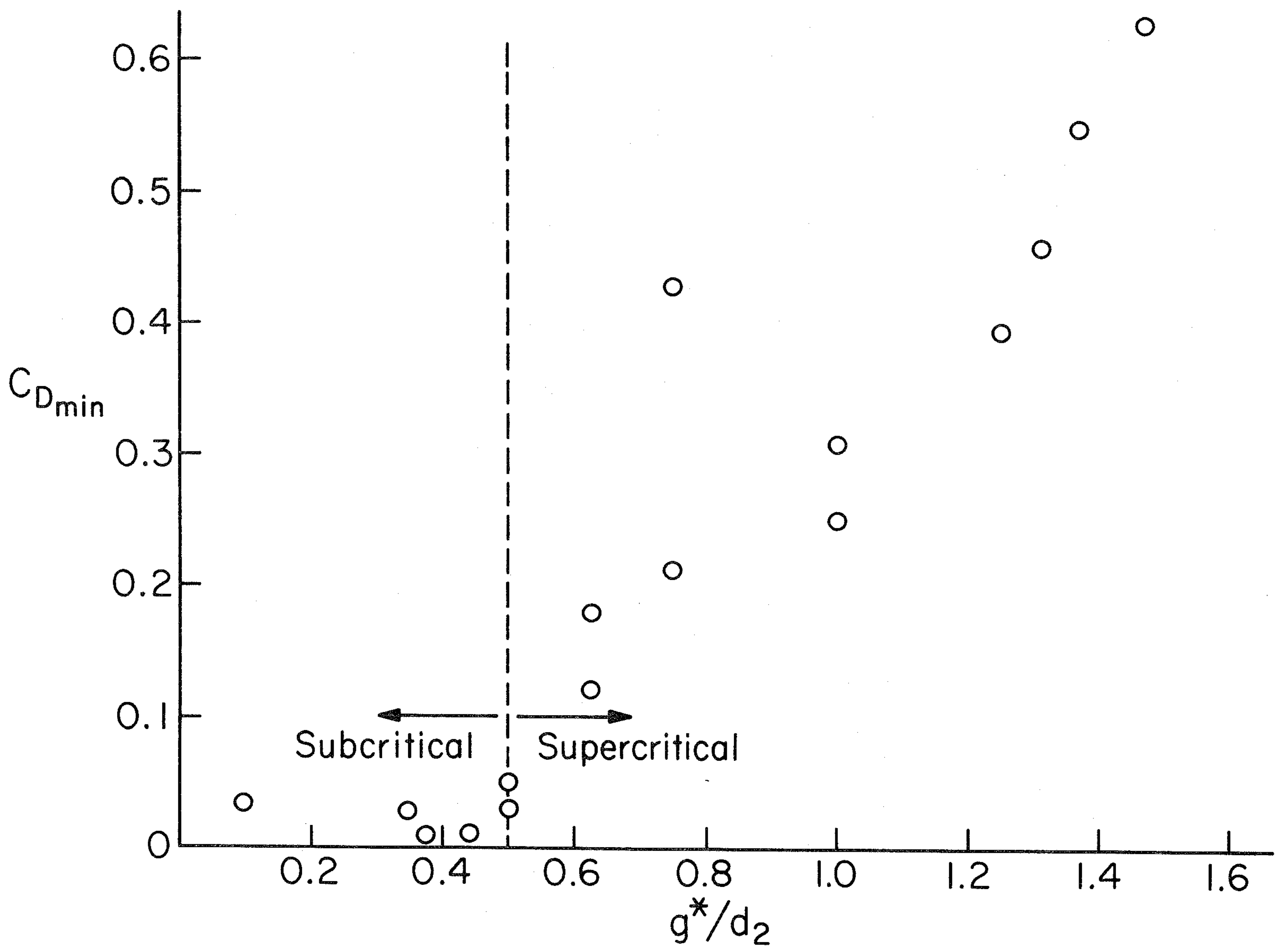

FIGURE 27 DRAG AT OPTIMUM GAP

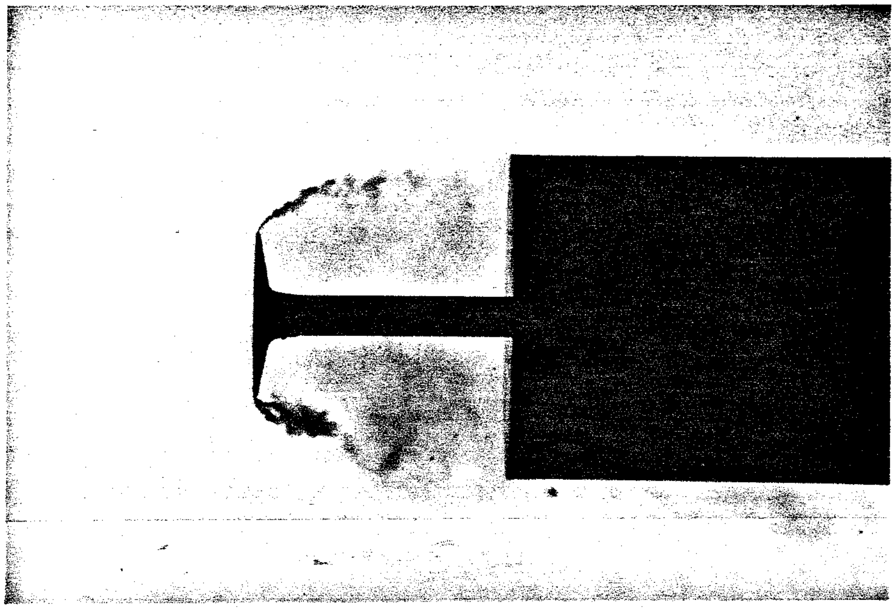

a) Supercritical, $d_1/d_2 = 0.5$, $g/d_2 = 0.75$, $C_D = 0.212$

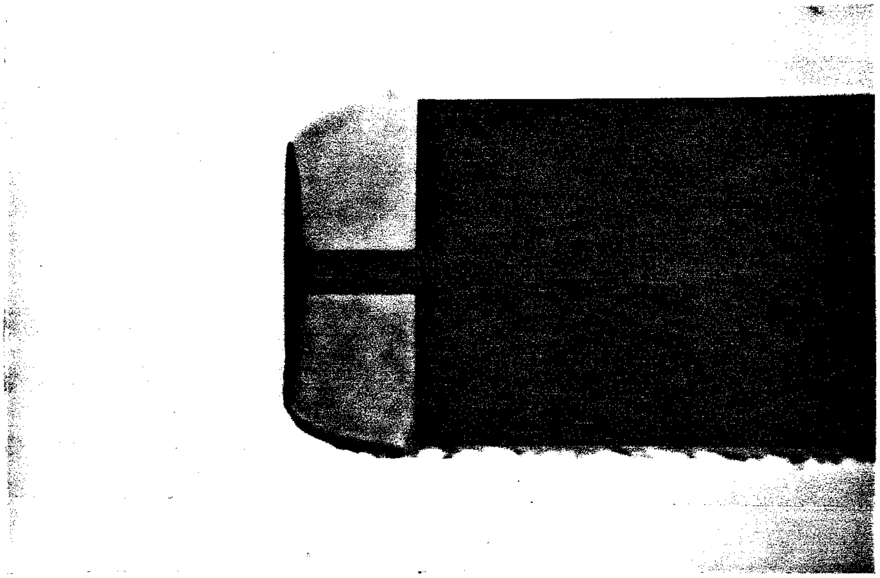

b) Subcritical, $d_1/d_2 = 0.75$, $g/d_2 = 0.375$, $C_D = 0.010$

FIG. 28 COMPARISON OF SUPERCRITICAL & SUBCRITICAL FLOWS

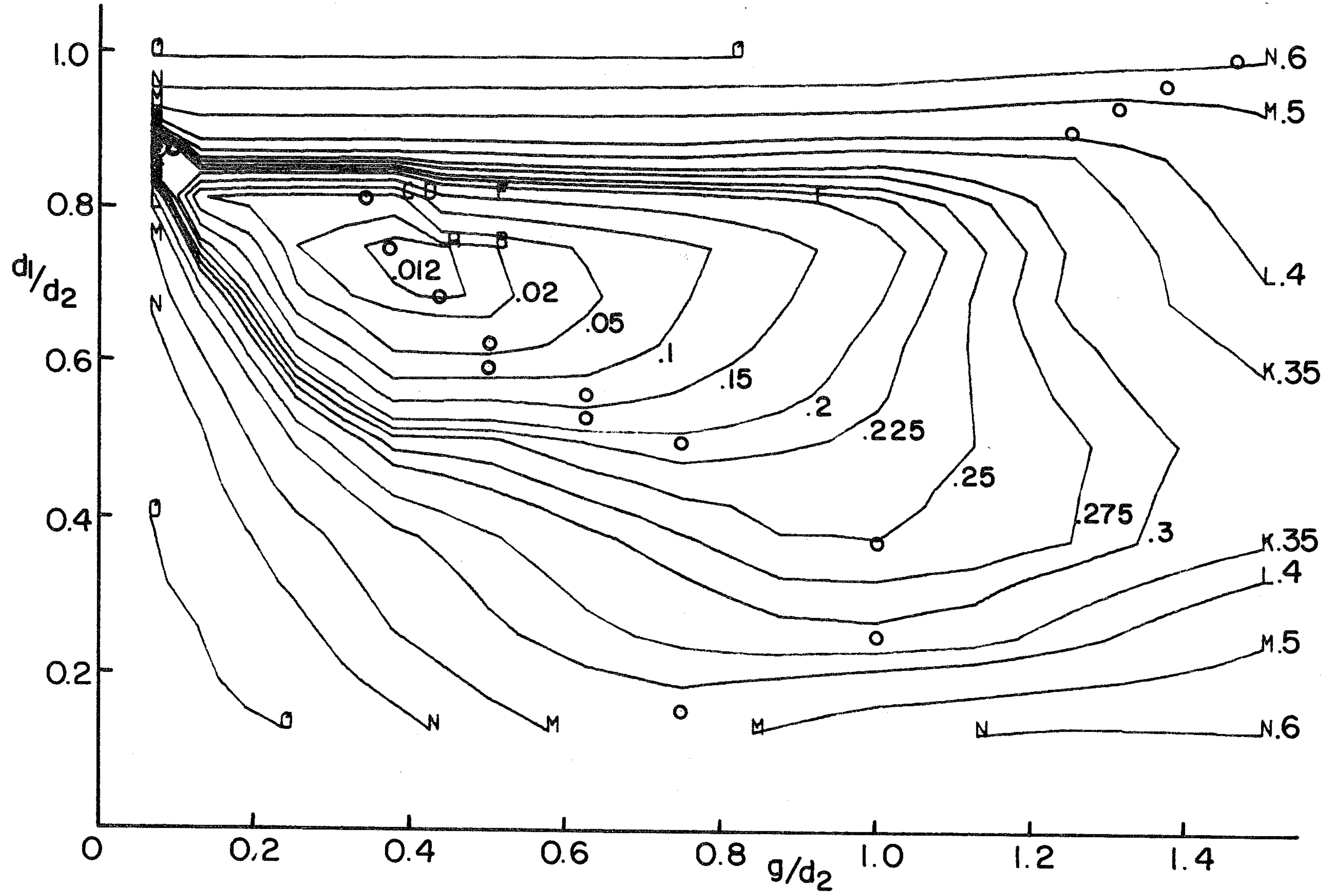

FIG. 29 CONTOURS OF CONSTANT FOREBODY DRAG

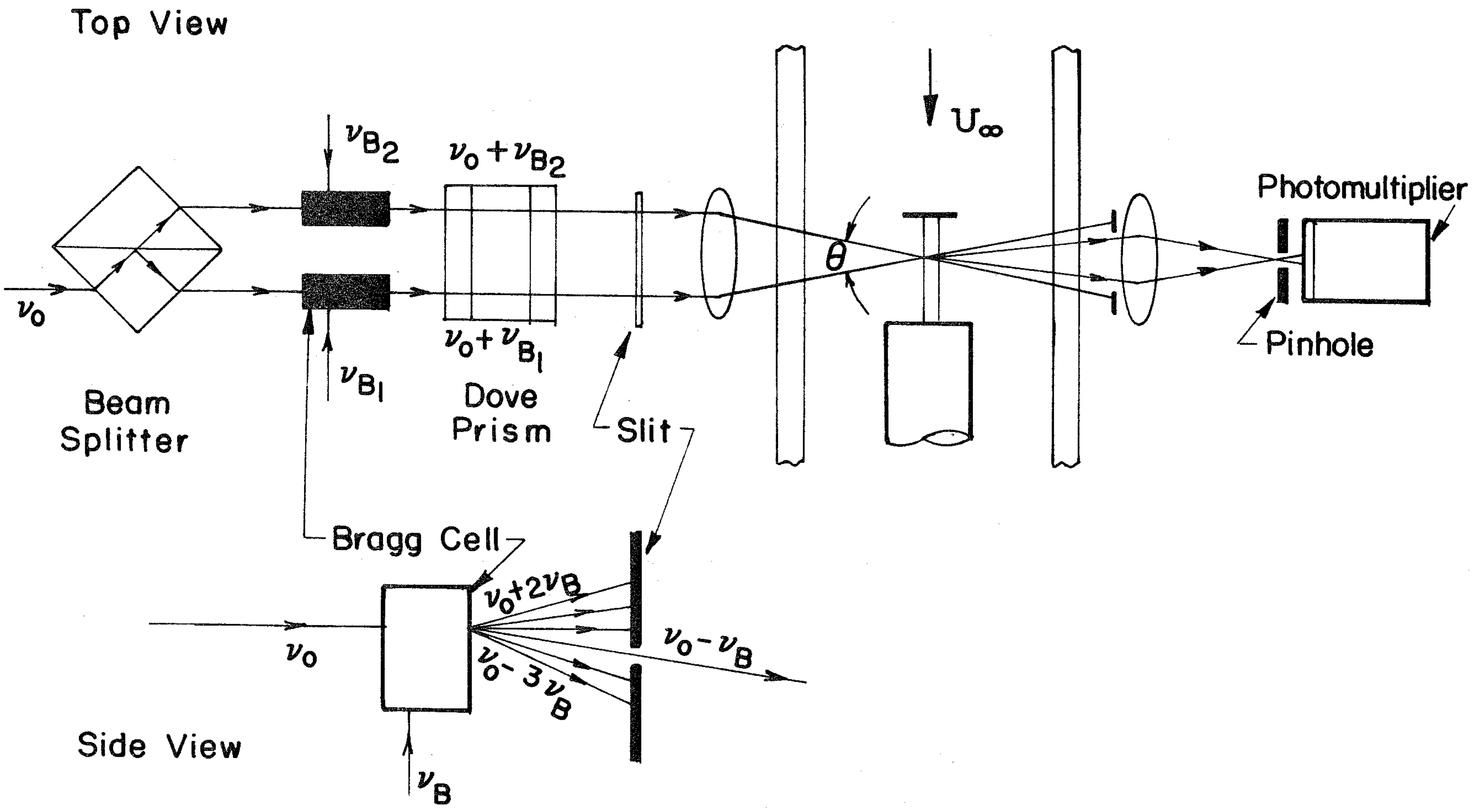

FIG. 30 LASER DOPPLER VELOCIMETER OPTICAL ARRANGEMENT

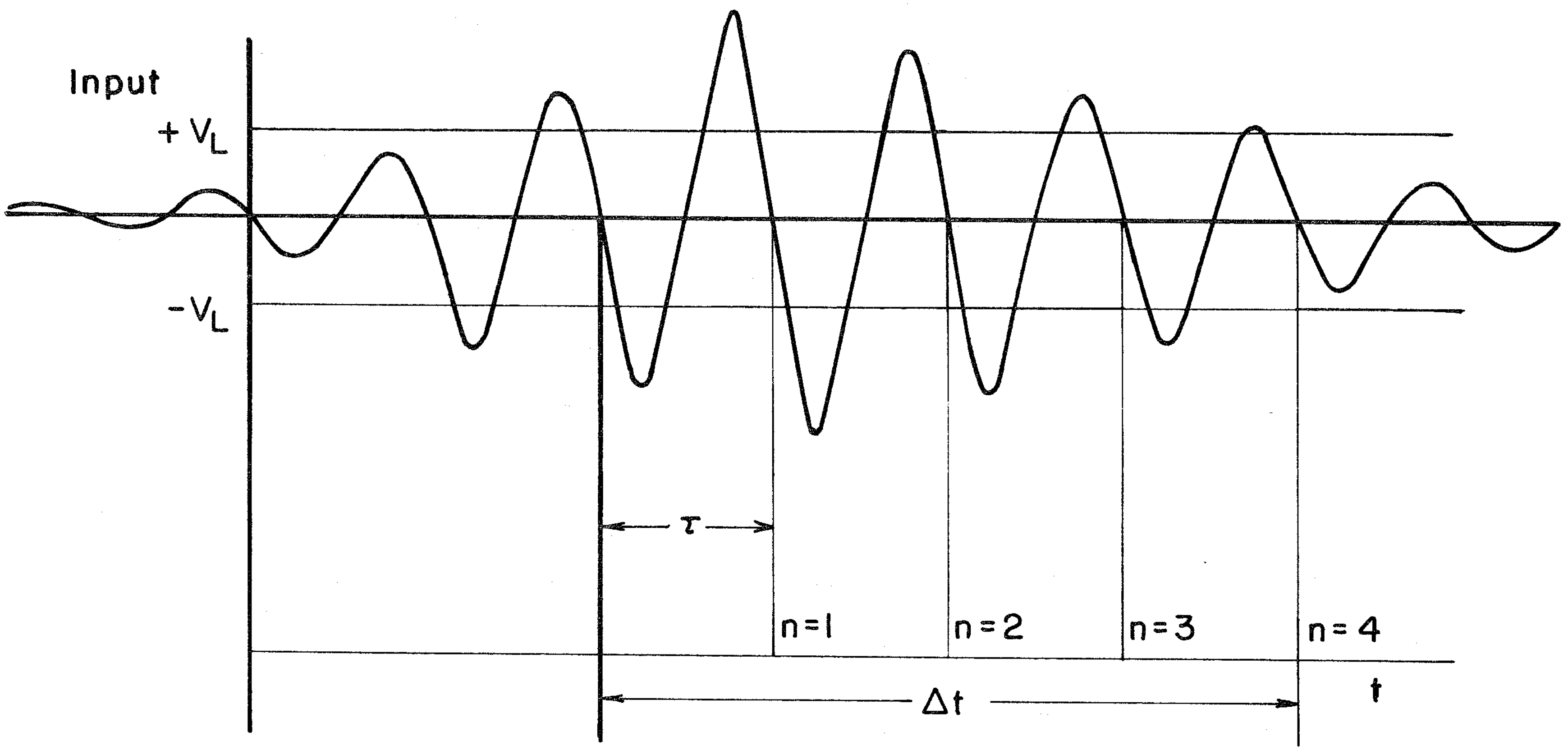

FIG. 31 PARTICLE BURST WAVEFORM

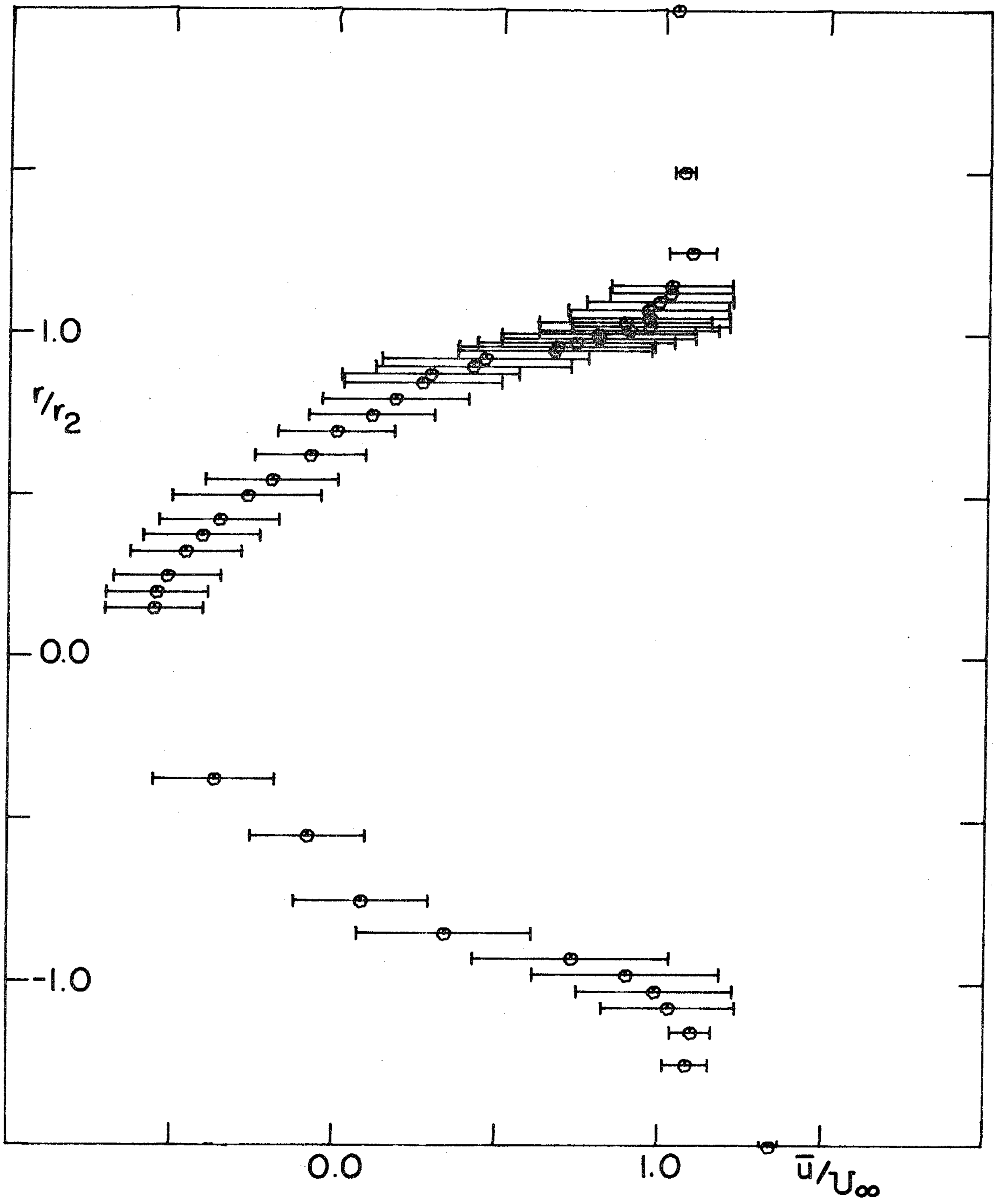

FIG. 32 STREAMWISE VELOCITY PROFILE $d_1/d_2 = 0.5$, $g/d_2 = 0.75$, $x/g = 0.67$

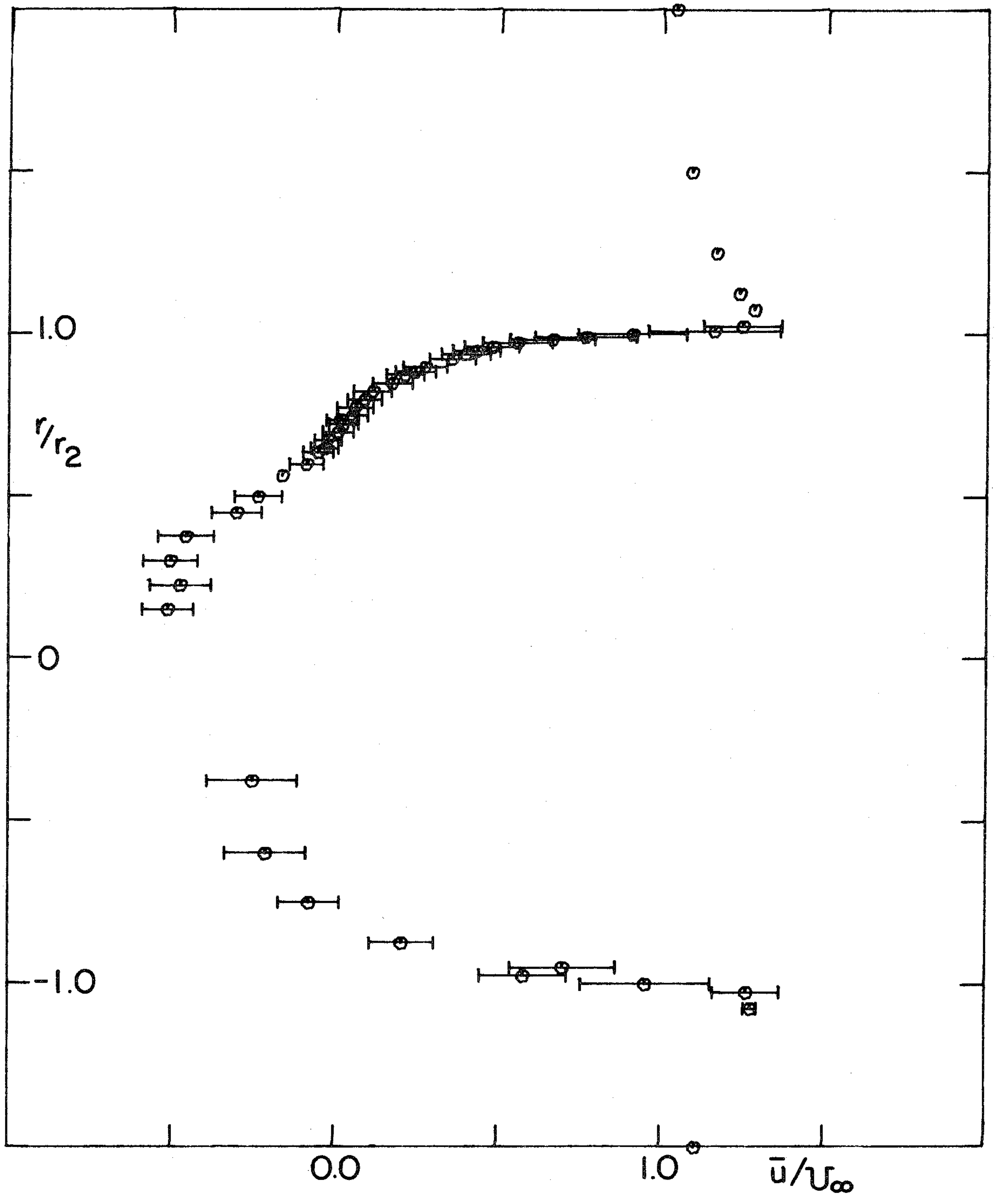

FIG. 33 STREAMWISE VELOCITY PROFILE $d_1/d_2 = 0.75$, $g/d_2 = 0.375$, $x/g = 0.5$

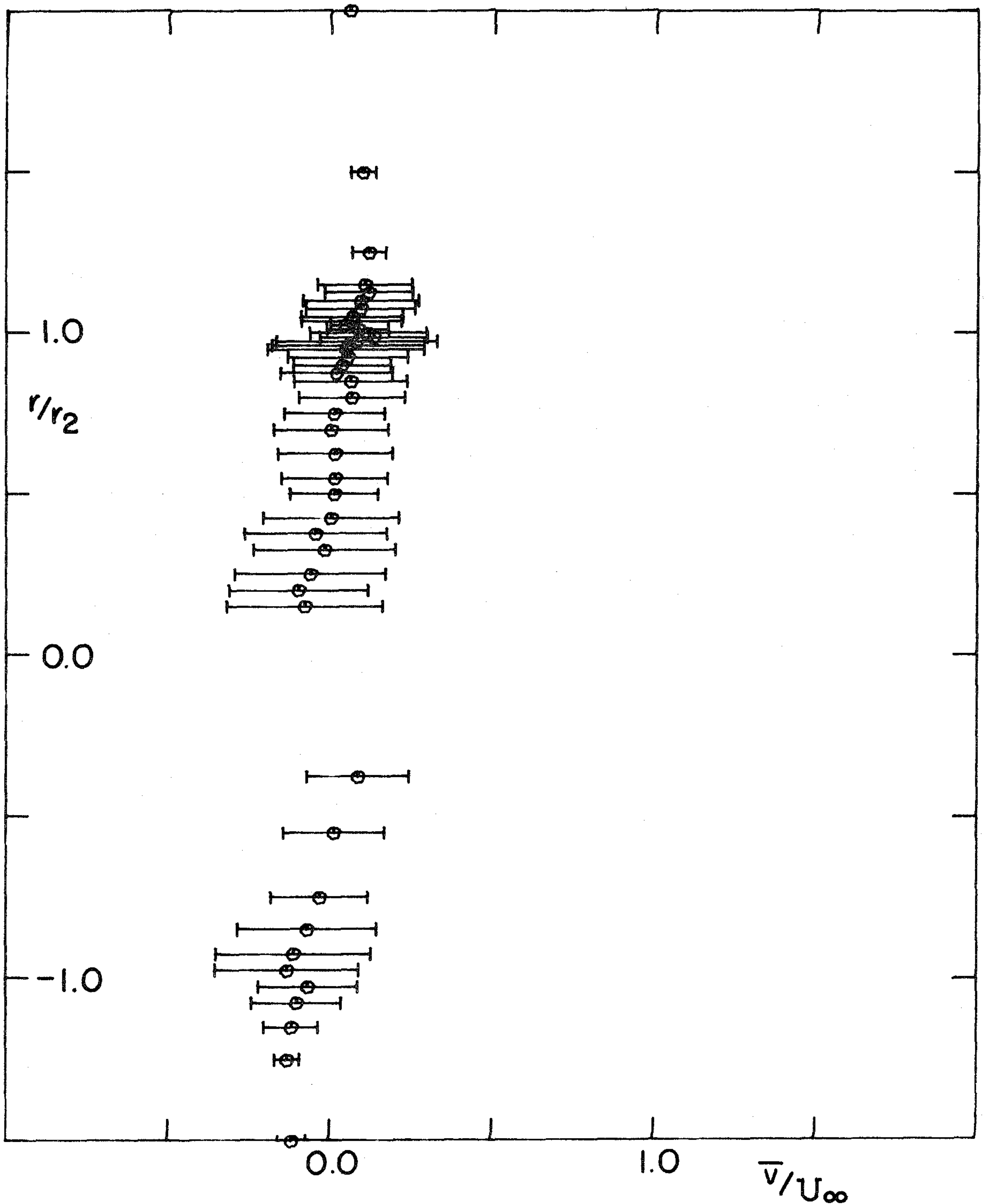

FIG. 34 RADIAL VELOCITY PROFILE $d_1/d_2 = 0.5$, $g/d_2 = 0.75$, $x/g = 0.67$

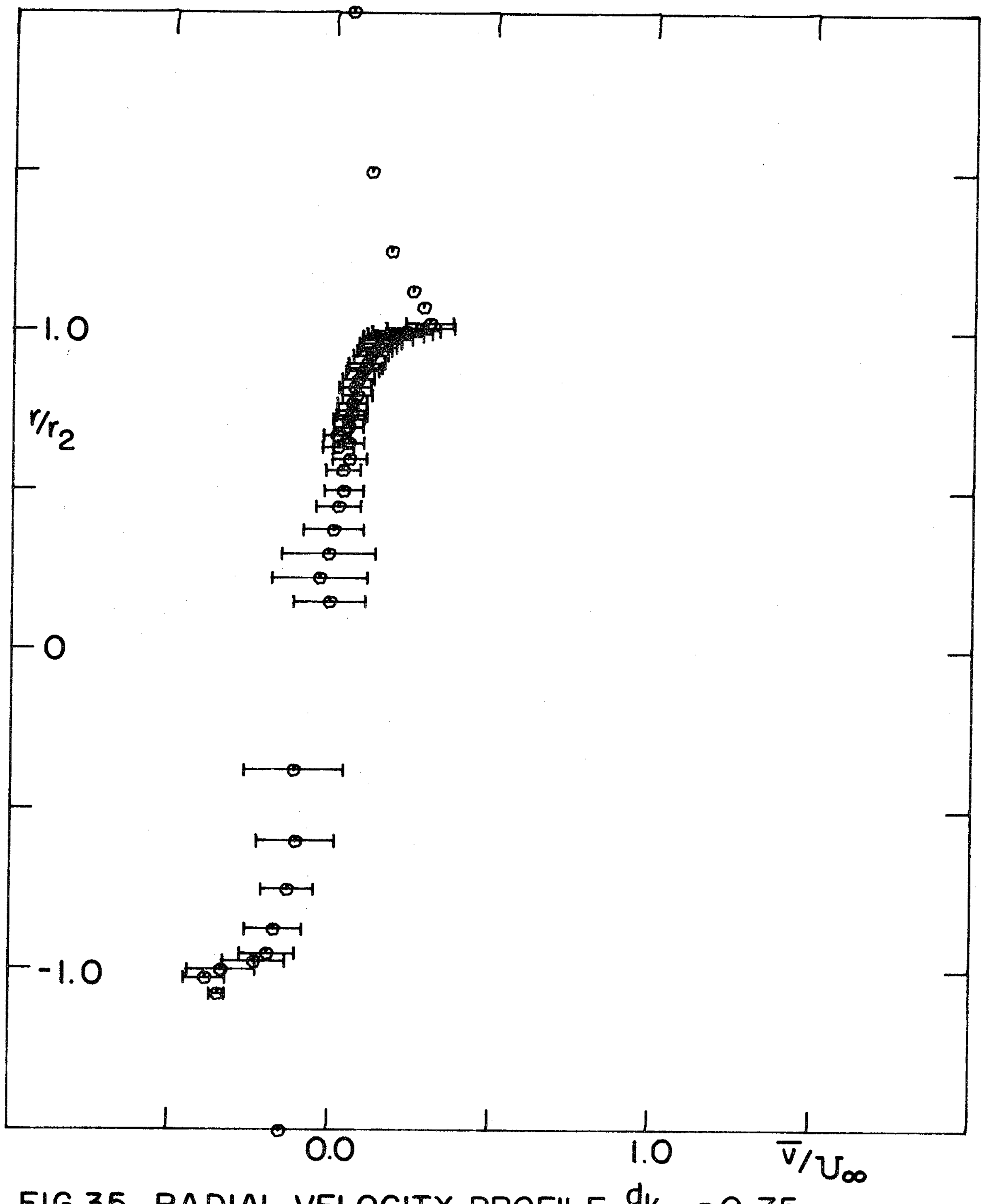

FIG.35 RADIAL VELOCITY PROFILE $d_1/d_2 = 0.75$, $g/d_2 = 0.375$, $x/g = 0.5$

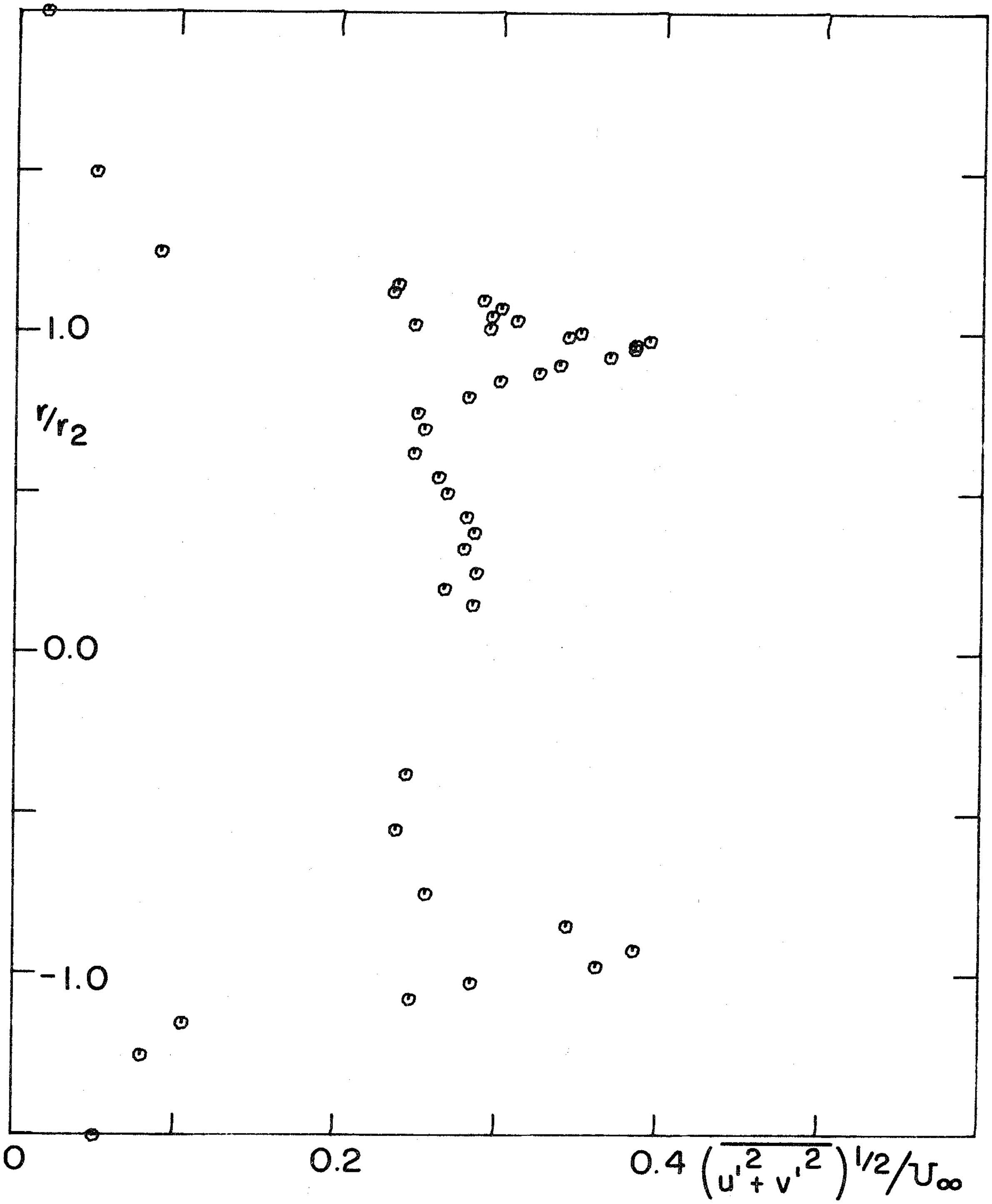

FIG. 36 TURBULENCE INTENSITY PROFILE $d_1/d_2 = 0.5$, $g/d_2 = 0.75$, $x/g = 0.67$

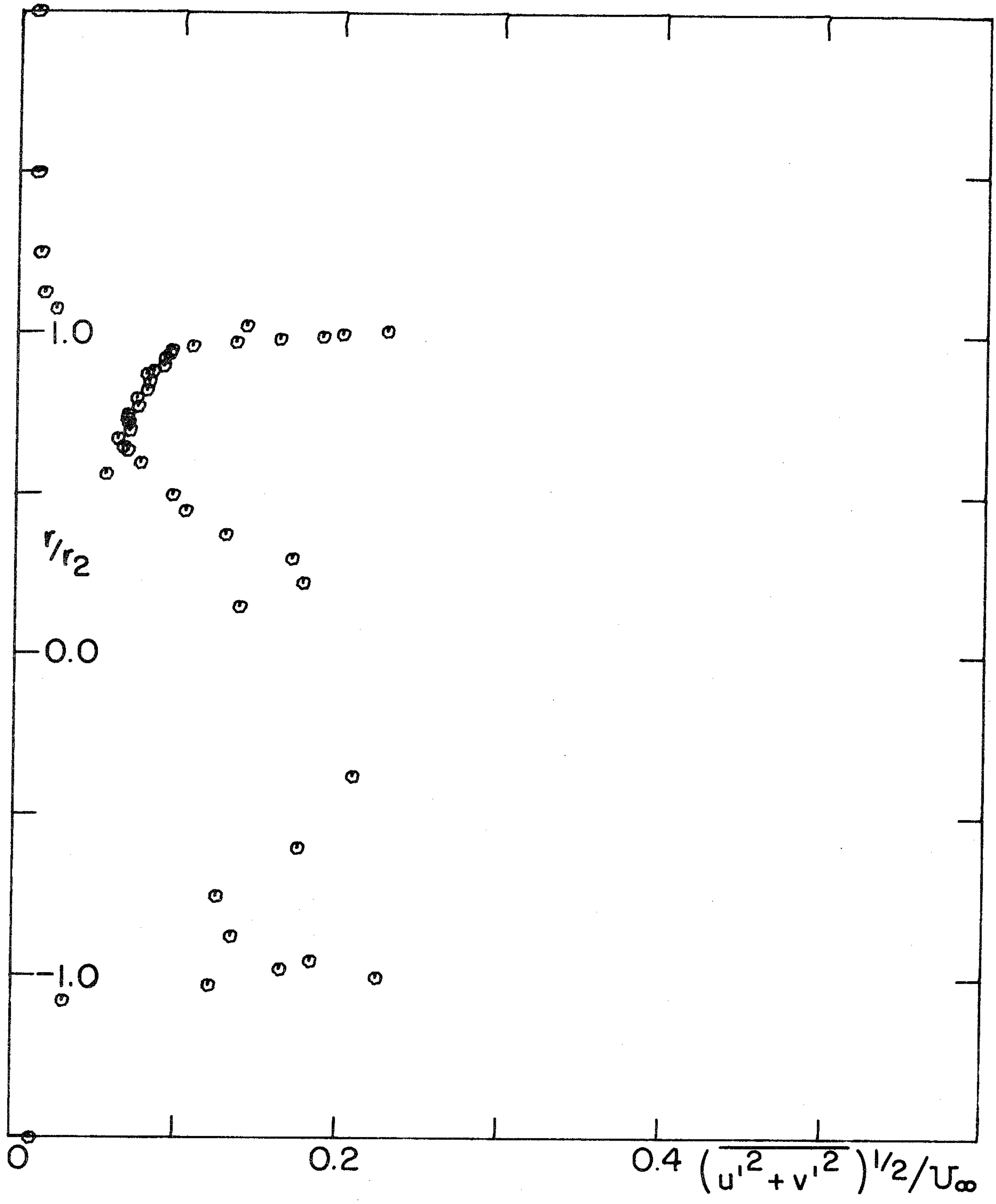

FIG. 37 TURBULENCE INTENSITY PROFILE $d_1/d_2 = 0.75$
$g/d_2 = 0.375$, $x/g = 0.5$

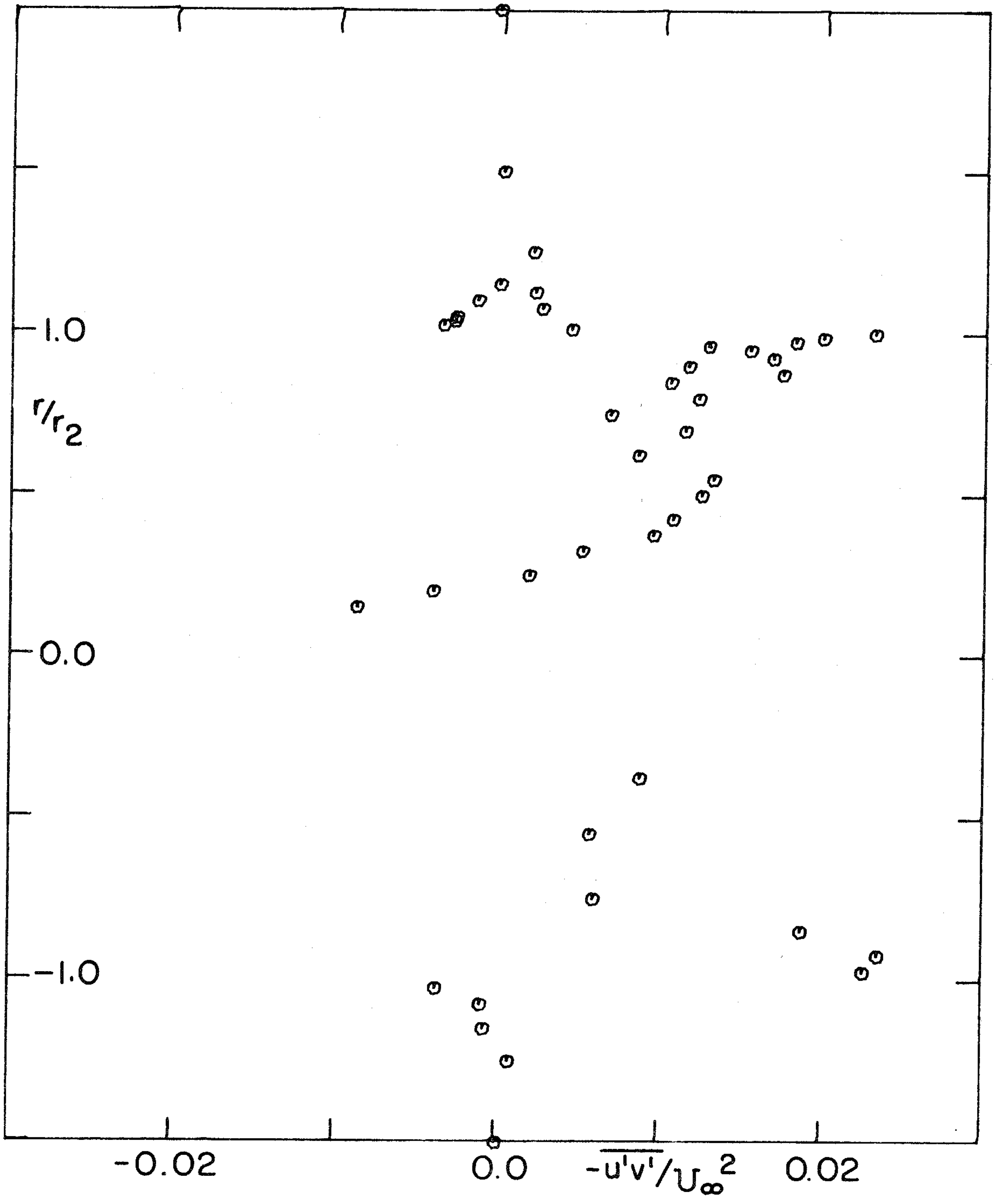

FIG. 38 REYNOLDS STRESS PROFILE $d_1/d_2 = 0.5$, $g/d_2 = 0.75$, $x/g = 0.67$

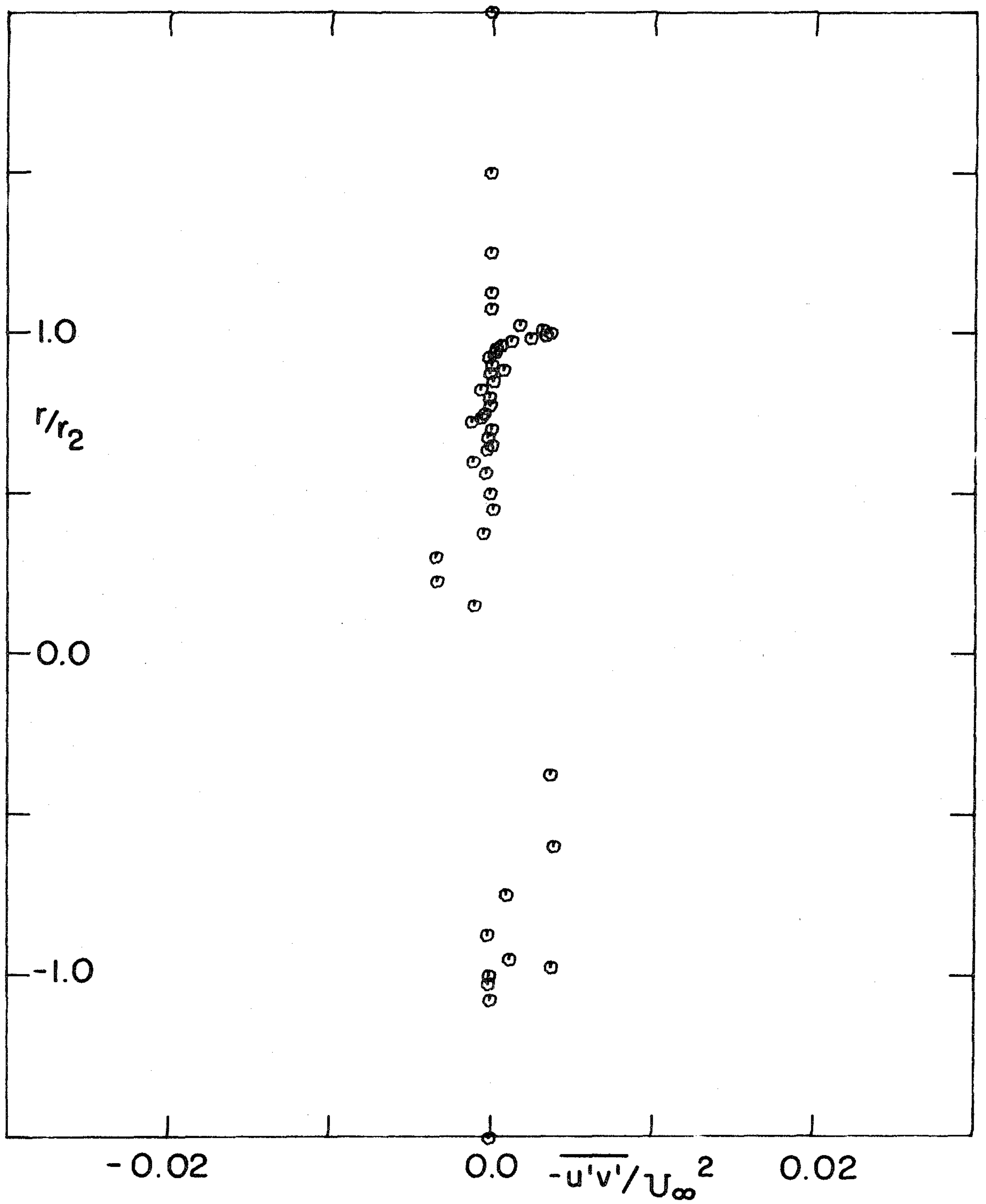

FIG. 39 REYNOLDS STRESS PROFILE $d_1/d_2 = 0.75$, $g/d_2 = 0.375$, $x/g = 0.5$

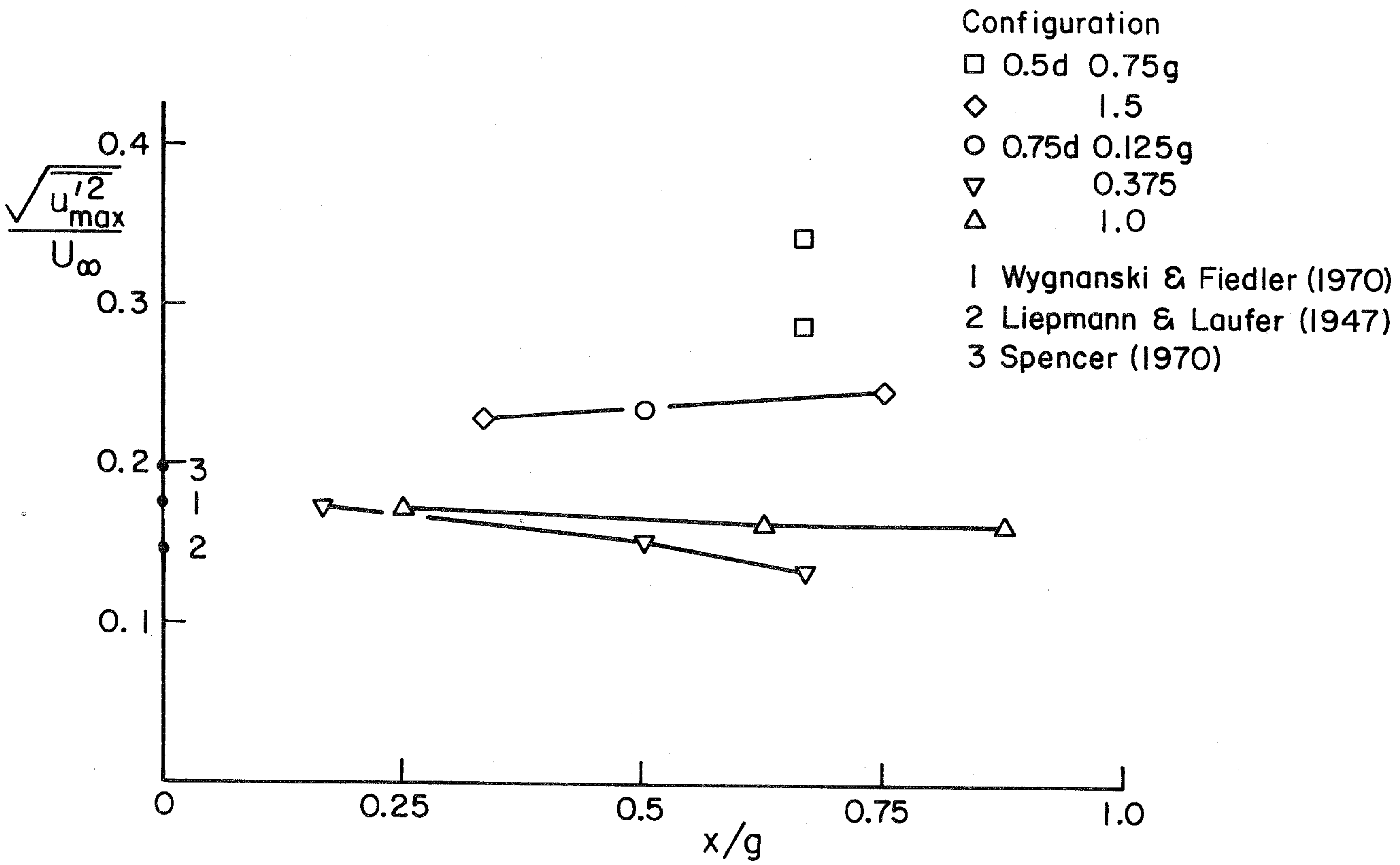

FIGURE 40 MAXIMUM STREAMWISE VELOCITY FLUCTUATIONS

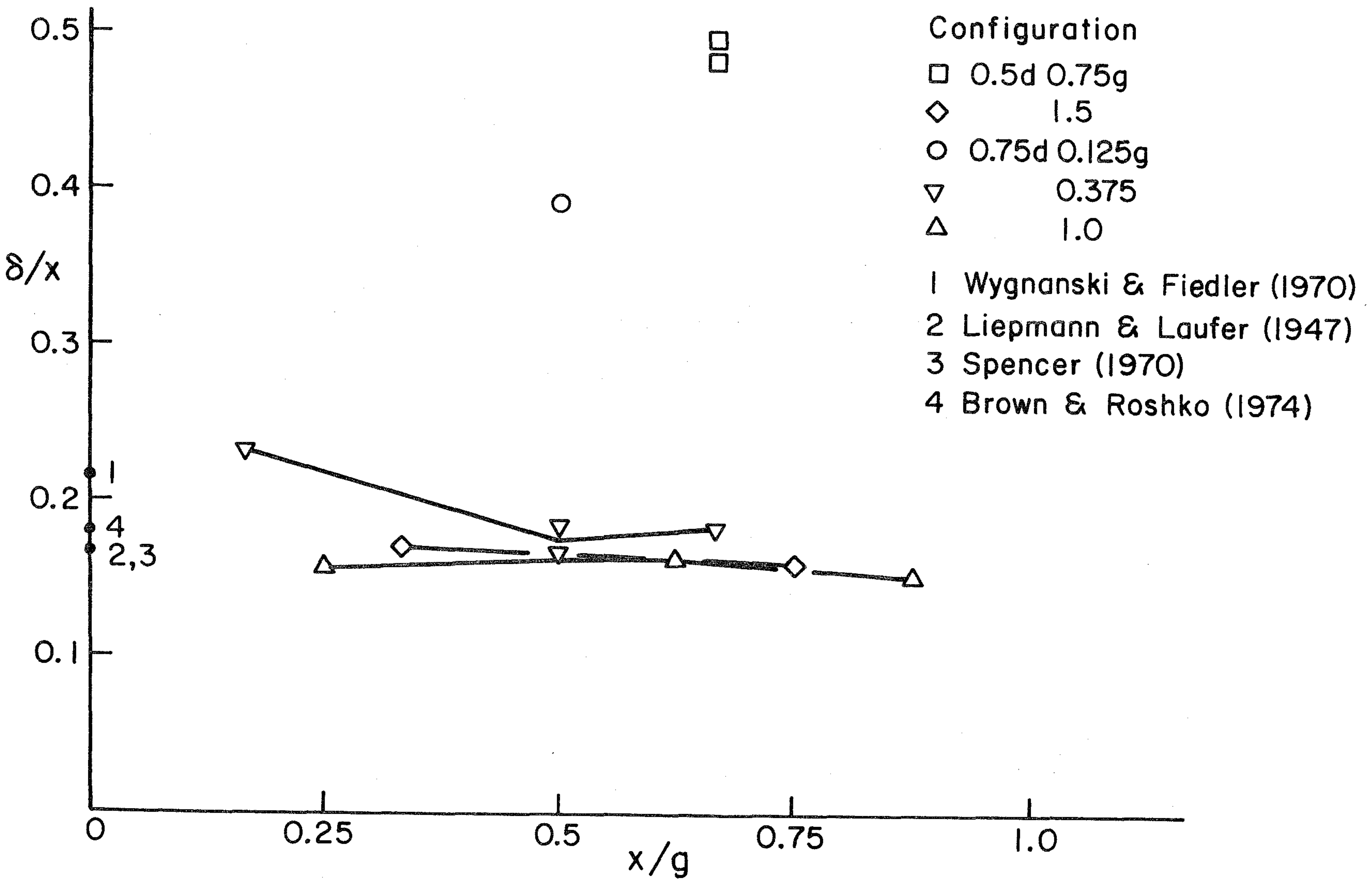

FIGURE 41 SHEAR LAYER GROWTH RATE

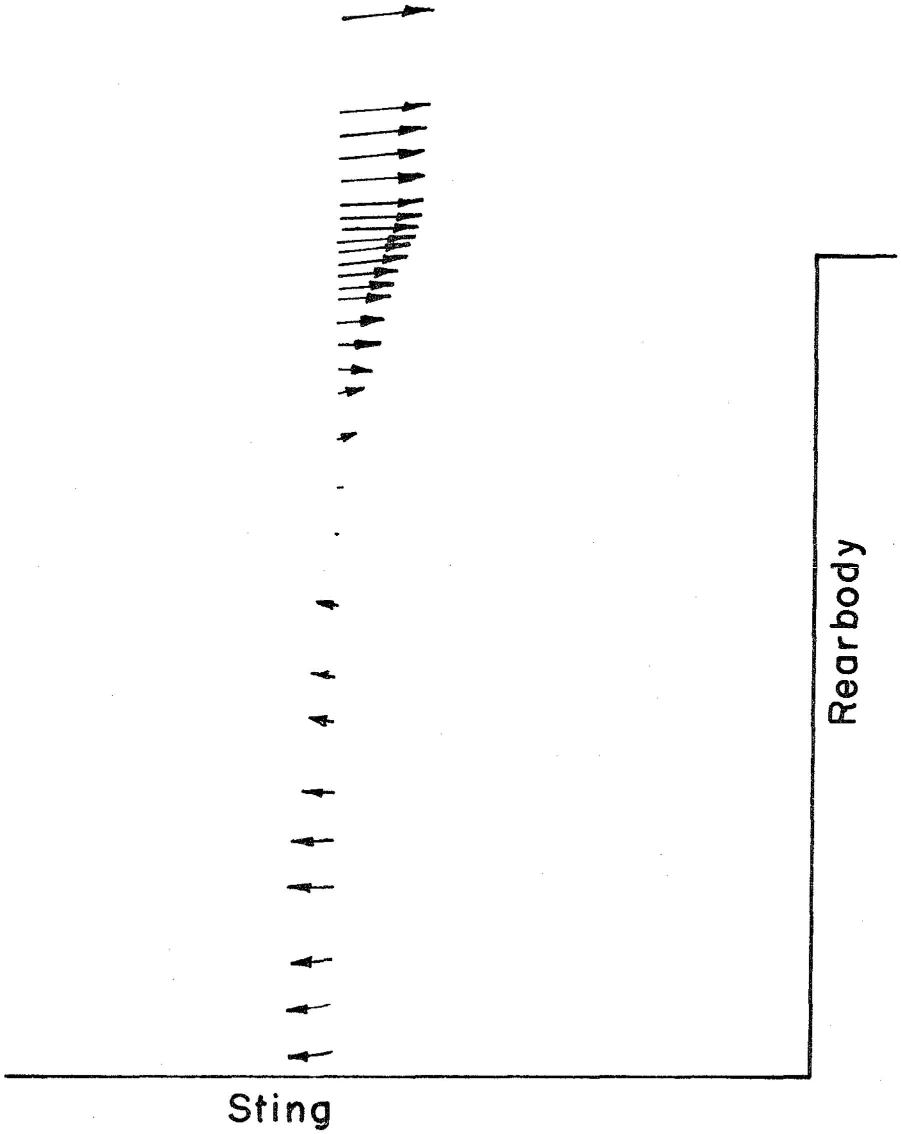

FIG. 42 VELOCITY VECTORS
$d_1/d_2 = 0.5$, $g/d_2 = 0.75$, $x/g = 0.67$

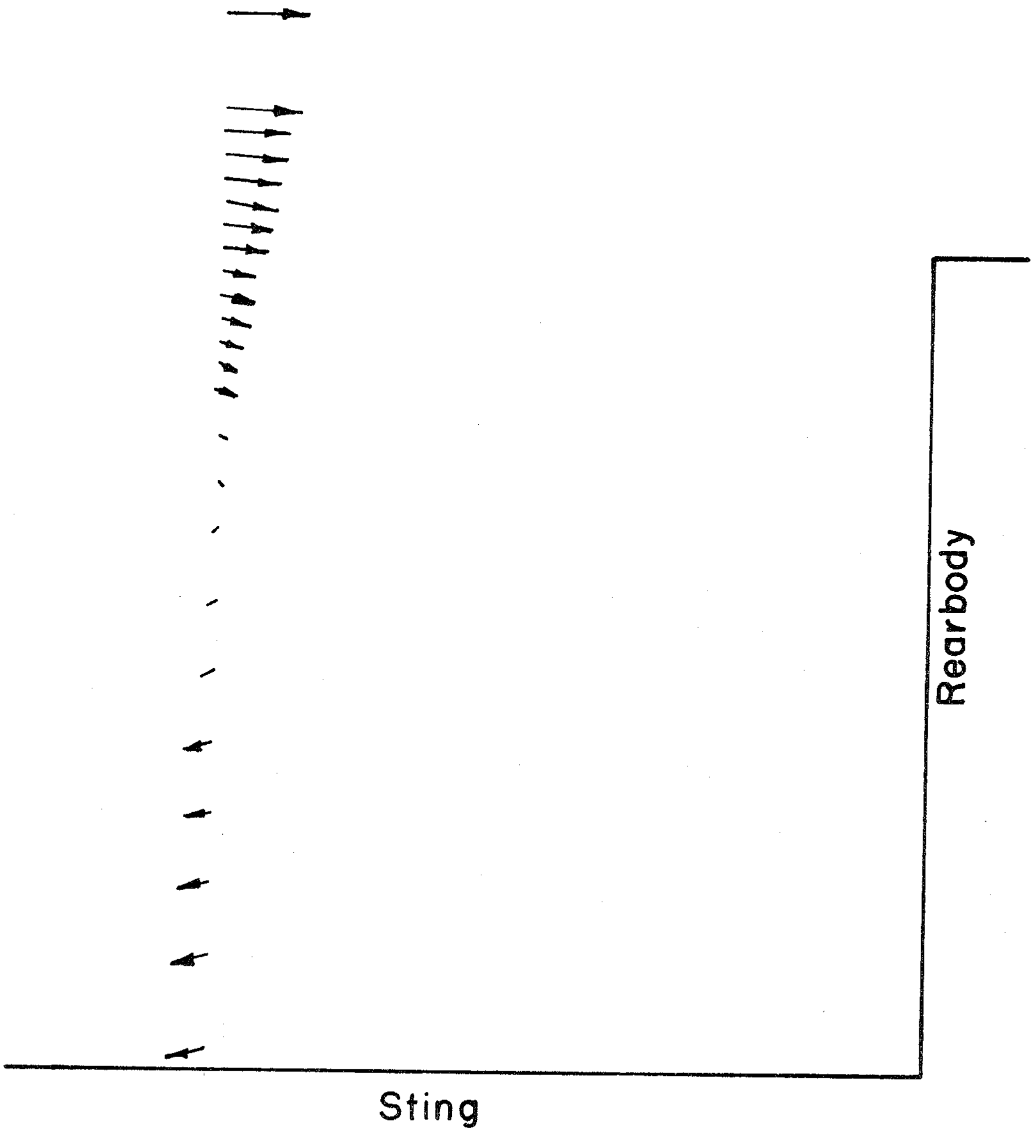

FIG. 43 VELOCITY VECTORS
$d_1/d_2 = 0.5$, $g/d_2 = 1.5$, $x/g = 0.75$

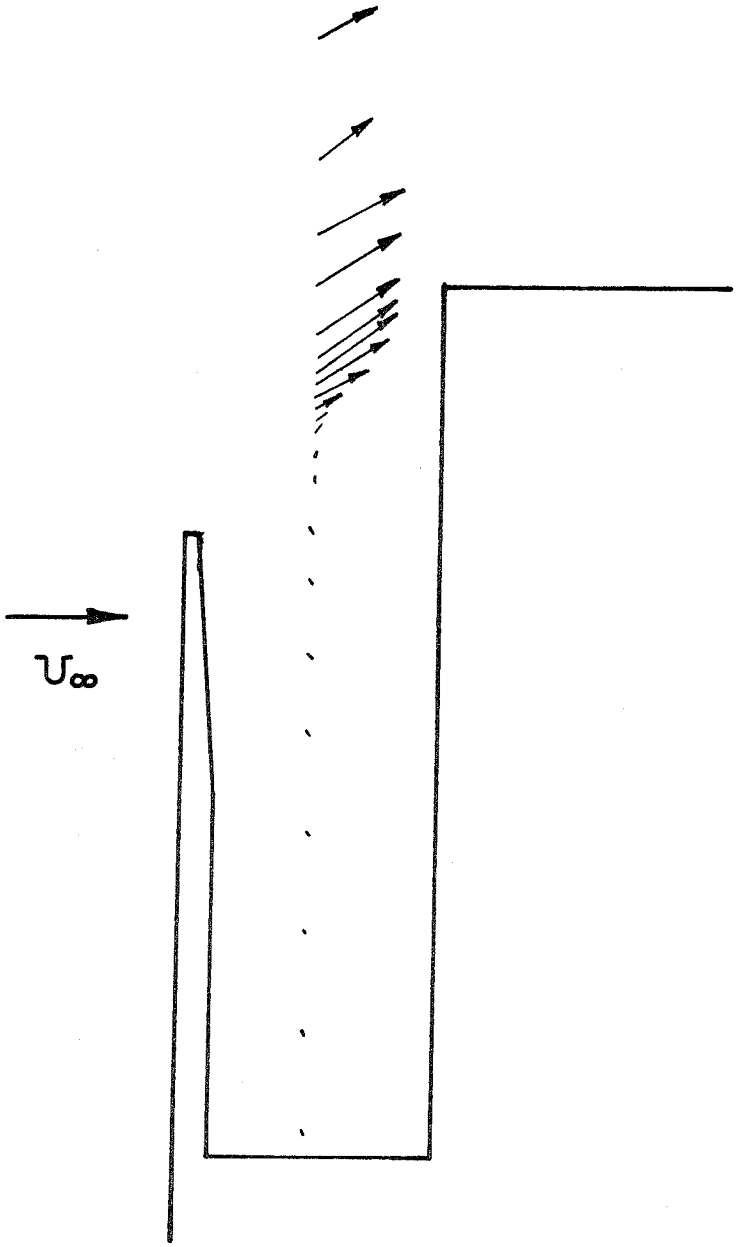

FIG.44 VELOCITY VECTORS
$d_1/d_2 = 0.75, g/d_2 = 0.125, x/g = 0.5$

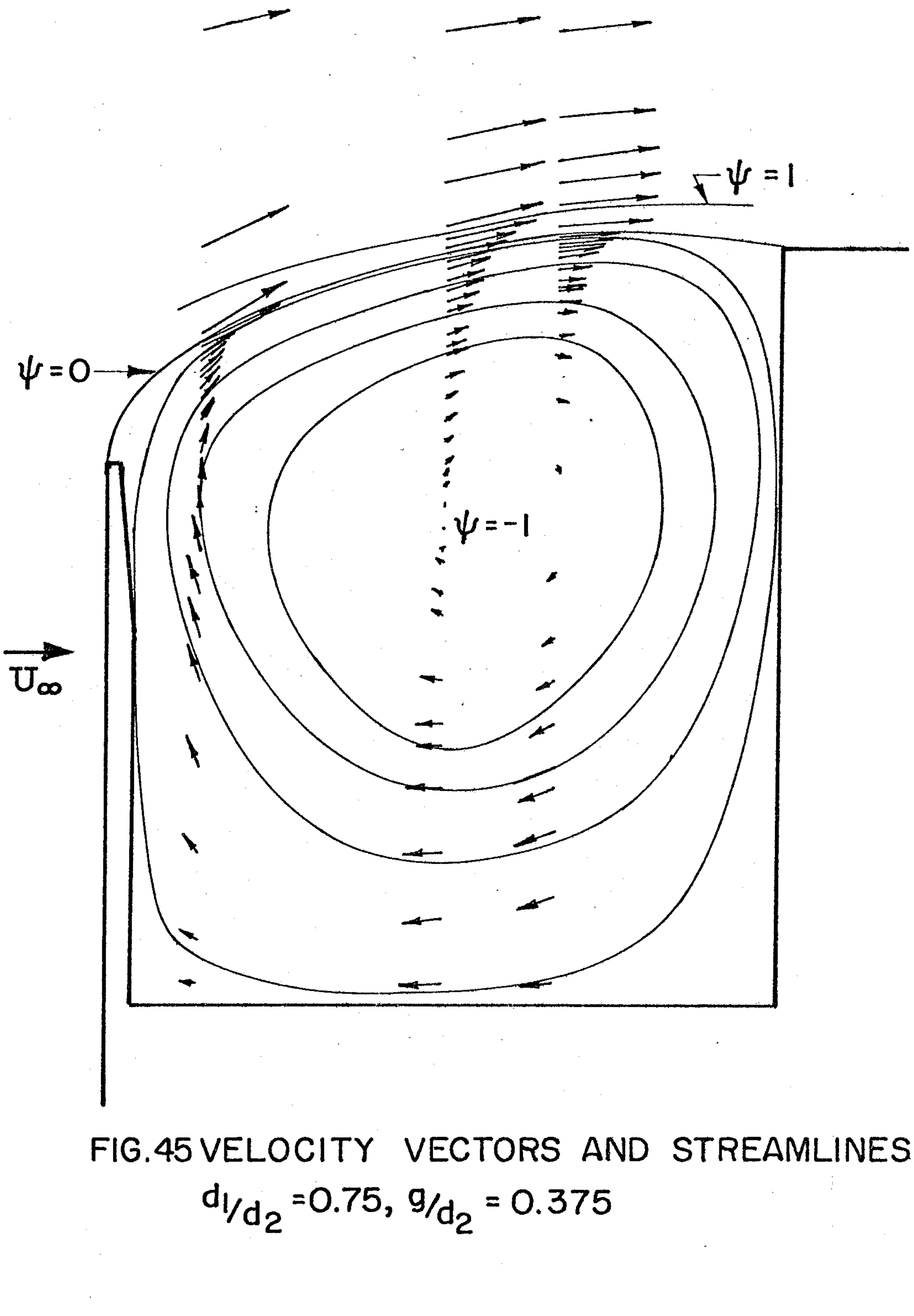

FIG. 45 VELOCITY VECTORS AND STREAMLINES
$d_1/d_2 = 0.75$, $g/d_2 = 0.375$

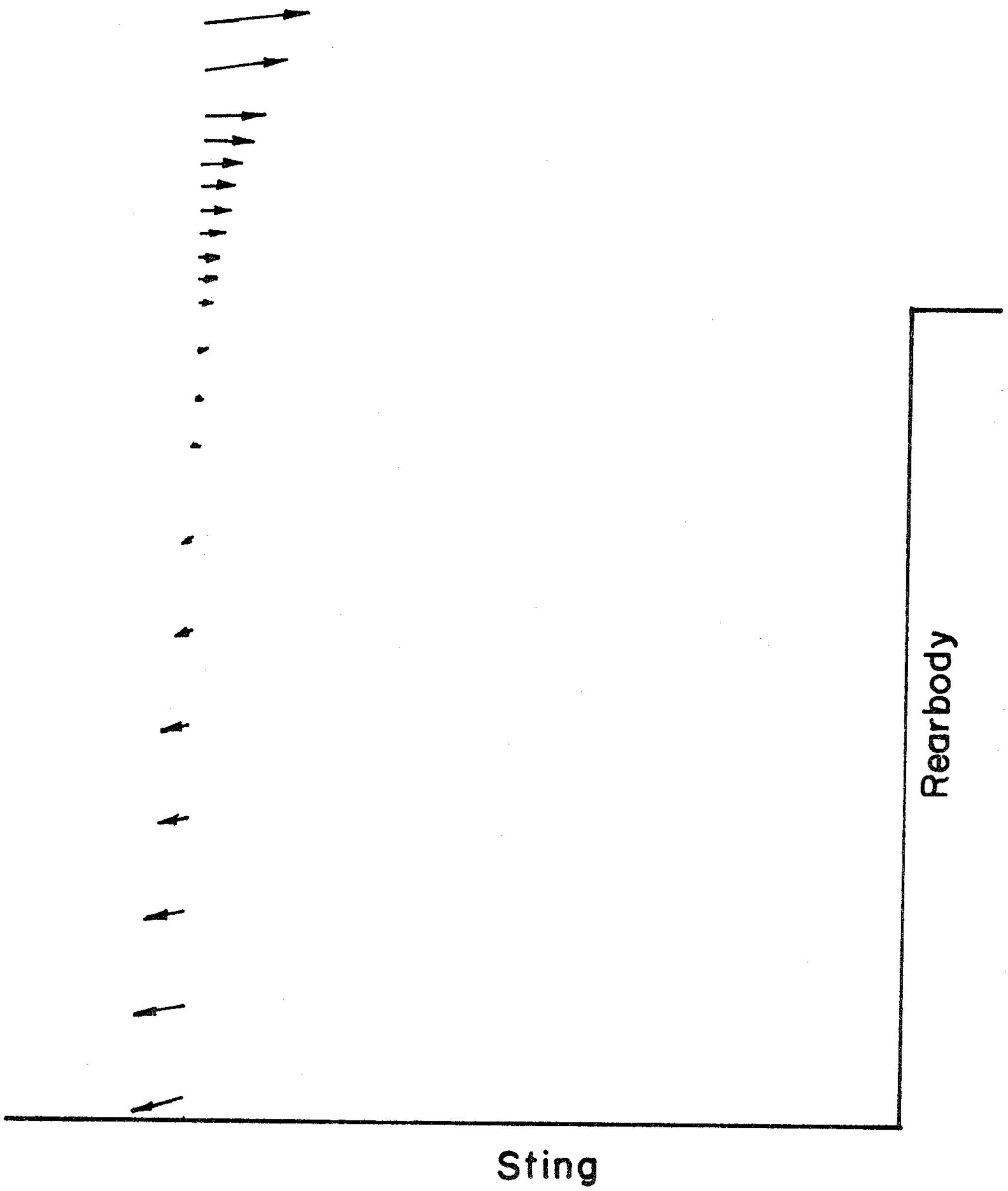

FIG. 46 VELOCITY VECTORS

$d_1/d_2 = 0.75, g/d_2 = 1.0, x/g = 0.62$

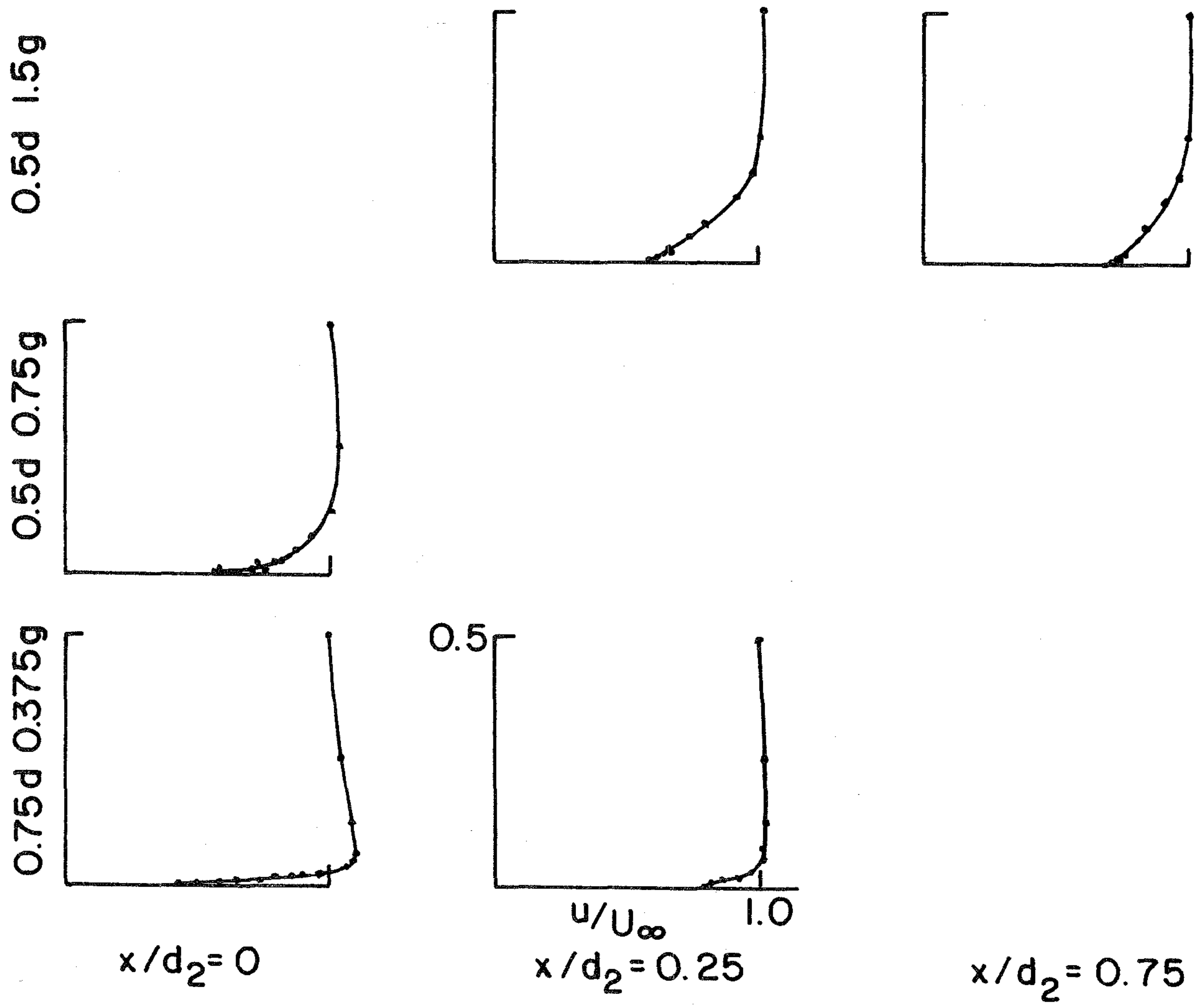

FIG. 47a REARBODY BOUNDARY LAYER PROFILES

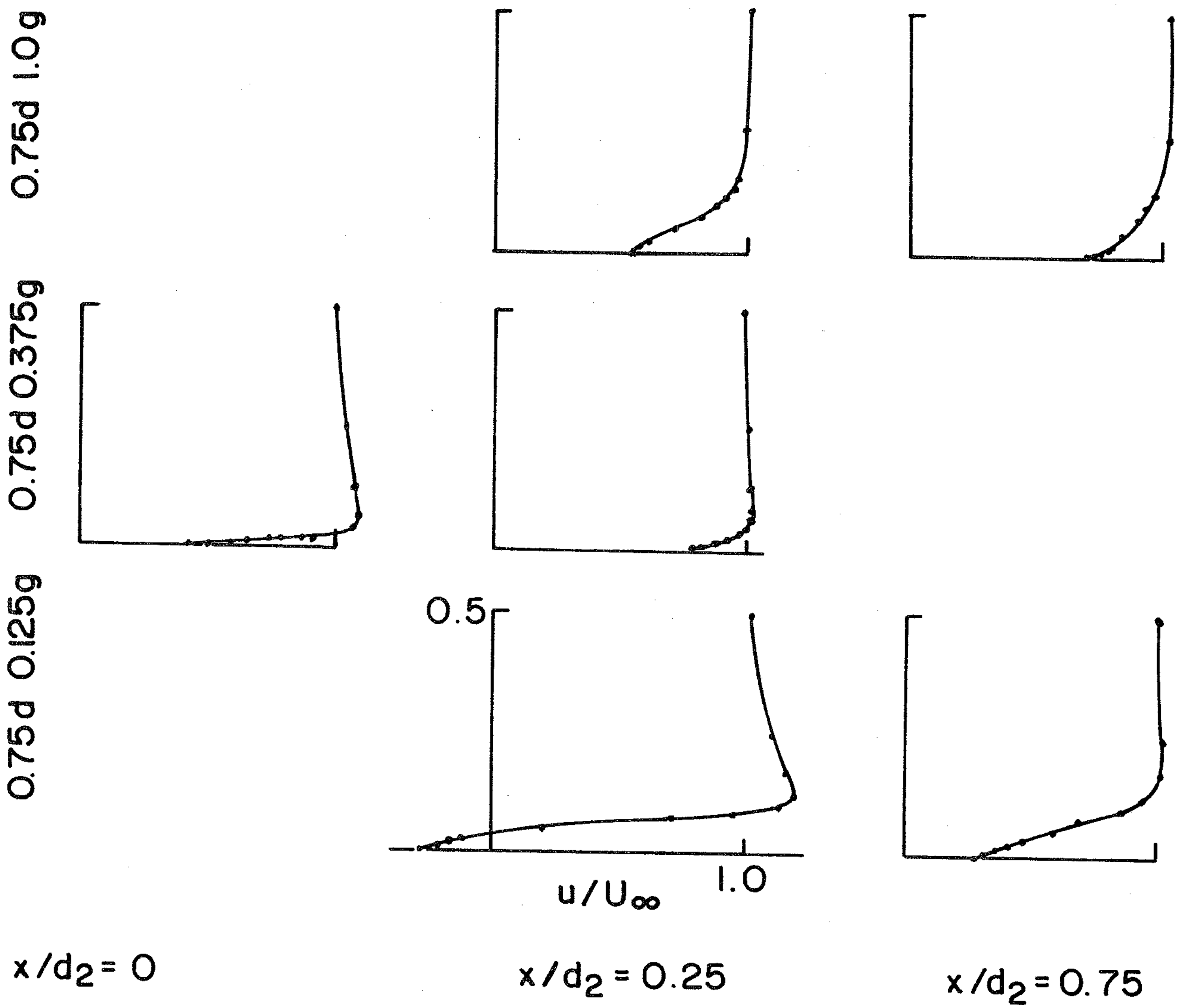

FIG. 47b REARBODY BOUNDARY LAYER PROFILES

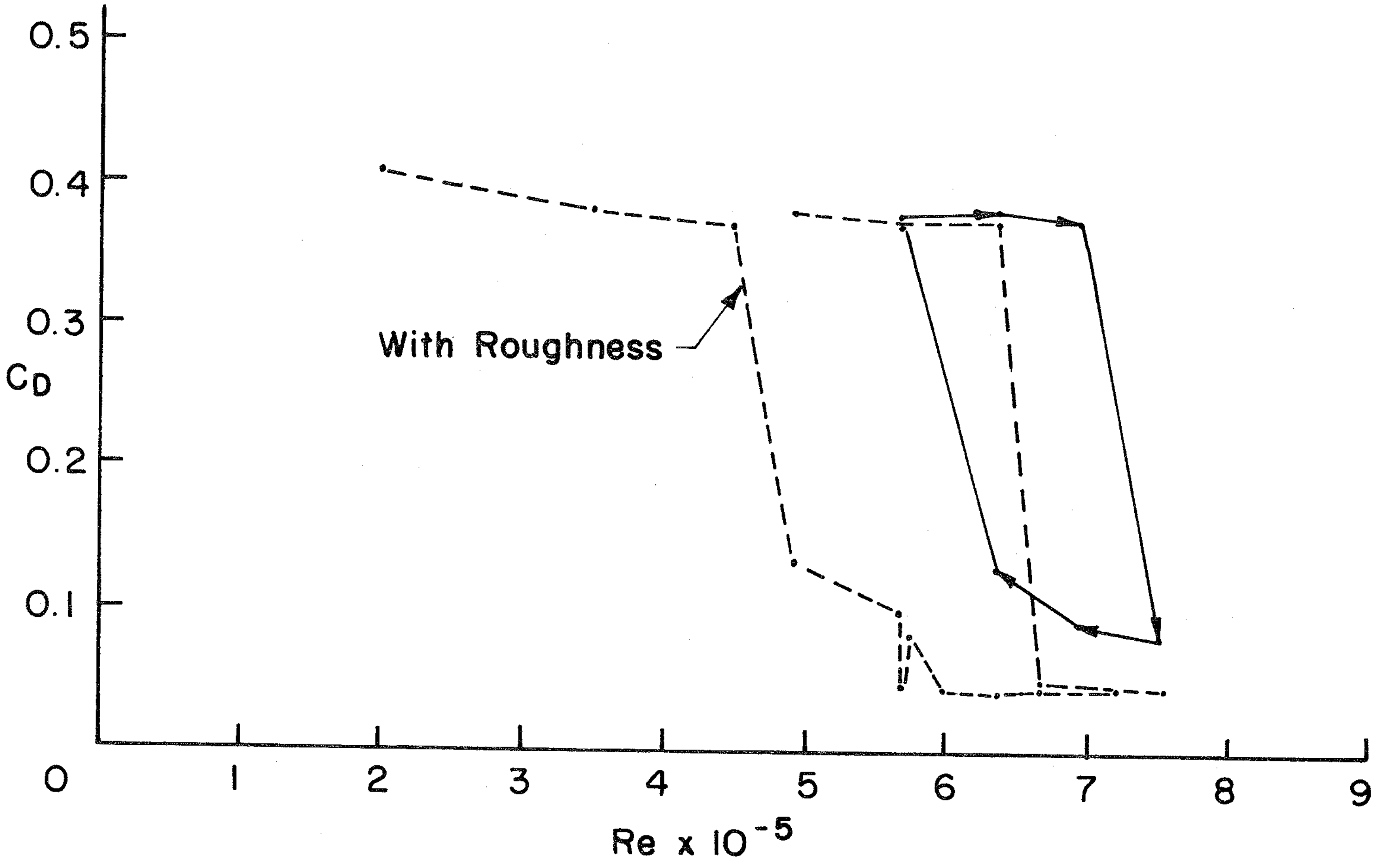

FIG. 48 REYNOLDS NUMBER DEPENDENCE OF $d_1/d_2 = 0.875$, $g/d_2 = 1.0$ FOREBODY DRAG

(a) $d_1/d_2=0.375$, $g/d_2=0.375$

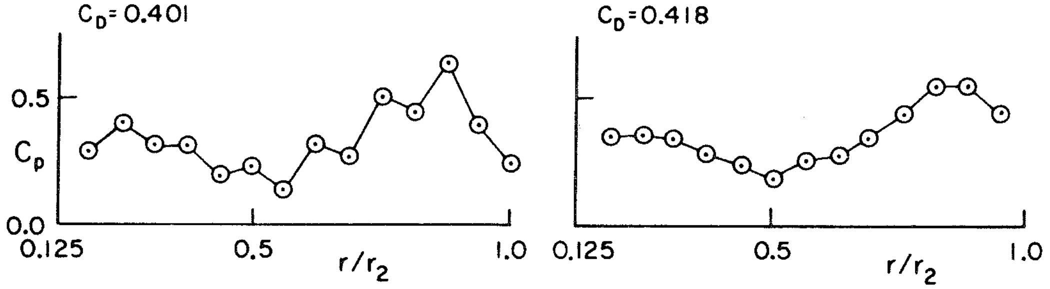

(b) $d_1/d_2=0.625$, $g/d_2=0.75$

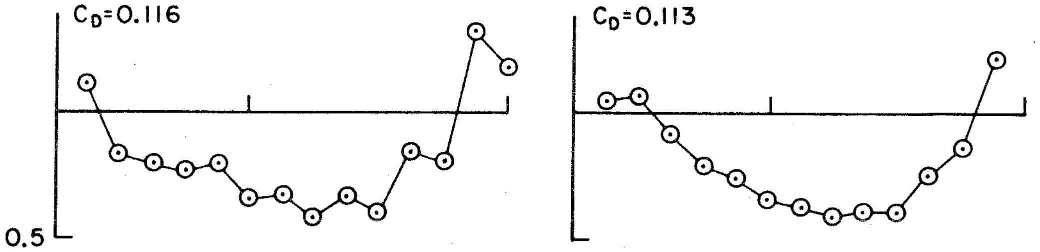

(c) $d_1/d_2=0.75$, $g/d_2=0.375$

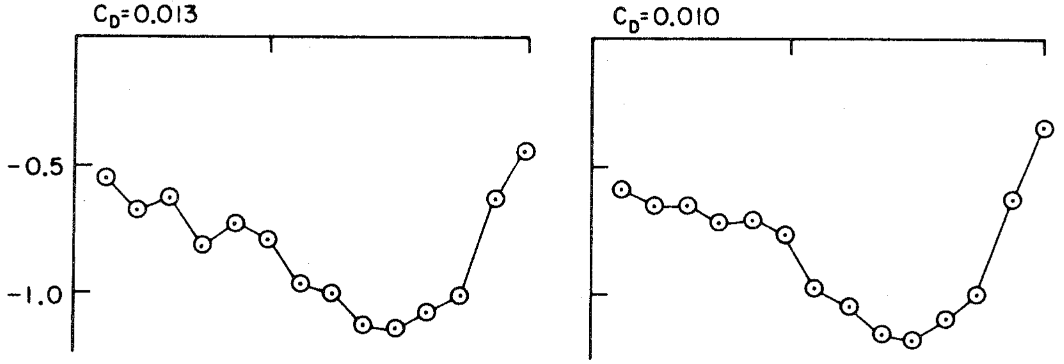

(d) $d_1/d_2=0.75$, $g/d_2=1.0$

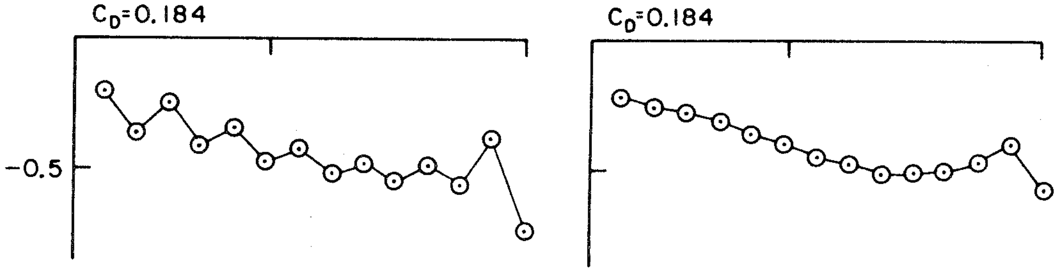

FIGURE 49 EFFECTS OF MODEL ASYMMETRIES ON FACE PRESSURE DISTRIBUTIONS

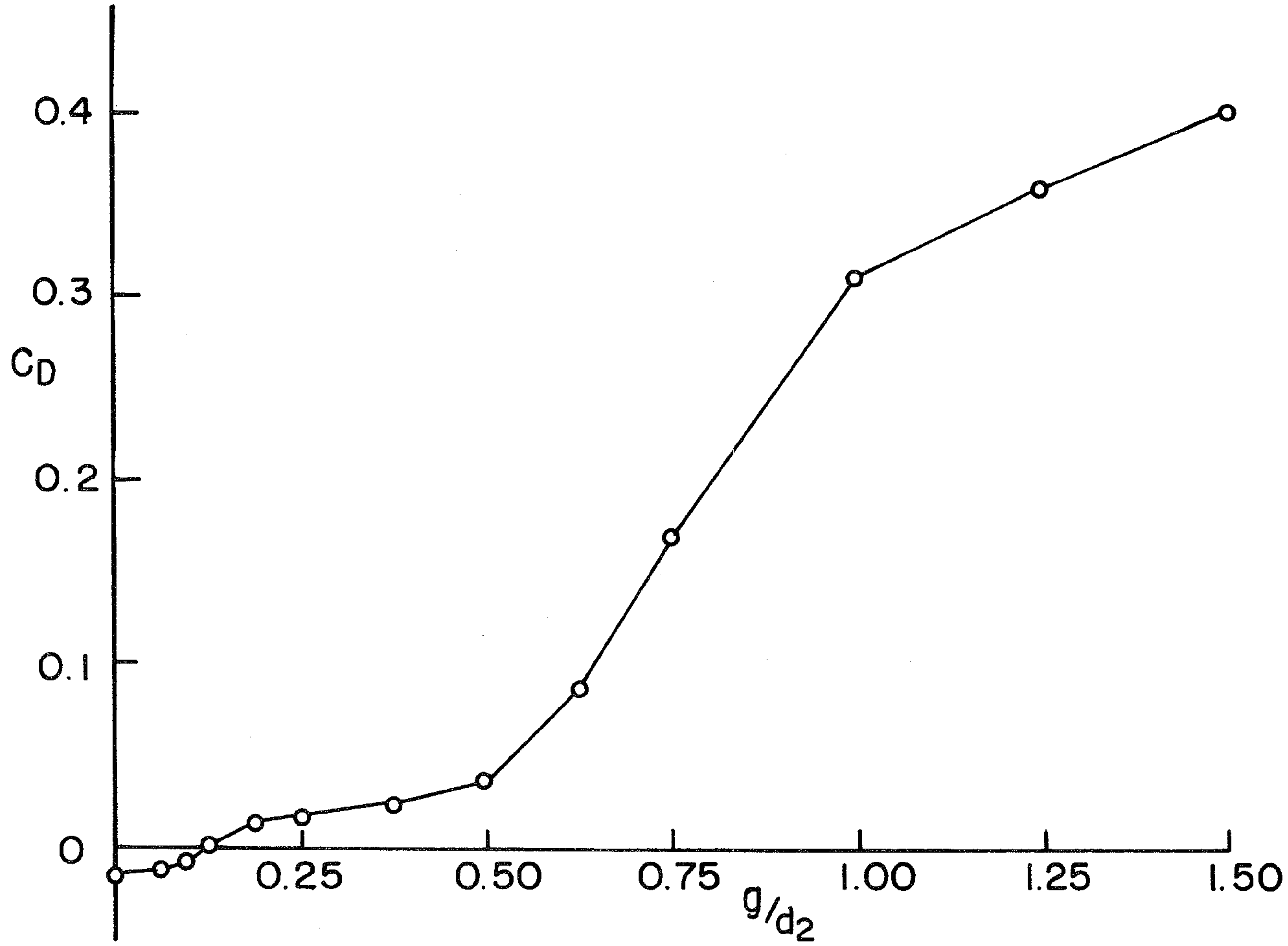

FIG. 50 HEMISPHERICAL FRONTBODY DRAG, $d_1/d_2 = 1.0$

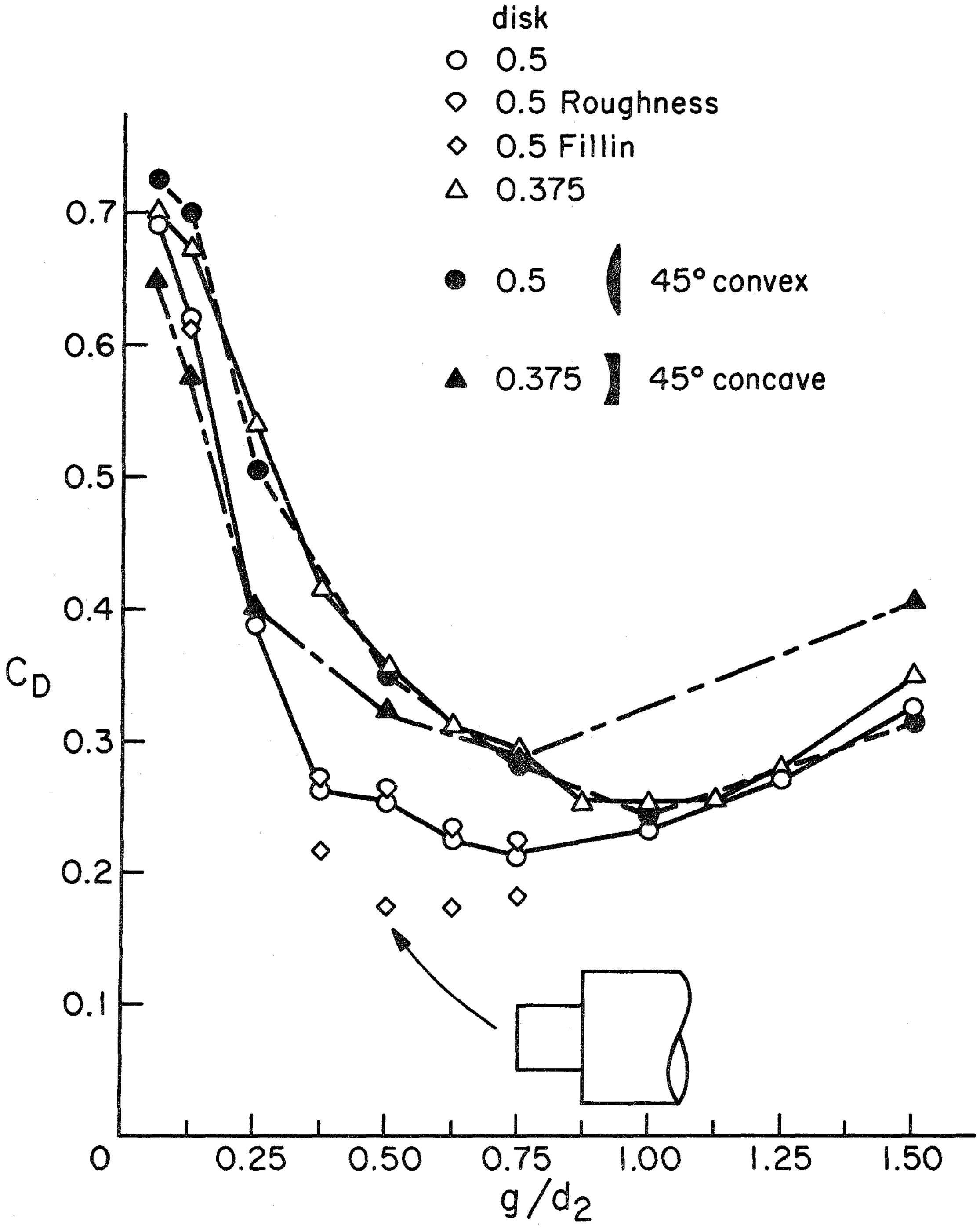

FIGURE 51 EFFECTS OF MODIFICATIONS, $d_1/d_2 = 0.5$

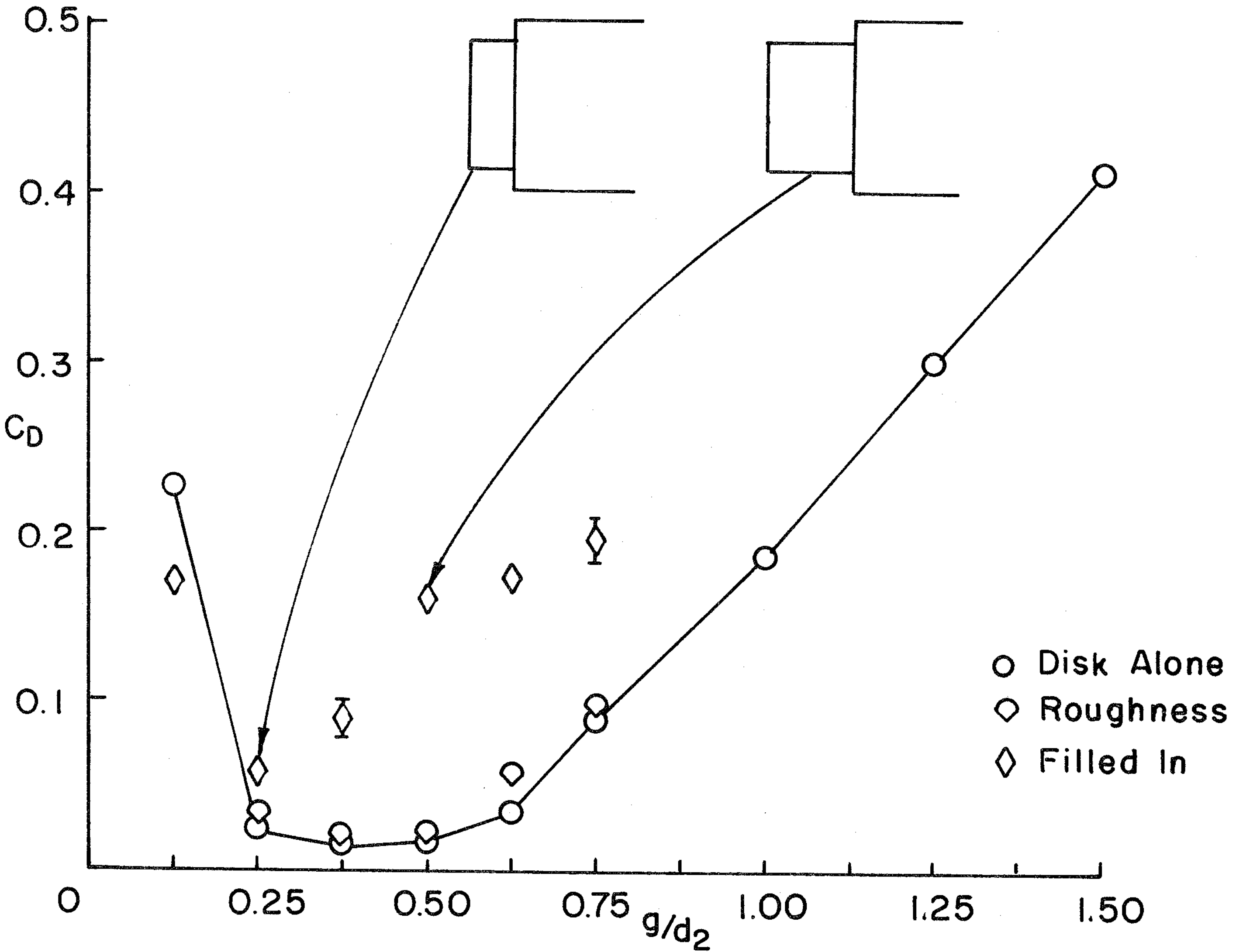

FIG.52 EFFECTS OF MODIFICATIONS ON FOREBODY DRAG, $d_1/d_2 = 0.75$

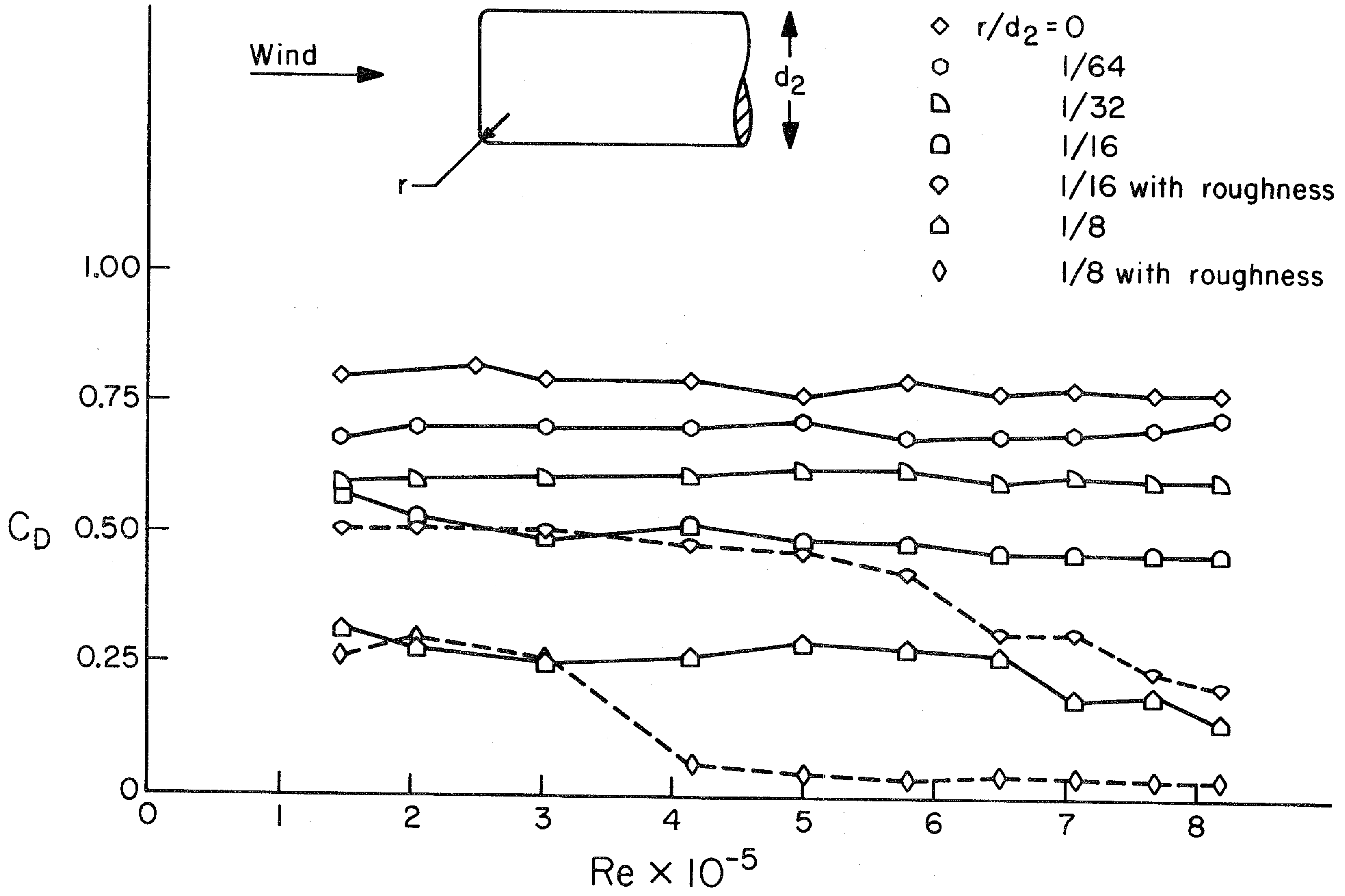

Figure 53 Effect of Corner Radius and Reynolds Number

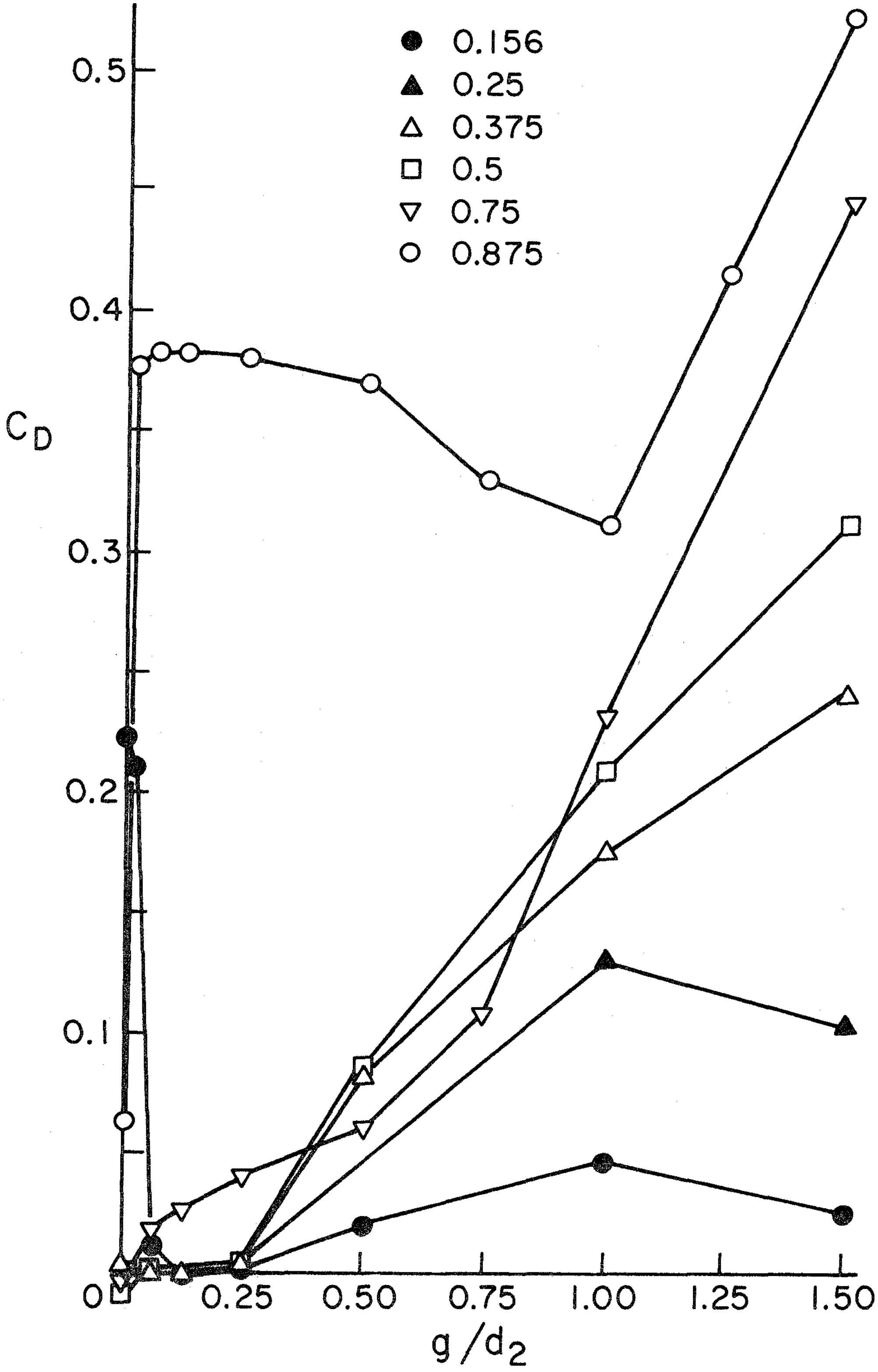

FIGURE 54 FOREBODY DRAG OF AXISYMMETRIC MODEL WITH ROUNDED REARBODY

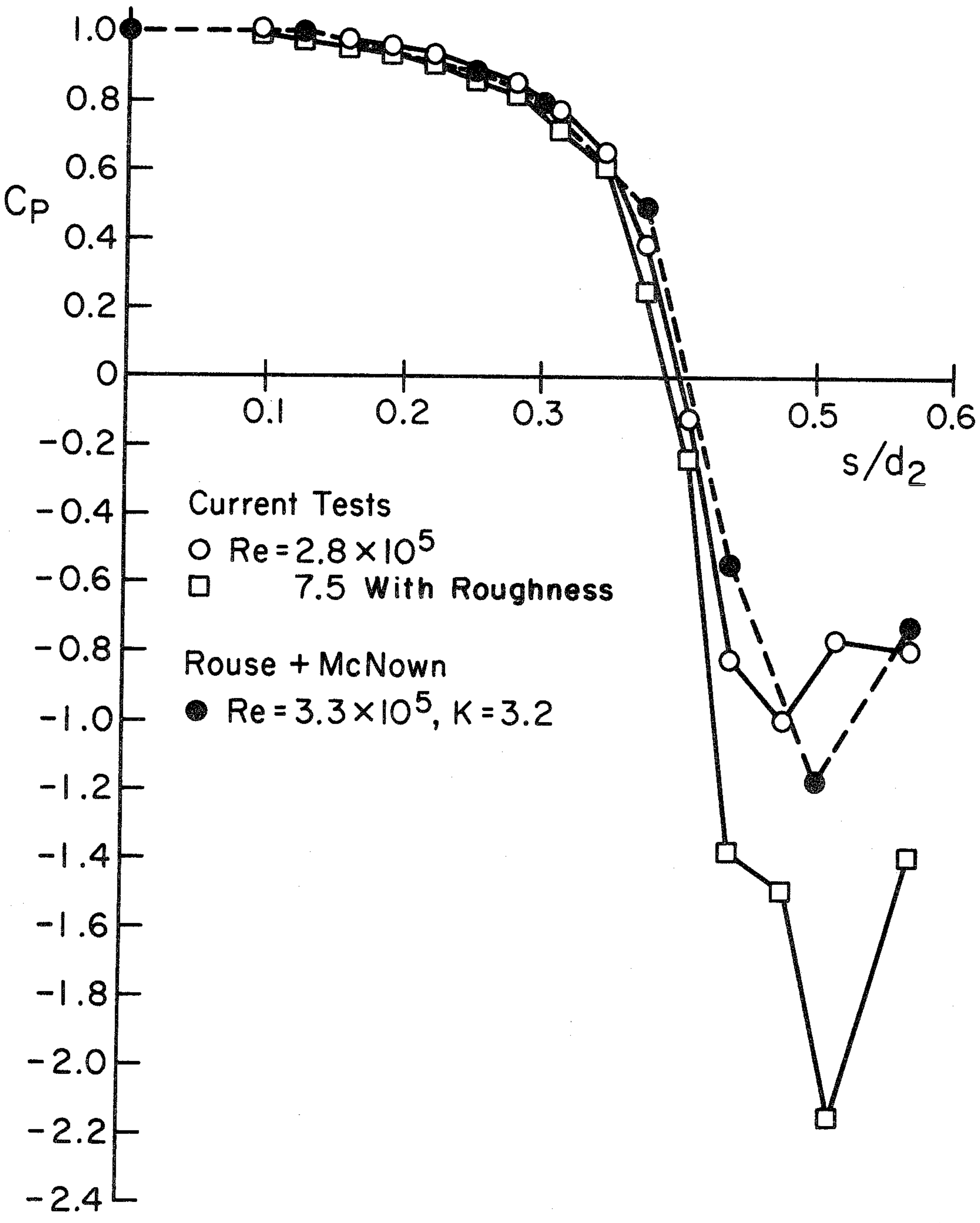

FIGURE 55 . ROUNDED CYLINDER FACE PRESSURE DISTRIBUTIONS

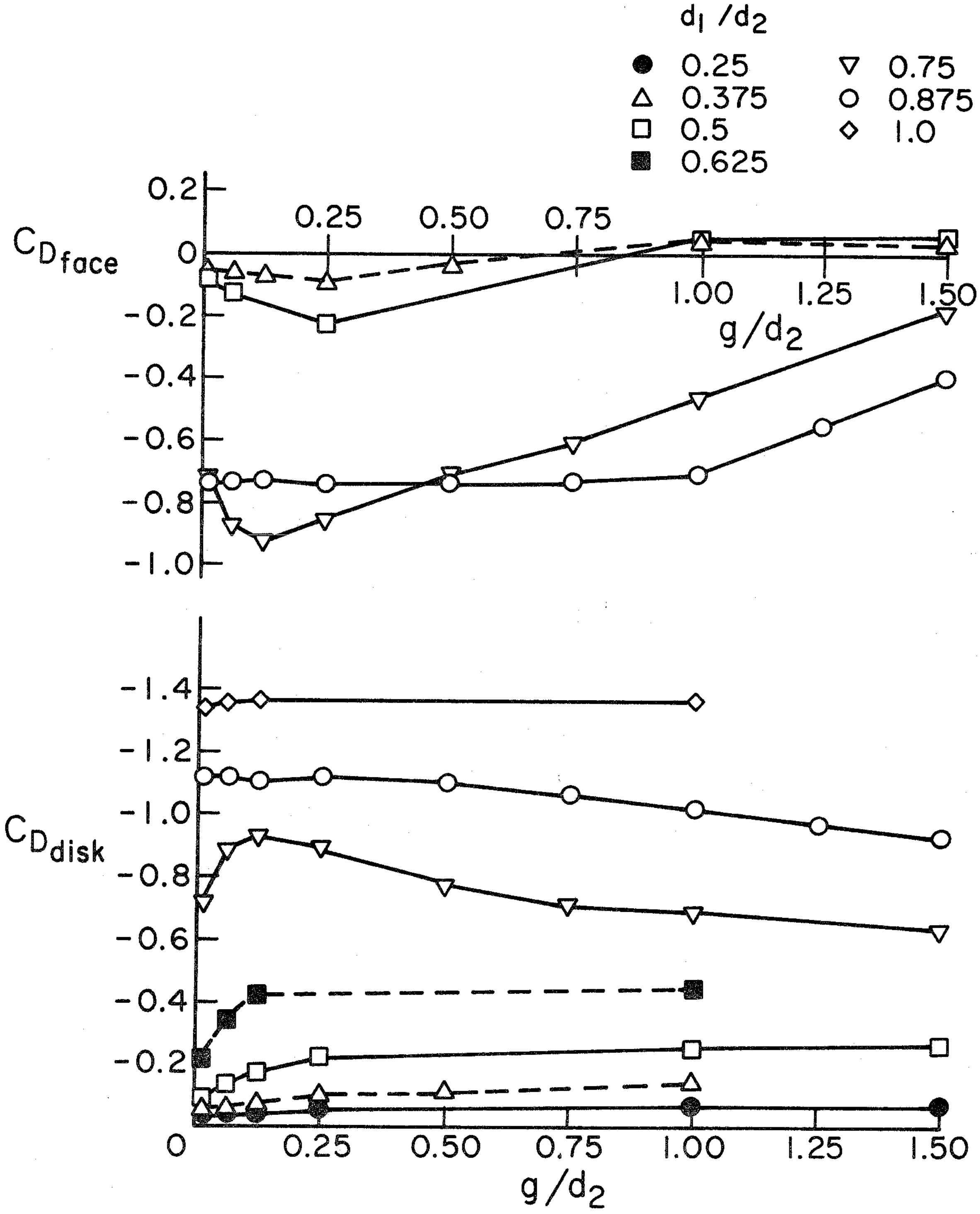

FIGURE 56 DRAG BREAKDOWN FOR ROUNDED AXISYMMETRIC REARBODY

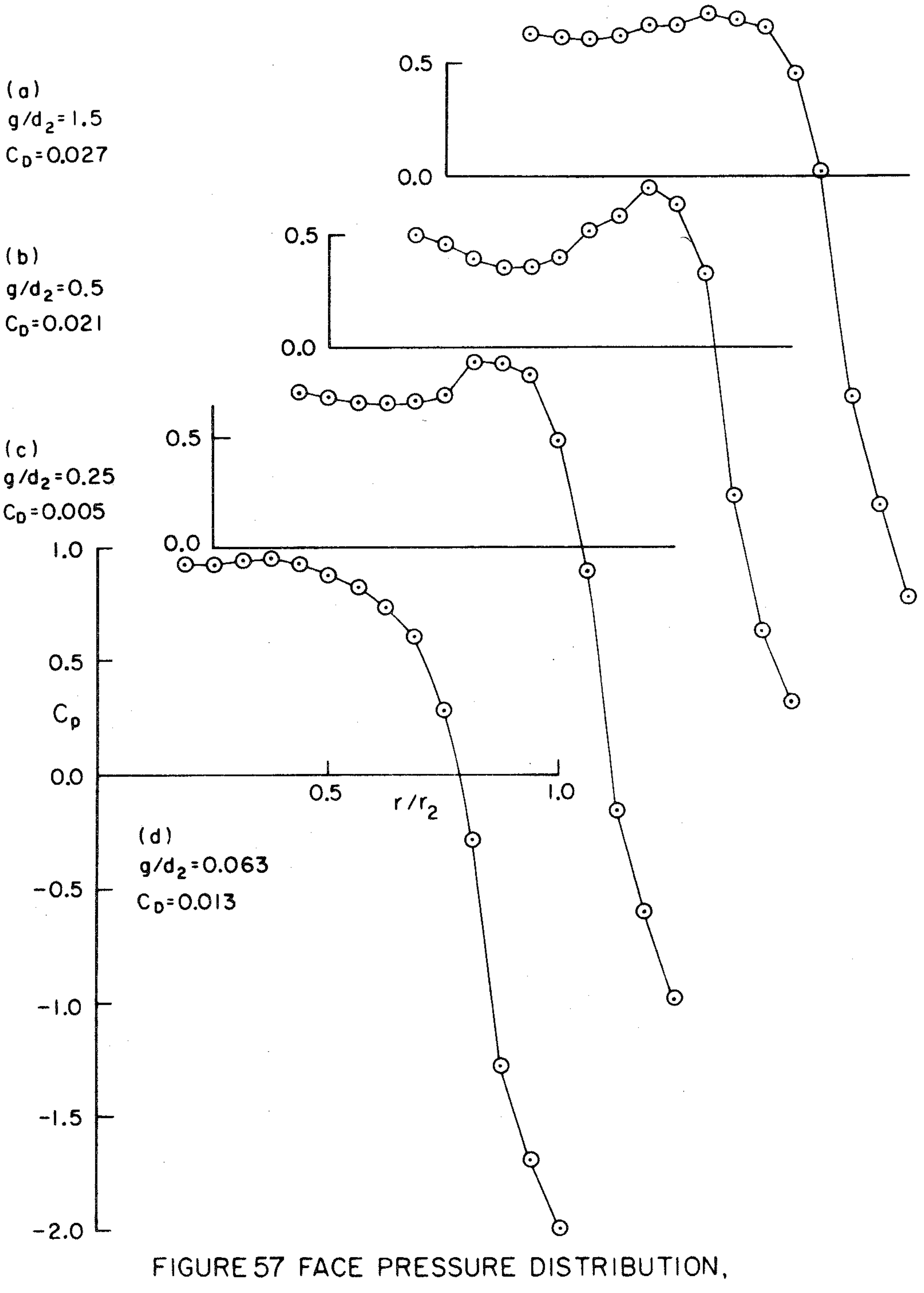

FIGURE 57 FACE PRESSURE DISTRIBUTION, ROUNDED REARBODY, $d_1/d_2=0.156$

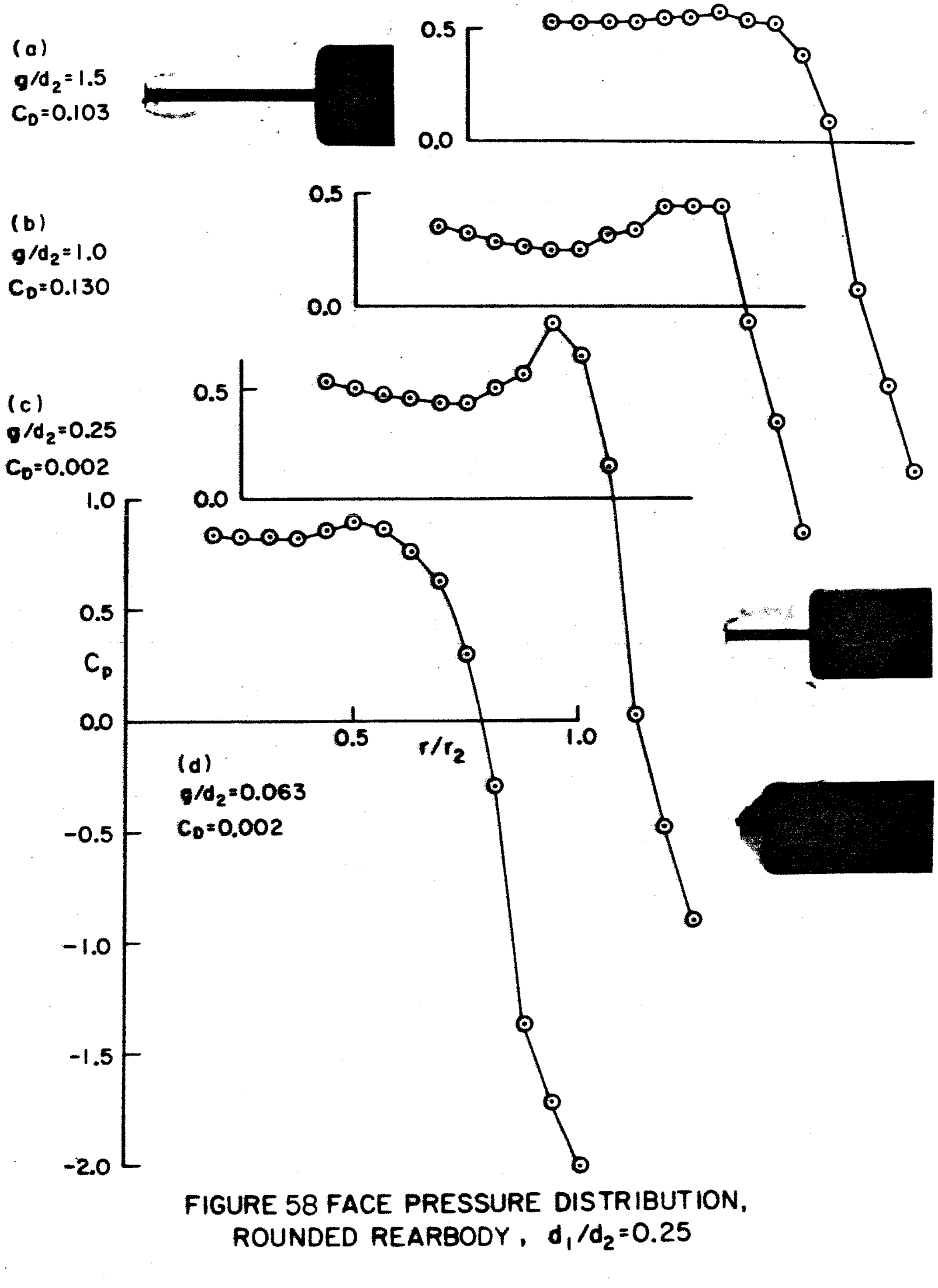

FIGURE 58 FACE PRESSURE DISTRIBUTION, ROUNDED REARBODY, $d_1/d_2=0.25$

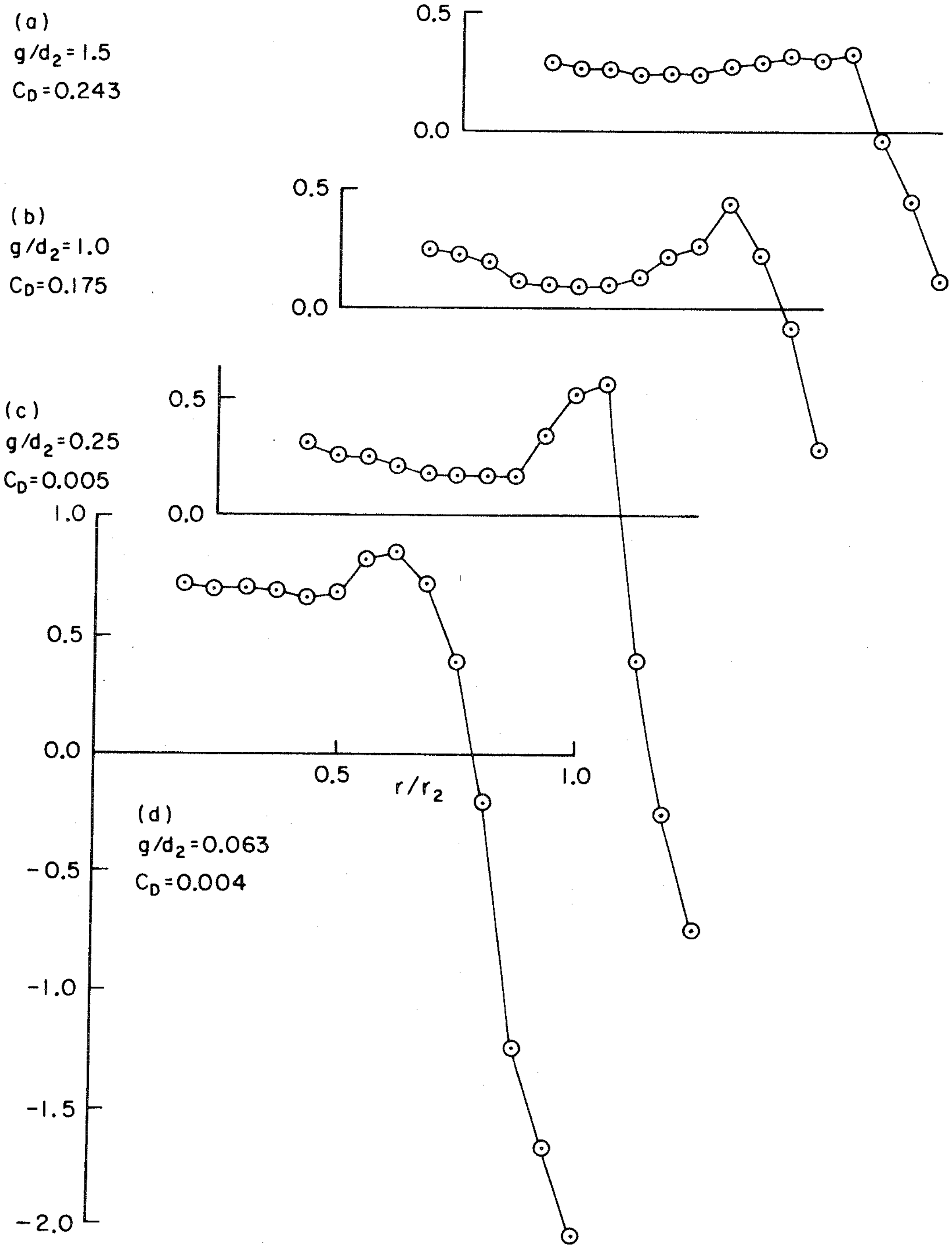

FIGURE 59 FACE PRESSURE DISTRIBUTION, ROUNDED REARBODY, $d_1/d_2=0.375$

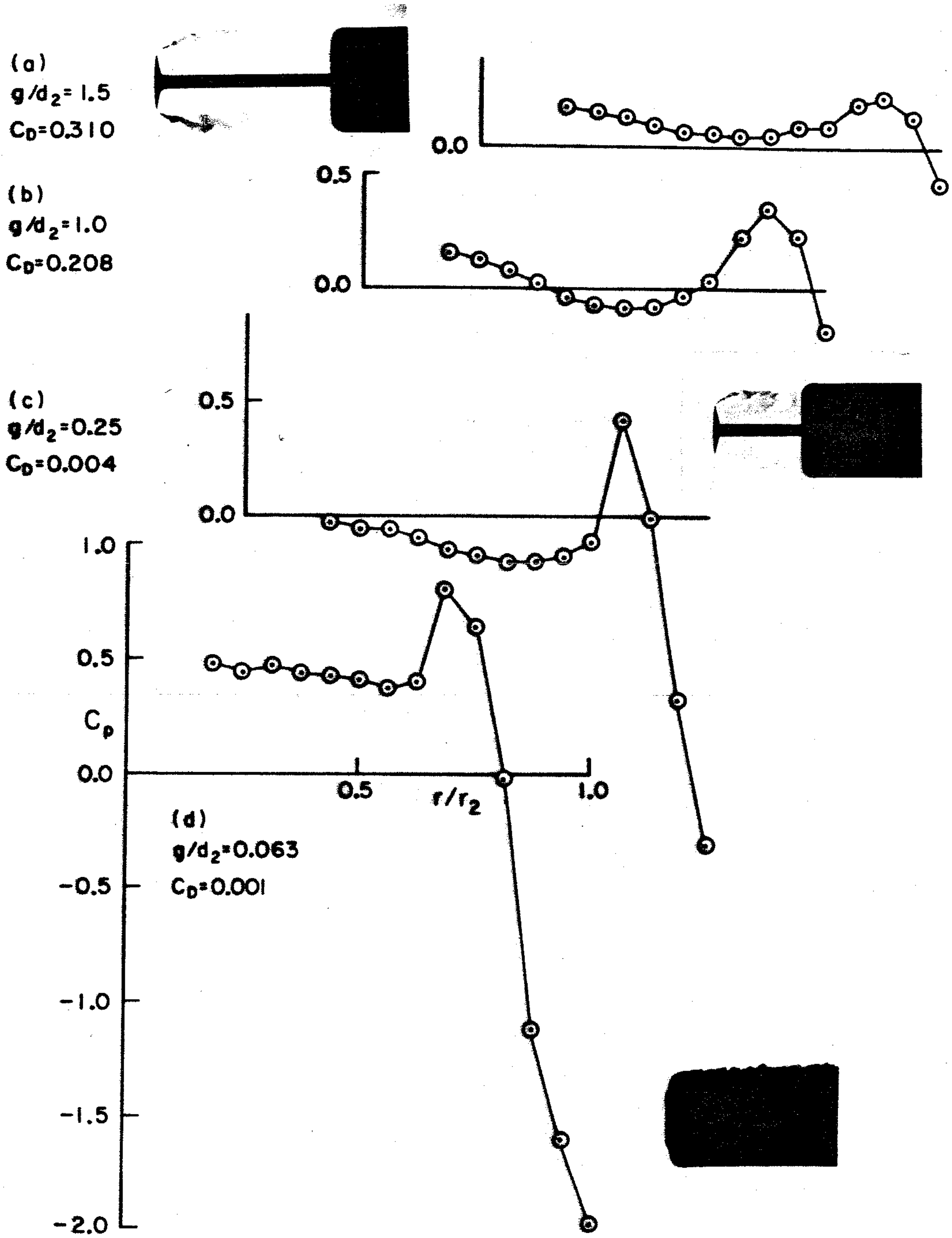

FIGURE 60 FACE PRESSURE DISTRIBUTION, ROUNDED REARBODY, $d_1/d_2=0.5$

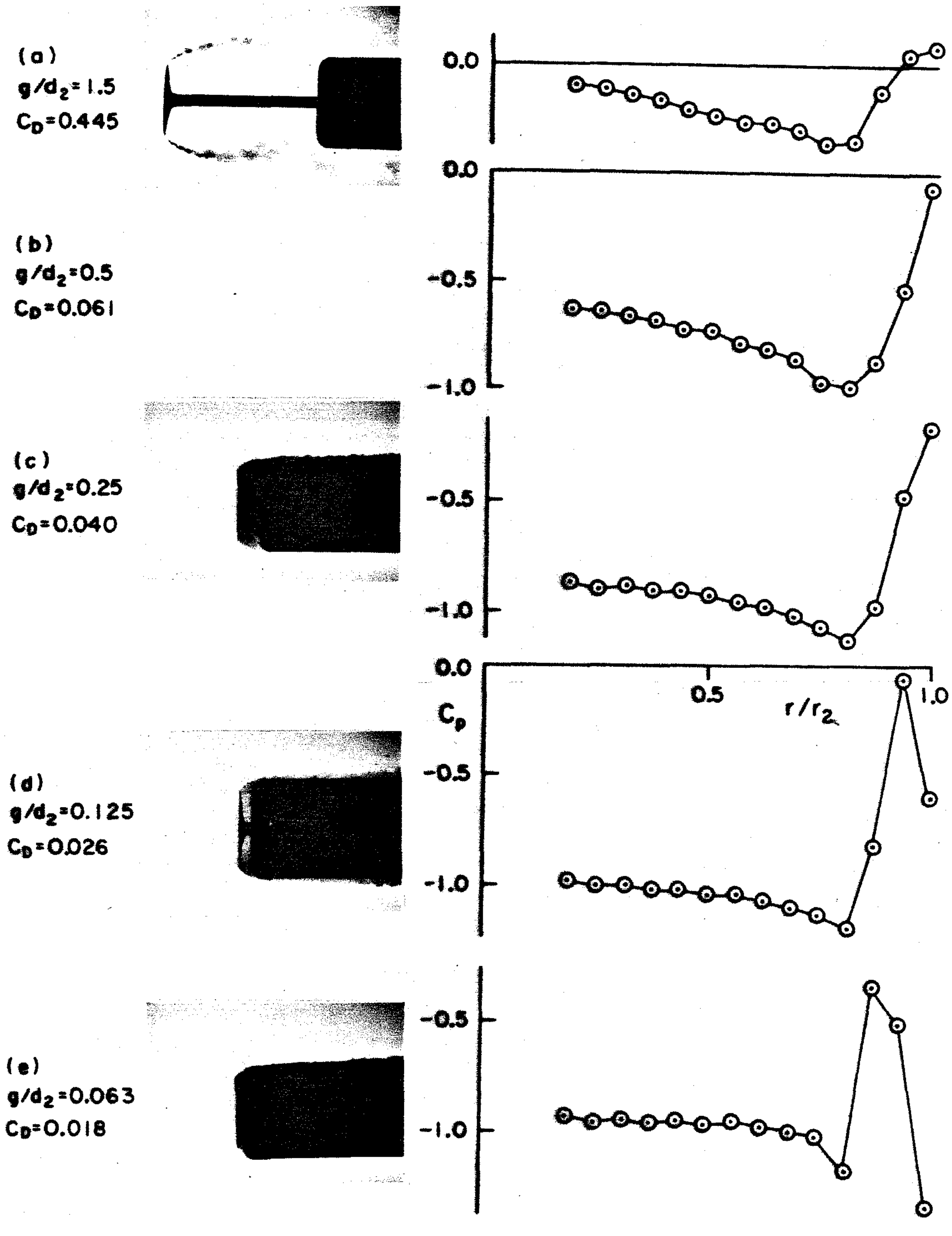

FIGURE 61 ROUNDED REARBODY FACE PRESSURE DISTRIBUTION, $d_1/d_2=0.75$

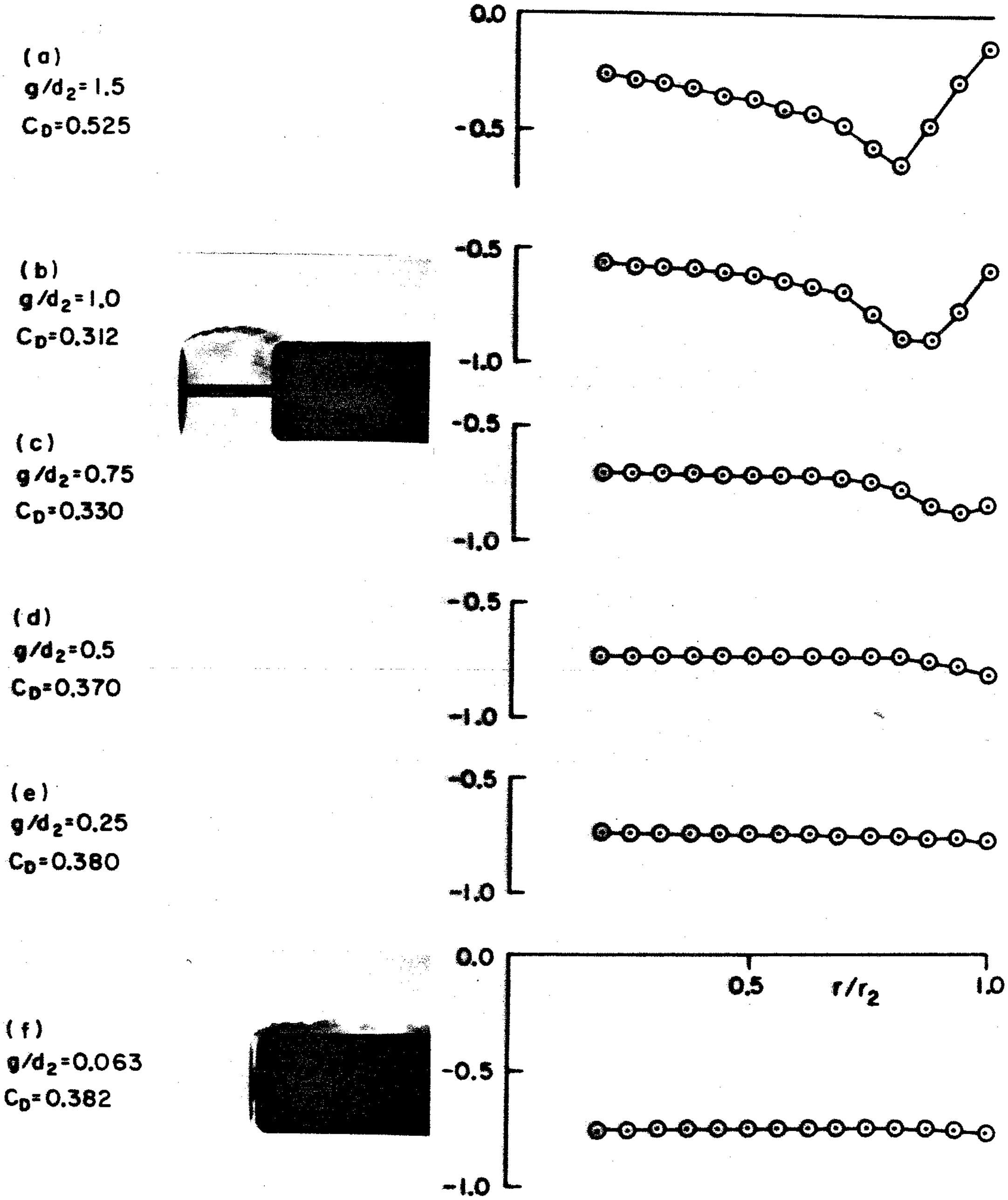

(a) $g/d_2 = 1.5$ $C_D = 0.525$

(b) $g/d_2 = 1.0$ $C_D = 0.312$

(c) $g/d_2 = 0.75$ $C_D = 0.330$

(d) $g/d_2 = 0.5$ $C_D = 0.370$

(e) $g/d_2 = 0.25$ $C_D = 0.380$

(f) $g/d_2 = 0.063$ $C_D = 0.382$

FIGURE 62 ROUNDED REARBODY FACE PRESSURE DISTRIBUTION, $d_1/d_2 = 0.875$

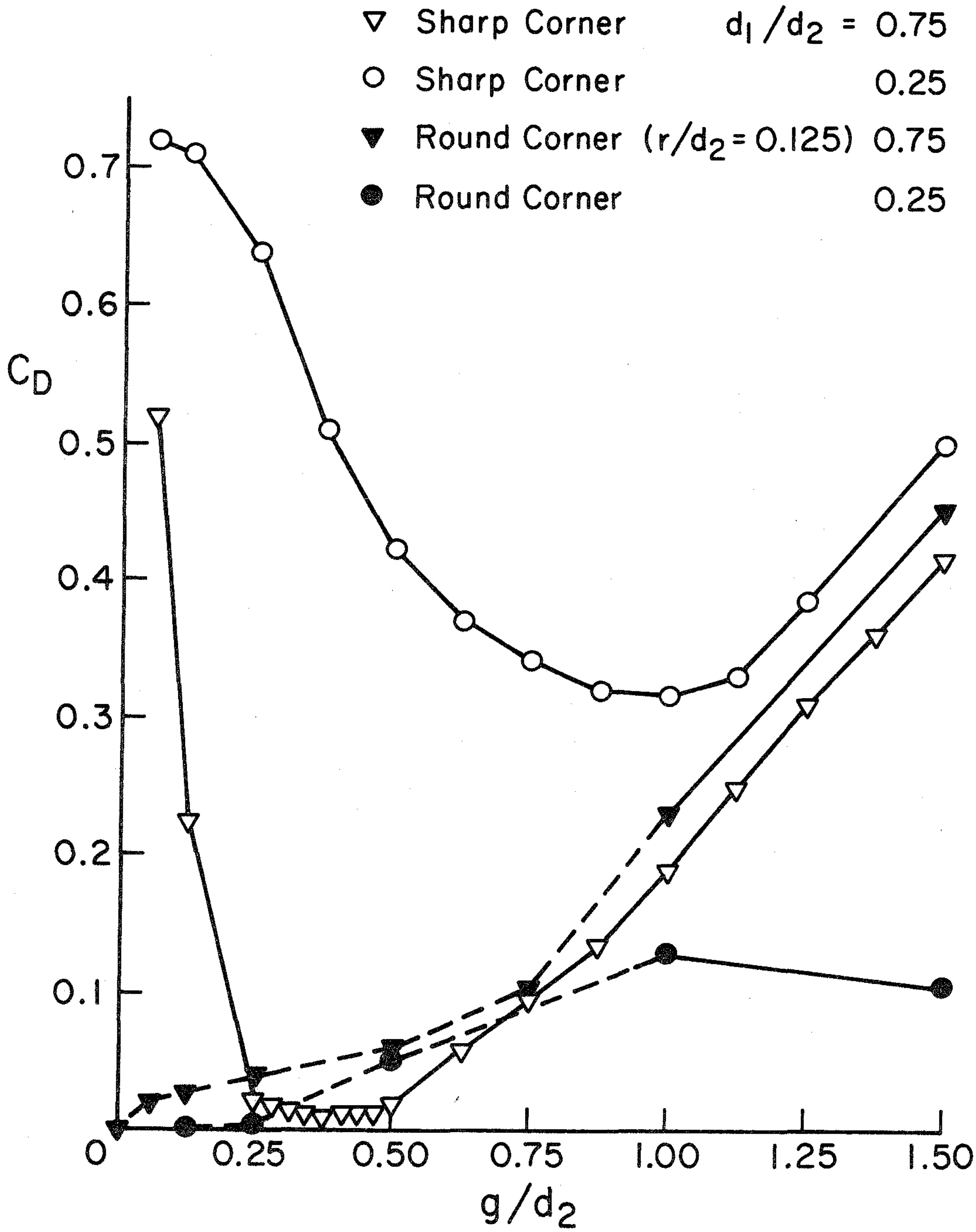

FIGURE 63 EFFECT OF REARBODY FACE GEOMETRY ON FOREBODY DRAG

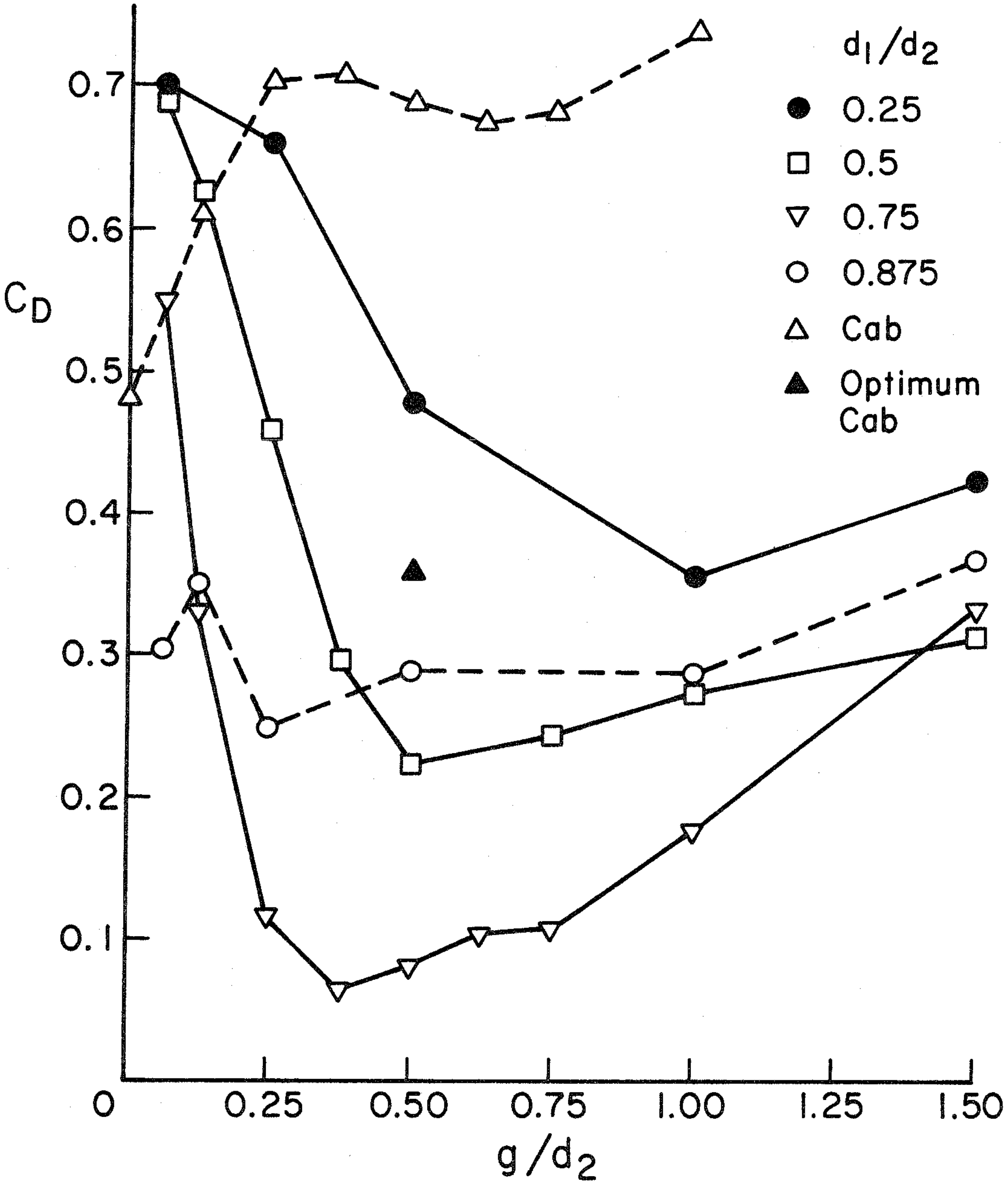

FIGURE 64 SQUARE CROSS-SECTION FOREBODY DRAG

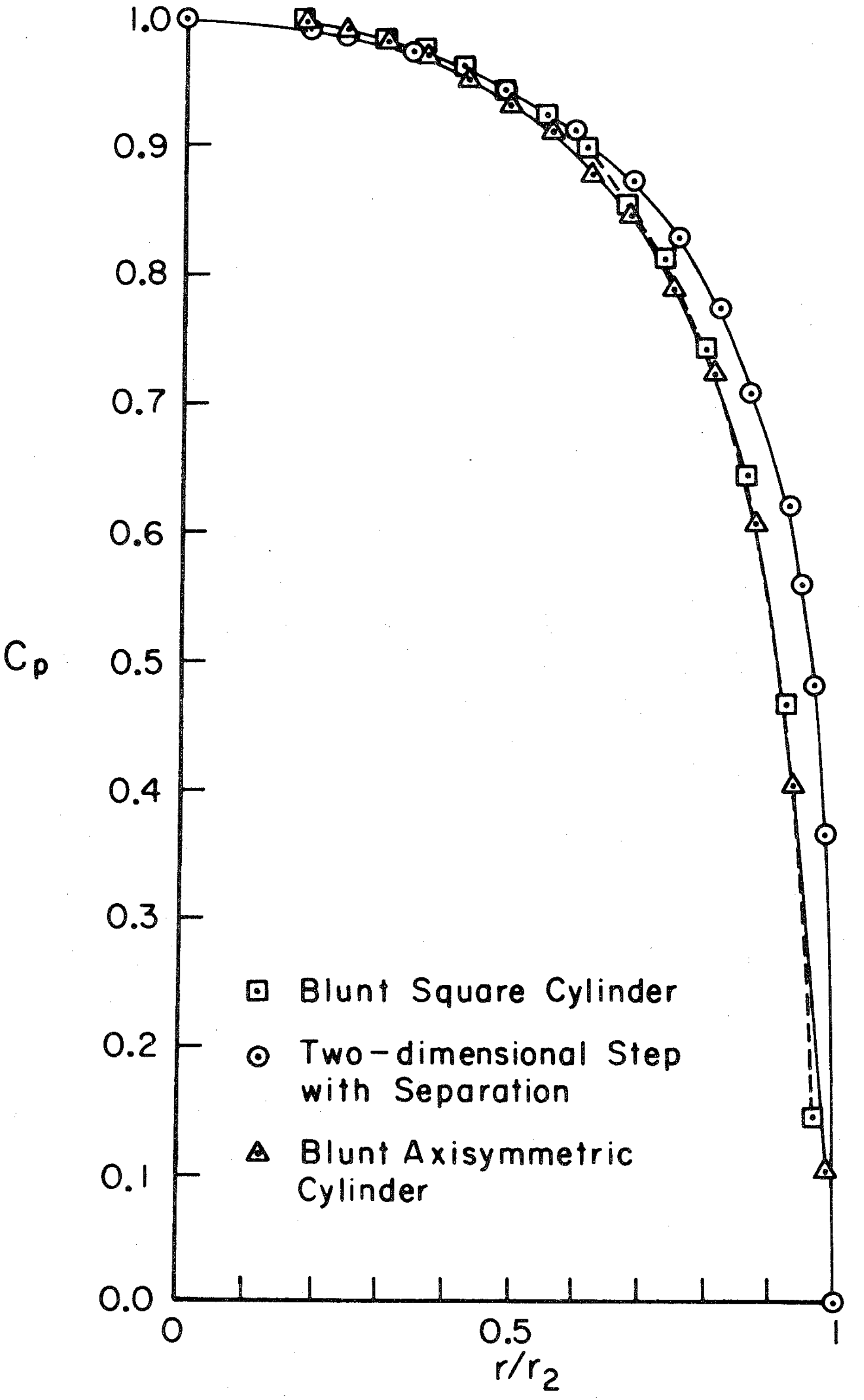

FIGURE 65 EFFECT OF CROSS-SECTION ON BLUNT CYLINDER FACE PRESSURES

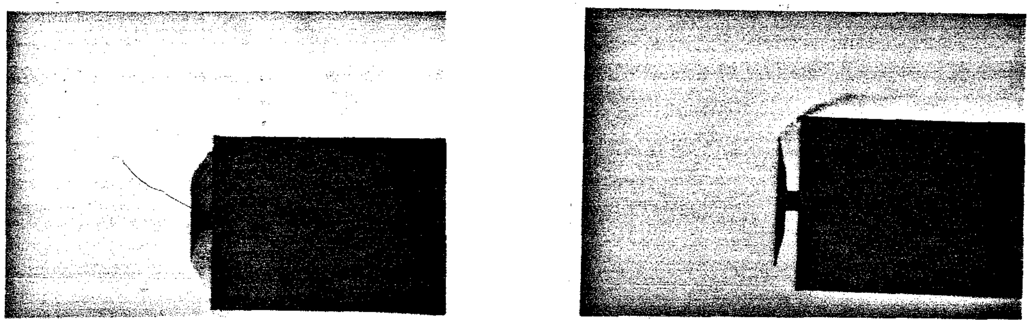

$d_1/d_2 = 0.5, \ g/d_2 = 0.125$ $d_1/d_2 = 0.75, \ g/d_2 = 0.125$

$C_D = 0.355$ $C_D = 0.626$

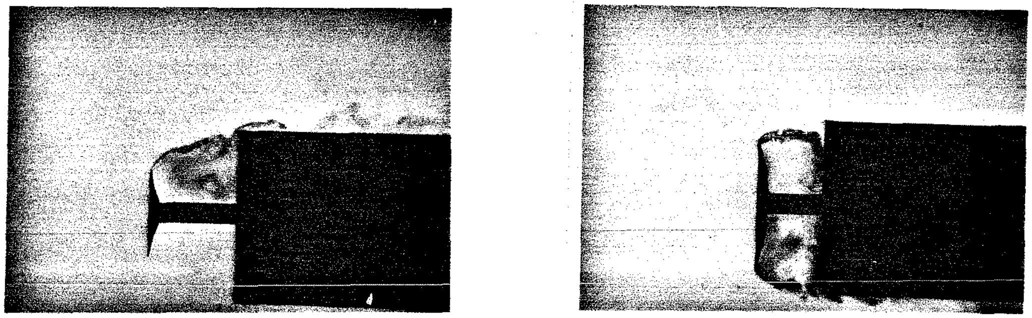

$d_1/d_2 = 0.5, \ g/d_2 = 0.5$ $d_1/d_2 = 0.75, \ g/d_2 = 0.375$

$C_D = 0.219$ $C_D = 0.065$

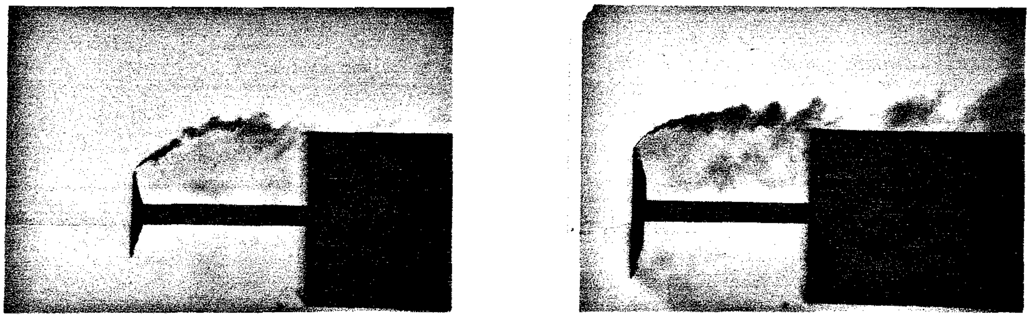

$d_1/d_2 = 0.5, \ g/d_2 = 1.0$ $d_1/d_2 = 0.75, \ g/d_2 = 1.0$

$C_D = 0.271$ $C_D = 0.107$

FIG. 66 SQUARE CROSS-SECTION FLOW VISUALIZATION

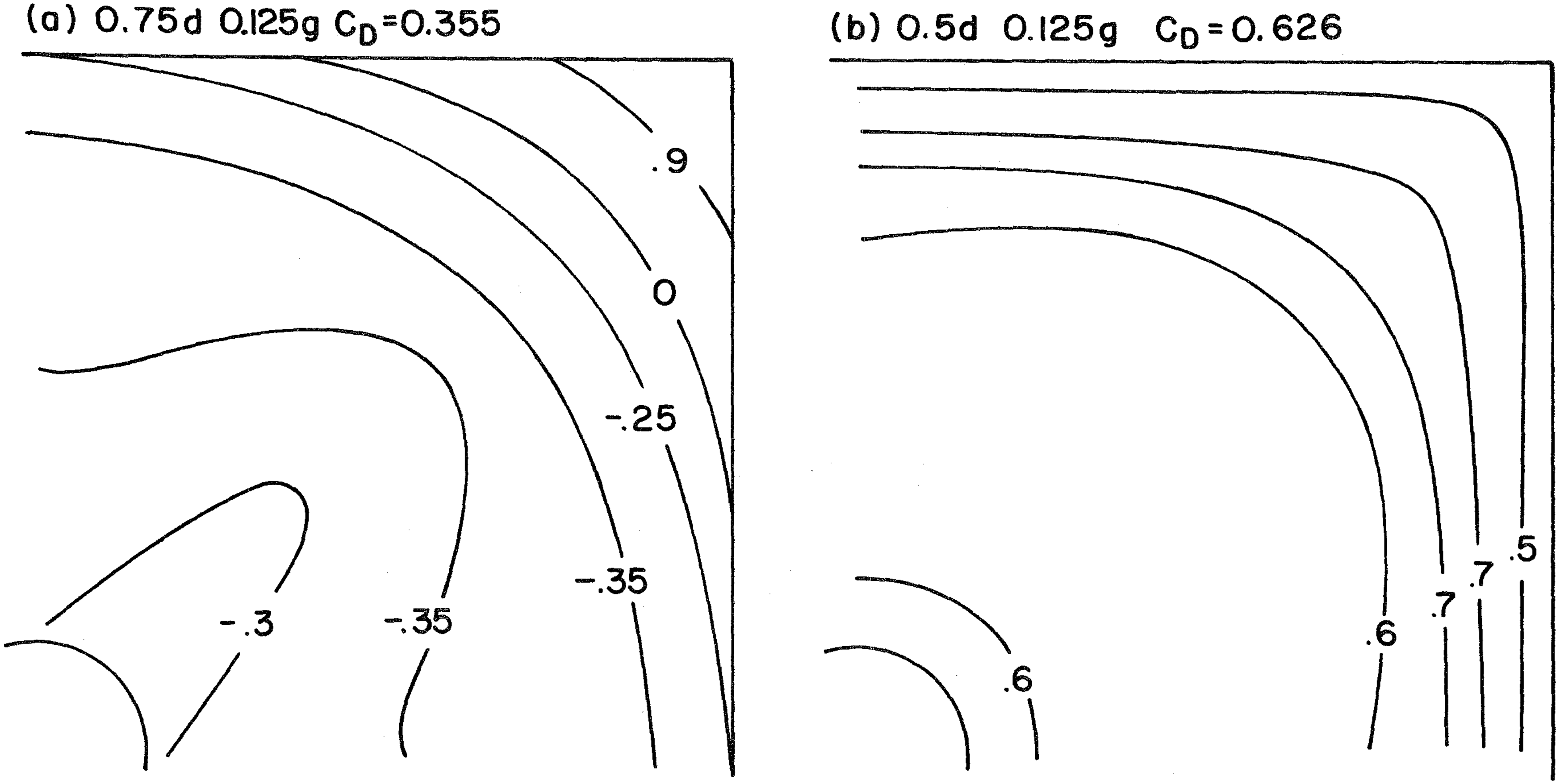
(a) 0.75d 0.125g $C_D=0.355$

(b) 0.5d 0.125g $C_D=0.626$

FIG.67 SQUARE CROSS-SECTION REARBODY FACE PRESSURE DISTRIBUTION

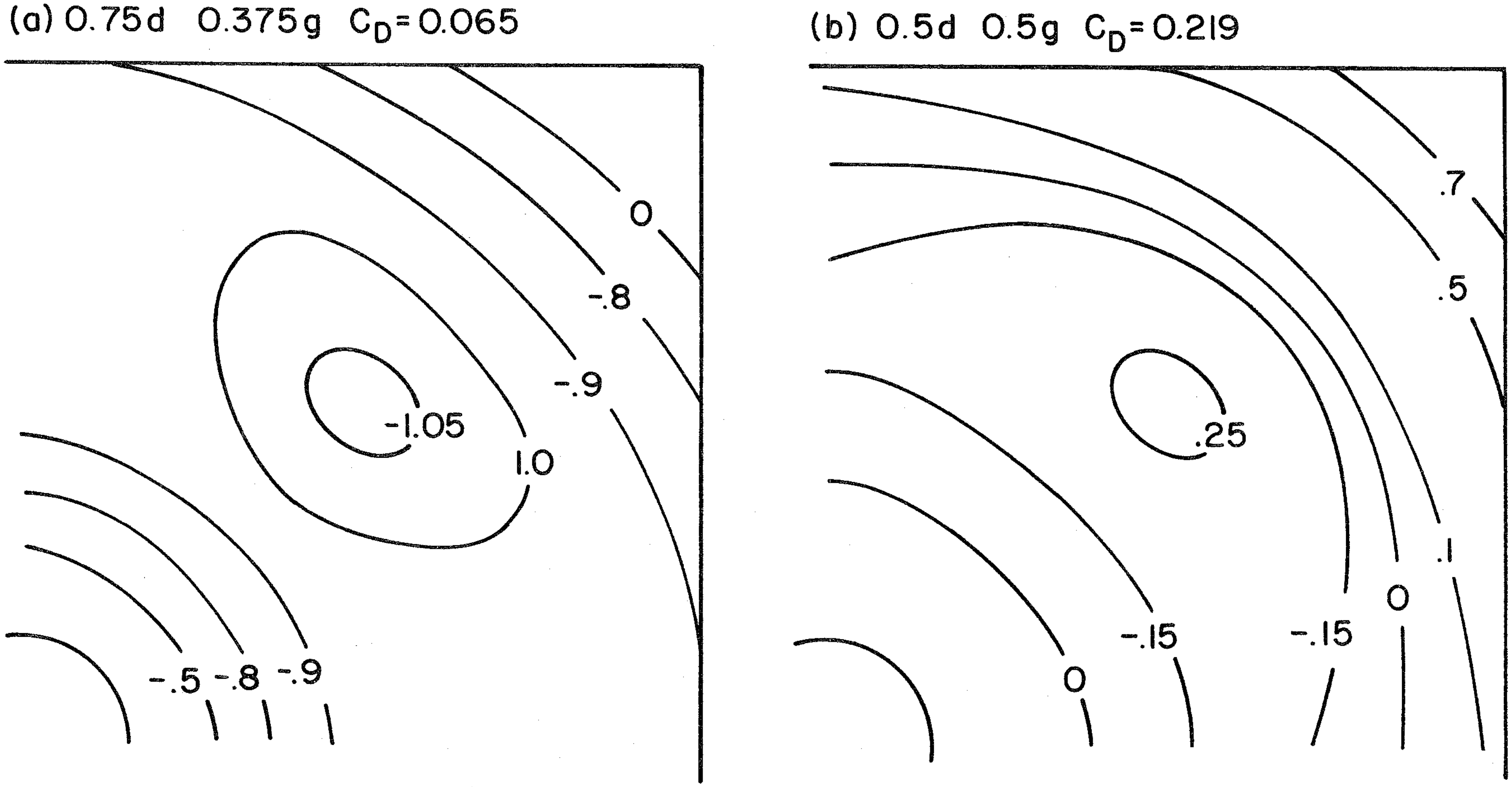
(a) 0.75d 0.375g $C_D = 0.065$

(b) 0.5d 0.5g $C_D = 0.219$

FIG. 68 SQUARE CROSS-SECTION REARBODY FACE PRESSURE DISTRIBUTION

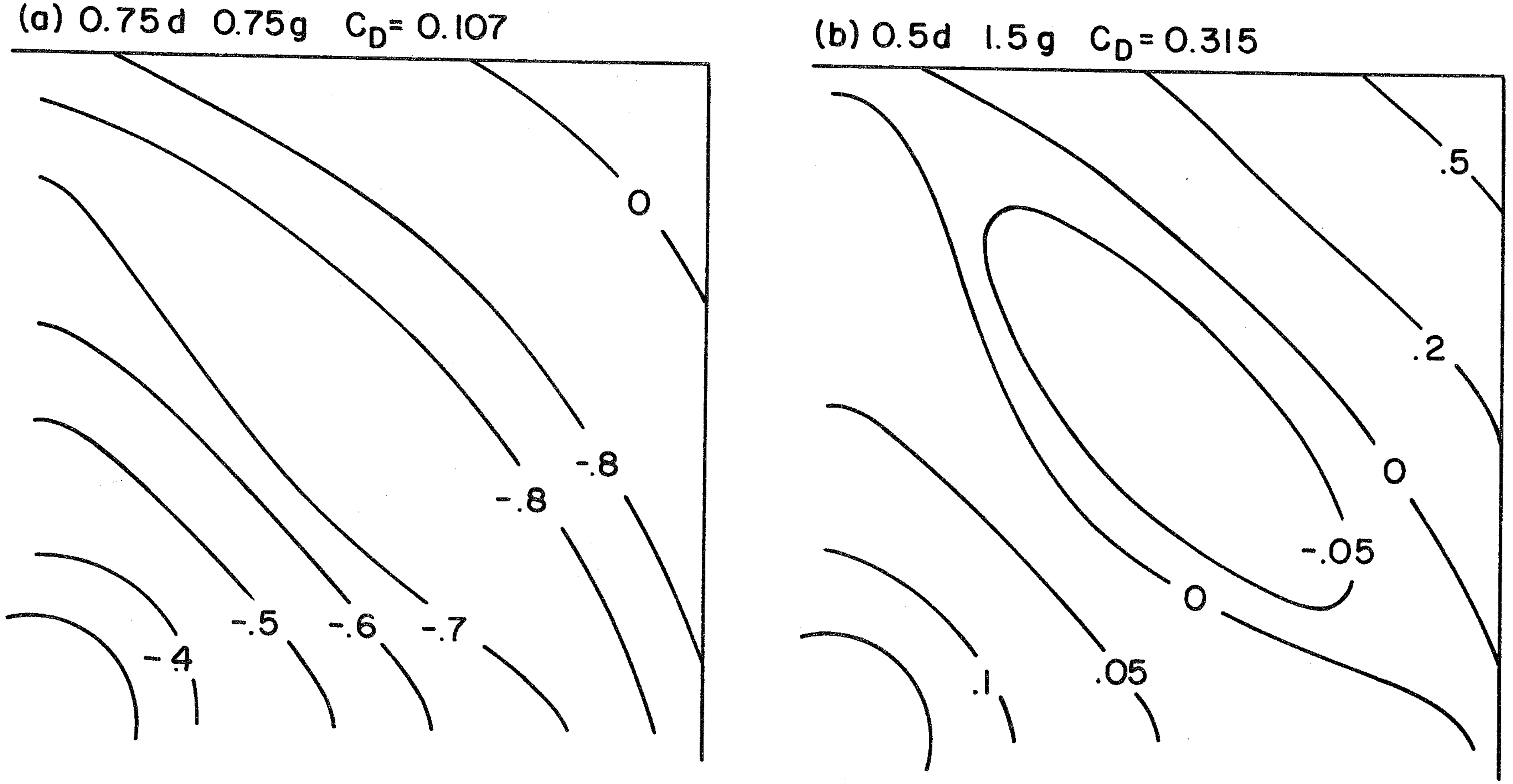
(a) 0.75d 0.75g $C_D = 0.107$

(b) 0.5d 1.5g $C_D = 0.315$

FIG.69 SQUARE CROSS-SECTION REARBODY FACE PRESSURE DISTRIBUTION

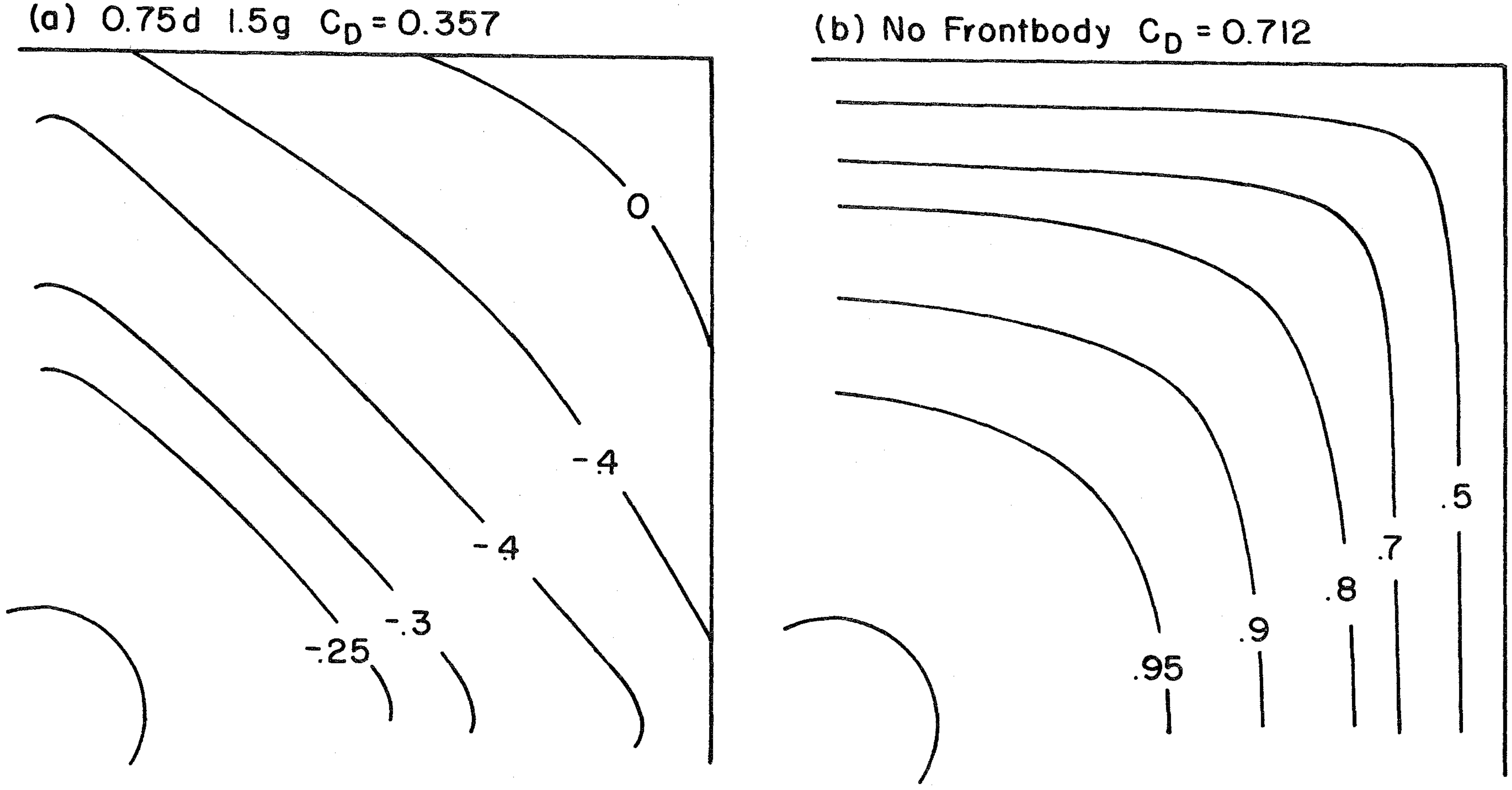
(a) 0.75d 1.5g $C_D = 0.357$

(b) No Frontbody $C_D = 0.712$

FIG.70 SQUARE CROSS-SECTION REARBODY FACE PRESSURE DISTRIBUTION

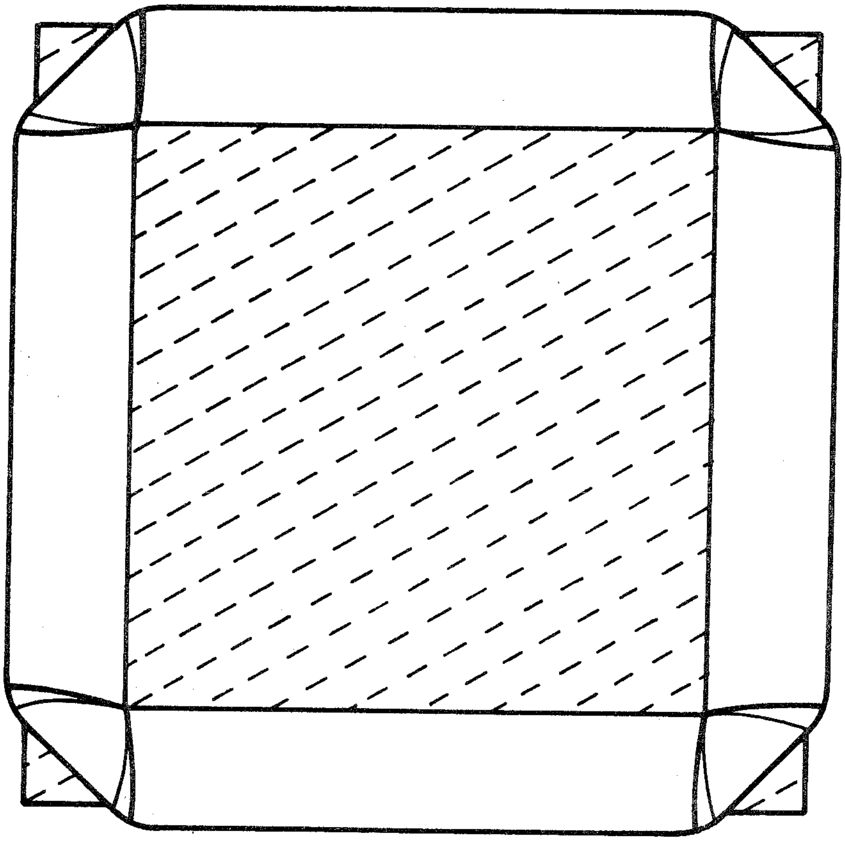

Front View of Separation Surface of Square Cross Section at Optimum Gap. Cross-Hatched Areas Denote the Exposed Faces of the Front and Rear Bodies.

FIGURE 71

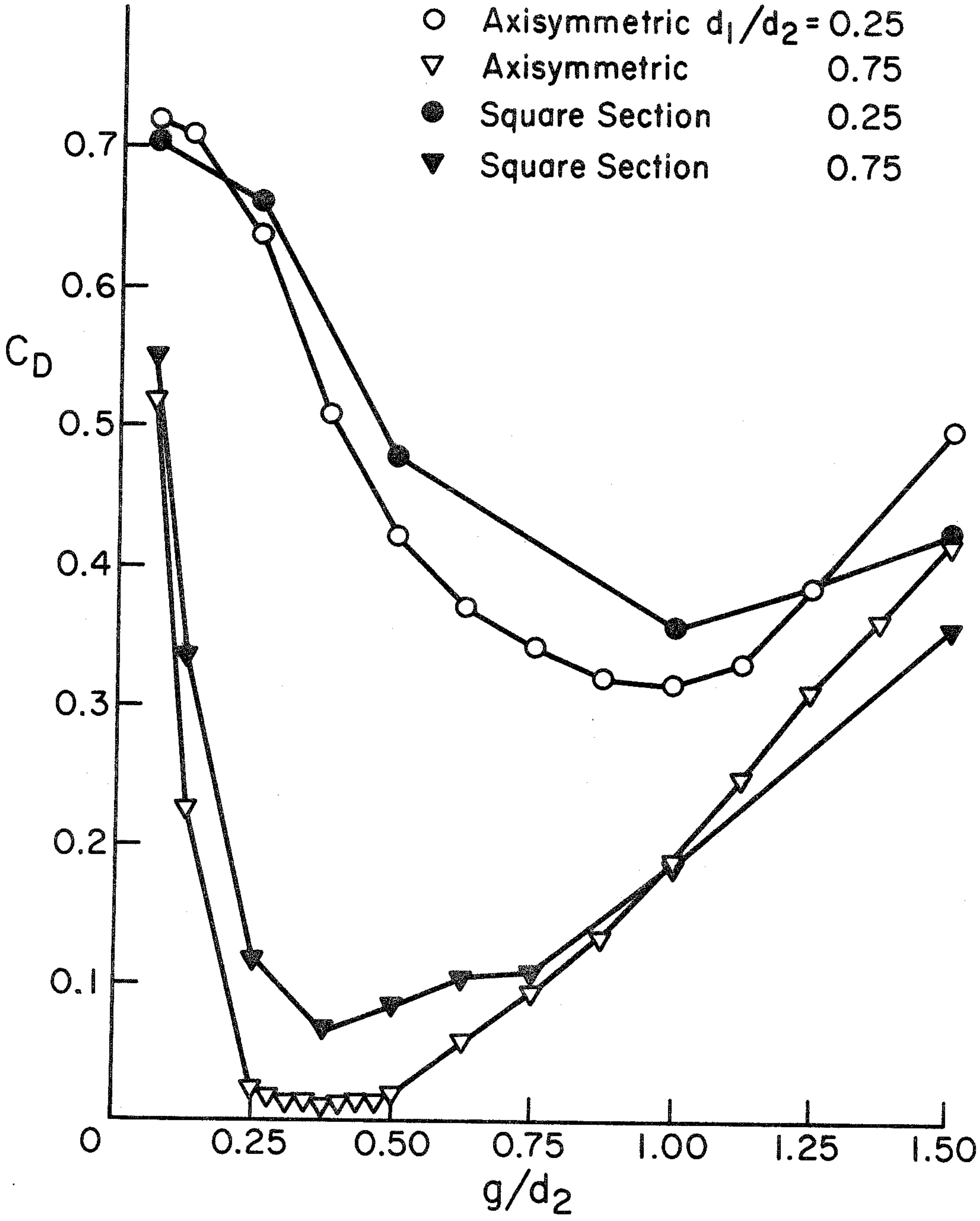

FIGURE 72 EFFECT OF CROSS-SECTION SHAPE

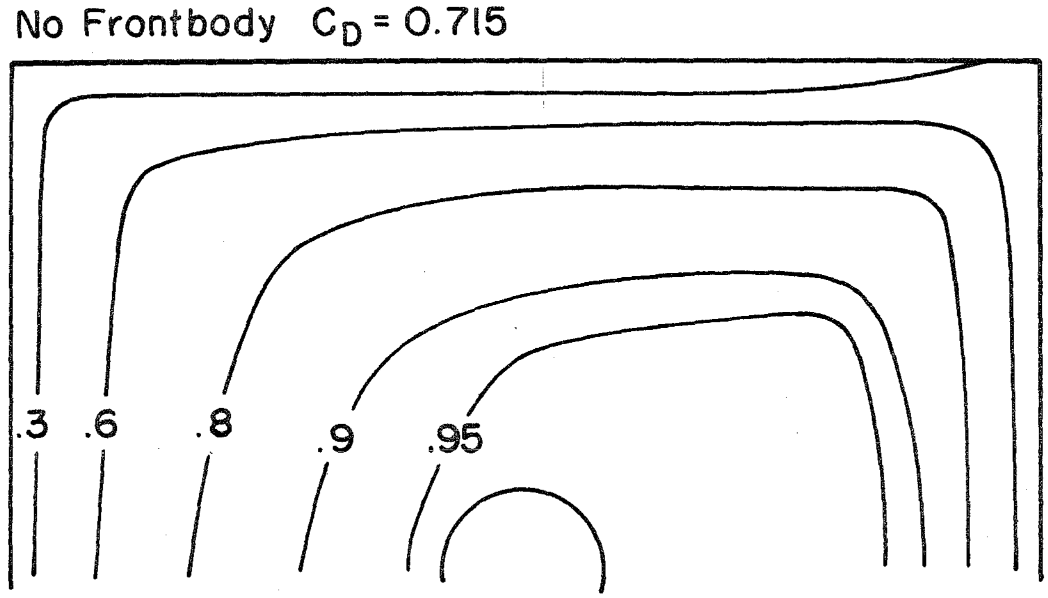

FIG.73 SQUARE CROSS-SECTION REARBODY FACE PRESSURE DISTRIBUTION, 10° YAW

(a) 0.75 d 0.375g $C_D \sim 0.3$

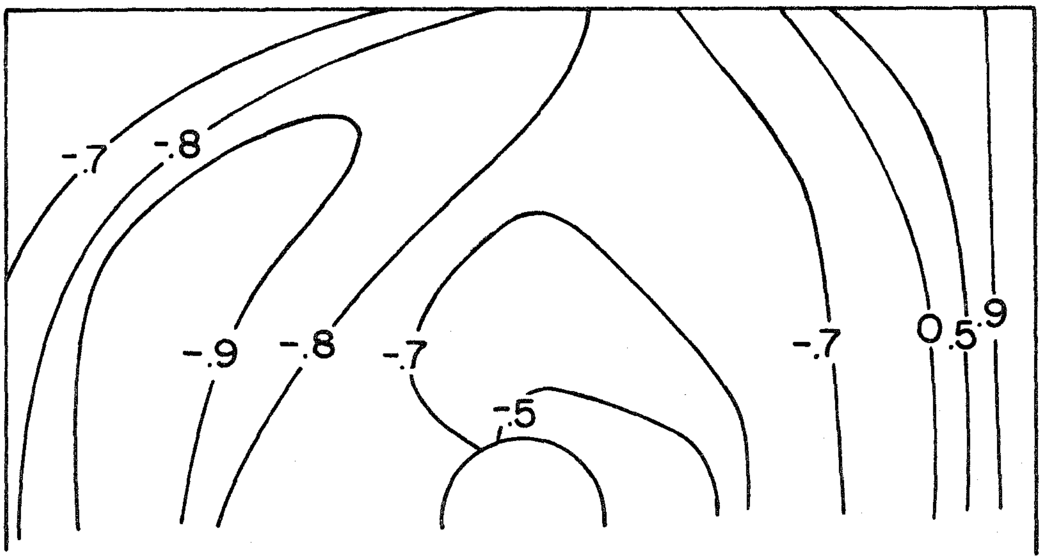

(b) 0.5 d 0.5g $C_D = 0.580$

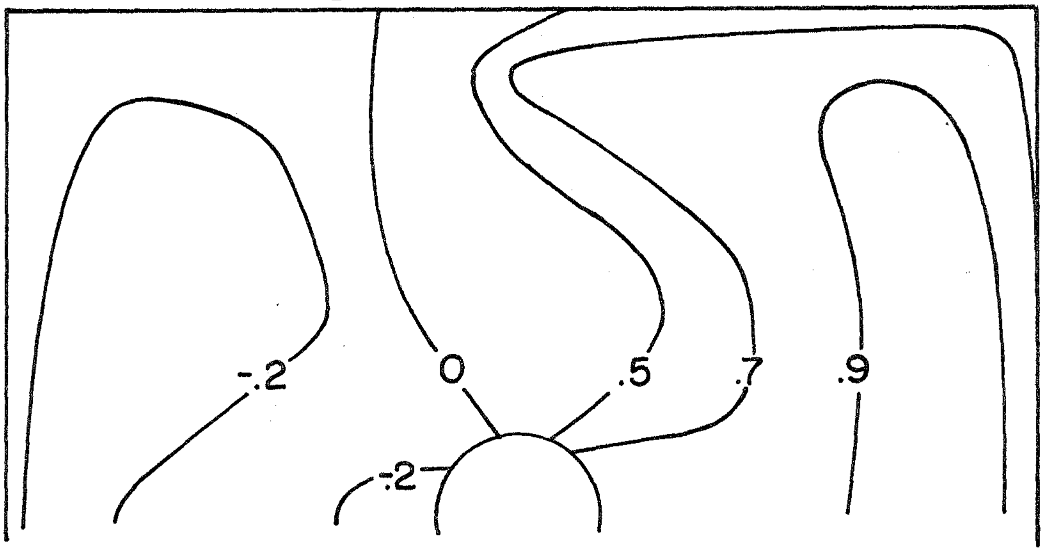

FIG.74 SQUARE CROSS-SECTION REARBODY FACE PRESSURE DISTRIBUTION, 10° YAW

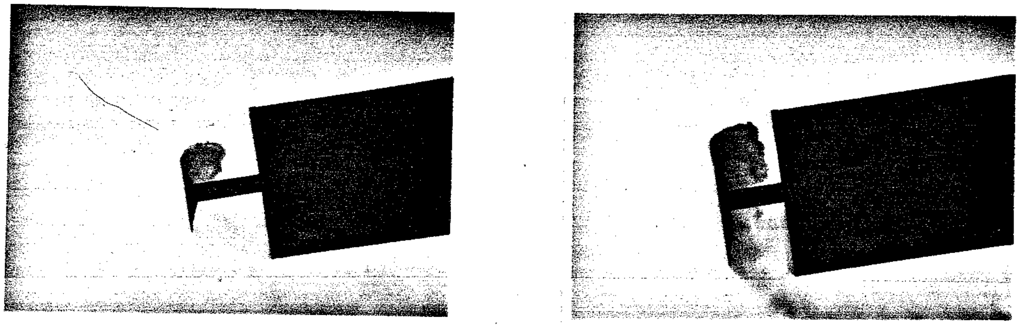

a) $d_1/d_2 = 0.5$, $g/d_2 = 0.5$
10° Yaw, $C_D = 0.580$

b) $d_1/d_2 = 0.75$, $g/d_2 = 0.375$
10° Yaw, $C_D \sim 0.3$

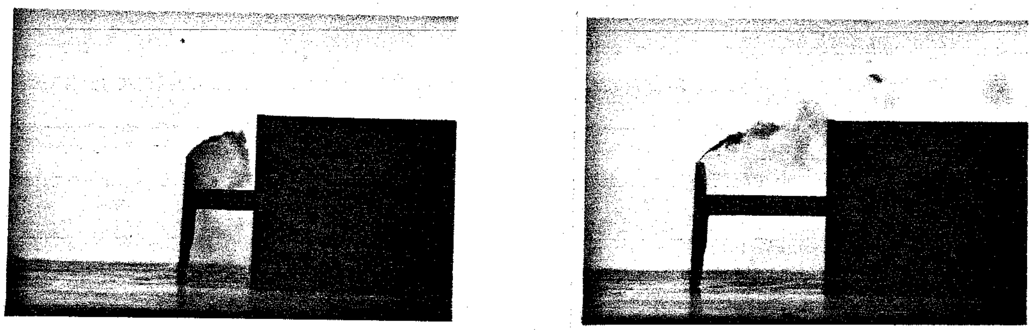

c) $d_1/d_2 = 0.75$, $g/d_2 = 0.375$,
Offcenter Plate,
No Ground Plane Gap

d) $d_1/d_2 = 0.75$, $g/d_2 = 0.75$
Offcenter Plate,
No Ground Plane Gap

FIG. 75 SQUARE CROSS-SECTION ASYMMETRIC FLOW VISUALIZATION

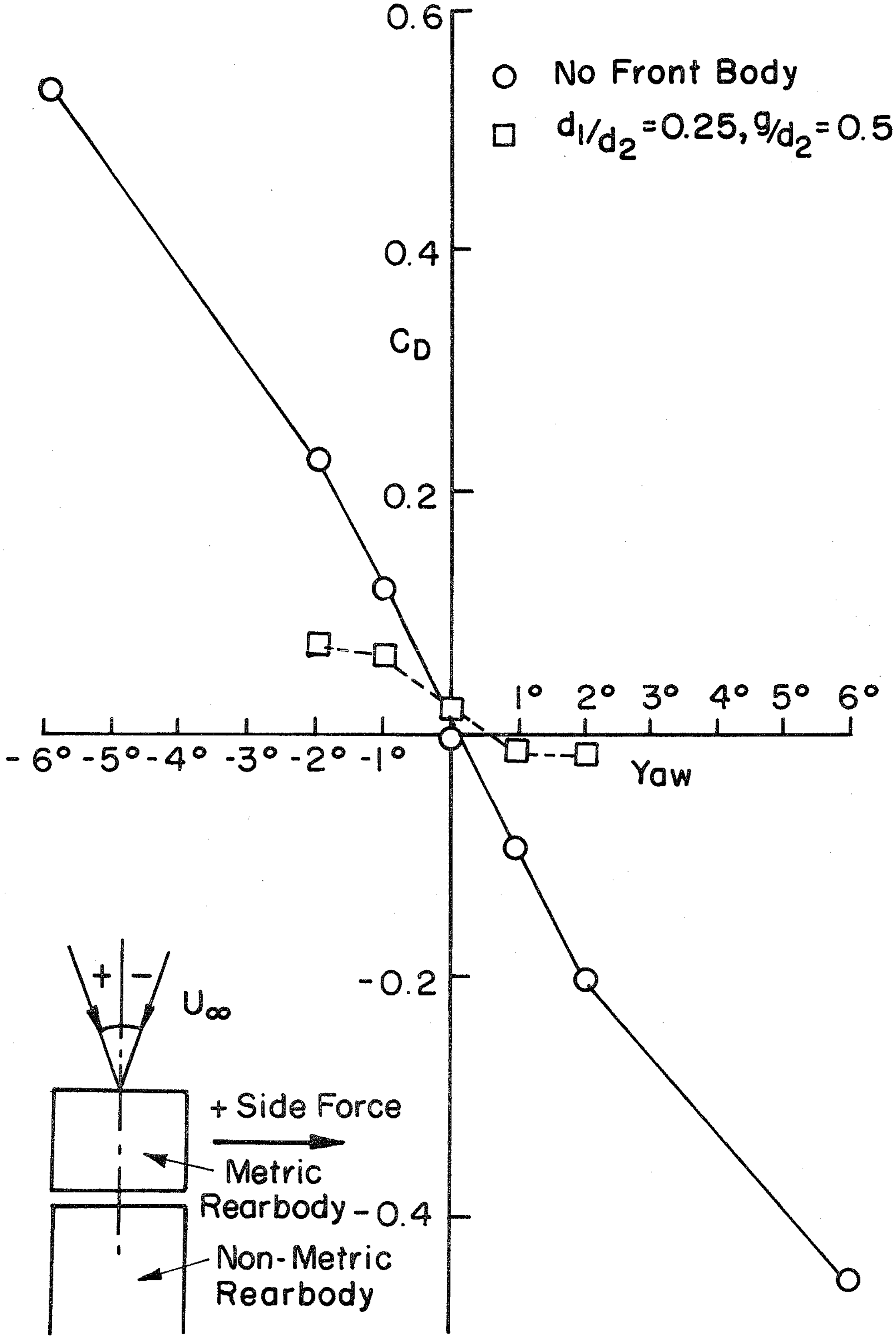

FIG.76 SIDE FORCE DEPENDENCE ON YAW

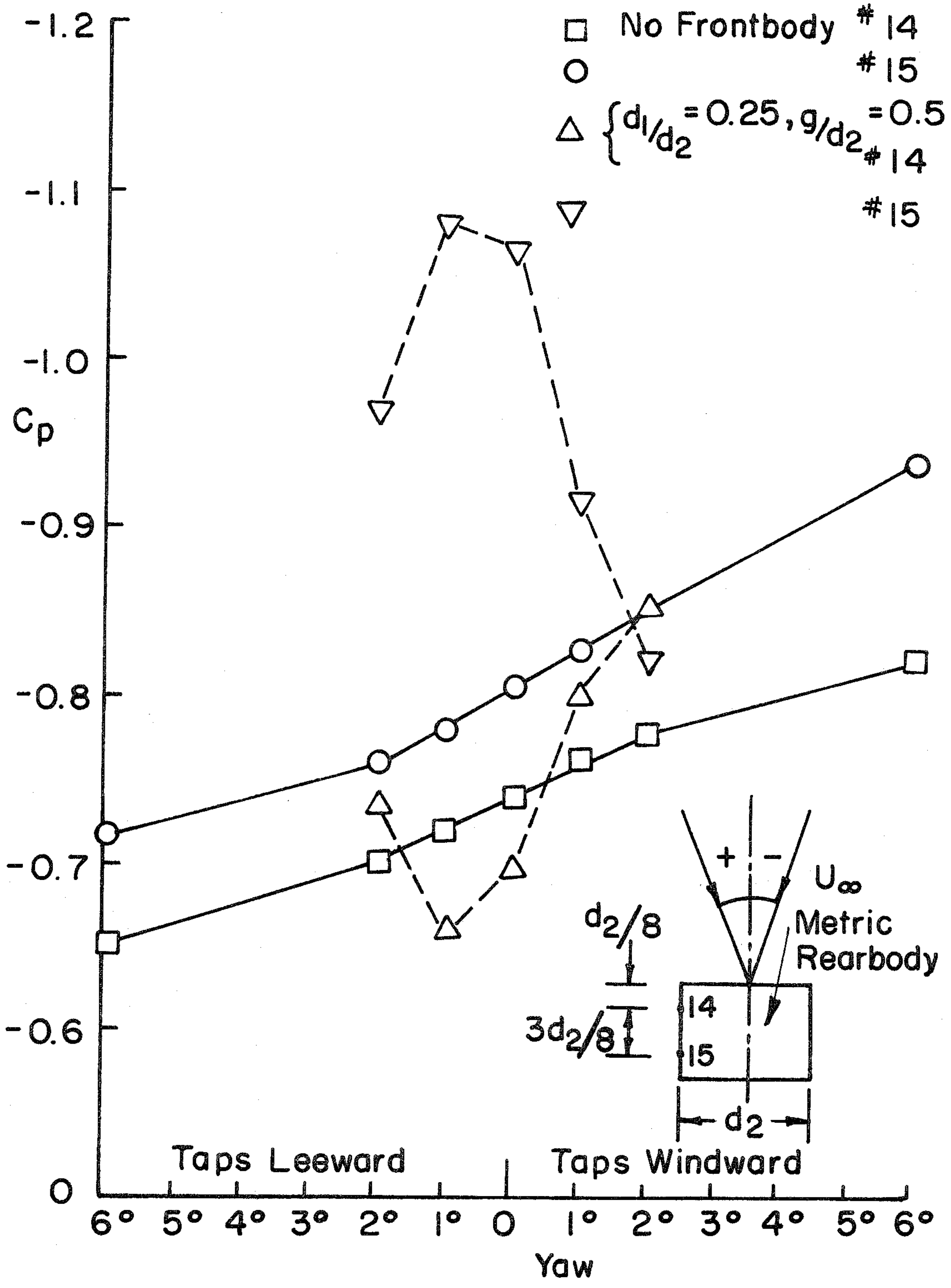

FIG.77 YAW DEPENDENCE OF SQUARE CROSS-SECTION SIDE PRESSURES

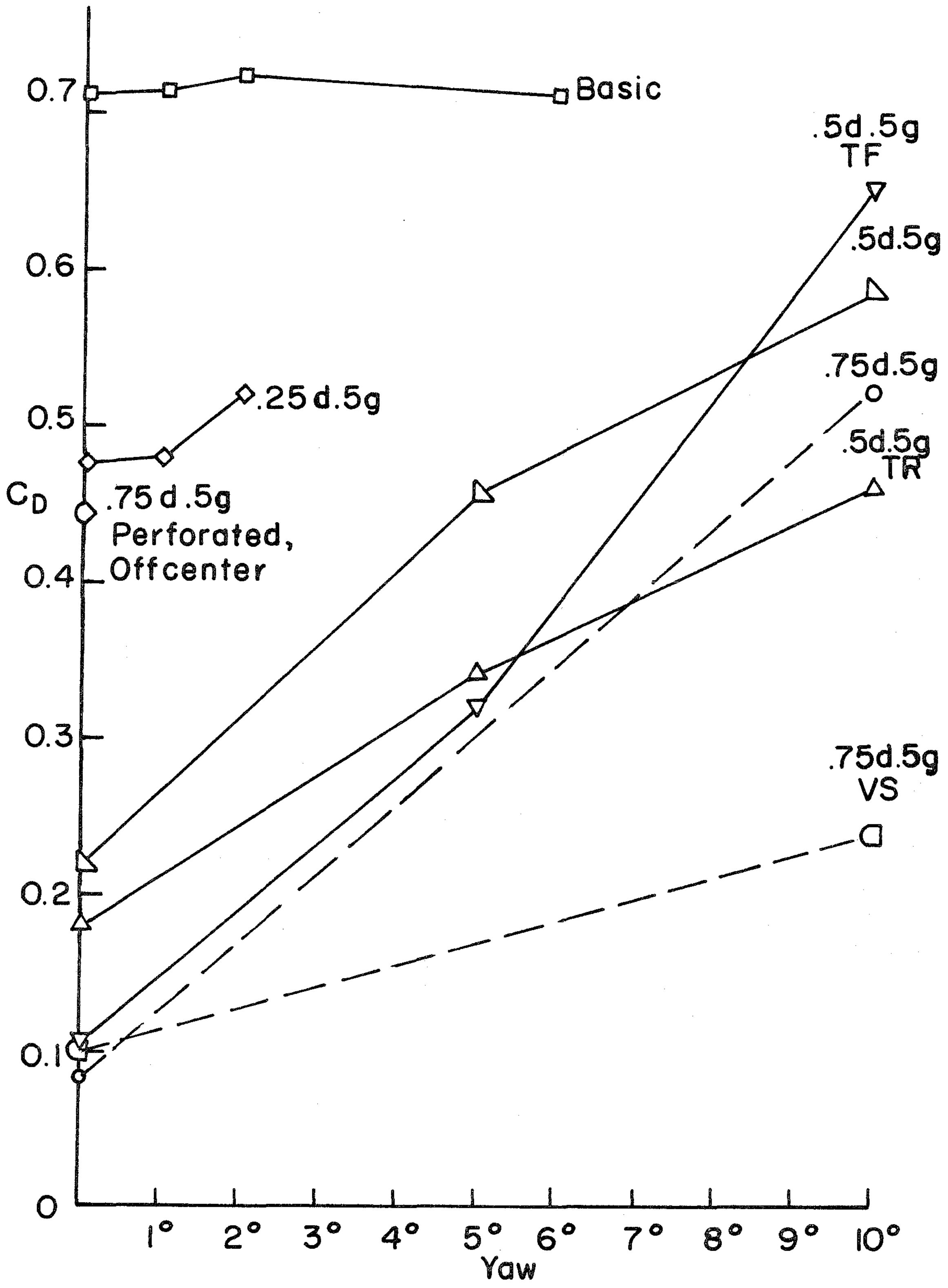

FIG.78 EFFECTS OF YAW AND MODIFICATIONS ON SQUARE CROSS-SECTION FOREBODY

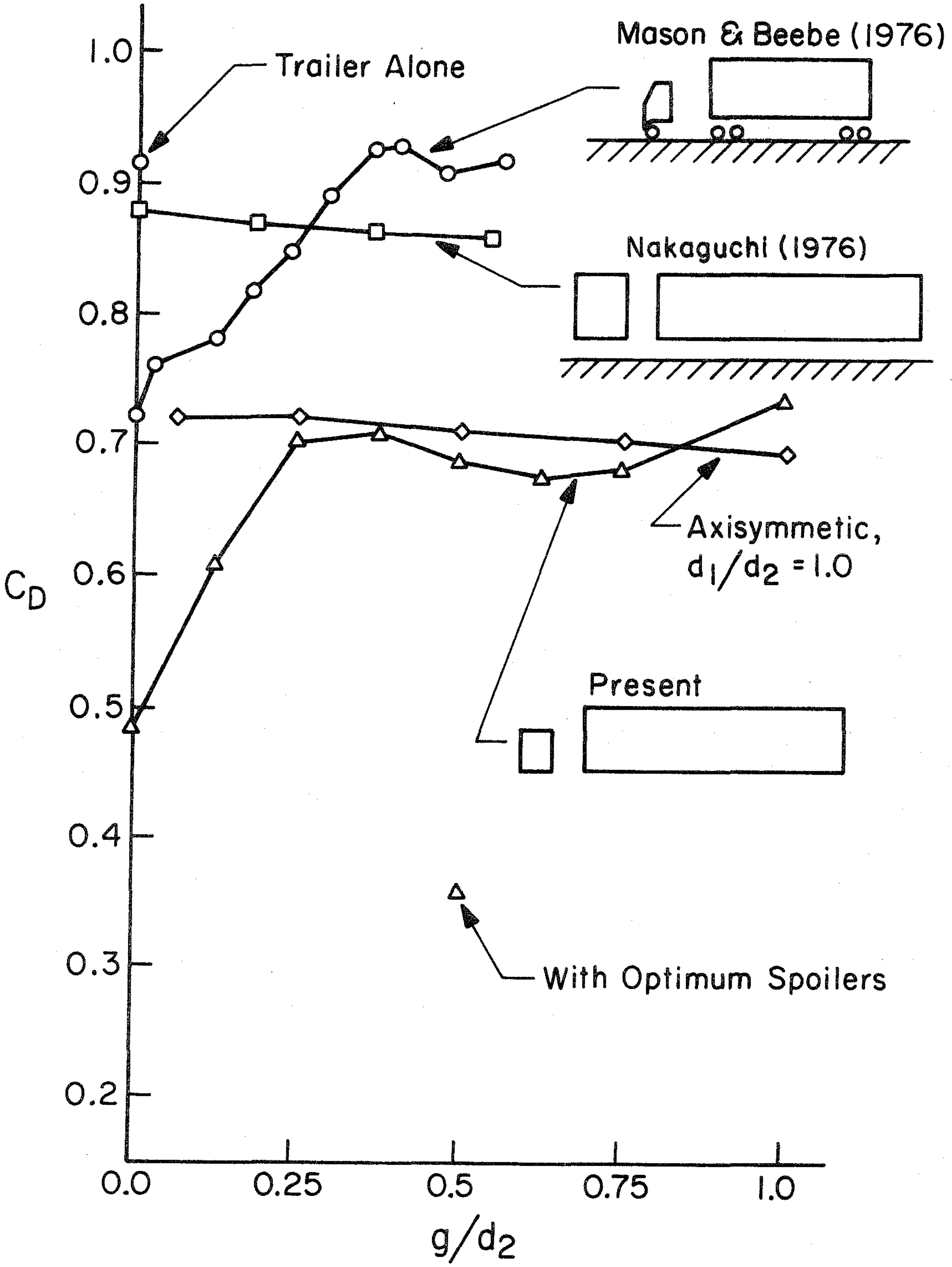

FIGURE 79 COMPARISON OF GAP EFFECTS ON SIMPLIFIED TRACTOR TRAILERS

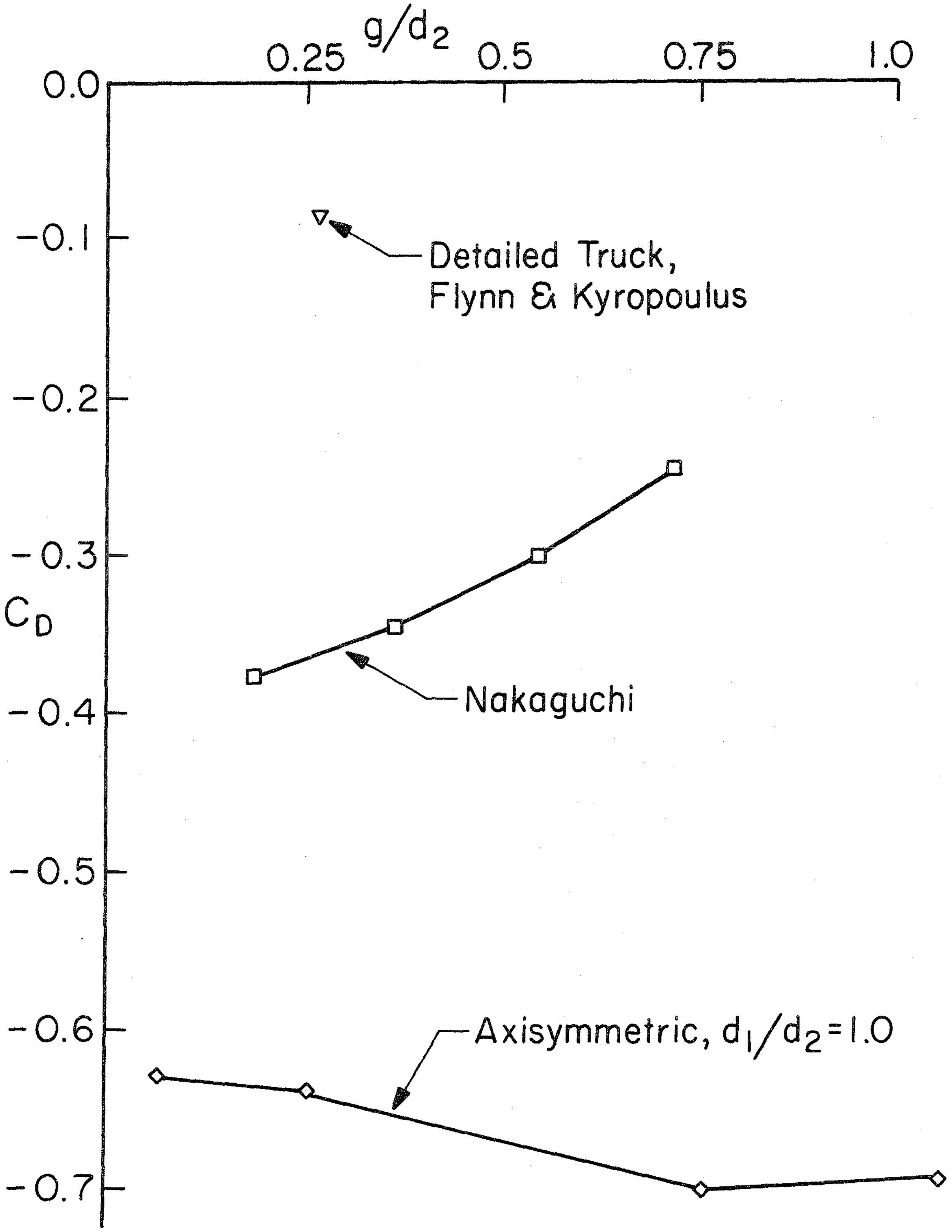

FIGURE 80 COMPARISON OF REARBODY DRAG FOR AXISYMMETRIC AND TRUCK-LIKE GEOMETRIES

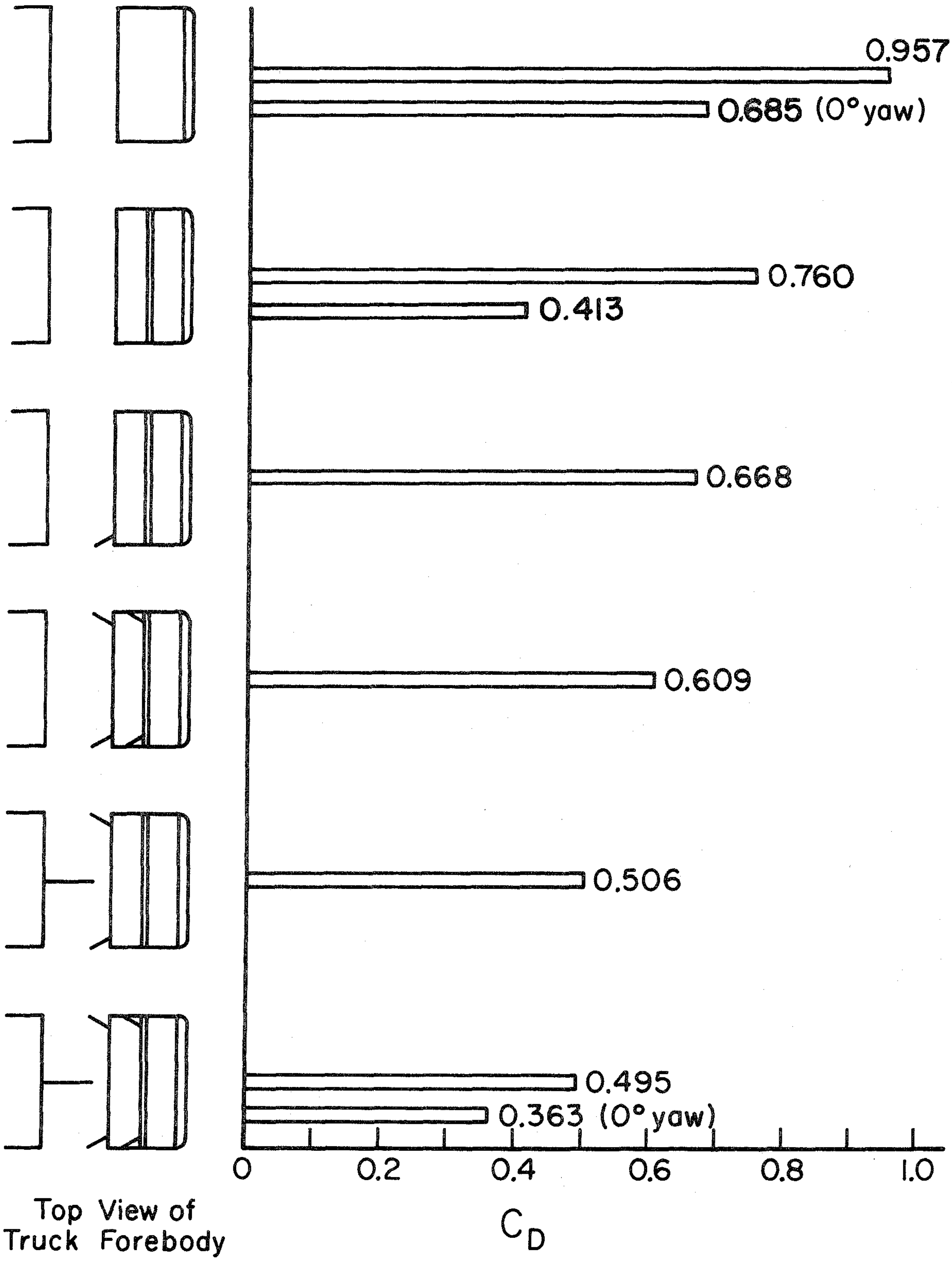

Figure 81 Effect of Various Appendages at 10° Yaw

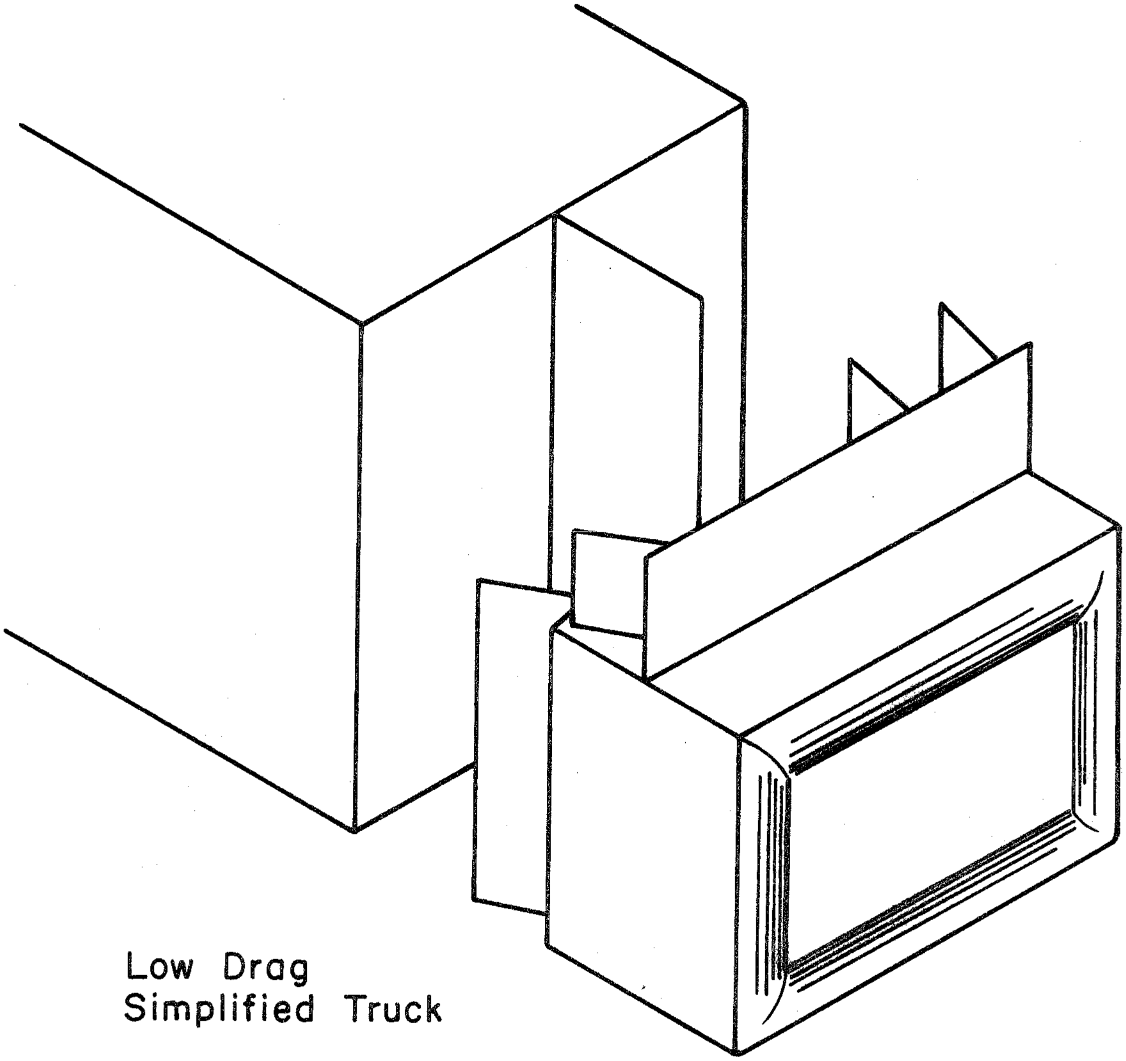

Low Drag
Simplified Truck

FIGURE 82

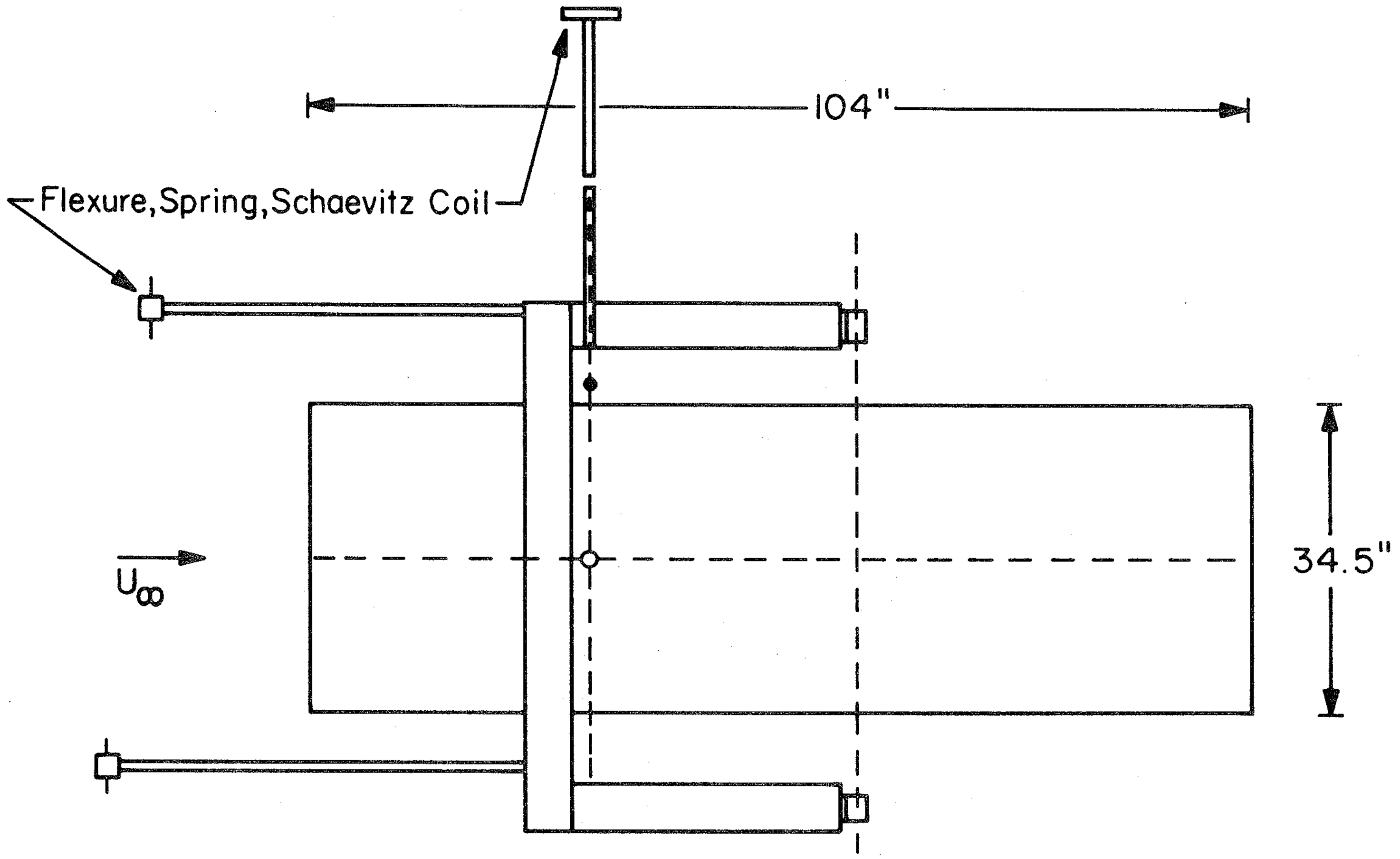

FIGURE **A 1a** MERRILL WIND TUNNEL TEST SECTION AND FORCE BALANCE

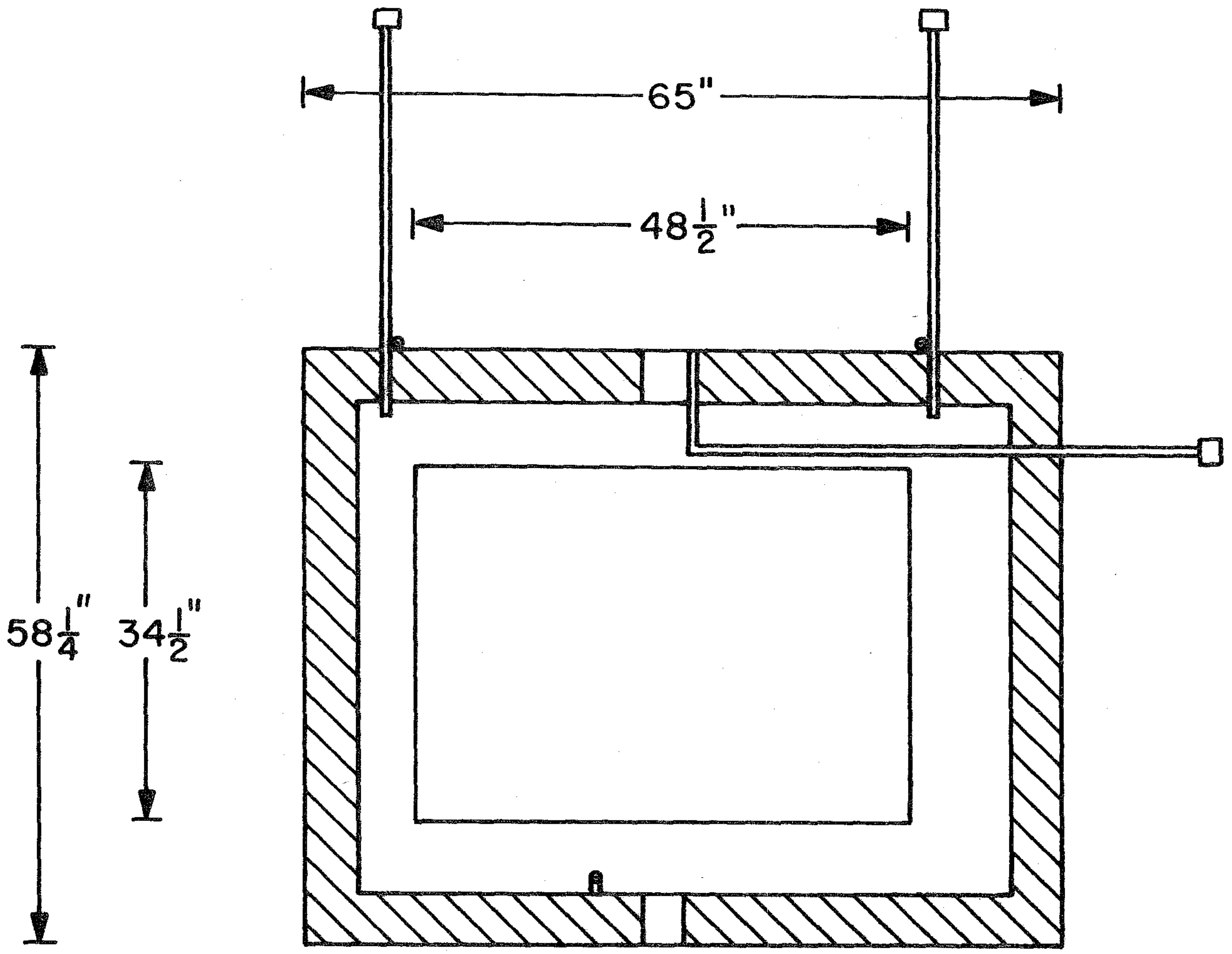

FIGURE A 1b MERRILL WIND TUNNEL TEST SECTION AND FORCE BALANCE

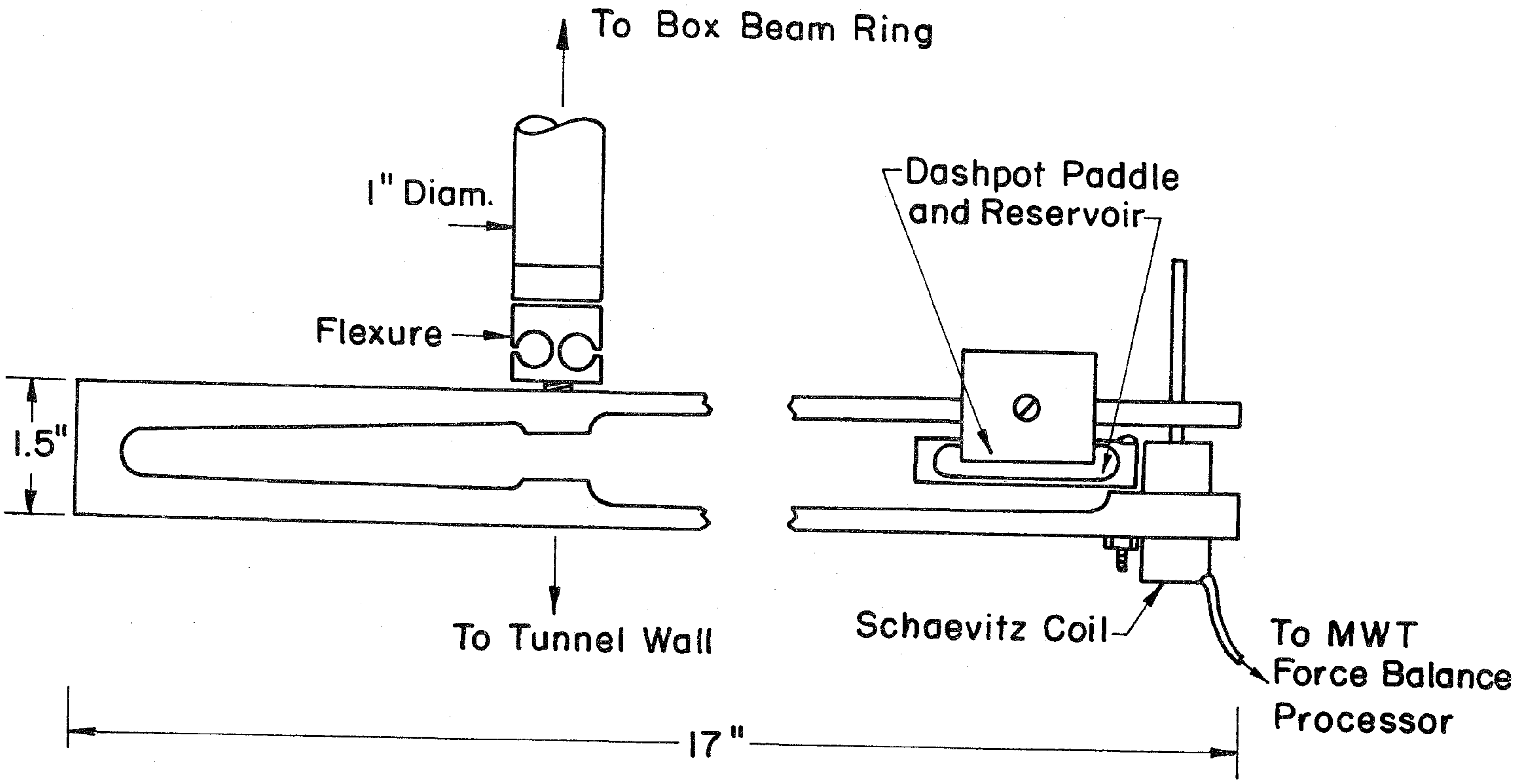

FIG. A2 DETAIL OF FLEXURE, SPRING AND SCHAEVITZ COIL ASSEMBLY

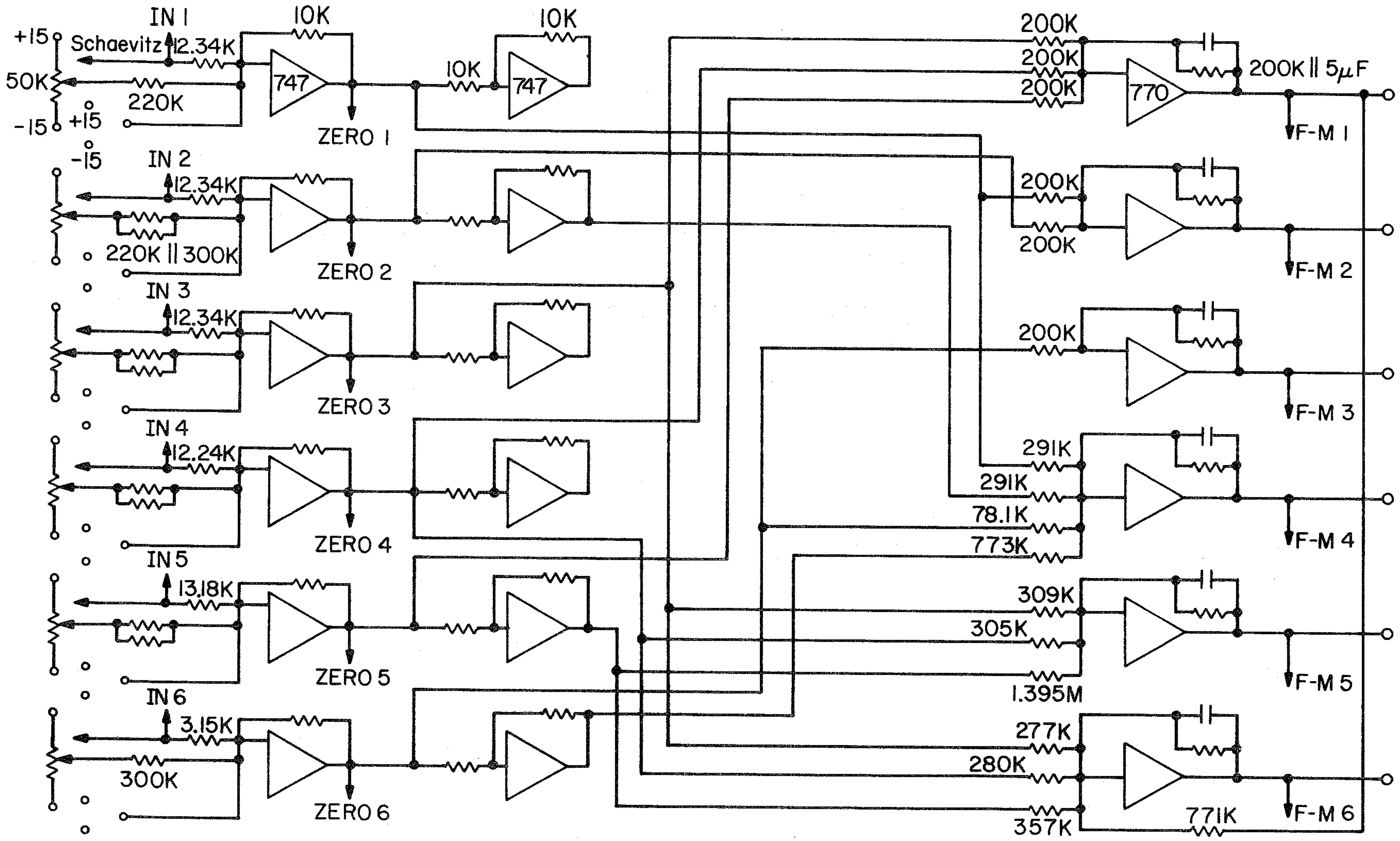

FIGURE A3 MWT FORCE BALANCE PROCESSOR SCHEMATIC, CHANNELS 1-6

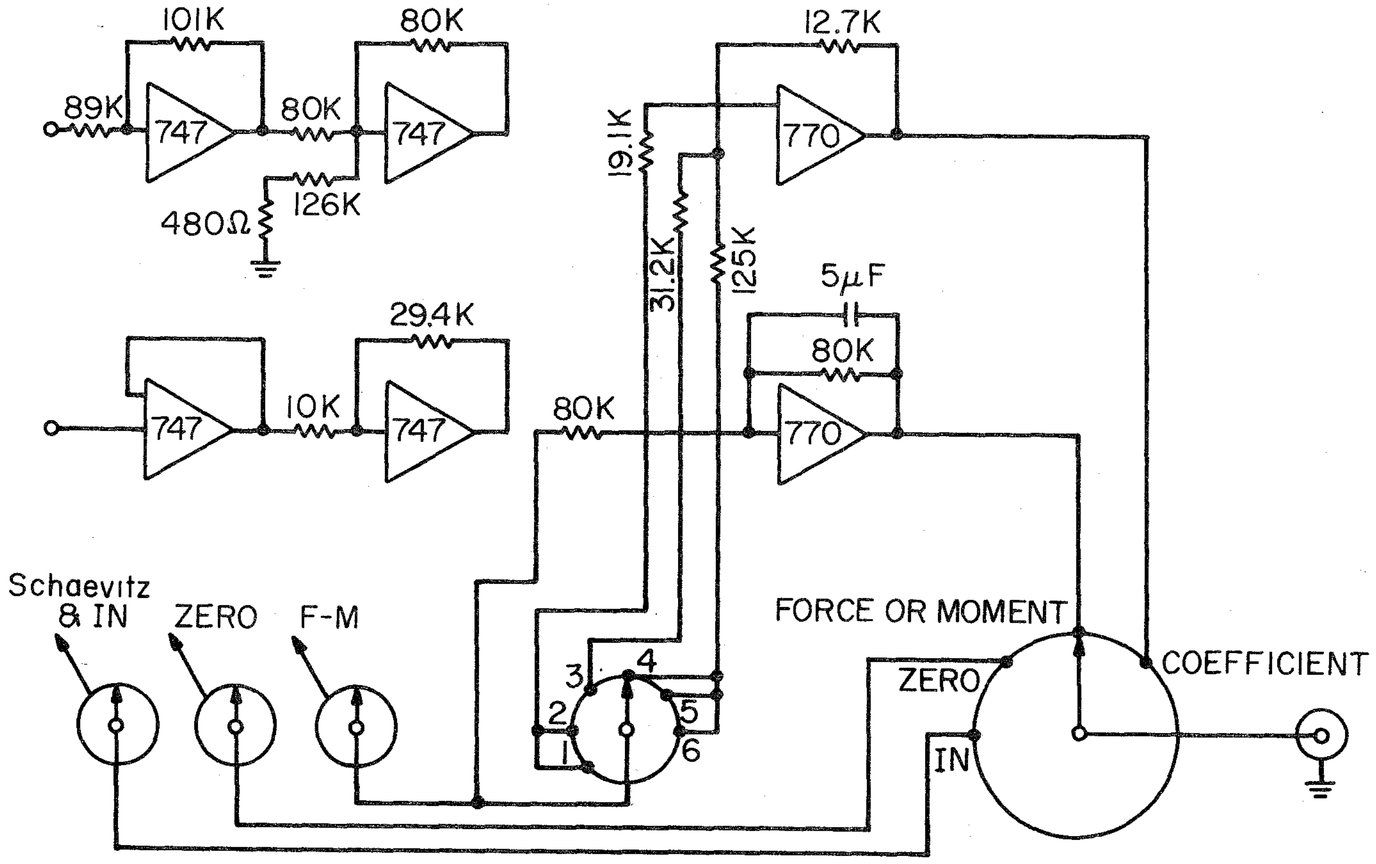

FIGURE A4 MWT FORCE BALANCE PROCESSOR SCHEMATIC, CHANNELS 7,8 & SWITCHES

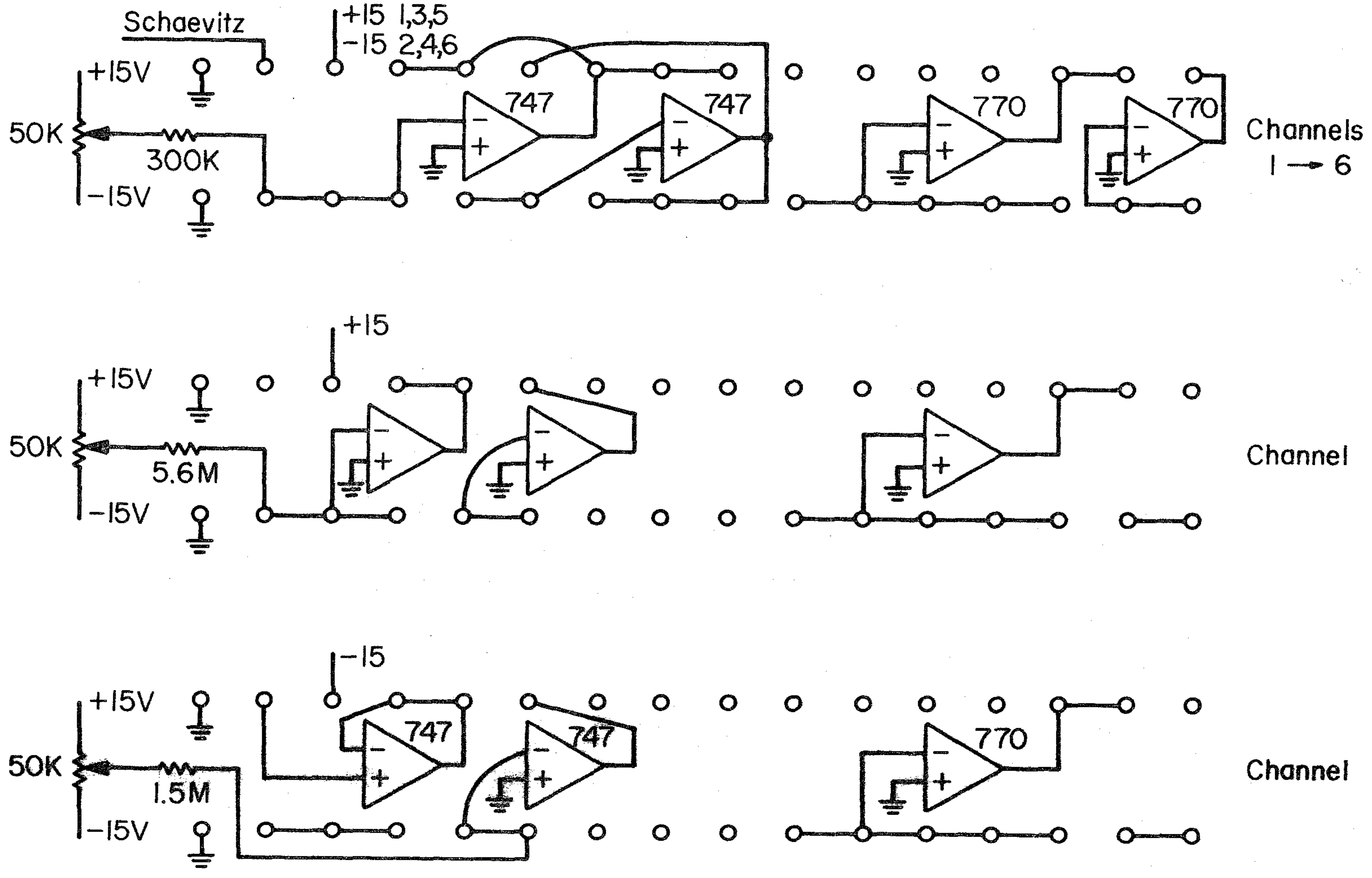

FIGURE A5 MWT FORCE BALANCE PROCESSOR WIRING DIAGRAM